THERMAL AND SPECTROSCOPIC INVESTIGATIONS ON IONIC LIQUIDS AND THEIR APPLICATIONS

Thesis submitted to the
University of Calicut in partial fulfilment of the
requirements for the award of the degree of

DOCTOR OF PHILOSOPHY

in

PHYSICS

Under the faculty of Science

By

THASNEEMA K.K

DEPARTMENT OF PHYSICS
UNIVERSITY OF CALICUT
KERALA, INDIA, 673635
NOVEMBER 2019

CERTIFICATE

This is to certify that the thesis entitled '**THERMAL AND SPECTROSCOPIC INVESTIGATIONS ON IONIC LIQUIDS AND THEIR APPLICATIONS**' submitted to the department of Physics, University of Calicut by **Mrs. Thasneema K.K** in partial fulfilment of the requirements for the award of the degree of Doctor of Philosophy in Physics is the original work carried out by her under my supervision and guidance. No part of this thesis has been submitted previously for the award of any other degree of any other University.

Calicut University
07/11/2019

Dr. Mohamed ShahinThayyil
Assistant Professor
Department of Physics
University of Calicut

UNIVERSITY OF CALICUT
Department of Physics

Calicut University P.O.,
Kerala, 673635, INDIA
0494 2407416, 9961824725
Email : shahin@uoc.ac.in
www.universityofcalicut.info

Dr. Mohamed Shahin Thayyil
Assistant Professor

CERTIFICATE

I hereby certify that **Ms. THASNEEMA K.K**, research scholar working under my guidance and supervision had incorporated all the comments, modifications and suggestions forwarded by both the adjudicators in the final copy of the thesis entitled '**Thermal and Spectroscopic Investigations on Ionic Liquids and Their Applications** submitted to the Directorate of Research, University of Calicut.

Dr. Mohamed Shahin Thayyil

29/06/2020
Kozhikode

DECLARATION

I hereby declare that the work presented in this thesis entitled "**THERMAL AND SPECTROSCOPIC INVESTIGATIONS ON IONIC LIQUIDS AND THEIR APPLICATIONS"** is the result of research work carried out byme under the guidance and supervision of Dr. Mohamed Shahin Thayyil, department of Physics, University of Calicut. It has not been included any other thesis submitted previously for the award of any other degree.

Calicut University
07/11/2019

Thasneema K.K

ACKNOWLEDGEMENTS

This thesis would not have been possible without the help and support of many people. To all of them I would like to express my heartfelt gratitude. First and foremost, I thank god almighty for his blessings in the completion of my thesis.

I am greatly indebted to my supervisor, Dr. Mohamed Shahin Thayyil. for offering me an opportunity to work in this exciting and fruitful research project, for his patience, encouragement, guidance and support on my research work. He did whatever was required, for the successful completion ofthe endeavour. I am gratified to have been a member of his group and part of his achievement.

I would like to thank to Dr. A. M Vinod Kumar, head of the department, for his support to completion of my thesis work. I am forever devoted to Prof. Antony Joseph, Prof. P. P Pradyumnan, Prof. M. M Musthafa, Dr. C.D Ravikumar and Dr. Libu K. Alexander for offering their personal and institutional support.

I extremely thankful to former Vice Chancellor, University of Calicut, Dr. M. Abdu Salam for his limitless support and encouragement.

I am deeply grateful to Dr. A. B Moideen Kutty, former HOD, department of Arabic, University of Calicut, for his advice, encouragement and support for completion of my PhD work.

I would like to express my sincere thanks to Dr. Jisha, Dept. of Folklore, University of Calicut, and all staff members of Folklore department (Mr.Baiju, Mr. Shanmughan, Mrs. Dhurga Devi) for providing me a friendly support for completion of my work.

My deepest thanks go to Dr. V. B Panicker, former director, KMCT group of institutions, for his support and inspiration throughout my PhD work. My special thanks goes to Dr. Muraleedaran, department of Chemistry, University of Calicut for his help to do DSC experiment.

My sincere thanks go to Dr. Hafis Mohammed, famous psychologist and writer, for his advice and support during my PhD work. My special tributes go to all other teachers who have taught me and helped me to rise to this level.

I express my sincerest thanks to Sahra Mohamed, Sulaiman M.K, Aboothahir Afsal, Nighil Nath,Shabeeba, Binesh, Jamshi Has, Safna Hussan, Nithu Asok, Sravan Das, Jumana, Shabeer and all non-teaching staff of the department of Physics,(Mrs. Vasanthi, Mr.Baijith Kumar, Mr.Saidalavi, Mr.Rasheed, Mr.Abdul Rahman and Mr. Udayappan), University of Calicut for their help and co-operation.

I express my special thanks to Dr.Sindhu S (Asst.Professor, Dept of Nano Science), Dhanya and Sangeetha (Assistant and Librarian, Dept of Nano Science) for providing a pleasant place to work. I would like to thank all my friends of the department of Nano Science.

I offer my heartful thanks toJency Mohan, Shamsiya, Jaseela, Dipin, Shyam, Nadira, Jithin, Anju and Shivanand Department of Chemistry, for their kind cooperation and unfailing support. Shameema, Raina, Sumesh, (AD)Shahina (DSFC), Baby Sumam (GA) (Assistants, University of Calicut) and Haseena Office attendant (GA) deserve special acknowledgements for their encouragement and support to complete my thesis work.

I would like to thank my colleagues of office attendants (Mrs Baby, Moly, Jamal, Rajini, Ajitha) and all staff members of DOR, all staff members of CSIF,University of Calicut, for their assistance and lasting support for completion of my work.

I would like to thank JayantKolte, IIT Mumbai and Saharuba, NIIST, Trivandrum, for their valuable help in completion of my thesis.I offer my special thanks to Prof. Somnath Chanda Roy, Midhunlal PV, Swati and Geethu PM of IIT Madras for their help in DSC experiment.My Special thanks go to Dr.Govindaraj G and Dr. N.S Krishna Kumar, Department of Physics, Pondichery University, for their help in BDS data analysis.

I gratefully acknowledge the UGC, Govt. of India for the financial assistance through BSR fellowship. I would like to extend my sincere gratitude to the Central Sophisticated Instrumentation Facility (CSIF),University of Calicut.

Finally, my parents, my husbandand my son deserve my deepest thanks and appreciation, for their love, for laughs, for tears, for support,for goodwill,for everything, upon which I have been able to rely in difficult timesand encouraging me to pursue my dream of Ph.D. I thank all those who have challenged me and helped me think through and clarifymy ideas.

Thasneema K.K

"Everybody is a genius. But if you judge a fish by its ability to climb a tree it will live its whole life believing that it is stupid"

Albert Einstein

Dedicated to

My son Ajeer Muhammed Hamdan

"To steal ideas from one person is plagiarism, to steal from many is research"

Wilson Mizner

CONTENTS

LIST OF TABLES

LIST OF FIGURES

ABBREVIATIONS

DFT	Density functional theory
DSC	Differential scanning calorimetry
FT IR	Fourier transform infra red
IL	Ionic liquid
RTIL	Room temperature ionic liquid
PVA	Poly vinyl alcohol
$[P_{14,6,6,6}][NTf_2]$	Trihexyltetradecylphosphoniumbis(trifluoromethylsulfonyl)amide
$[P_{14,6,6,6}][N(CN)_2]$	Trihexyltetradecylphosphoniumdicyanamide
$[P_{14,6,6,6}][Cl]$	Trihexyltetradecylphosphonium chloride
MW	Molecular weight
TGA	Thermogravimetric analysis
BDS	Broadband dielectric spectroscopy
HN	Havriliak -Negami
KWW	Kohlrausch Williams Watts
Tg	Glass transition temperature
VFT	Vogel FulcherTammann

POMPetra, Osiris, Molinspiration

LIST OF PUBLICATIONS/ PAPERS PRESENTED

1. Dielectric relaxation and electrochemical studies on trihexyltetradecyl phosphonium chloride [P14,6,6,6][Cl] ionic liquid **Thasneema K K**, Shabeeba P, Mohamed ShahinThayyil,Pillai M P, Krishna Kumar N S, Govindaraj G,Saheer V C, NighilNath MP, Journal of Molecular Liquids 252,488–494 (**2018**)

2. Conductivity relaxation and charge transport of trihexyltetradecylphosphoniumdicyanamide ionic liquid by broadband dielectric spectroscopy **Thasneema K. K**, M. ShahinThayyil, Krishna Kumar N. S, Govindaraj G, and V. C. Saheer,AIP Conference Proceedings 1942, 070031 (**2018**)

3. Thermal and spectroscopic investigations on three phosponium based ionic liquids for industrial and biological applications **K. K. Thasneema** , Mohamed ShahinThayyil , TanciaRosalin , K. K. Elyas , T. Dipin , Pramod K. Sahu, N. S. Krishna Kumar, V. C. Saheer, MouslimMessali, Taibi Ben Hadda, Journal of Molecular Liquids 307, 112960, (2020).

4. A high voltage supercapacitor based on ionic liquid with anactivated carbon electrode Shabeeba Pilathottathil, **K KThasneema**, Mohamed ShahinThayyil, M P Pillaiand C V Niveditha,Mater. Res. Express 4,075503 (**2017**)

5. A graphene-based flexible supercapacitor usingtrihexyl (tetradecyl) phosphoniumbis (trifluoromethanesulfonyl) imide ionic liquid electrolyte ShabeebaPilathottathil, **K KThasneema**, Mohamed ShahinThayyil, M P Pillaiand C V Niveditha, Mater. Res. Express 4,085501 (**2017**)

6. Inorganic salt grafted ionic liquid gel electrolytes for efficient solid state supercapacitors: Electrochemical and dielectric studies. Shabeeba P,**Thasneema K K,** Mohamed ShahinThayyil, Pillai M P, Jemshihas AP,Journal of Molecular Liquids 264,72–79 (**2018**)

7. PMMA-RTIL electrolyte for high –energy supercapacitors: A comparison of different anions Shabeeba P,Mohamed ShahinThayyil, Pillai M P, **Thasneema K K,**,Journal of Molecular Liquids 294,111671 (**2019**)

8. Studies on molecular dynamics and in silico ADMET analysis of Lidocaine docusate and Ranitidine docusate Ionic liquids (revision requested) **K. K. Thasneema**, Mohamed ShahinThayyil, T. Dipin , Pramod K. Sahu, N. S. Krishna Kumar, V. C. Saheer&MouslimMessali, Journal of Molecular Liquids (2020).

9. Dielectric relaxation and charge transport on phosphonium based ionic liquid mixtures containing a common cation and its application in dye removal (Under review). **K. K. Thasneema**, Mohamed ShahinThayyil, Pramod K. Sahu, N. S. Krishna Kumar, MouslimMessali, Taibi Ben Hadda, Journalof Chemical & Engineering Data.

10. Investigations on Dielectric relaxation dynamics of Trihexyltetradecylphosphoniumbis(trifluoromethylsulfonyl)amide ionic liquid and its prediction of in silico analysis, biological activity and extraction of dyes (Under review) **K. K. Thasneema**, Mohamed ShahinThayyil, Pramod K. Sahu, N. S. Krishna Kumar, MouslimMessali, Taibi Ben Hadda,Journal of Molecular Liquids.

11. Removal of toxic dyes, phenolic compounds and metal oxides using phosphonium based ionic liquids (Under review) **K. K. Thasneema**, Mohamed ShahinThayyil, Pramod K. Sahu, N. S. Krishna Kumar, MouslimMessali, Taibi Ben Hadda,Journal of hazardous materials.

12. Attended and participated in the 62nd DAE- Solid state Physics symposium held at Bhabha Atomic Research Centre, Mumbai during 26/12/2017-30/12/2017

13. Attended and participated in the DAE-BRNS 6th interdisciplinary symposium on Materials Chemistry held at Bhabha Atomic Research Centre, Mumbai during 06/12/2016-10/12/2016

14. Attended a Workshop on spectroscopic Techniques from 30/04/2014-03/05/2014 by the Central Instrumentation Facility, Pondichery University, Puducherry

OUTLINE OF THE THESIS

Sample selection is the first stage of a research work. Quality and performance of the samples are evaluated according to their physical, chemical, thermal, mechanical, electrical and optical properties taking into consideration of their practical applications.

Ionic liquids (ILs- molten salts with melting point below 100℃) are getting ever-growing interest due to their unique properties as low melting point, low vapour pressure,high thermal stability, high electrochemical stability,high ionic conductivity and non-flammability. As a new class of materials, they are resulting more and more applications in both industrial, scientific fields and medical field as electrolytes, solvents, extraction media, co−catalysts&drugs respectively. More exciting is that ILs can be modified to cooperative different applications by changing their ion combinations (both cations and anions), hence ILs are indicated as designer solvents.Due to their superior structure ILs are likely to have 10^{18} different types.They are easily glass forming materials.

Commonly used cations include: 1) ammonium, 2) imidazolium, 3) phosphonium, 4) pyridinium, 5) cholinium, 6) pyrazolium, 7) pyrrolidinium, 8) sulfonium, 9) picolinium, 10) thiazolium, 11)triazolium, 12)thiolanium, 13) oxazolidinium, 14)morpholinium, 15) piperidinium, 16)thianium and 17) guanidiniumandanions could be inorganic and are, chloride $[Cl]^-$, bromide $[Br]^-$, iodide [I], dicyanamide $[(N(CN)_2]^-$, hexafluorophosphate $[PF_6]^-$, tetrafluoroborate $[BF_4]^-$, nitrate$[NO_3]^-$, chloroaluminate $[AlCl_3]^-$, sulfate $[SO_4]^{2-}$, trifluoroborate $[BF_3]^-$ and organic anions contains formate $[HCOO]^-$, thiocyanate$[SCN]^-$,tetraphenyl borate$[B(C_6H_5)_4]^-$, triflate $[CF_3SO_3]^-$,bis (trifluoromethylsulfonyl) imide $[NTf_2]^-$ or $[N(SO_2CF_3)_2]^-$, trifluoroacetate $[CF3COO]^-$, trifluoromethanesulfonate $[CF_3SO_3]^-$ and tosylate $[(CH)_7SO_3]^-$.Among them phosphonium based ILs are more attracting due to their high thermal stability, high electro chemical stability, high ionic conductivity and low melting point.

Totally Nine ILs were used for different measurement techniques and application studies in this thesis. Three phosphonium ILs,four binary mixtures (synthesised with phosphonium based ILs)and two pharmaceutical ILs were used for this studies. Studies include phosphonium based ionic liquids, in which the anion was systematically varied, have revealed that the anion chemical structure has a significant impact on the structural dynamics and charge transport properties of ILs. As the anion becomes larger and more asymmetrical, ionic mobility increases strongly as a consequence of an increased flexibility.The anions selected for this study were chloride[$Cl]^-$,dicyanamide[$N(CN)_2]^-$ and bis(trifluoromethylsulfonyl) amide[$(NTf)_2]^-$.The common cation for phosphonium based ILs used here are trihexyltetradecylphosphonium ([$P_{14,6,6,6}$]).

Vibrational analysis, thermal properties,dielectric measurementsand the applications of ILs in electrochemical analysis of supercapacitor, in textile dye removal, removal of heavy metals and removal of phenolic compounds by liquid−liquid extraction method, in biological activities like in vitro anti−cancer studies by MTT assay, anti−bacterial studies by agar disc diffusion method, anti−oxidant properties by DPPH free radical scavenging assay and *in silico* analysis (drug likeness & toxicity)by molinspiration,admetSAR and OSIRIS softwares of the selected ILs were studied and analysed. The thesis consists of seven chapters.

Chapter 1 gives the fundamental aspects ofILs.At First, the history of ILs were explained and then some of their applications in electrochemicalarenas, pharmaceutical industry, in separation technology, in biological fields and in polymerisation were shortened.

Chapter 2deals with description about the materials used for this study. Seven phosphonium based ionic liquids and two pharmaceutical ionic liquids (ranitidine docusate and lidocaine docusate) were introduced.Three phosphonium based ILs were purchased and four of them were synthesised in the laboratory and were described in detail. Various dyes used for removal process by liquid−liquid extraction method are also introduced.

In chapter 3, details of some of the measurement techniques can be found, as TGA,DSCand broadband dielectric spectroscopy (BDS)arepresented, FT−IR, FT−Raman spectroscopy,and discussing the ideas and basic theoretical background of measurement techniques were well-defined and computational details of the structures, FT−IR and FT−Raman were explained using DFT calculation.Electrochemical characterisation of supercapacitor, removal of textile dyes, removal of harmful heavy metals and phenolic compounds by liquid−liquid extraction method and biological activities include MTT assay, agar disc diffusion method and DPPH radical scavenging assay also described in detail.

In chapter 4 results of thermal, spectroscopic and electrochemical investigations of nine ILs were described in detail. TGA, DSC and BDS analysis of nine ILs were explainedenormously. The thermal stability and glass forming ability parameters of all ILs were studied. Glass transition temperatures of all ILs both from DSC measurement and from dielectric were compared. Fragility, activation energy and VFT parameters were explained in detail.From the results, all ILs were shows high thermal stability and also shows that they are easily glass forming materials.

Chapter 5 explain the details about applications of ILs in separation technology. Taking advantage of its other superior qualities, removal of textile dyes, phenolic compounds andother toxic heavy metalsby liquid–liquid extraction method were followed.The results shows that the ILs used for dye removal, removal of harmful metals and phenolic compounds were an efficient strategy for removing them by liquid–liquid extraction in advantage with hydrophobic nature of ILs.The provision for the reuse of ILs after the extraction has a better significance from the economic side, since it reduces the total cost of ILs and diminishes problem to the environment.

Chapter 6 include drug likeness properties and biological activities of ILs.The results shows that all ILs act as good anti-cancer &anti-bacterial agents, and which displays better anti−oxidant property. *In silico* analysis (drug likeness and toxicity)

in three phosphonium ILsshows the good pharmacokinetic profile of the ILs, we used a well validated *in silico*ADMET (absorption, distribution, metabolism, excretion and toxicity) prediction tools.In the last chapter, the major results of the works were summarized and the future outlooks of the dielectric spectroscopy of ILswere shared.

CHAPTER 1
FUNDAMENTALS OF IONIC LIQUIDS

1. INTRODUCTION

Inorganic salts (NaCl, $CaCl_2$, KCl, and $AlCl_3$) melt at very high temperatures (801°C, 782°C, 770°C and 190°C respectively) due to their strong interaction between cations and anions, which reduce their predictable use as solvents for chemical processing.[1] The new class of solvents, referred to as "Ionic liquids (ILs)" are molten salts with melting points below 100°C and that comprises of discrete asymmetric giant organic cations (aromatic or occasionally non–aromatic) associated with symmetric organic or inorganic anions.[1-3] Many of them are liquid at room temperature due to feeble coordination of their ions.[4,5] Usually ILs have a bulky organic cation weakly coordinated to a small organic or inorganic anion, the huge difference in the size of asymmetric cation and anion prevents the packing of crystal lattice, results in remain liquid at room temperature.[5] Room temperature ionic liquids (RTILs) whose melting temperature is below room temperature have occurred as a greener alternative to the traditional volatile organic solvents with innumerable potential in application fronts of diverse technological interests.[2] Schematic diagram displaying packing of ions in ionic solid and ionic liquid was shown in figure 1.1. There are two broad categories of ILs: RTILs that melt below 25°C and frozen ILs (FILs) which are typically solids at room temperature (25°C) but melt below 100°C.[6]

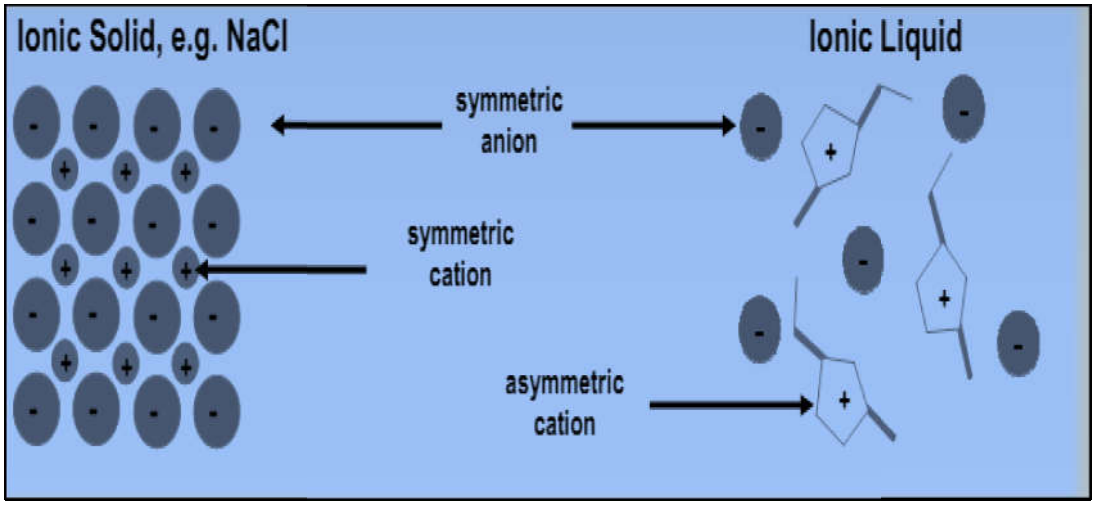

Figure 1.1. Schematic diagram displaying packing of ions in ionic solid and ionic liquid.

Based on the cation segment, ILs are categorized into following types: 1) ammonium, 2) imidazolium, 3) phosphonium, 4) pyridinium, 5) cholinium, 6) pyrazolium, 7) pyrrolidinium, 8) sulfonium, 9) picolinium, 10) thiazolium, 11) triazolium, 12) thiolanium, 13) oxazolidinium, 14) morpholinium, 15) piperidinium, 16) thianium and 17) guanidi nium.[1,2,6,7] Anions could be either inorganic viz., chloride $[Cl]^-$, bromide $[Br]^-$, iodide [I], dicyanamide $[(N(CN)_2]^-$, hexafluorophosphate $[PF_6]^-$, tetrafluoroborate $[BF_4]^-$, nitrate $[NO_3]^-$, chloroaluminate $[AlCl_3]^-$, sulfate $[SO_4]^{2-}$, trifluoroborate $[BF_3]^-$ etc. or organic anions contains formate $[HCOO]^-$, thiocyanate $[SCN]^-$, tetraphenyl borate $[B(C_6H_5)_4]^-$, triflate $[CF_3SO_3]^-$, bis (trifluoromethyl sulfonyl) amide $[NTf_2]^-$ or $[N(SO_2CF_3)_2]^-$, trifluoroacetate $[CF3COO]^-$, trifluoromethanesulfonate $[CF_3SO_3]^-$ and tosylate $[(CH)_7SO_3]^-$.[1,2,7] The apparent number of anion–cation combinations are nearly possible to 10^{18} different ILs.[12] Some of the common cations and anions were listed in figure 1.2 (a) and figure 1.2 (b) respectively.[1,2] Pharmaceutically active selected cations and anions are listed in table 1.1.

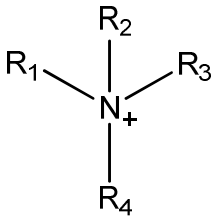

Ammonium

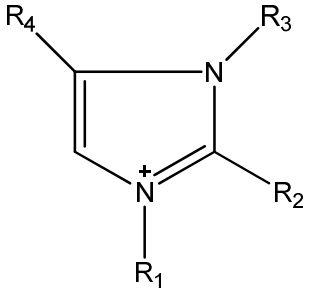

Imidazolium

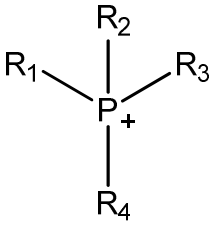

Phosphonium

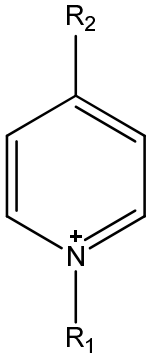

Pyridinium

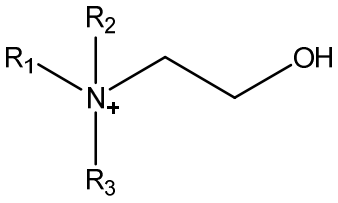

Cholinium

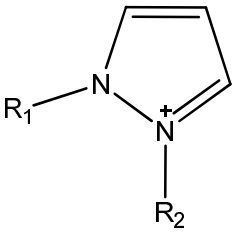

Pyrazolium

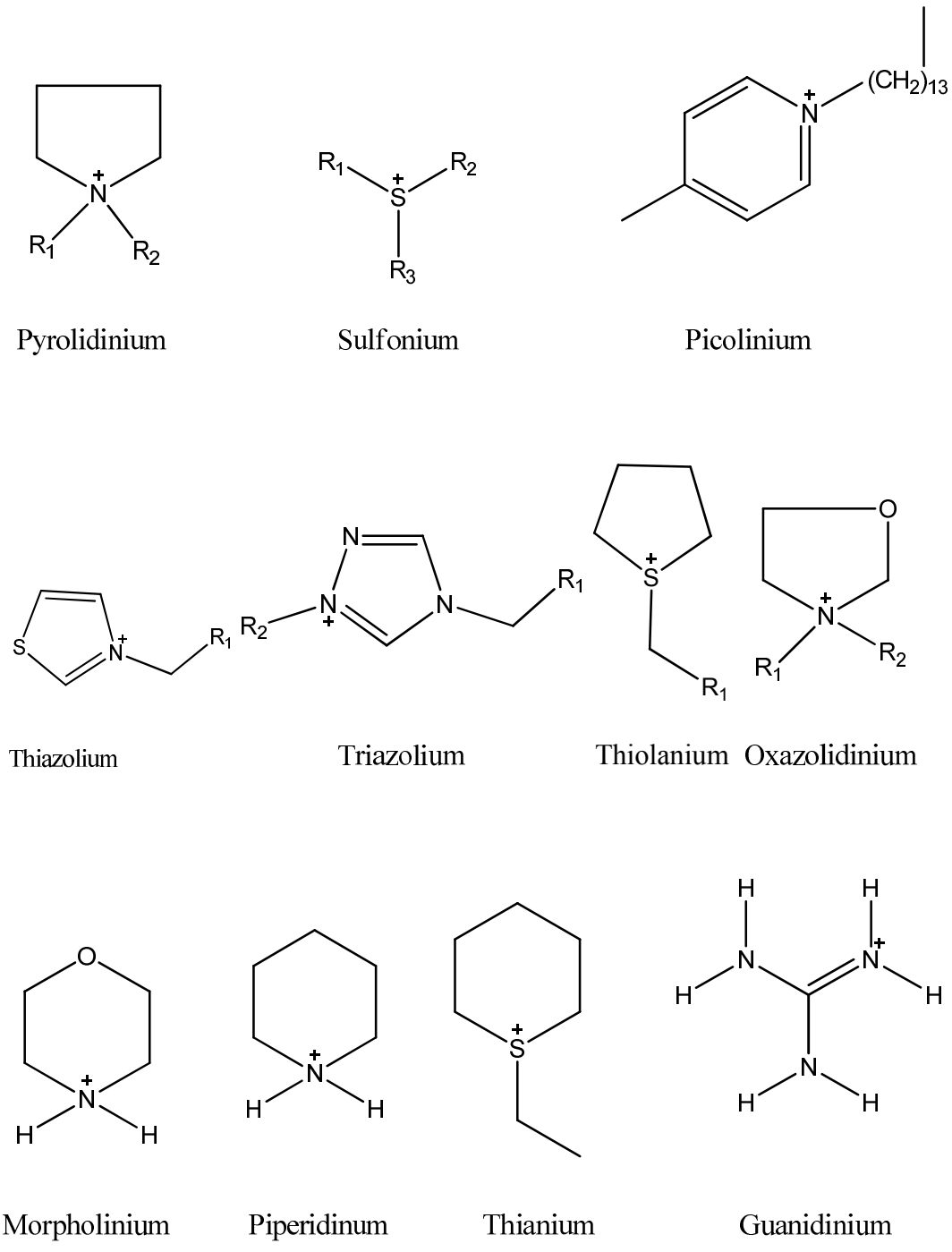

Figure 1.2 (a). Structure of common cations of ILs.[1,7]

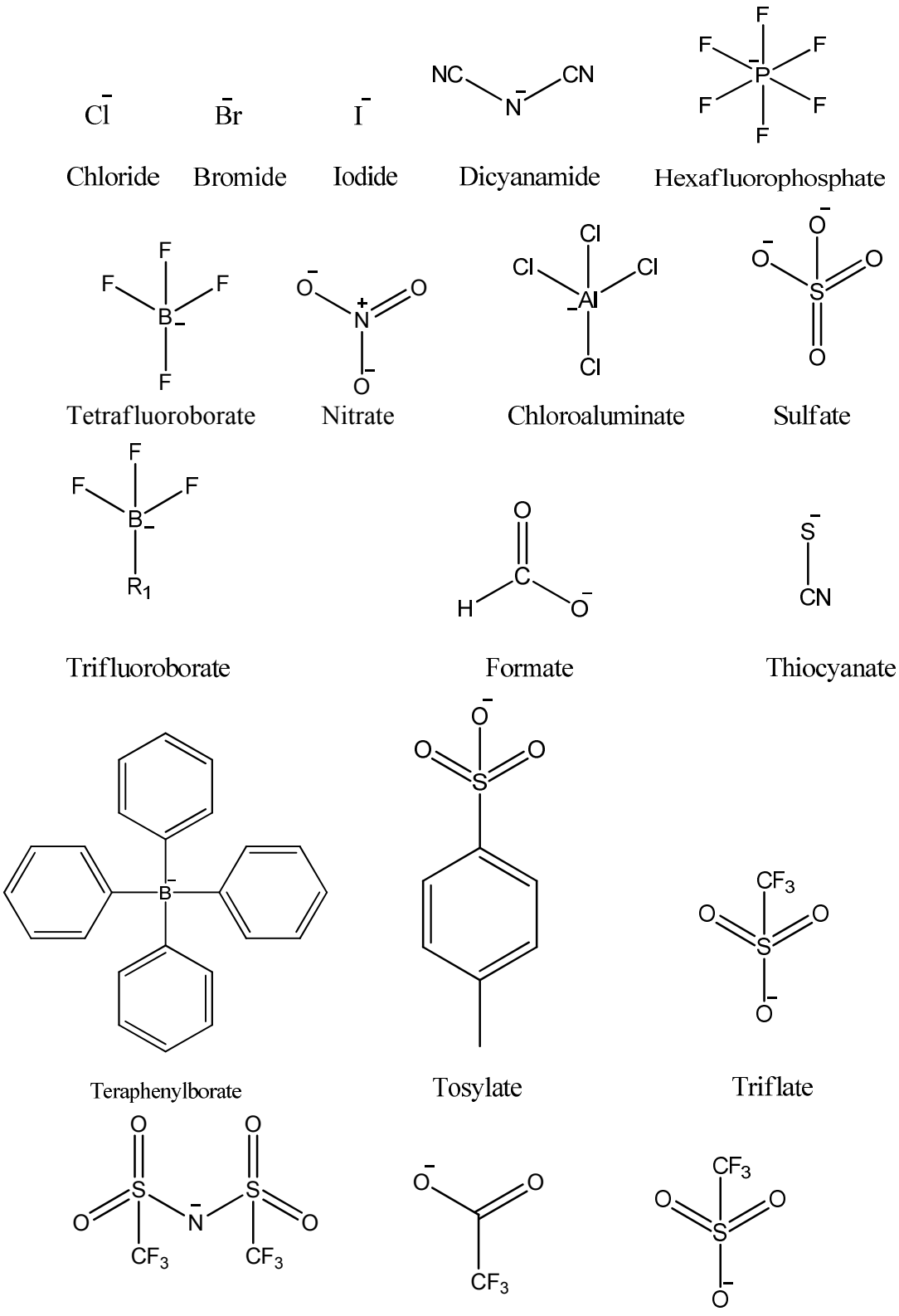

Figure 1.2 (b). Structure of common anions of ILs.[1,7]

Table 1.1. *Pharmaceutically active selected cations and anions.*[8]

Cation	Anion	IL
Benzalkonium chloride function: anti-bacterial 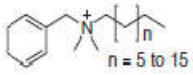 	Sodium ibuprofenate function: anti-inflammatory 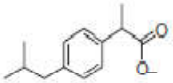	[Benzalkonium][Ibuprofenate][a] Form: Yellow gel Melting point: −41 °C *T* (glass transition): −77 °C
Didecyldimethylammonium bromide function: anti-bacterial 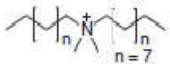 	Sodium ibuprofenate function: anti-inflammatory 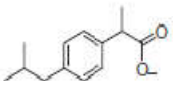	[Didecyldimethylammonium]- [Ibuprofenate][b] Form: Yellow liquid Melting point: Liquid at RT *T* (glass transition): −73 °C *T* (liquid–liquid transition): 69 °C
Benzalkonium chloride function: anti-bacterial 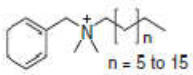 	Colawet MA-80 function: wetting agent 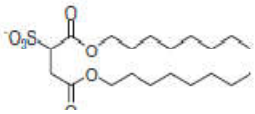	[Benzalkonium][Colawet MA-80][a] Form: Clear liquid Melting point: Liquid at RT *T* (glass transition): −28 °C *T* (liquid–liquid transition): 77 °C
Benzalkonium chloride function: anti-bacterial 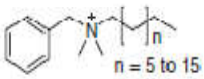 	Sodium sulfacetamide function: anti-acne 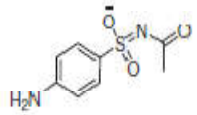	[Benzalkonium][Sulfacetamide][a] Form: Yellow gel Melting point: Liquid at RT *T* (glass transition): 46 °C
Lidocaine hydrochloride function: pain reliever 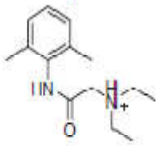	Sodium docusate function: emollient 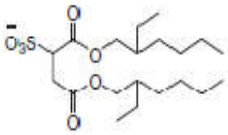	[Lidocainium][Docusate][b] Form: Colorless gel Melting point: Liquid at RT *T* (glass transition): −29 °C *T* (liquid–liquid transition): 78 °C
Ranitidine hydrochloride function: histamine H_2-receptor antagonist 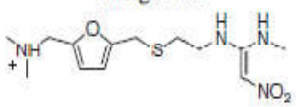	Sodium docusate function: emollient 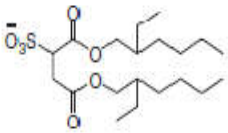	[Ranitidinium][Docusate][b] Form: Dark red liquid Melting point: Liquid at RT *T* (glass transition): −12 °C *T* (liquid–liquid transition): 29 °C

ILs have unique and attractive properties that provide a significant opportunity for new science and technology.[7] ILs can reduce the use of hazardous and polluting organic solvents due to their unique properties as well as involved in various synthesis process.[5] ILs are favourable materials in research and industrial fronts for diverse technological applications[7] as well as for resolving some of the fundamental issues in material science, since they exhibit unique features such as

low melting point,[3] negligible vapour pressure,[4] wide liquid range,[5,8,9] low volatility,[2,8] high chemical and thermal stability,[4,5] non–flammability,[6] high ionic condu ctivity,[4] good electrical conductivity,[12] high solubility,[2] low-combustibility, recyclability,[2,5] high heat capacity,[9,11] wide electrochemical windows,[6] very low corrosivity,[10] high polarit y,[5,11] hydrophobicity[5,11] and they express the different properties from those of molecular liquids. These physico chemical properties can be altered by selecting different combinations of cations and anions[5] and hence ILs are referred to as designer solvents.[2]

Considering the unique properties, ILs are the favourable materials in technological applications such as synthesis,[1] catalysis,[1] electrochemistry,[1] analytical chemistry,[1] reaction media,[3] plasticizers, lubricants,[8] solvents in nanotechnology,[2] biotechnological and engineer ing fields;[2] solvents in UV visible and IR absorption spectroscopies, as green solvents for synthesis and catalysis;[2,10] as separation tools for mixtures and extraction process,[1] in medical applications,[8] in liquid crystals, image devices, for heat storage and thermal fluids,[10] electro lytes in batteries,[4,12] solar cells,[12] in photovoltaic cells,[12] super capacitors,[4] fuel cells,[4,12] actuat ors[5], electrochemical sensors,[5] biosensors,[3] biocatalytic reaction,[3] biopreservation,[3] protein stabilization,[3] metal finishing, coating; used in electrochemical deposition of metals and semi conductors,[13] gas separation,[5] extractive distillation, spinning–liquid mirrors for lunar telesco pes,[6] extraction of proteins and their crystallization,[13] and as solvents in physical chemistry.[13] They cannot be evaporated in the form of gases, hence ILs cannot create air pollution or emit harmful gases during chemical experiments and they should be considered as environmentally friendly solvents to replace volatile organic compounds. ILs also have significant roles in nuclear energy.[12]

Among the different categories of ILs, imidazolium, ammonium and phosphonium based salts are most commonly used ones due to their particular set of properties.[7] Consi dering the thermal stability (in some cases up to 400°C)[2], high chemical stability, good electrical conductivity, high ionic mobility, wide electrochemical window, low vapour press ure and other relevant properties,

phosphonium-based ILs are more appealing among these.[7] They are found to be more resilient to reactive metals and strong bases than imidazolium based ILs.[7] They are used as a powerful phase transfer catalysts for Halex reaction and palladium catalysed Heck and Suzuki reactions. They have been used for CO_2 capture and act as strong bases in Grignard reagents.[2,7]

The properties like viscosity, heat capacity, conductivity, thermal stability, chemical stability, hydrophobicity/hydrophilicity etc. can be adjusted by selecting a distinct cation/ anion pair to achieve them for desired characteristics and select for suitable industrial applications.[6,14] The properties of ILs intensely dependent on the anion, cation and the stru cture of the ion.[14] Cation is more responsible for physical properties such as melting point, viscosity, density etc.[1,15,16] and the anion controls chemical properties and reactivity.[1,10] Mostly, the anions are used to regulate the water miscibility, hydrophobicity or hydrogen bonding ability, acidicity and coordination ability.[1,10,15] Water miscibility of ILs are widely accepted in biphasic reactions. Degree of miscibility in water depends on degree of coordination of ions present in the ILs. $[NO_3]^-$ ion can strongly interact with water, whilst acidic ions are non-coordinating and pH neutral ions ($[BF_4]^-$, $[NTf_2]^-$) are weakly coordinating ions. The length of the cation in ILs also affects the hydrophobicity, longer the alkyl chain more is hydrophobicity of IL. ILs have reasonably good ionic conductivities related with those of conventional organic solvents.[16] The conductivity and viscosity of ILs are inversely connected. Conductivity is correlated with the temperature and anti correlates with viscosity. Usually, ILs are more viscous than common molecular solvents and their viscosities were between 10 mPas and 500 mPas at room temperature.[16]

Common ILs are polar and miscible with polar solvents like acetone, methanol, dichloromethane, dimethyl sulfoxide (DMSO) etc.[1,7] They are immiscible with non-polar solvents such as hexane, toluene and diethylether.[1,7] The type of cation or anion of ILs has a major impact on polarity, hydrophobicity, hydrophilicity and lipophilicity.[2,3] Hereafter they can be designed to be immiscible with some organic solvents and may be apt in two phase systems.[1,7]

1.1. HISTORY OF IONIC LIQUIDS

Ionic liquids can be recognized as elements with a long history. The first ionic liquid indicated in the literature was ethanol–ammonium nitrate with a melting point of 52°C-55°C, which was synthesized by S. Gabriel and J. Weiner in 1888.[2,5,15] Ethyl-ammonium nitrate ($[C_2H_5NH_3]$ $[NO_3]$) was the first room temperature protic ionic liquid with a melting point 12°C, synthesized by the reaction of ethylamine with concentrated nitric acid in 1914 by Paul Walden and it has the potential to be used as a non–aqueous solvent for biochemical systems and the importance of its network of hydrogen bonds in controlling its solvent properties.[2,5,15] In 1948, the first pyridinium based ILs were established and used for electroplating.[2] Hurley and Weir had discovered a room temperature IL 1- ethylpyridinium bromide-aluminium chloride ($[C_2py]BrAlCl_3$) by mixing 1-alkylpyridinium halides with 'true inorganic salts', such as metal halides.[15,17] In 1960s Yoke at Oregon State University found that solid copper (I) chloride and alkyl ammonium chloride formed a liquid at room temperature.[18] The battery cells were gathered with aluminium and chlorine electrodes using numerous molten salt electrolytes with an IL 1–ethylpyridinium bromide–$AlCl_3$ mixture in 1968.[18]

In 1970s and 1980s, Osteryoung *et al*. and Hussey *et al*. carried out widespread research on organic chloride–aluminium chloride room temperature ILs.[15] V. R. Koch *et al.* used pyridinium cation IL as a media for several organic reactions in 1976 and therefore increased its interest in electrochemistry as an electrolyte. The chemical and physical properties of 1-butylpyridinium chloride aluminium chloride mixture (BPC–$AlCl_3$) were measured and published in 1978.[18] Charles Hussey and John Wilkes initiated an effort to discover substitute chloride salt that would make a low melting chloro aluminate IL in 1979.[18] The ILs based on $AlCl_3$ can be viewed as the first generation of ILs.[2,15] A favourable current approach is the use of bio–renewable or bio–based natural compounds as substrates for the preparation of the ILs. Y. Fukaya *et al.* established a series of ILs composed of naturally–derived biomaterials,[19] such as hydrogen maleate, propionate and hydrogen succinate anions provided bio–ILs upon combination with the choline

cation.[19] K. Fukumoto *et al.* established innovative task-specific ILs by pointing on the amino acids as anions with diverse characteristics.[20] They have described the ILs that are prepared by coupling the imidazolium cation with 20 varied natural amino acids.[20] In 1992, Wilkes and Zawarotko prepared and categorized air and water stable 1-ethyl-3-methylimidazolium based ILs including different anions.[15]

Ohno focused on the synthesis of a series of polymerizable ILs and their polymerization to prepare a new class of ion conductive polymers.[15] The research for innovative water-soluble ILs was defined by Fuller *et al*., using a series of ILs from the dialkylimidazolium cations combined with different anions (tetrafluoroborate, hexafluorophosphate, nitrate, acetate, and sulfate). A numbers of ILs based on imidazolium cations and different anions such as tetrafluoroborate, hexafluorophosphate and nitrate were developed in 1990s, which were more stable in hydrolysis.[18]

In the field of chiral ILs (CILs), ILs have proficient developments in recent years. By means of the technology development, advanced methods of synthesizing stable and structurally varied ILs have been predictable. This has directed to identify unspecified applications of CILs besides improving efficiency of formerly identified applications.[21,22] Herrmann *et al*., synthesized N–heterocyclic carbenes of imidazoles in 1996 and a chiral imidazolium chloride IL was obtained as an intermediate during this reaction.[21,22] Howarth *et al.*, was reported the first attempt of CILs in asymmetric synthesis (Diels–Alder reaction).[21] Conversely, they were not effective in finding stereo selectivity.[21] Vo-Thanh and coworkers were reported as in 2004, the first successful chiral induction who used a chiral ephedrinium IL as the reaction media in an asymmetric Baylis–Hillman reaction to obtain 44% enantiomeric excess in the product.[21] ILs are favourable materials for the biological and pharmaceutical sciences not only for use as reaction media, but as pharmaceutical solvents or co–solvents for the delivery of drugs with poor water solubility and bioavailability. They are also applied in micro–emulsion systems, which can facilitate the dissolution of drugs that are insoluble or poorly soluble in water.[23] The anti–microbial activity for ILs is growing interest for the development

of new bioactive materials as antiseptics.[23] These progresses are the beginning of the affluent existing research on ILs.[2,15]

1.2. APPLICATIONS OF IONIC LIQUIDS

1.2.1. Electrochemical applications

ILs have much broad application spectrum and advances are being instating as a result of its various unique properties. Ionic conductors have a revolutionary growth in research area by their potential use in many electrochemical device applications in the last few decades.[4] Among different energy storage systems, the electrochemical energy storage (EES) systems comprising batteries, fuel cells, as well as electrochemical capacitors or super capacitors (ESs) are most effective and regularly used in several applications.[24] The energy–producing processes performed in these three devices were at the electrode/electrolyte interfaces.[24] Because of high power density and long cyclic life, super capacitors have drawn considerable importance related with batteries and fuel cells in both academia and industry.[24] Better electrolytes are essential in order to raise the performance of the device applications. ILs are used as new electrolytes with improved conductivity, stability, durability and operating temperature range.

The growth of efficient energy storage devices has significantly delighted developing energy demands for industrial and domestic needs. Super capacitors have developed as high performance storage devices for long lifetime functioning conditions and high power density, low maintenance cost, and environmental approachability.[4,24-26] However, the major complic ations occurred in their prevalent use are their limited performance arised out of the lower operating window, stability issues, shorter lifespan and other industrial and practical difficulties. To progress their performance, the use of high capacitive materials with better electrolytes having improved voltage window, keeping in view other practical and environmental issues.[27]

IL opened an effective mechanism to enhance the operating potential window (OPW) as a potential electrolyte in the arena of super capacitor research.[27]

This becomes much signi ficant because of a couple of ins and outs. Mainly, the attainable voltage influenced by the electrolyte potential window, which could not be achieved by the conventional aqueous solutions, whereas ILs can give a three to four–fold rise in power as well as energy density related to the conventional ones.[27] Further, the non–volatile nature makes it as an apt candid ate to achieve the cyclic stability demanded by the automobile and other industries.[27] The distinctive properties like good conductivity, low volatility, non–flammability, high chemical, thermal and electrochemical stability and recyclability of ILs overshadows the other promo ted merits of aqueous and organic electrolytes to consider them as a promising electrolyte for the future electrochemical devices.[27] Phosphonium based ILs can provide some visions to resolve these difficulties.[27]

1.2.2. Pharmaceutical applications

ILs play an important role for their potential application in the pharmaceutical industry in the recent time periods.[28-30] The ionic conductivity of amorphous ILs are much higher than that of their crystalline counterparts, the enhanced properties can be utilized for varied range of applications.[28-30] Formulating strategies to retain the activity of a pharmaceutical from its manufacture since it is absorbed with optimal bioavailability, is a herculean task for both chemists as well as pharmaceutical scientists.[28-30] Crystalline forms are the most desired ones among of drug preparation for oral delivery, because of its easiness in drug management and other thermodynamic considerations like purity, thermal stability, manufacturability and ease of handling.[28-30] Unfortunately, bioavailability of many of the solid API formulations *via* oral route are restricted due to poor aqueous solubility of these drugs in the gastrointestinal track. Severity of the condition may be agreed from the fact that 40% of drugs in use and nearly 90% of newly discovered drug molecules waiting for the market approval are poorly water soluble.[28-30] To overcome this shortcoming, methods to attain improved solubility may be formulated. Techniques like pH adjustment, changing drugs into hydrochloric salts, surfa ctant solubilisation, use of polymeric matrixes, cyclodextrins, microparticles and stabilization of amorphous drug, the formation of polymeric micelles, size reduction and nano ionization, the formation of solid–liquid

nano particles, liposome and polyprosomes, micro-emulsion and drug delivery systems are some of the examples.[28-30]

Another way to limit the clutches of crystalline bonds, which limits the solubility is to transform the API to amorphous form, where the superiority of higher free energy can overcome many of the above mentioned issues.[28-30] As a result of random orientation and lack of periodicity, the amorphous phase develops the bio-availability *via* higher enthalpy, higher specific volume, greater molecular mobility and chemical reactivity, enhanced wettability and dissolution rate etc. Moreover, easiness in shaping the tablets during production and other technical and economic considerations make these appealing. In spite of all the advantages, the commercial use of amorphous drugs is restricted. This is occurred as all the benefits attained because of molecular mobility due to the thermodynamic metastability of glassy and super cooled phases can initiate crystal nucleation and its growth.[28-30]

Eventually, the drug reverts to its crystalline form during storage. Depending upon the thermodynamic conditions, devitrification takes a few seconds to as long as years in the amorphous state.[28-30] Recent reports have further speculated that there could be links to the onset of crystallization even in the glassy APIs and intense investigations are on to reveal the mechanism.[28-30] It seems to be a fundamental issue not only to the pharmaceutical industry, but also to the glass forming systems as a whole. One way to bypass the crystallization tendencies of amorphous drugs during storage is to convert it into IL form where the asymmetry of anion–cation constituents can effectively prevent the system to join to a single periodic lattice.[28-30] ILs propose a suitable technique to investigate the properties of altera tions in the structures on the resultant physical and chemical properties. They can be designed to be non–toxic, non–flammable and non–corrosive. In addition to the above, the ionic conductivity relaxation of these pharmaceuticals can illuminate the physics of ion diffusion in ionically conducting glassformers.[28-32] So the development of IL is an easy and effective approach for the increased solubility and dissolution rate. The behaviour of returning process to the crystalline form during storage, amorphous pharmaceutical ingredients can be treated by providing it as an IL, which cancel the unwanted side effects of amorphous pharmaceu ticals.[28-32] Pharmaceutically active

ILs characterize a thermodynam ically stable phase, which avoid the difficult issues related with polymorphism.[28-32]

The ILs formed on biologically active cations and anions, commonly selected by ILs based on active pharmaceutical ingredients (IL–APIs), are interesting compounds for use in pharmaceutical applications.[8] Lidocaine docusate, ranitidine docusate, dodecyl dimethyl amm onium ibuprofen, benzalkonium ibuprofen etc. are the examples of promising IL–APIs that were newly synthesized. Lidocaine docusate is prepared by combining the lidocaine HCl cation (a local anesthetic) with the anion sodium docusate (an emollient). It is an IL with bett er efficiency than lidocaine hydrochloride in topical anaesthesia. Ranitidine docusate is produced by combining the same anion with the cation ranitidine HCl which is a histamine H_2–receptor antagonist. It has the advantage over the ranitidine hydrochloride to avoid poly morphism and impurity problems.[8]

1.2.3. Applications in separation technology

One of the most important processes in many different industries are colouring of products, such as carpet and paper, plastics, leather, rubber, dyestuffs, textiles, pharmaceu tical, food, and cosmetics, in which large amounts of dyes and significant volumes of water are used. Textile and other industries produce huge amounts of dyes annually in worldwide and are discharged in to soil as liquid wastes that contain organic and inorganic compounds. Subsequently, a considerable amount of coloured wastewater is formed.[33-40] Dye stuffs have recognized to be problematic among the major classes of water pollutants. The majority of dyes in textile waste water are toxic and carcinogenic not only to aquatic environments but also to a wide variety of organisms. Mainly azo dyes are not readily biodegradable. Several studies show that ILs express a major role in the extraction of various dyes.[33-40] In this situation, removal of dyes from aqueous effluents is crucial.

Diverse technologies have been recognised for the removal of dyes from water and wastewaters, including biological wastewater treatment, physical (membrane filtration, adsorption, coagulation, flocculation, precipitation, reverse osmosis, ion exchange etc.) and chemical processes (oxidation, ozonation etc.).[37-39]

However, most of these techniques have advantages and also demonstrate major drawbacks have been widely reviewed. ILs are considered as highly efficient eco–friendly solvents for liquid−liquid extraction, adsorption of organic dyes and heavy metals.[38] The elimination of different ionic dyes (e.g., eosin yellow, methylene blue, malachite green, methyl orange, orange G, conco red, aslizarin red S and rhodamine B) are probable by liquid–liquid extraction or adsorption process.[37-39] Dye remov al percentage from aqueous phase rises with the drop in dye concentration or with the increase in surfactants concentration. Furthermore, the physicochemical properties of ILs can be designed by the proper choice of their cation/anion combinations and which allows them to be tuned for specific applications, such as in extraction processes can replace conventional volatile solvents and whereby recovery of solvent and reuse of dyes are possible.[37-39]

Non–biodegradable heavy metals such as arsenic, chromium, cadmium, copper, zinc, lead, mercury and harmful phenolic compounds are the most dangerous ones among the industrial pollutants of water. As a result of hasty industrial development, they are released into the environment through contaminated waste water resulting in destruction to ecosystems and human health. Their toxicity, persistence and accumulation in human bodies and other living organism causes health effects, hence are a source of increasing concern in many countries. Therefore, removal of them is to be a challenge by waste water treatment owing to its environmental toxicity and persistence. The traditional methods include ozonation, adsorption and extraction, photo catalytic degradation, biological, chemical oxidation or reduction, chemical precipitation, reverse osmosis, ion exchange, filtration, membrane processes, evaporation and coagulation. Conversely, adsorption methods for removing them give a most promising separation and purification method due to their high efficiency, low cost, ease of handling, and the possibility of reusing the materials involved. Among them, liquid–liquid extraction method is easy and environmentally benign technique to remove the toxic compounds.[37-39]

The main components of greenhouse gases such as carbon dioxide (CO_2), methane (CH_4) and nitrous oxide (NO_2) are continuously emitted into the atmosphere.[41-43] These gases are invented to be the principal source of global warming. 60% of global warming consequences are supposed by contribution of

CO_2.[41-43] Hence, the most needed challenges of our time is balancing the increasing world energy demand with the need to economically reduce carbon dioxide emissions. ILs has been proposed as a novel approach to capturing of CO_2, removal of CO_2 by depressurization.[41-43] It has been revealed that the solubility of CO_2 in the IL increased intensely with increasing pressure. Understanding the phase behaviour of CO_2 with various ILs is dynamic to designing and understanding these systems. The system persisted two distinct phases, even under pressures up to 400 bar.[41-43] There are many techno logies for CO_2 separation as, pressure swing absorption (PSA), physical or chemical solvent scrubbing and gas membrane separation. In recent years, the dramatic environmental impact of sulfur oxides contained in engine exhaust emissions has been widely predictable. As a result, specifications concerning sulfur content in fuels are becoming more and more severe and desulfurization of gasoline has attracted wide attention. In European countries, it was limited to a maximum 50 μg/mL in 2005 and gasoline will be sulfur–free in 2011.[41-43]

Nuclear energy is economically good and environmentally clean compared to most other forms of energy used for electricity production.[44] Radioactive wastes are the major problem challenged the operation of nuclear reactors. Recently, increasing attention has been paid to ILs for efficient removal and reliable storage of radioactive iodine and other radioactive wastes.[44]

1.2.4. Biological applications

ILs are interested ones due to their biological properties and are a promising compound for anti–microbial agents, anti–oxidants, local anaesthetic and anti–cancer activities that are the potential target of pharmaceutical industry. Accordingly, tunable properties and low toxi cities of ILs could potentially be designed to impart maximum efficacy with minimal toxicity as anti–cancer, anti–microbial, anti–oxidants, anti–viral and other therapeutic agents.[45-46] Anti –cancer activity of ILs shows limited reports. Recently, three classes of ILs (imidazolium, phosphonium and ammonium) were investigated for anti–cancer activity towards 60 human cell lines by the National Cancer Institute's (NCI).[47] It was proven that the length of the alkyl chain on the cation plays a crucial role in the antitumor activity and cytotoxicity of ILs.[47] The analysis reported that certain types of phosphonium–

based ILs were found to be more active and less cytotoxic in comparison to the ammonium and imidazolium–based ILs.[47] Skin and soft tissue infections (SSTIs) are a major worldwide public health problem. As reported by health services, the main anti–bacterial agents are escherichia coli, enterobacterias pseudomonas aeruginosa (macerated ulcers), staphylococcus aureus and streptococcus pyog enes. Nowadays, World Health Organization of the United Nations (WHO-UN) has warned and kept surveillance over the resistances to control them. It has been reported that ILs are the most innovative compounds to control the bacterial infection.[45-47]

Anti–oxidants are the substances that significantly reduce the negative effect of radicals on the functioning of the human body *via* two oxidation pathways: H–atom or electron transfer.[48-49] Current studies are concentrated on the use of natural anti–oxidant acids as mate rials for preparation of various forms of ILs.[49] Anti–microbial activity of ILs have attracted the attention of researchers recently.[49] The medical and industrial potentials of ILs have revea led that numerous types of ILs inhibited growth of various bacterial and fungal species. Imidazolium, pyridinium, pyrrolidinium, piperidinium, ammonium and other ILs were displayed to inhibit growth of pathogenic and non–pathogenic bacteria and fungi may be used as a valuable property in medicine.[49] Recent studies have also proved that the potential appli cation of certain ILs to unveil excellent anti–microbial activity, thus presenting the exciting possibility as biocidal agents in the control of microorganisms in the environment for contamination and infection control.[50]

ILs have been reported as alternative 'green' solvents for design of chemical products and processes of a wide range of reactions which reduce the use of hazardous substances.[50] In the development of sparkling manufacturing processes, the design of safe and environmen tally benign solvents has become increasingly important.[50] Conventional organic solvents are often toxic, flammable and volatile which when released into the environment can have potentially devastating effects. ILs have offered as potential reagents, which have to replace many harmful volatile organic solvents.[50]

1.2.5. Polymerisation

Polymers are striking views for immobilizing ILs.[51] Especially, the flexibility of both polymer and IL composition enables the synthesis of a virtually

infinite number of ionogels.[51] By combination of appropriate polymer and IL, properties can be tuned for useful applications.[51] Presently, polymer based ionogel membrane have received worldwide attenti on due to their intrinsic properties like thin film forming ability, low cost, transparency, flexibility, high ionic conductivity, ease of large scale manufacture and wide electrochemical window.[52] These properties enable them to use in electrochemical applications like lithium batteries, solar cells, super capacitors, fuel cells, sensors, solid state batteries etc.[52] The leadi ng benefit of ionogel is that it will maintain all the properties of IL along with the features of the host matrix.[53] Mainly, PVA was promising representative and was chosen as a polymer host among the polymers owing to its capability of environmentally stable, nontoxic, water soluble and has good film–forming capacity.[53-54] Now, it has to fulfil various restraints in regards to amorphous nature, non–conductivity and band offsets process ability etc. To tune the properties such as morphology, thermal, dielectric and conductivity, wide modification has to be done with PVA films.[53-54] Some of the applications of ILs were shown in brief in figure 1.3.

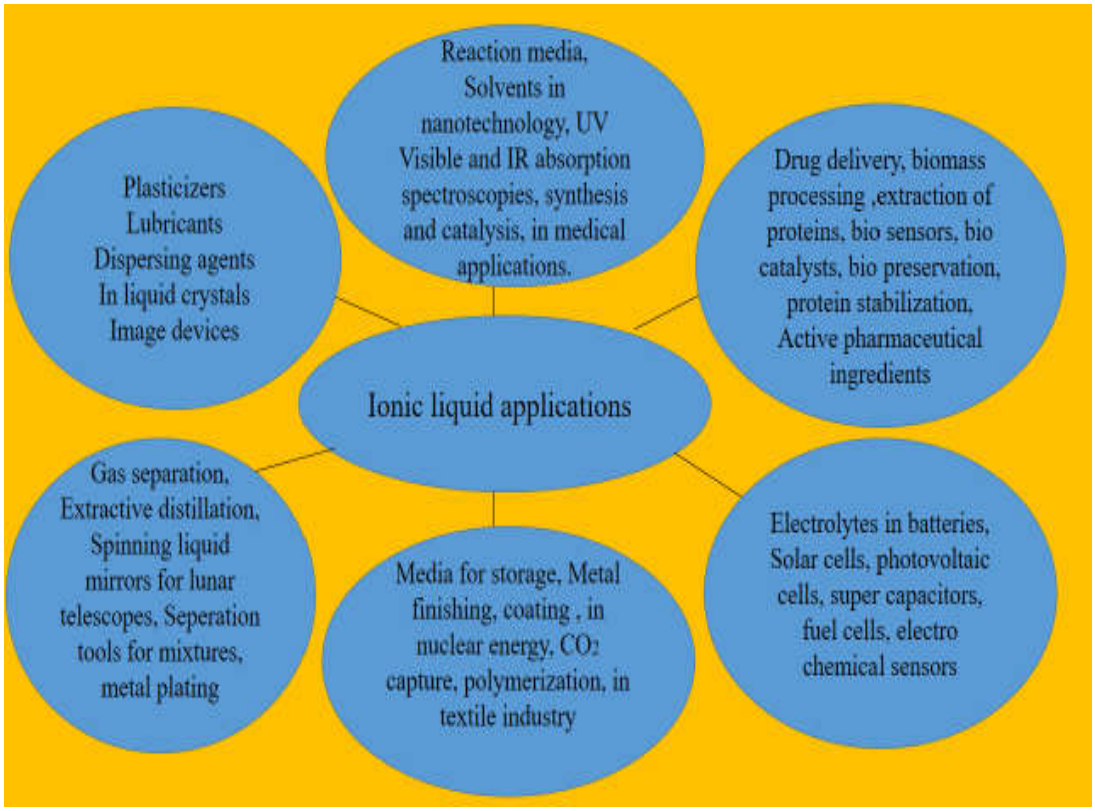

Figure 1. 3. Some of the potential applications of ionic liquids.[1-12]

The main objectives of this study include;

- To probe the glass forming nature of the ILs and their thermal properties using differential scanning calorimetry (DSC) and thermogravimetry analysis (TGA).
- To characterize ILs with potential applications for industrial, pharmaceutical, energy fronts and extract further insights about the dielectric relaxation dynamics relevant to the glass transition phenomenon and charge transport by broadband dielectric spectroscopy (BDS).
- To investigate their applications in separation technology and medical field.

Systematic review had been carried out by different groups by varying size, structure, choosing the same cation and varying anions or vice versa. In view of the huge database of million combinations of ILs, to get a deeper insight about the ion dynamics and other properties, judicious choice of ILs with selected applications had to be explored for resolving pertaining issues. Based on the above objectives and considering the diverse technological applications due to their properties like high thermal stability, non–flammability, non–volatility, high ionic conductivity etc., we selected the following phosphonium based ILs, its binary mixtures and two pharmaceutical ILs,

1. Trihexyl tetradecyl phosphonium bis (trifluoromethyl sulfonyl) amide ($[P_{14,6,6,6}][NTf_2]$)
2. Trihexyl tetradecyl phosphonium dicyanamide ($[P_{14,6,6,6}][N(CN)_2]$)
3. Trihexyl tetradecyl phosphonium chloride ($[P_{14,6,6,6}][Cl]$
4. Trihexyl tetradecyl phosphonium bis (trifluoromethyl sulfonyl) amide [chloride] ($[P_{14,6,6,6}][NTf_2][Cl]$)
5. Trihexyl tetradecyl phosphonium dicyanamide [chloride] $[P_{14,6,6,6}][N(CN)_2][Cl]$
6. Ionogel of PVA and $[P_{14,6,6,6}][NTf_2]$
7. Ionogel of PVA and $[P_{14,6,6,6}][N(CN)_2]$
8. Ranitidine docusate
9. Lidocaine docusate

Here, first three samples are phosphonium based ILs with same cation trihexyl tetradecyl phosphonium ($[P_{14,6,6,6}]$) and changing anions such as chloride $[Cl]^-$, dicya namide ($[N(CN)_2]^-$) and bis (trifluoromethyl sulfonyl) amide ($[NTf_2]^-$). Samples 4 and 5 were synthesized from mixing $[P_{14,6,6,6}][NTf_2]$ and $[P_{14,6,6,6}][N(CN)_2]$ with $[P_{14,6,6,6}][Cl]$. Samples 6 and 7 were synthesized from PVA with $[P_{14,6,6,6}][NTf_2]$) and $[P_{14,6,6,6}][N(CN)_2]$. Samples 8 and 9 were two synthesised pharmaceutical samples. Influence of anion on the structural dynamics, charge transport and different applications (in separation technology and biological activities) of the selected ILs were studied in this dissertation. The experimental techniques used for this study includes differential scanning calorimetry (DSC), thermogravimetric analysis (TGA), broadband dielectric spectroscopy (BDS) and other spectroscopic techniques of pure phosphonium based ILs, its binary with appropriate polymers and testing their applications with suitable methods as liquid–liquid extraction, biological activities (MTT assay, agar disc diffusion method and DPPH assay) and *in silico* analysis of drug likeness and toxicity studies using Molinspiration, AdmetSAR and OSIRIS softwares.

CHAPTER 2

MATERIALS USED FOR THE STUDY

2. MATERIALS

The materials used for this study are trihexyl tetradecyl phosphonium bis (trifluoromethyl sulfonyl) amide ($[P_{14,6,6,6}][NTf_2]$), trihexyl tetradecyl phosphonium dicyana mide ($[P_{14,6,6,6}][N(CN)_2]$), trihexyl tetradecyl phosphonium chloride ($[P_{14,6,6,6}][Cl]$), trihexyl tetradecyl phosphonium bis (trifluoromethyl sulfonyl) amide [chloride] ($[P_{14,6,6,6}][NTf_2][Cl]$), trihexyl tetradecyl phosphonium dicyanamide [chloride] ($[P_{14,6,6,6}][N(CN)_2][Cl]$), ionogel of PVA and trihexyl tetradecyl phosphonium bis (trifluoromethyl sulfonyl) amide, ionogel of PVA and trihexyl tetradecyl phosphonium dicyanamide, ranitidine docusate and lidocaine docusate. All the samples have high thermal stability, high ionic conductivity and high chemical stability. The impurities are probable to yield great uncertainty in the phase transitions and other measurements. Hence, all the samples were dried in one day without heating to avoid degradation of the samples by kept under low pressure to remove water and other potential pollutants.

2.1. Trihexyl tetradecyl phosphonium bis (trifluoromethyl sulfonyl) amide ($[P_{14,6,6,6}][NTf_2]$)

Trihexyl tetradecyl phosphonium bis (trifluoromethyl sulfonyl) amide $[P_{14,6,6,6}][NTf_2]$ is a colourless viscous fluid with emperical formula $[CH_3(CH_2)_5]_3P[N(SO_2CF_3)_2](CH_2)_{13}CH_3]$ and MW = 764 g/mol. It was obtained from Sigma Aldrich with (≥ 98%) purity. It is hydro phobic in nature. Density of the sample reported as 1.07 g/mL at 20°C. The sample was dried under vacuum prior to measurements. The chemical structure and optimized structure of $[P_{14,6,6,6}][NTf_2]$ by DFT calculation using RB3LYP method with the Gaussian 09 package were shown in figure 2.1 (a) and 2.1 (b) respectively.

a) b)

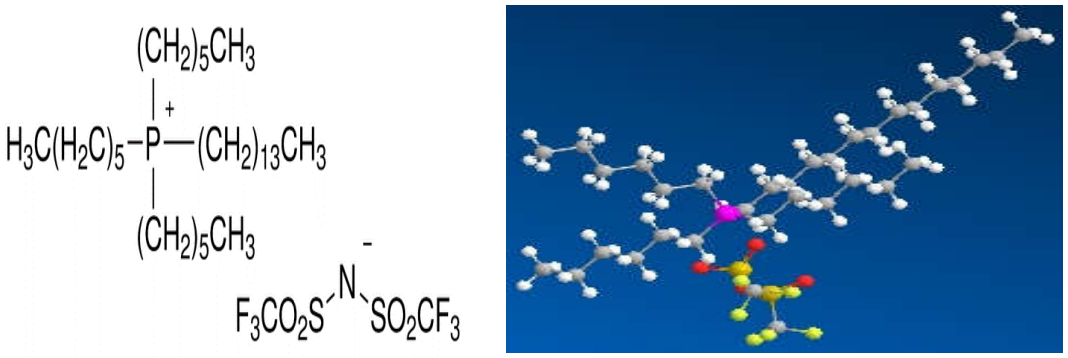

Figure 2.1 (a). The chemical structure and **(b)** optimized structure of $[P_{14,6,6,6}][NTf_2]$ IL.

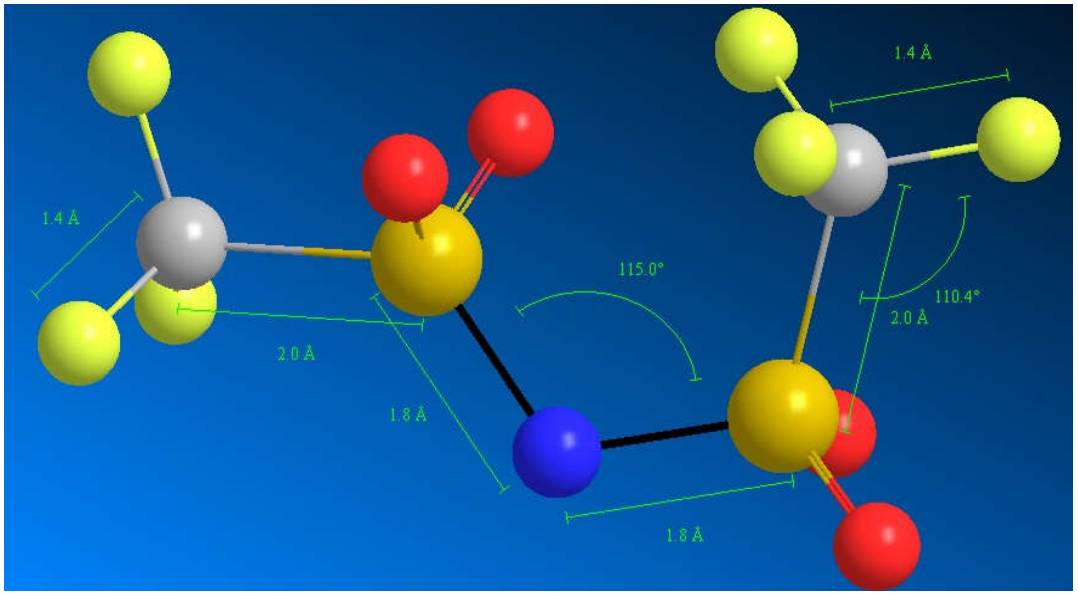

Figure 2.2. Bond length and bond angle of $[NTf2]^-$ anion by DFT RB3LYP method with Gaussian 09 package.

Figure 2.2 shows the bond length & bond angle of $[NTf2]^-$ anion and the details were listed in table 2.1.

2.2. Trihexyl tetradecyl phosphonium dicyanamide ($[P_{14,6,6,6}][N(CN)_2]$)

It is a colourless liquid with emperical formula, $[CH_3(CH_2)_5]_3 P[N(CN)_2](CH_2)_{13} CH_3]$, MW = 549.90 g /mol. It was obtained from Sigma Aldrich with (≥ 98%) purity. Density of the sample was noted as 0.9 g/mL at 20℃. It is a

hydrophobic sample. The sample was dried under vacuum prior to measurements. The chemical structure, bond length and bond angle of $[N(CN)_2]^-$ anion is shown in figures 2.3 (a & b), 2.4 respectively.

a) b)

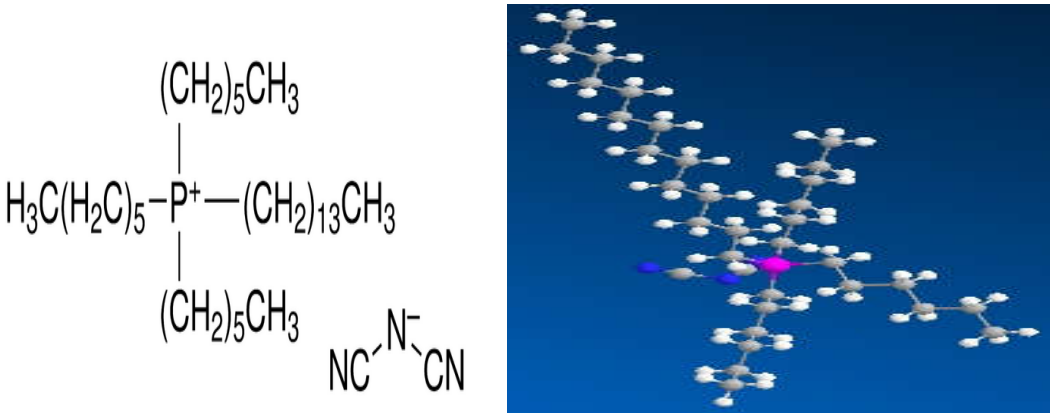

Figure 2.3. (a). The chemical structure and **(b)** optimized structure of $[P_{14,6,6,6}][N(CN)_2]$ IL.

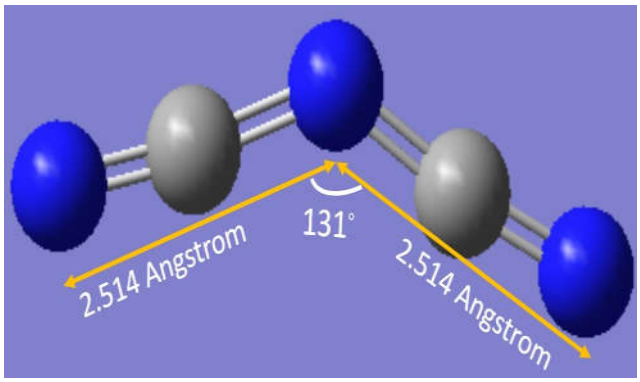

Figure 2.4. Bond length and bond angle of $[N(CN)_2]^-$ anion by DFT RB3LYP method with Gaussian 09 package.

In addition to the ionic interaction between the cation and anion, subsequent interactions between them resulting some bond lengths. Figure 2.4 shows the bond length & bond angle of $[N(CN)_2]^-$ anion and the details were listed in table 2.1.

Table 2.1. *Bond length and bond angle of $[N(CN)_2]^-$ anion and $[NTf_2]^-$ anion.*

Ionic liquid	Dipole moment (D)	Bond length (Å)	Bond angle (degree)
$[P_{14,6,6,6}][Cl]$	15.01		-
$[P_{14,6,6,6}][N(CN)_2]$	11.99	C-N (2.514) N-S(1.8)	C-N-C(131) S-N-S(115.0)
$[P_{14,6,6,6}][NTf_2]$	13.89	C-S(2.0) C-F(1.4) S-F(2.0)	S-C-F(110.4)

2.3. Trihexyl tetradecyl phosphonium chloride ($[P_{14,6,6,6}][Cl]$)

It is a colourless liquid with emperical formula, $[CH_3(CH_2)_5]_3P[Cl)](CH_2)_{13}CH_3$, MW = 519.31. It was acquired from Sigma Aldrich with (≥ 98%) purity and is hydrophobic. Density of the sample is 0.895 g/mL at 20°C. The sample was dried under vacuum prior to measurements. The chemical structure and optimized structure of $[P_{14,6,6,6}][Cl]$ by DFT calculation using RB3LYP method with the Gaussian 09 package were shown in figure 2.5 (a & b).

a)

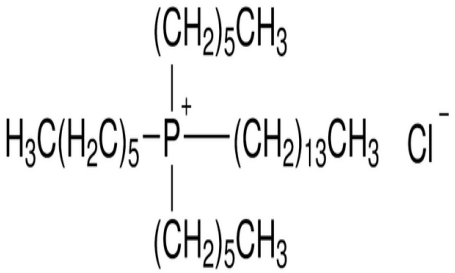

b)

Figure 2.5. (a) The chemical structure and (b) optimized structure of $[P_{14,6,6,6}][Cl]$ IL.

2.4. $[P_{14,6,6,6}][NTf_2][Cl]$

$[P_{14,6,6,6}][NTf_2]$ and $[P_{14,6,6,6}][Cl]$ were obtained from Sigma Aldrich with (≥ 98%) purity. The binary mixtures $[P_{14,6,6,6}][NTf_2][Cl]$ were prepared by dissolving 50 ml

of $[P_{14,6,6,6}][Tf_2N]$ in 50 mL of $[P_{14,6,6,6}][Cl]$ by vigorous stirring with a magnetic stirrer until complete dissolution takes place and kept for one day before dielectric measurements.[55-56] Before the measurements all samples were dried under suitable conditions.

2.5. $[P_{14,6,6,6}][N(CN)_2][Cl]$

$[P_{14,6,6,6}][N(CN)_2]$ and $[P_{14,6,6,6}][Cl]$ were obtained from Sigma Aldrich with ($\geq$ 98%) purity. The binary mixtures $[P_{14,6,6,6}][N(CN)_2][Cl]$ were prepared by dissolving 5 ml of $[P_{14,6,6,6}][N(CN)_2]$ in 5 mL of $[P_{14,6,6,6}][Cl]$ by vigorous stirring with a magnetic stirrer until complete dissolution takes place and kept for one day before dielectric measurements. Before the measurements, all samples were dried under suitable conditions.[55-56]

2.6. PVA and $[P_{14,6,6,6}][NTf_2]$ ionogel

5 g of PVA was dissolved in 50 mL of hot distilled water by vigorous stirring with a magnetic stirrer at 90°C until complete dissolution takes place. After getting gel type PVA addition of $[P_{14,6,6,6}][NTf_2]$ was followed in order to obtain the mass concentration of 75:25 of PVA/$[P_{14,6,6,6}][NTf_2]$. Before the measurements, all samples were dried under suitable conditions.[57-60]

2.7. PVA and $[P_{14,6,6,6}][N(CN)_2]$ ionogel

5 g of PVA was dissolved in 50 mL of hot distilled water by vigorous stirring with a magnetic stirrer at 90°C until complete dissolution takes place and a homogeneous slurry was obtained. After getting gel type PVA, addition of $[P_{14,6,6,6}][N(CN)_2]$ was followed in order to obtain the mass concentration of 75:25 of PVA–$[P_{14,6,6,6}][N(CN)_2]$. Before the measurements all samples were dried under suitable conditions.[57-60]

2.8. Ranitidine docusate

The ranitidine docusate was prepared by combining ranitidine hydrochloride and sodium docusate. It is a dark red liquid. The cation starter, ranitidine HCl is a pale yellow crystalline powder with emperical formula $C_{13}H_{22}N_4O_3S$•HCl, molecular mass 350.86 g/mol. It is soluble in water, ethanol, methanol etc., while

insoluble in chloroform and other common organic solvent. Sodium docusate (sodium dioctyl sulfosuccinate) is used as the anion for drug preparations, which has empirical formula – $C_{20}H_{37}NaO_7S$ and molecular mass of 444.56 g/mol is an emollient white crystalline powder. All the parent drugs were purchsaed from M/s. Sigma Aldrich with specific purity of ≥ 98%. The solvents acetonitrile (reagent grade) and dichloromethane were also procured from Sigma Aldrich. All chemicals were used without further purification. Ranitidine HCl (H_2–receptor antagonist) is an anti–ulcer drug commonly known as Zantac, has been the subject of wide process over polymorphic forms and purity. Ranitidine HCl combine with sodium docusate(an emollient) forms an IL, ranitidine docusate[8] which provide advantages over cation ranitidine HCl. It will not crystallize and avoid problems with polymorphism and impurities. The chemical structure and optimized structure by DFT/RB3LYP method of ranitidine docusate is shown in figure 2.6 (a & b).

Method of preparation

Sodium docusate (1.90 g) was dissolved in 20 mL acetonitrile in a 50 mL round–bottomed flask and continuously stirred with a magnetic stirrer. 1.50 g of ranitidine hydro chloride is added to the above mixture and stirred overnight. Precipitated NaCl, thus formed was removed under vacuum and the deep red-brown residue was extracted with dichloro methane, the resulting solution then being flash chromatographed on silica, eluting with dichloromethane. Removal of the dichloromethane yielded the product (1.60 g, 3.83 mmol, 89%) as a deep, red-brown syrup.[8]

a) b)

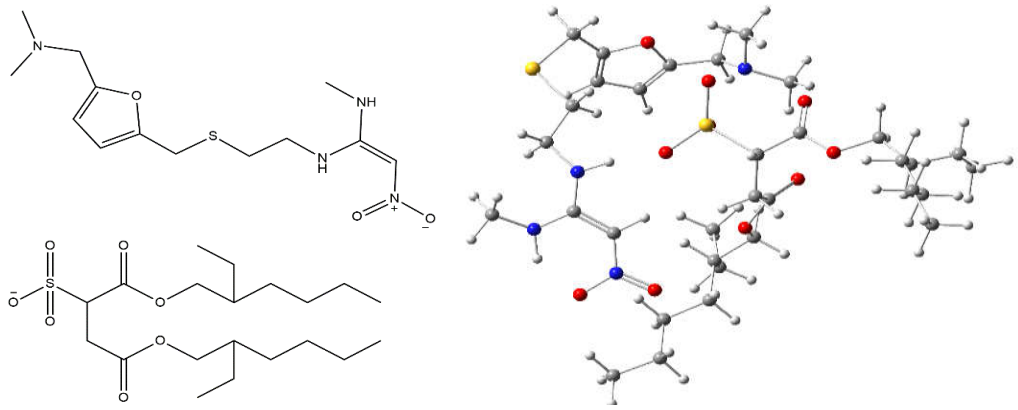

Figure 2.6 (a). Chemical structure and **(b)** optimized structure of ranitidine docusate.

2.9. Lidocaine docusate

Lidocaine docusate was prepared by dissolving lidocaine HCl and sodium docusate. It is a colourless gel and liquid at room temperature. The cation, lidocaine HCl is a white crystalline power $C_{14}H_{23}ClN_2O$ and molecular weight is 270.80 g/mol. It is soluble in alcohol, chloroform, benzene etc. All the parent drugs were purchsaed from M/s. Sigma Aldrich with specific purity of ≥ 98%. The solvents acetonitrile (reagent grade) and dichlo romethane were also procured from Sigma Aldrich. All chemicals were used without further purification. Lidocaine HCl use as a topical anesthetic for the treatment of post surgical, local anesthetic in dentistry and neuropathic pain.[8] Hydrophobic lidocaine HCl combine with hydrophobic sodium docusate forms hydrophobic lidocaine docusate ionic liquid that has shown better efficacy than lidocaine HCl, which has been recognized the enhancement of bioavailability and chemical reactivity on rats. It can be prove that lidocaine docusate will not show any polymorphism and crystallization tendency during cooling into glassy state.[8] The structure of lidocaine docusate is shown in figure 2.7 (a & b).

Method of preparation

In a 100 mL round-bottomed flask charged with a magnetic stirrer, 1.55 g (3.49 mmol) of sodium docusate was dissolved in 25 mL acetonitrile. To the stirred mixture, 0.945 g (3.49 mmol) lidocaine hydrochloride was added. The suspension was further stirred overnight, and the solvent was removed in vacuum. The white residue was extracted with 25 mL of dichloromethane, which was combined and flash filtered through small plugs of silica. The colourless solution was evaporated to leave 1.88 g (2.86 mmol, 82%) of the desired lidocaine docusate salt as a clear, colourless syrup.[8]

a) b)

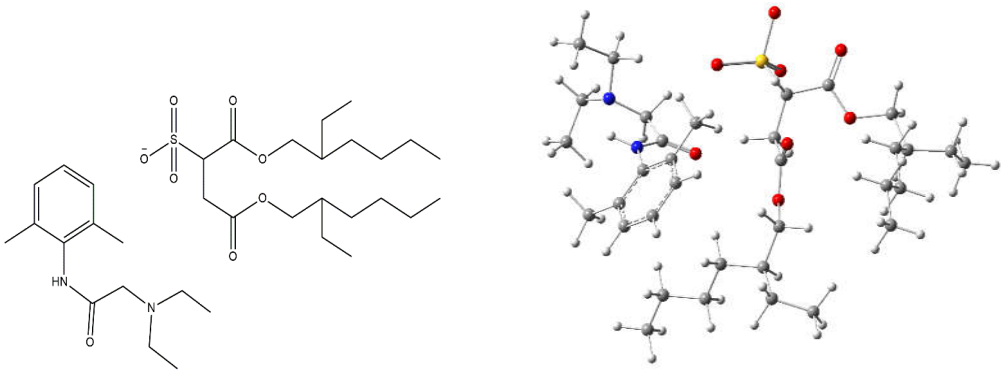

Figure 2.7. (a) Chemical structure and **(b)** optimized structure of lidocaine docusate by DFT/RB3LYP method**.**

3. Dyes, heavy metals and phenolic compounds used for liquid–liquid extraction

The dyes used for the study are rhodamine B, methylene blue, methyl orange, malachite green, conco red and alizarin red S. The chemical structural formulas of the investigated dyes used for the extraction process were shown in figure 2.8 (a & b), 2.9 (a & b), 2.10 and 2.11 respectively. Methylene blue (3,7–bis(dimethylamino)–phenothiazin–5-ium chloride), a catio nic dye, $C_{16}H_{18}ClN_3S$ having a molecular weight 319.85 g/mol with maximum absorption wavelength of 665 nm is used for the study. Methyl orange, an anionic dye, $C_{14}H_{14}N_3O_3SNa$ having a molecular weight 327.33 g/mol with maximum absorption wavelength of 464 nm and rhodamine B (RhB) a cationic xanthenic dye (fluorescent dye) $C_{28}H_{31}ClN_2O_3$ having a molecular weight = 479.02 g/mol and (λmax = 554 nm). Malachite green, is a cationic dye, $C_{23}H_{25}ClN_2$ having molecular weight 364.24 g/mol with an absorption maxima of 618 nm. alizarin red S, $C_{14}H_7Na_2O_7S$ having a molecular weight 342 g/mol with an absorption maxi ma of 445 nm. Conco red, $C_{32}H_{22}N_6Na_2O_6S_2$ having molecular weight 696.7 g/mol with an absorption maxima 497 nm. All dyes were obtained from Sigma–Aldrich. All chemicals were used without further purification.[33-40]

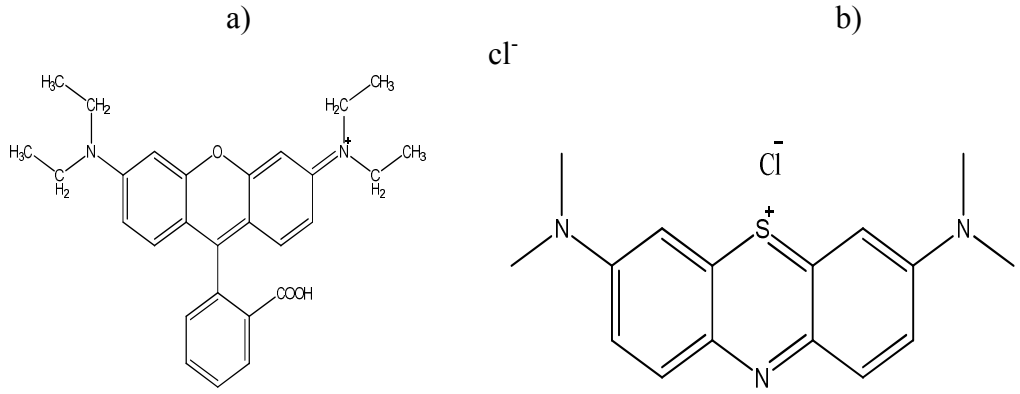

Figure 2.8. Chemical structures of **(a)** rhodamine B & **(b)** methylene blue.

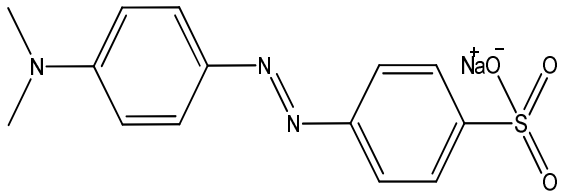

Figure 2.9. Chemical structure of methyl orange dye.

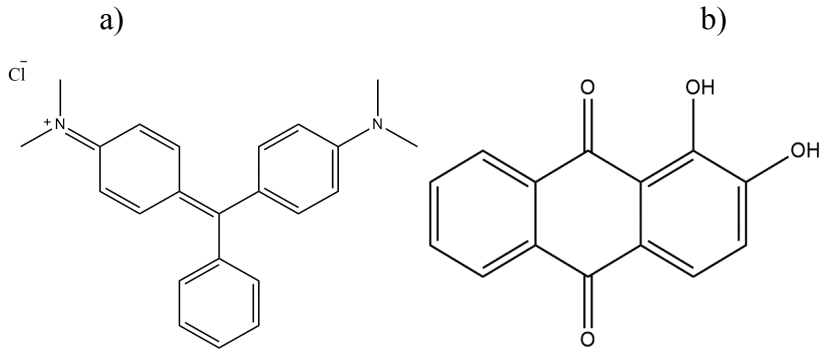

Figure 2.10. Chemical structure of **(a)** malachite green & **(b)** alizarin red S.

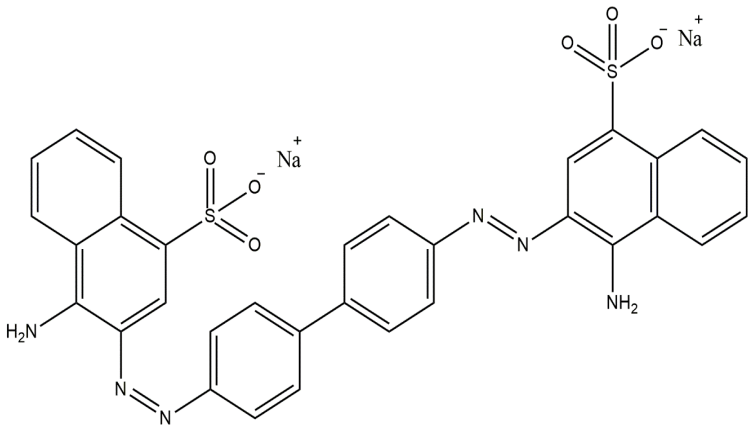

Figure 2.11. Chemical structure of conco red.

CHAPTER 3

MEASUREMENT TECHNIQUES

3.1. VIBRATIONAL ANALYSIS

Spectroscopy compacts with interaction of matter with electromagnetic energy and it is a marvellous method to study about atoms and molecules. Vibrational spectroscopy has been used to make major involvement in many areas of physics and chemistry as well as in other areas of science, used to understand the study of intra molecular and inter molecular forces, identification and characterization of new molecules and molecular structure determinations. [61-65] It includes different techniques, the most important of which are infrared (IR) and Raman spectroscopy. Infrared and Raman spectra are electromagnetic spectra in the optical range (between the visible and microwave regions).[61-65] IR Spectroscopy has delivered detail ed information to detect various characteristic functional groups, to perceive impurities in a compound, on hydrogen bonding, to find whether the compound is aromatic or aliphatic, to catch the carbon skeleton of the sample and interionic interactions. Infrared absorption spectra and Raman spectra are closely unified in that both give rise to the vibrational bands. The advantage of Raman spectroscopy over IR is the ability of Raman spectrum to recognize discrete types of vibrations.[61-65]

When IR light is handed through the material, the vibrational and rotational energies were enhanced. The common vibrations found in the molecules are stretching and bending. In stretching, the distance between the two atoms in the sample may increase or decrease, but the atoms remain in the same bond axis. In bending vibrations, the positions of the atoms modified with respect to the original bond axis. Here, we can reveal that, the stretching absorption reach at high frequency range compared to the bending absorptions. The stretching vibrations are divided by symmetric and asymmetric stretching. Symmetric stretching includes the movement of the atoms with respect to a particular atom in a molecule in the same direction. But, asymmetric stretching occur due to the movement of one of the atoms that approaches the central atom; however the other move to opposite side.[61-65]

Similarly, bending vibrations consists of scissoring, rocking, wagging and twisting vibrations. In scissoring vibrations, two atoms approach each other. In

rocking vibration, movement of the atoms takes place in the same direction. In wagging, the two atoms move up and down with regard to the central atom and in twisting, one of the atoms move up while the other moves down relating to the central atom. Infrared spectra are grouped into middle infrared that cover the range (4000–400 cm^{-1}) and far infrared (400–10 cm^{-1}) range. In this region, most molecules show absorption or emission bands rising from symmetry-allowed interaction with the radiation arena.[61-65] The band intensities can be explained either as transmitttance (T) or as absorbance (A). Transmittance is the ratio of the radiant power transmitted by the compound to the radiant power incident on that compound. Absorbance is the reciprocal of the transmittance, A = log10 (1/T). The absorption intensity is governed by how the infrared photon energy can be transferred to the molecule. This depends on the variation in the dipole moment that happens as a result of molecular vibration. A molecule will absorb infrared light only if the absorption causes a change in the dipole moment. The energy of the absorbed and emitted light quanta is corresponding to the energy difference between the lower vibrational states of the electronic ground state of a molecule.[61-65] The spectra are plotted as either transmittance or absorption against wave number. Some vibration modes can be ascribed to specific functional groups. C–H (3100–2700 cm^{-1}) vibrations are rarely diagnostically useful for C–H bonds, O–H (3600–2500 cm^{-1}) vibrations are for hydroxyl group and N–H (3500–3300 cm^{-1}) absorption peaks appear at same position of hydroxyl group but they can be distinguished by the appearance of sharp peaks.[61-65]

Here, vibrational analysis was done with FT–IR spectrometer (JASCO 4100) in the range of 4000 to 400 cm^{-1} using KBr pellets. The simple working principle of FT–IR comprises a source of light, a stationary mirror, a moving mirror, a beam splitter, a sample and a detector. Primarily, light source passes through the beam splitter and goes to stationary mirror and a moving mirror. Then, the light beam comes back and combines, again passes through the sample. Moving mirror is always moving and stationary mirror is at rest throughout the process. [61-65]

Raman spectra are emission spectra excited by monochromatic radiation in the ultraviolet (25000–14300 cm^{-I}) or near infrared (14300–4000 cm^{-1}) region. They

are owing to modulation of incident light by molecular vibrations.[61-65] This is an inelastic scattering proc ess of low possibility. The emitted faint spectral lines whose energy difference related to the energy of the exciting line are equal to the energy difference between the lower vibrational states. In the present study, Raman spectra were recorded with Bruker MultiRAM FT–Raman spectrophotometer.[61-65]

In the present study, we report a comprehensive series of vibrational band assignments for a series of synthesised samples, Phosphonium based ILs $[P_{14,6,6,6}][NTf_2][Cl]$, $[P_{14,6,6,6}][N(CN)_2][Cl]$, PVA–$[P_{14,6,6,6}][NTf_2]$ ionogel, PVA–$[P_{14,6,6,6}][N(CN)_2]$ ionogel and two pharmaceutical samples: ranitidine docusate and lidocaine docusate. The vibrational band assignments have been accomplished using experimental and theoretical vibrational spectra (both FT–IR and FT–Raman) of six ILs above stated and compared with results obtained from computational calculations.

3.2. COMPUTATIONAL ANALYSIS

The computational characterization was conducted using Density functional theory (DFT) calculations as employed in the Gaussian 09 software to evaluate the structural features, IR signatures and Raman peak analysis of the ILs. FT–IR is the most useful in providing information about presence or absence of functional groups and can be used for the identification of the samples.[27] The calculations were optimized by RB3LYP with LANL2DZ basis set and associated with in the region of 3500–400 cm^{-1}.[27] In this study, we present results from density–functional–theory (DFT) calculations of the structure and vibrational modes of Phosphonium based ILs $[P_{14,6,6,6}][NTf_2][Cl]$, $[P_{14,6,6,6}][N(CN)_2][Cl]$, $[P_{14,6,6,6}][Cl]$ and two pharmaceutical samples: ranitidine docusate and lidocaine docusate.

3.3. THERMAL ANALYSIS

Thermal analysis is used in a lot of technical fields for the development of technologies and for detection of specific properties of materials. Every thermal analysis studies and measures the property as a function of temperature.[66-68] It is promising to detect thermal stability, to find phase changes, for cooling, heat

treatment and other manufacturing processes. Thermal analysis of the ILs was carried out by differential scanning calorimetry (DSC) and thermogravimetric analysis (TGA) techniques.

3.3.1. Thermogravimetric analysis (TGA)

TGA measures the quantity of change in the weight of a sample as a function of temperature or time in a controlled atmosphere on a controlled heating program.[66-69] The heat is applied regularly until the sample is demolished completely. This is done in existence of nitrogen and in absence of oxygen.[66-69] The result can show amount of mass destroyed in each stage of testing the sample. Decomposition of samples recognized from weight loss is often not very precise because mass change characteristics of a material are strongly dependent on the factors such as sample mass, volume, physical form, the shape and nature of the sample holder, the nature and pressure of the atmosphere in the sample chamber and the scanning rate have significant influences on the characteristics of the recorded TGA curve.[66-69] TGA measurements provide the selection of materials for certain applications and evaluate sample performance. The technique is mainly useful for the subsequent types of measuremen ts .[66-69]

- Thermal stabilities
- Oxidative stabilities
- Estimation of product lifetimes
- Decomposition kinetics
- Effects of reactive atmospheres on materials
- Moisture and volatile contents

To check the thermal stability and degradation studies of ILs used for the present study, thermo gravimetric analysis (TGA) was carried out under nitrogen atmosphere with a TA instruments using Perkin Elmer TGA Q50 instrument, 6-8 mg of ILs were used from 300 K to 900 K at 10 K/min heating rate under an air

atmosphere to indicate mass loss and thermal degradation on heating. The sample pan was cleaned and carefully placed onto the sample platform. The sample was placed in the centre of the pan. The appropriate inputs were entered into Q50 TGA programme. The sample was destroyed in the presence of nitrogen and in the absence of oxygen. Once the run is finalized, the pan is carefully cleaned. The temperature was increased from 100°C –700°C at 20°C/min under a nitrogen atmosphere and then held at 700°C for 10 minutes under an air atmosphere.[66-69] In this thesis work, we report the TGA analysis of phosphonium based ILs $[P_{14,6,6,6}][NTf_2]$, $[P_{14,6,6,6}][N(CN)_2]$, $[P_{14,6,6,6}][Cl]$, $[P_{14,6,6,6}][NTf_2][Cl]$, $[P_{14,6,6,6}][N(CN)_2][Cl]$, PVA–$[P_{14,6,6,6}][NTf_2]$, PVA–$[P_{14,6,6,6}][N(CN)_2]$ and two pharmaceutical samples: ranitidine docusate and lidocaine docusate.

3.3.2. Differential scanning calorimetry (DSC) analysis

The thermal technique calorimetry measures heat exchanges in different reactions. Calorimeter is used to exactly determine the heat exchange occurring in chemical reactions. In this study, thermal behaviour and heat capacities of ILs were used for the calorimetric analysis by differential scanning calorimetry.[70-78] DSC is a thermo dynamical tool to direct evaluation of the heat energy uptake, which occurs in a sample within a regulated increase or decrease in temperature. The figure 3.1 shows the DSC apparatus. The DSC measures the difference in the heat flow rate to the sample and to a reference while they are subjected to a controlled temperature program and its behaviour is noted for phase transition analysis and heat capacity calculations. Phase transitions such as fusion, crystallization and the glass transition can be observed using this method.

To get an opening overview about the samples, calorimetric measurements were performed on a differential scanning calorimeter Mettler Toledo DSC 822e by a continuous method rapidly and with high precision using a linear heating and cooling rate of 10 K/min in a dry nitrogen atmosphere with a flow rate of 20 mL/min with a guaranteed purity more than 99.99% in a hermetically closed aluminium pan. The sample of 6 mg were used in a sealed pinhole aluminium pan and empty pan

itself act as a reference to permit a fast heat transfer between the sample and its surroundings and well closed to avoid mass loss of lengthways measurements.[70-78]

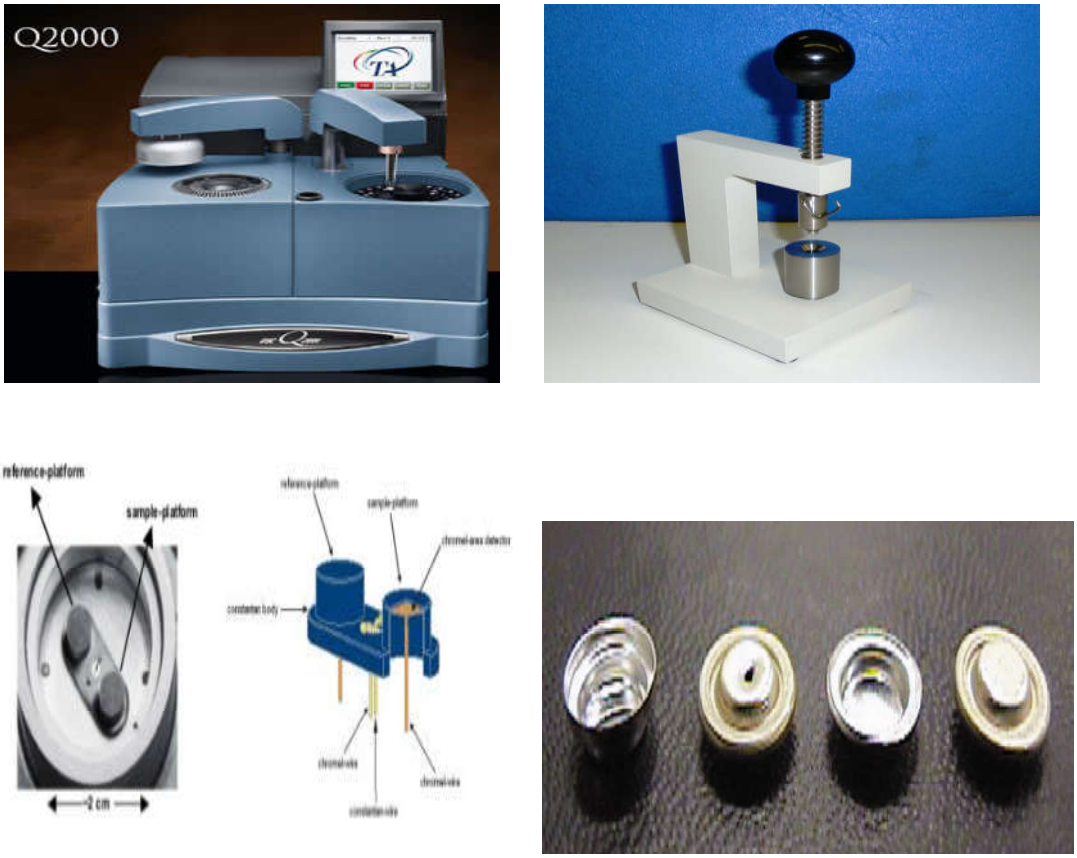

Figure 3.1 DSC apparatus with aluminium pan and crimp set up

DSC records the amount of heat energy absorbed/liberated by it. The samples are cooled from room temperature to -150°C and held for 15 minutes, and then the sample is again heated to room temperature at a constant heating and cooling rate of 10°C/min. DSC plots were collected during heating. Melting point was considered as the onset of the melting endotherm whereas T_g was taken as the peak maximum of the glass transition endotherm. The DSC instrument was calibrated using indium as standard prior to the experiment.[70-78] DSC plot of an amorphous sample indicating the glass transition temperature (T_g), the crystallis ation temperature (T_c) and the melting temperature (T_m) is shown in figure 3.2. In this study, we report the DSC analysis of Phosphonium based ionic liquids $[P_{14,6,6,6}][NTf_2]$, $[P_{14,6,6,6}][N(CN)_2]$, $[P_{14,6,6,6}][Cl]$, $[P_{14,6,6,6}][NTf_2][Cl]$,

$[P_{14,6,6,6}][N(CN)_2][Cl]$, PVA–$[P_{14,6,6,6}][NTf_2]$, PVA–$[P_{14,6,6,6}][N(CN)_2]$ and two pharmaceutical samples: ranitidine docusate and lido caine docusate.

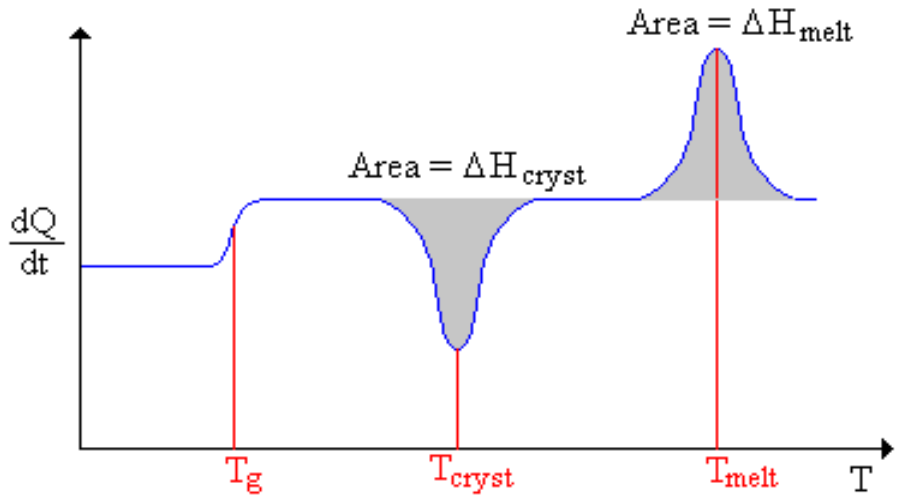

Figure 3.2. DSC plot of a typical amorphous material representing the glass transition temperature (T_g), the crystallisation temperature (T_c) and the melting temperature (T_m).

3.4. DIELECTRIC MEASUREMENTS

3.4.1. Broadband dielectric spectroscopy (BDS)

The instrumental set up of the broadband dielectric spectrometer is shown in figure 3.3. Dielectric measurements of the examined samples were carried out using a Novocontrol alpha dielectric analyzer (Novocontrol Technologies GmbH, Germany) by keeping the liquid sample between two parallel plate electrodes of about 30 mm diameter, separated by Teflon strips ensuring a spacing of 0.1 mm to get an empty cell capacitance of ≅ 60 pF. The experiments were covered in the frequency window of 10^{-2}–10^{7} Hz over a temperature from 123.15 K to 283.15 K to cover the range from deep glassy state to the liquid state. The temperatures were controlled by Novocontrol Quatro Cryosystem using a dry nitrogen gas purge to achieve temperature stability better than 0.1 K. The AC electric field applied was 1V. Dielectric measurements were performed after vitrifying the IL by fast cooling from room temperature to deep glassy state and subsequent isothermal measurements during heating.[99,105] In this present work, we report the dielectric

measurements of phosphonium based ILs $[P_{14,6,6,6}][NTf_2]$, $[P_{14,6,6,6}][N(CN)_2]$, $[P_{14,6,6,6}][Cl]$, $[P_{14,6,6,6}][NTf_2][Cl]$, $[P_{14,6,6,6}][N\ (CN)_2]\ [Cl]$, PVA– $[P_{14,6,6,6}][NTf_2]$, PVA–$[P_{14,6,6,6}][N(CN)_2]$ and two pharmaceutical samples: ranitidine docusate and lidocaine docusate.

Figure 3.3. Broadband dielectric spectrometer

Broadband dielectric spectroscopy turns out to be an ideal experimental tool for characterizing ILs. Because of the ease, they are polarized in an electric field and information related with dynamics (molecular as well as collective), charge transport etc. can be conveniently explored by applying very low electric field.[79-85] Ability of broadband dielectric spectroscopy opens up a marvellous technique by which it can measure the complex dielectric function over many orders of magnitude in an extremely wide frequency and temperature ranges using highly refined and specialized electrical techniques. It analyses the collective response of a material to the applied electric field.[79-85]

The most significant property of a dielectric is its capability of polarisation under the action of an external electric field. By the application of an external field, the atoms and molecules of dielectrics create dipoles and the dipoles attempt to maintain alignment with the field with a finite time that is different for each polarization mechanism. Application of an electrical field (current, potential) to an electrical circuit causes the presence of a response to the system.[67] When an external electric field is applied across the faces of a parallel plate capacitor having a

dielectric material, the atomic and molecular charges in the dielectric are displaced from their equilibrium positions and the material is said to be polarised.[86-86] Polarisation of dipoles created due to their orientation in the direction of the field and distortion in charge distribution of the material are termed as orientational polarisation and distortion polarisation respectively. Orientational polarisation refers to polar molecules which are freely floating in a dielectrically inert non polar fluid and consequently no restoring forces tending to impose a preferred direction. The distortion polarisation is the sum of atomic (PA) and electronic polarisation (PE). When electron clouds of atoms are displaced due to external field from their equilibrium positions with respect to the atomic nucleus, an induced dipole is produced in a direction of field and known as electronic polarisation, which is extremely fast and its resonant frequency is in the UV–visible range of electromagnetic spectrum.[80-90]

The polarisation found in molecules that consist of two different atoms about C and H and the application of an external field will cause deflection of these ions from their equilibrium positions creating an induced dipole moment causing atomic polarisation. i.e., relative motion of atoms in the direction of field gives rise to atomic polarization. Its resonant frequency is found in the infra–red region of electromagnetic spectrum. Hence, both electronic and atomic polarisation have high resonant frequencies that fall within the dominion of vibrational spectroscopy and both are resulted from induced dipoles.[90-99] The total polarisation (P) is the sum of the contributions of orientation polarisation (PO) and distortion polarisation. Accordingly, P = PO + PE + PA. The schematic diagram of ionic, atomic and electronic polarisation is shown in figure 3.4.

Dielectric spectroscopy is a linear response technique, investigating the dynamics of the dipole moment of a macroscopic sample of a polarisable material.[100-110] It is highly sensitive and hence provides a wealth of information about the dynamics of polarization modes active in a medium. It considers the polarisation mechanisms that include polarisation due to charge migration and polarisation due to orientation of permanent dipoles. The migration of charge deals with conductivity and the dipole orientation, means the materials contain permanent dipoles applied by electric field, dipole orientation or dipolar polarisation is

produced as a result of the alignment of dipoles in the direction of applied electric field.[110-120] The spectrum of electromagnetic waves are shown in figure 3.5 below.

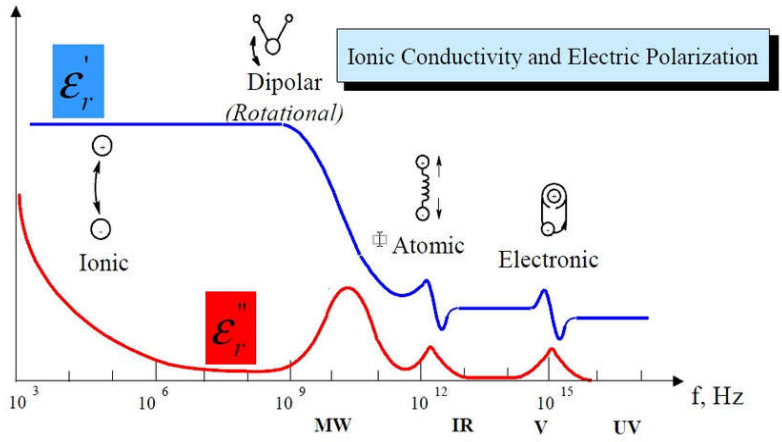

Figure 3.4. Schematic diagram characterises ionic, atomic and electronic polarisation.

In ionic conduction, hopping movement of ions occur. In the presence of nonlinear processes, are more easily understood in terms of the dielectric response to time dependent signals. In most of the engineering applications of dielectrics with linear systems involve response to harmonic signals (sinusoidal waves) of definite frequencies, hence very powerful measuring techniques exist with measurements of such signals using frequency as a param eter with very accuracy instead of time.[90-95]

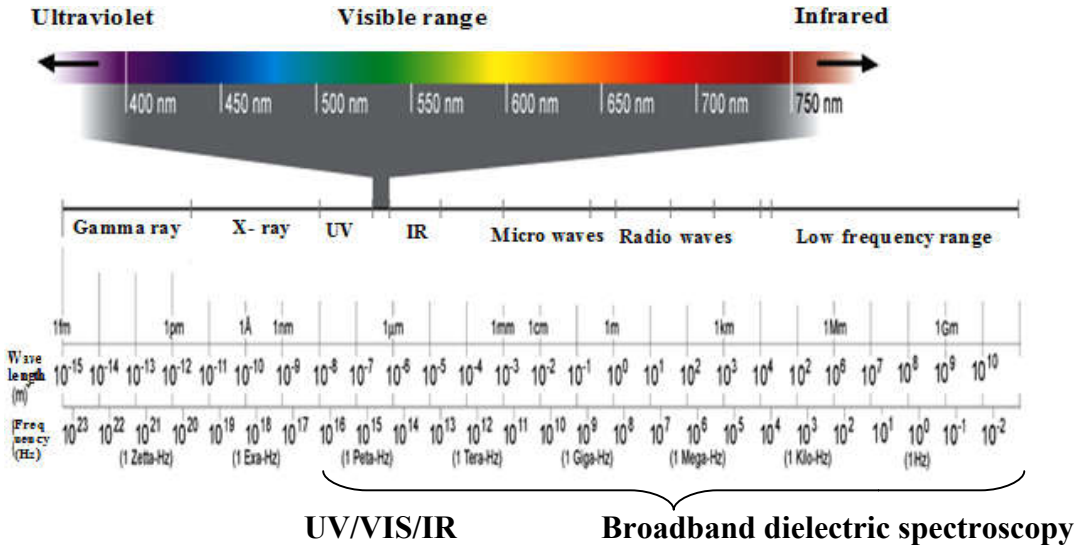

Figure 3.5. The spectrum of electromagnetic waves

3.4.1.1. Complex impedance analysis

The interaction of electric field with solid or liquid samples can be investigated by using two methods. (1) When a voltage V_0 is applied at t = 0 to the sample, a time varying current I (t) is measured. The ratio V_0 / I (t) measures the impedance. It is considered as the time domain measurement. (2) The impedance is measured directly in the frequency domain by applying a single AC frequency voltage V (t) = V_0 sin ωt to the sample and measuring phase shift Φ and amplitude I_m of the resulting current. I (t) = I_m sin (ωt + Φ).[81,90-95] In recent years, the ionic transport phenomenon in single/polycrystalline and amorphous/glassy super ionic conducting materials has been increasingly used to investigate by means of impedance spectroscopy and can be used in five representations, complex impedance, Z^* (ω, T), complex admittance, Y^* (ω, T), complex dielectric permittivity, ε^* (ω, T), complex conductivity σ^* (ω, T) and complex modulus, M^* (ω, T).[81-88] The presence of different resistive and capacitive components in the samples retain different relaxation times due to various processes.[81] The complex impedance and complex admittance plane representations can be analysed to obtain the electrical response of the samples whereas dielectric response of the samples were obtained by the analysis of complex modulus and complex permittivity spectra.[81,85]

In 1969, Bauerle was the first to use impedance spectroscopy technique to measure AC conductivity of solid electrolytes.[86] The schematic diagram of an impedance analyser is shown in figure 3.6. The impedance of the system obeys Ohm's law as ratio of voltage to current in the time domain when an AC signal is applied to a system. Since both amplitude and phase angle of the applied voltage may vary with respect to the current (sinusoidal), the impedance Z (ω) is expressed as a complex quantity, having both magnitude $|Z|$ & phase angle (Φ) between current and voltage and can be represented as[81,90-95]

$$Z(\omega) = |Z| \exp(-j\Phi)$$
$$Z(\omega) = |Z| \cos\Phi - j\,|Z| \sin\Phi \qquad (1)$$
$$Z^*(\omega) = Z'(\omega) - j\,Z''(\omega)$$

The real and imaginary parts of impedance of the sample were measured concurrently as a function of frequency. The measured impedance data can be represented in the other three forms, using the inter relations as follows.[81,90-95]

Complex impedance, $Z^*(\omega) = Z'(\omega) - j\,Z''(\omega)$

Complex Admittance, $Y^*(\omega) = Z^*(\omega) = Y'(\omega) + j\,Y''(\omega) = 1/\,Z^*(\omega)$

Complex permittivity, $\varepsilon^*(\omega) = \varepsilon'(\omega) - j\,\varepsilon''(\omega)$

Complex Modulus, $M^*(\omega) = M'(\omega) + j\,M''(\omega)$

Complex conductivity, $\sigma^*(\omega) = \sigma'(\omega) + j\,\sigma''(\omega) = j\omega\varepsilon_0\varepsilon^*(\omega)$

(2)

where $j = \sqrt{-1}$. The impedance and modulus are series functions that can be measured at high frequencies whereas the admittance and permittivity are parallel functions that can be measured at low frequencies. The presence of different resistive and capacitive components in the materials retain different relaxation times due to various methods.[90-95]

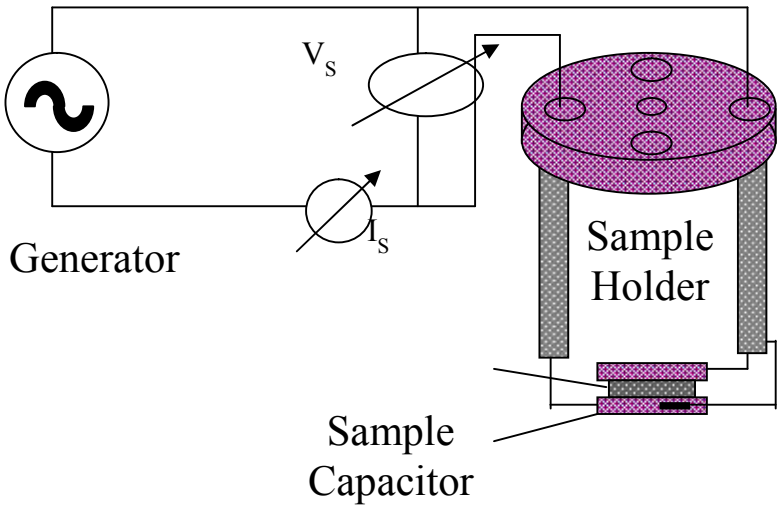

Figure 3.6. Schematic diagram of a dielectric spectrometer

3.4.1.2. Complex electrical conductivity

Conductivity representation relates with movement of ions from macroscopic to microscopic measurement.[95] The electrical conductivity can be characterized as DC and AC conductivity (σ_{dc} & σ_{ac} respectively). The DC conductivity delivers only quantitative information of the materials that characterize a single dynamic response in the glassy ionic conductor, whereas, AC conductivity can hut significant influence on the microscopic nature of the ionic conducting process in the material.[81, 90-95] In general, conductivity measurements were prepared by applying DC bias across the material, which results in the polarization at the electrode/electrolyte interface of the material and hence ionic current decreases with time. This difficulty can be circumvented with (i) DC technique with four electrode configurations or two reversible electrodes and (ii) AC technique. There are two main contributions in dielectric losses in the classical dielectric region: (a) conduction losses due to free charge carriers and (b) dispersion losses due to dipolar relaxations or polarisation method.[81, 90-95]

AC conductivity is virtually independent of frequency at lower frequencies and frequency is decreased as it approaches the DC conductivity. A distinctive frequency depend ence of conductivity spectrum shown in figure 3.7 discloses three distinguished regions: (a) a low frequency dispersion region, (b) an intermediate frequency plateau and (c) an extended dispersion at high frequency region. The variation of conductivity in the low frequency region is due to the polarisation effects at the electrode and electrolyte interface. Increasingly, charge accumulation occurs at the electrode & electrolyte interface as the frequency reduces, and hence, conductivity is dropped. In the intermediary frequency, (plateau region) conducti vity is almost found to be frequency independent due to random diffusion of the charge carriers *via* activated hopping and is equal to DC conductivity σ_{DC}.[81-95] The DC conductivity is caused by translational diffusion of the mobile ions. In the high frequency region, the AC conductivity exhibits dispersion that increases roughly in a power law manner with the frequency which indicates a non–random process wherein the ions perform correlated forward–backward motion and finally becoming nearly linear at even higher frequencies. The AC conductivity is much less

temperature dependent than the DC conducti vity in a power law behaviour. As the temperature increases, the transition from DC to the dispersive region transfers towards the higher frequency range. The frequency dependence of AC conductivity is expressed by a simple relation, Jonscher's universal dielectric response (power law) as ($\sigma_{AC} = \sigma_0 + A\omega^s$), where, σ_0 is the DC conductivity, A is a temperature dependent parameter and s the frequency exponent having its value within $0 < s < 1$ for ion conducting materials.[81-95]

Complex permittivity ($\varepsilon^*(\omega)$) is connected with complex conductivity, ($\sigma^*(\omega)$) with the relation, $\sigma^*(\omega) = \sigma'(\omega) + j\,\sigma''(\omega) = j\omega\varepsilon_0\,\varepsilon^*(\omega)$. When the contribution of σ_0 (DC conductivity) subtracted from $\varepsilon^*(\omega)$, then $\sigma^*(\omega) = \sigma_0 + j\omega\varepsilon_0\,\varepsilon^*(\omega)$, where $\varepsilon^*(\omega)$ represents the complex dielectric constant. The real part of the above equation is given by $\sigma'(\omega) = j\omega\varepsilon_0\,\varepsilon''(\omega)$.[81-90]

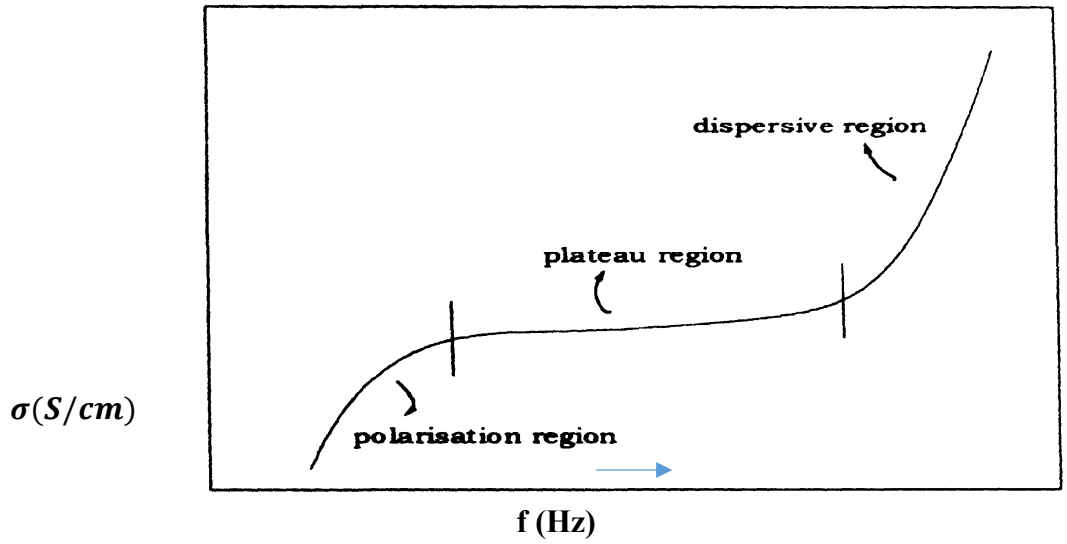

Figure 3.7. Schematic representation of AC conductivity vs. frequency.[105]

3.4.1.3. Complex dielectric permittivity

Dielectric constant (permittivity) is a measure of the capacity of a material to get polarized in the existence of an applied electric field or the ability of material to store the applied electrical energy in the form of polarization. Permittivity representation can be distributed as static permittivity and dynamic permittivity.

Dielectric materials having a permanent dipole moment, when employed in a steady electric field, all types of polarizations can maintain equilibrium with it and is called as static permittivity. When a dielectric material is placed in the electric field of varying frequency, then permittivity of the material changes with the change in frequency of applied field is termed as dynamic permittivity.[90-99]

The only practical method for finding ε for highly conducting liquids is broadband dielectric relaxation spectroscopy in the microwave region. When a field is applied across a sample, the applied field 'V' relocates the charges within the sample and the charges were accumulated at the interface.[97] Dipoles were created with a moment P = qd, where d is the separation of distance between the charges and q is the charge. Here, q = CV, where C is the capacitance of the material and is given by C = C_0 $\varepsilon/\varepsilon_0$ and $C_0 = \varepsilon_0$ A/t where ε_0 is the permit ivity of free space, A is the area of cross section and t is the thickness of the material.[97] Complex permittivity $\varepsilon^*(\omega)$ consists of a dielectric dispersion component $\varepsilon'(\omega)$ (in phase) and a dielectric loss component $\varepsilon''(\omega)$ (out of phase), $\varepsilon^*(\omega) = \varepsilon'(\omega) - j\,\varepsilon''(\omega)$.[96-99] In figure 3.8, with decreasing frequency $\varepsilon'(\omega)$ increases due to the contribution of accu mulation of charges at the interface, whereas at high frequencies ε' results in a constant value due to the periodic reversal of the field that takes place so rapidly, and hence no accumulation of the charge at interface exist. The static dielectric constant ε_s is obtained as the zero frequency limit of the dispersion curve, lim $\varepsilon'(\omega \to 0)$,[96] while ε'' exhibits a maximum value at $\omega = 1/\tau$ where the charges absorbs a maximum energy.[81, 90-99]

$$\varepsilon^*(\omega) = \varepsilon'(\omega) - j\,\varepsilon''(\omega) = 1/(j\,\omega C_0 Z^*(\omega))$$

Where

$$\varepsilon'(\omega) = 1/(\omega A \varepsilon_0 [Z''(\omega)/Z'^2(\omega) + Z''^2(\omega)]) \qquad (3)$$

$$\varepsilon''(\omega) = 1/(\omega A \varepsilon_0 [Z'(\omega)/Z'^2(\omega) + Z''^2(\omega)])$$

$$\tan\delta = \varepsilon''(\omega)/\varepsilon'(\omega)$$

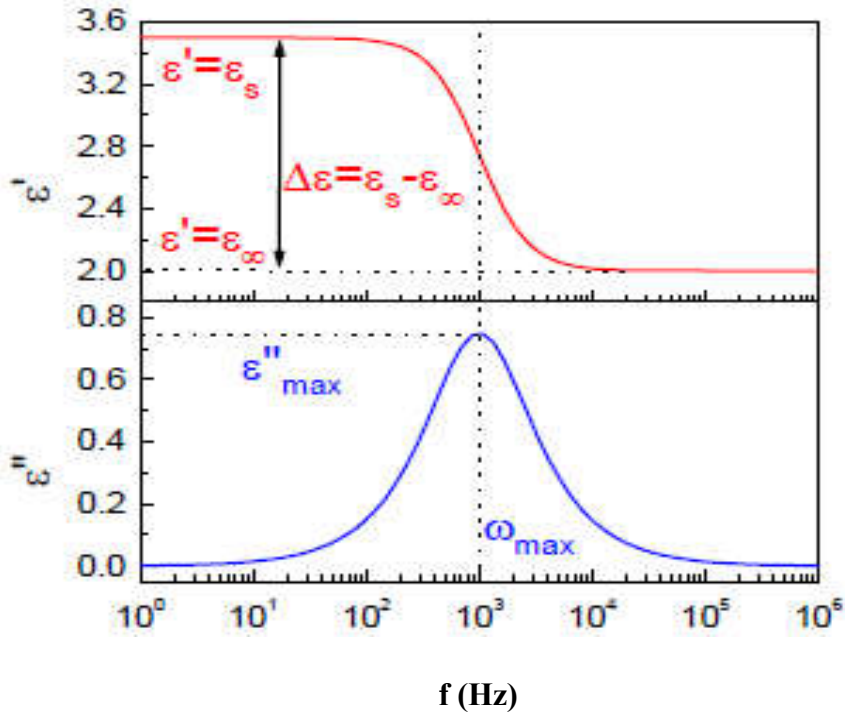

Figure 3.8. Dielectric response ε′ & ε″ as a function of frequency.[120]

3.4.1.4. Complex electric modulus

Most of the dynamical features are supplemented by the motion of charge carriers (orientational polarisation and motion of ions). Hence, dielectric technique quantifies the response to an applied field. In ion conducting glasses or materials, ε″ (ω) have no correspon ding feature found for ionic mobility.[121] Hence, dielectric modulus is a novel and interesting experimental representation for measuring dielectric relaxation which can mask the DC conductivity contribution into a visible peak in M″. The complex electric modulus formalism (developed in 1972) of Moynihan et al. indicate a measure of the distribution of ion energies or configurations in the structure and describe the electrical relaxation in ionic glasses as the microscopic properties of the samples,[98] i.e., which permits to study charge transport processes in ion conductors and eliminates electrode polarization effect.[81, 90-97]

$$M^*(\omega) = M'(\omega) + j\,M''(\omega) = j\omega C_0 Z^*(\omega) = j\omega C_0 (Z'(\omega) - j\,Z''(\omega))$$

$$M'(\omega) = (\omega A \varepsilon_0 Z''(\omega))/t \qquad (4)$$

$$M''(\omega) = (\omega A \varepsilon_0 Z'(\omega))/t$$

where C_0 is the vacuum capacitance and $\omega = 2\pi f$ is the angular frequency. The relation conec ting with dielectric permittivity and conductivity can be given as[105, 121,130]

$$M^*(\omega) = 1/\varepsilon^*(\omega) = \frac{j\omega\varepsilon_0}{\sigma(\omega)} \qquad (5)$$

The real and imaginary parts given by[105, 121,130]

$$M'(\omega) = \varepsilon'(\omega)/\varepsilon'^2(\omega) + \varepsilon''^2(\omega) = \frac{\varepsilon_0 \omega \sigma''(\omega)}{((\sigma'(\omega))^2 + (\sigma''(\omega))^2)}$$

$$M''(\omega) = \varepsilon''(\omega)/\varepsilon'^2(\omega) + \varepsilon''^2(\omega) = \frac{\varepsilon_0 \omega \sigma'}{((\sigma'(\omega))^2 + (\sigma''(\omega))^2)} \qquad (6)$$

The real and imaginary part of modulus representation $M'(\omega)$ and $M''(\omega)$ are shown in figure 3.9.

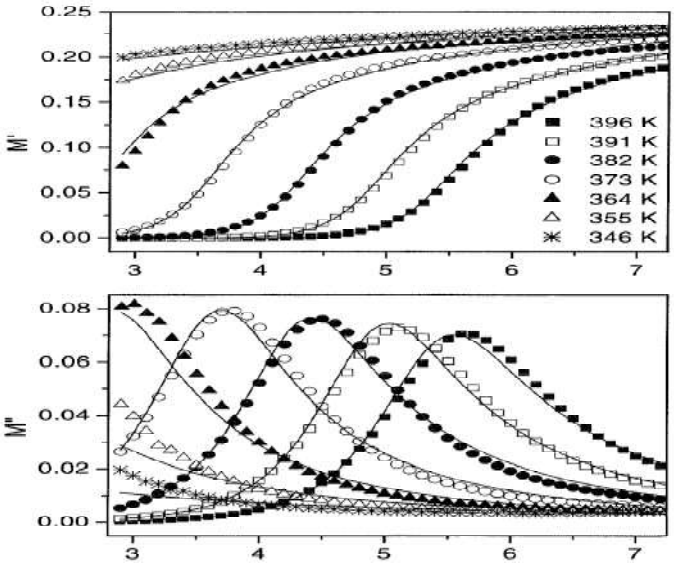

Figure 3.9. Plots of $M'(\omega)$ & $M''(\omega)$ vs log f.[97]

3.4.2. Glassy dynamics and charge transport in ionic liquids

Cooling a liquid below its melting point usually results in crystallisation characterized by long–range order.[67,79] However, if the system is exposed to high enough cooling rates, the molecules do not get sufficient time to rearrange themselves to establish structural ordering and reach a super cooled liquid state (having higher energy than crystal), on further cooling viscosity of the super cooled liquid increases (10^{12} Pa.s) and the resulting material is a glass or amorphous solid.[67,80-82] At liquid state (above melting temperature), molecules are highly disordered and mobile, with vibrational, rotational and translational (diffusing) components.[80] The character of glass former means that below melting point, the super cooled material retains its liquid character falling out of the equilibrium down to it when glass temperature T_g is reached. i.e., the liquid structure becomes blocked at the glass trans ition temperature T_g.[67,80-82] Most of the IL retain their super cooled liquid state when cooled below their melting point and finally reach the glassy state on further cooling.[83]

When an electric field is applied to a dielectric, the decay of polarization to zero value is not instantaneous, but takes a finite time and this time required for the dipoles to revert to a random distribution in equilibrium with the temperature of the medium from a field oriented alignment is described by the term dielectric relaxation. Generally, the study of the relaxation process forms a powerful method for obtaining information about the nature and types of molecular motions of the given IL in super cooled and glassy state. If crystallization can be avoided, the characteristic relaxation times drop below the nanosecond regime and finally reach at 100 s at the glass transition temperature T_g, which sets the low temperature limit to the equilibrium of the material used.[67,82-99] Possible transitions of a liquid to glass is shown in figure 3.10 (a & b) below.

A number of methods have been established to determine ion mobility and charge transport of ionic liquids in their supercooled liquid state and the glassy state under an electric field. Normally, the complete characterization of different relaxation behaviour requires the use of a variety of techniques in order to extent the

relevant ranges in frequency. Some important experimental techniques that can be used for studying molecular motions in ionic liquids are Dielectric spectroscopy in the microwave and far-infrared regime, Optical kerr effect (OKE) spectroscopy, Pulsed field gradient nuclear magnetic resonance (PFG NMR), Quasi elastic neutron scattering (QENS), Electron spin resonance (ESR), and Time–resolved fluorescence spectroscopy.[1] Among them, broadband dielectric relaxation spectro scopy (BDS) is a powerful tool to assess in situ the dynamical behaviour in the super cooled and glassy state of glass formers for investigating interaction of electromagnetic waves over a wide frequency range from 10^{-2} to 10^{12} Hz and an extensive temperature range helps to study the molecular, collective fluctuations, charge transport, polarization effects and determine the dielectric properties of the material under study.[67,79, 86-90]

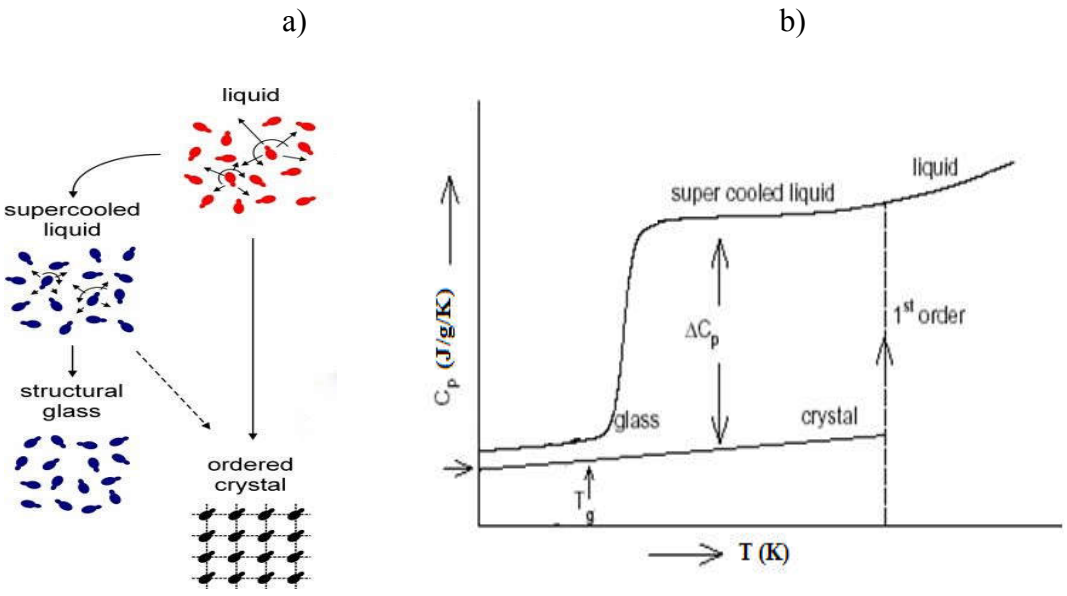

Figure 3.10. (a) Schematic diagram represent a transition from a liquid state to glassy state[122] and (b) plot of C_p (specific heat capacity) vs temperature.

Significant information about the different molecular dynamics and collective processes can be obtained through the study of dipolar reorientations covering a wide time scale (10^5 s to 10^{-12} s); different temperature steps and the experimental measurements were easy and pre cise, thus the dielectric data are the

most abundant.[87, 89] In fact, the dielectric spectroscopic technique facilitates the study of several processes, from slow cooperative molecular motions to relatively fast reorientations of entire molecules or side groups, as well as ionic condu ctivity. The technique is appropriate for exploring dielectric processes for both electrical and nonelectrical applications.[87]

Relaxation spectra can be described in time, frequency and temperature domains. The first two can be transformed into each other by Laplace transformation, while the under standing of the last is more difficult due to the temperature dependence not only of τ, but also of the relaxation strength. Glassy systems exhibits some relaxation processes. Generally, die lectric spectra in glassy dynamics represent in three relaxation process: DC conductivity, conductivity relaxation (structural relaxation or α relaxation) and secondary relaxation (β, γ, δ etc).[67,87-99] DC conductivity is due to translational motion of mobile ions present in the sample while conductivity relaxation (structural relaxation) and secondary relaxation are relat ed to rotational molecular motion.[87-99] The main or the structural α-relaxation, usually interp reted as due to the cooperative motions of molecules, which become kinetically frozen upon cooling the liquid to form a glass.[86-89]

Besides α-process, many glass formers exhibit one or more further relaxation processes, which usually have shorter relaxation times than the structural process and are well detectable below glass transition. In some systems, secondary relaxation process originates from motion of small portion (intra molecular origin) of the molecules such as side group.[86-89] This intra molecular secondary process is system dependent so that information on the universal aspects of the glass transitions is recognized. There are some other systems, supposed not to have internal molecular degrees of freedom, in which, the observed secondary relaxation process reflects the small angle motion of whole molecule (inter molecular origin), and is usually referred as Johari – Goldstein (JG) process.[67,87,96] In the early years, secondary relaxation, in general, were considered as originating from some intra molecular degrees of freedom, and hence, cannot be related to the intermolecular

cooperative α –relaxation. In 1970, Johari and Goldstein shocked the research community by showing the existence of secondary relaxation in a totally rigid small molecular glass-former. [67,96] Secondary relaxation or β-relaxation is a fast process and its relaxation time changes with temperature more slowly than that of the structural relaxation one, and it can be monitored in the glassy state over a wide range of temperature.[80-82] For this reason, the β process is a unique source of information on relaxa tion properties of a glassy state and consequently, it is considered by many researchers in the field as a fundamental characteristic of glasses.[80-82]

Dielectric techniques are commonly used to enumerate the response of an ionic liquid to a field induced perturbation.[91] It is exclusively sensitive to intermolecular interactions and is capable to monitor cooperative processes at the molecular level.[91-96] It enables different processes to be monitored in a single experiment, i.e., it allows observation of both the movement of ionic species in the presence of an electric field and the reorientational motions of dipolar molecules.[90] In fundamental research arena, ILs are appealing due to the dual advantages of ionic conductivity and glass forming nature.[86] The later opens up an avenue to investigate some of the fundamental queries on the dynamics of ionically conducting glass-formers in their liquid as well as in glassy states.[67, 86] They deal a rare avenue to address some of the basic reviews regarding the universal features of glass transition phenomena, namely, how the ionic conductivity is associated to the dynamics of glass transition, the question of the universality of secondary relaxation etc.[67]

One of the challenges of ILs is the understanding of motions of ions and how they affect the charge transport properties.[83] This is very important to understand their applicabili ty in energy sources. Charge transport and molecular dynamics in amorphous ion conductors are the topics of technological importance. Revealing charge transport mechanism in ILs is quantitatively necessitated by the demands to achieve efficient, optimal and eco-friendly power sources to replace the harmful electrolytes used in conventional batteries. Ion motion, whether by the interstitial or vacancy mechanism, below the vibrational frequencies can be pronounced by activated hopping between charge carriers. Motion of ions produces an electri cal

response which can be discovered by a variety of experimental techniques. Hopping cond uction has found specific applications in glassy materials and amorphous semiconductors.[101-114] The probability of a hopping may be determined by the distance between the two sites and the potential barrier that has to overcome the transition. The charge transport of ion conducting material was investigated in detail by the J. Dyre's random barrier model.[13, 83-94] Within the framework of this model, the charge transport in disordered systems may be explained in terms of hopping of charge carriers in spatially varying random energy landscape. The highest barrier determines DC conductivity σ_0 and the time corres ponding to the attempt rate to overcome the highest barrier is denoted by τ_e.[99,105] The ability of the charge carriers to overcome the randomly distributed energy barriers governs the transport process. The model approximates the complex dielectric function by the analytical equation given by[83-94,105]

$$\varepsilon * (\omega) = \varepsilon_\infty + \left(\frac{\sigma_0 \tau_e}{\varepsilon_0 (l\, n(1+ \mathrm{j}\, \omega\tau_e))}\right) \tag{7}$$

where $\varepsilon_\infty$is the high frequency relaxed value of ε', σ_0 is the dc conductivity and $\tau_e$is the electrical relaxation time.

On resolving the equation into real and imaginary parts, we get[82, 88,94,105]

$$\varepsilon'(\omega) = \left(\frac{\sigma_0 \tau_e \ln(1+\omega^2 {\tau_e}^2)}{\frac{1}{4} ln(1+\omega^2 {\tau_e}^2)^2 + 2\varepsilon_0 \,(\arctan\omega\tau_e)^2}\right)$$

$$\varepsilon''(\omega) = \left(\frac{\sigma_0 \tau_e \,(\arctan\omega\tau_e)}{\frac{1}{4}\ln(1+\omega^2 {\tau_e}^2)^2 + \varepsilon_0 \,(\arctan\omega\tau_e)^2}\right) \tag{8}$$

From the above, the conductivity can be obtained as[83-94, 105]

$$\sigma * (\omega) = \sigma_0 \left(\frac{\mathrm{j}\, \omega\tau_e}{\ln\,(1+ \mathrm{j}\, \omega\tau_e)}\right) \tag{9}$$

The real and imaginary part delivers as[83-94, 105]

$$\left.\begin{aligned}\sigma'(\omega) &= \left(\frac{\sigma_0\omega\tau_e \arctan(\omega\tau_e)}{\frac{1}{4}ln^2(1+\omega^2{\tau_e}^2)+(\arctan\omega\tau_e)^2}\right)\\ \sigma''(\omega) &= \left(\frac{\sigma_0\omega\tau_e \ln(1+\omega^2{\tau_e}^2)}{\frac{1}{2}ln^2(1+\omega^2{\tau_e}^2)+2(\arctan\omega\tau_e)^2}\right)\end{aligned}\right\} \quad (10)$$

Amorphous ion conductors are also considered due to their prospective applications in charge storage devices.[13,100] Universality of charge transport mechanisms and its role to the glassy dynamics in ILs had been one of the hot subject among the researchers. In early 1970s, an empirical formula was suggested by Barton–Nakajima–Namikawa (BNN), where the DC conductivity σ_0 and ω_e were correlated and is almost universal, vary weakly with temp erature.[13,83,100] It carries the important information about AC and DC conduction which are closely related to each other and are having the same mechanism. This approximate equality was derived by Einstein and Einstein–Smoluchowski equations, where, the DC conductivity can be described as[13,100-105]

$$\sigma_0 = nq\mu = n\frac{q^2D}{KT} = n\frac{q^2}{KT}\frac{\lambda^2}{2\tau_h} = n\frac{q^2}{KT}\frac{\lambda^2\omega_e}{2} \quad (11)$$

where n is the effective number density of ions, q is the elementary charge and D is the diffusion coefficient, ($D = \frac{\lambda^2\omega_e}{2}$) , λ is the hopping length of charge carriers and τ_h is the hopping time, $\tau_h \sim \tau_e = {}^1/_{\omega_e}$. σ_0 and ω_e are the main directly observable quantities characte rizing charge transport in ionic liquids and other ion conducting glass formers.[83,100] BNN plot for different liquids are indicated in figure 3.11 below.

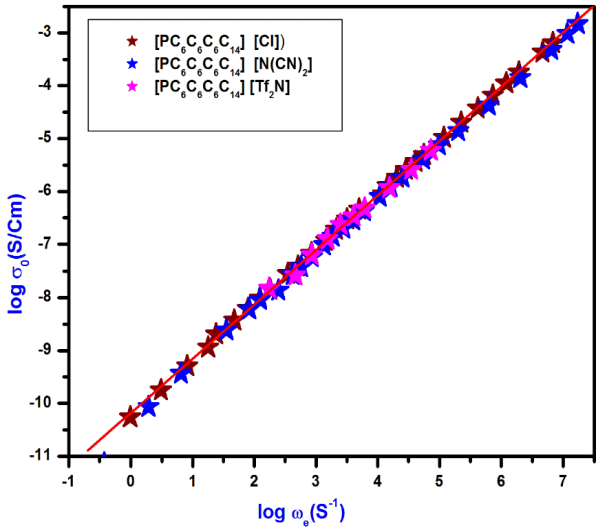

Figure 3.11. DC conductivity ($\boldsymbol{\sigma_0}$) versus the characteristic frequency (ω_e) (BNN plot) for different ionic liquids as indicated.

The properties of dielectric materials are generally represented by dielectric relaxation functions as Debye function, Cole– Cole, Cole– Davidson and Havriliak–Negami (HN) function. Debye's response model was the first theoretical function for the dielectric performance of the materials. Conversely, due to its limitations, this model is unable to explain in detail the dielectric response of a large number of solids and liquids.[105] In 1929, Debye conceived a simple model for the relaxation process, which described by the relation[78,105-106]

$$\varepsilon * (\omega) = \varepsilon_\infty + \frac{\Delta\varepsilon}{1 + j\,\omega\tau_D} \qquad (12)$$

where $\Delta\varepsilon = \varepsilon_s - \varepsilon_\infty$, ε_s is the static permittivity, ε_∞ is the permittivity at infinite frequencies and τ_D is the relaxation time of Debye function. The dielectric loss peak of the Debye type relaxation is symmetric with a half width of ω_D, i.e. the complex permittivity plot shows nearly a semicircle and gives a characterising response to it. In opposition, the behaviour of most dielectric materials leaves in varying steps from the Debye function and a more complete model based on experimental data on dielectrics was proposed by Cole and Cole in 1941. An asymmetric broadening is

shown in Cole– Cole function and this new formulation contains a parameter β which can assume values between 0 and 1 and is obtained as[78,105-106]

$$\varepsilon * (\omega) = \varepsilon_{\infty} + \frac{\Delta\varepsilon}{1+(\mathrm{j}\,\omega\tau_{CC})^{\beta}} \qquad (13)$$

where β=1-α, represents the angle of tilt of the circular arc from the real axis and has no physical significance. Davidson and Cole proposed a modification for Cole–Cole function in 1951 which gives a pear shaped plot with an angle of tilt $\gamma = 1-\beta$ and is represented by the equation[67, 105-106]

$$\varepsilon * (\omega) = \varepsilon_{\infty} + \frac{\Delta\varepsilon}{(1+\mathrm{j}\,\omega\tau_{CD})^{\gamma}} \qquad (14)$$

For $\beta = 1, \gamma = 1$, Debye type function is obtained in both model functions.[83] Certain dielectric behaviour which cannot represented by above functions as of both functions contain only one parameter to represent the shape of the plot. Hence, Havriliak– Nigami introduced a relation connecting combination of Cole – Cole and Cole– Davidson in 1966 given as[67, 105-106]

$$\varepsilon * (\omega) = \varepsilon_{\infty} + \frac{\Delta\varepsilon}{\left(1+(\mathrm{j}\,\omega\tau_{HN})^{\beta}\right)^{\gamma}} \qquad (15)$$

It is commonly used model function in glass forming materials. This two parameter function is able to fit in many of the observed results. Figure 3.12 (a & b) shows the real and imag inary spectra of Debye, Cole– Cole, Cole– Davidson and HN functions. The corresponding modulus function for HN function cannot be calculated accurately, but in a good approximation can be given as [67, 78,84]

$$M^{*}(\omega) = M_{\infty} + \frac{\Delta M}{\left(1+(-\mathrm{j}\,(\omega\tau_{HN})^{-1})\,^{\beta}\right)^{\gamma}} \qquad (16)$$

Here, exponents β and γ are parameters representing symmetric and asymmetric broadenings of the dielectric loss curve, $\Delta\varepsilon$ is relaxation strength, ω is an angular frequency and ε_{∞} is high-frequency limit permittivity.[78,84] When β was fixed to be equal to unity, the HN function goes into the Cole–Cole function.[83,105]

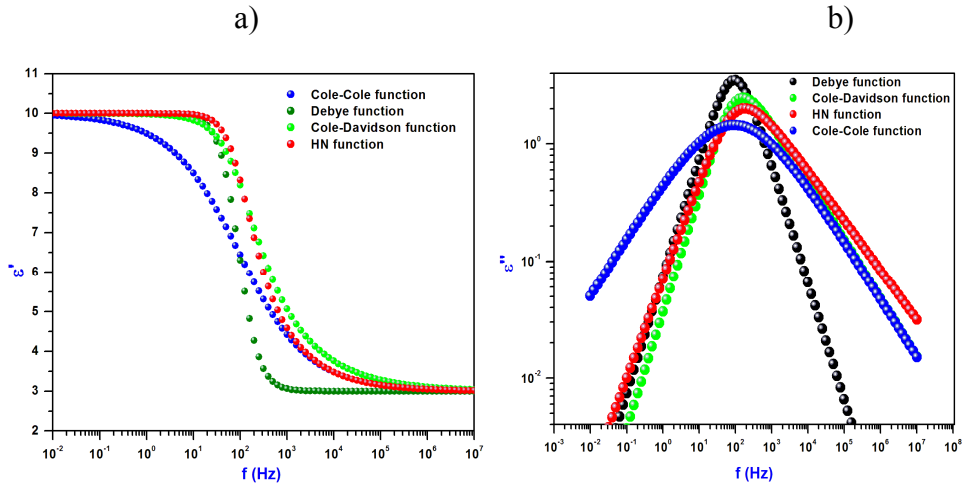

Figure 3.12. (a & b) Real and imaginary spectra of Debye, Cole–Cole, Cole–Davidson and HN functions.[78,84,105-106]

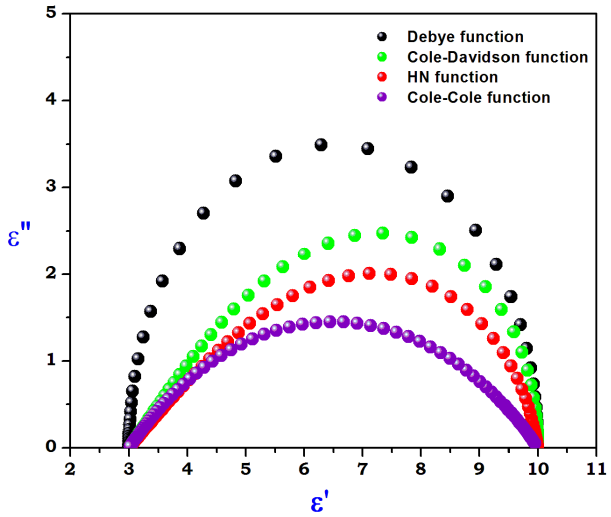

Figure 3.13. Cole– Cole diagram of Debye, Cole– Cole, Cole– Davidson and HN functions.

Above the glass transition temperature, dielectric data from the impedance measurem ents were fitted with HN function, which is capable of quantitatively describing the experim ental data, and below the glass transition temperature, dielectric data were fitted with Cole– Cole function. The Cole– Cole plot of all the above functions is shown in figure 3.13. From the figure, it can be shown that the Cole–Cole plot of Debye function is symmetric in nature, but all other functions shows an asymmetric behaviour.[67, 78,84] Conductivity relaxation (above T_g) shows

non Arrhenius Vogel-Fulcher-Tamman (VFT) behaviour in most of the amorphous systems. The VFT equation is widely used to fit the conductivity data to get the quantitative information about the glass-forming behavior of the ionic liquids and is expressed as[98-99,106]

$$\tau_\alpha (T) = \tau_\infty \exp\left(-\frac{B}{T-T_0}\right) \qquad (17)$$

where τ_∞ is the high temperature limit of the conductivity relaxation time, B is the fitting parameter controlling the curvature, B = D T_0 and T_0 is the Vogel temperature. The value of D expresses the deviation from Arrhenius behavior. The temperature dependence of the β relaxation (Secondary relaxation) exhibits a linear dependence and it is given as[98-99,105-115]

$$\tau_\beta (T) = \tau_\infty \exp\left(\frac{E_a}{RT}\right) \qquad (18)$$

where τ_∞ is the pre-exponential factor, E_a is the activation energy and R is the gas constant. It is intuitive to calculate the fragility or steepness index for getting further insights into various structural features and intermolecular interactions collectively contribute to the overall stability of amorphous phase of the three ILs.

Angell suggested a classification of the amorphous systems based on the temperature dependence of mean relaxation time (or viscosity) above Tg as of "strong" and "fragile" systems.[74-75,115-126] Strong glass formers display an Arrhenius type behaviour, with activation energy independent of temperature, whereas fragile glass formers show a non-Arrhenius dependence upon with the temperature characterized by temperature–dependent activation energy.[125-126] A way to estimate the fragility of glass-forming materials is given by[74,115-126]

$$m = \frac{d log_{10}\tau_\sigma}{d\left(\frac{Tg}{T}\right)}\Big/_{T=Tg} \qquad (19)$$

where m is the fragility parameter, τ_σ is the conductivity relaxation time and T is the temperature. A meaningful theoretical framework has been proposed by H. Tanaka in his two order parameter (TOP) model. According to this, a competition exists between long–range density ordering leading to crystallization and short–range

ordering promoting formation of locally preferred structures not consistent with the crystal geometry. When the former effect dominates, the system eventually favours crystallization. On the other hand, if the later effect leads, the system becomes frustrated and inhibits the crystallization.[74-75] Consequently, the fragility may be explained as the measure of degree of frustration and greater the fragility, more the tendency to recrystallize is expected[124] to get a quantitative deduced parameter ($D = B/T_0$) which expresses a degree of deviation from the Arrhenius law.[96,105] Accordingly, strong systems have a value of D > 25, while fragile systems have value D < 10.[96,105] Fragility is also one of the important parameters that predicts the stability of a system against recrystallization tendency during storage of an amorphous system though this property is not so relevant for ionic liquids.[123-126] It can be found that the typical values of m for strong glass formers have (m ≅ 16) and m ≅ 200 for fragile" ones. Hereafter, fragility has a key aspect in choosing the best temperature condition for storing amorphous pharm aceutical.[74-75] Angell plot (log τ (s) vs (T_g/T)) of a glass forming system is shown in figure 3.14 below.[125-127]

To define the conductivity relaxation process more quantitatively, we employed the empirical non–exponential one-side Fourier transform function in time domain given as, [96,105]

$$\phi(t) = \exp\left[-(t/\tau_\sigma)^{1-n}\right] \qquad (20)$$

proposed by Kohlrausch–Williams–Watts (KWW), where $\phi(t)$ is the relaxation function, *t* is time, τ denotes characteristic relaxation time, and 1 – n = β_{KWW} is the stretching parameter related to width of the relaxation peak, i.e. comparison of the shape of the spectra ($0 < \beta_{KWW} \leq 1$). Small value of β_{KWW} specifies the broad relaxation peak and $\beta_{KWW} = 1$ denotes the narrow width of relaxation peak (Debye type relaxation) and the values of β < 1 indicates the non–Debye relaxation.[128] The value of β_{KWW} provides the non-exponential character of the relaxation function in time domain. The molecular relaxation processes are typically non exponential and are normally characterized using the empirical KWW equation.[94-99, 128]

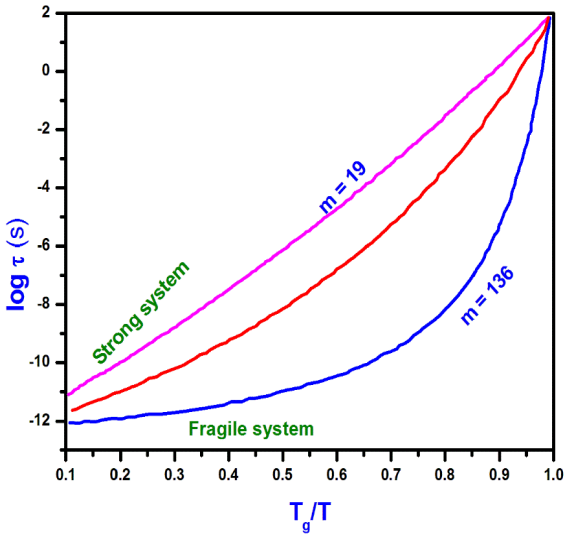

Figure 3.14. Angell plot (log τ (s) vs (T_g/T)) of a glass forming system[125, 127]

Getting visions about the origin and consequence of the slowest resolved secondary relaxation is of interest to the researchers working in amorphous materials.[128] This is because of the classic revelation of intermolecular secondary relaxation in all the rigid dipolar systems investigated by Johari and Goldstein as early as in 1970s.[67,96,161] Following investigations on glass formers of all kind revealed the presence of this secondary relaxation, which possesses non trivial coupling with the primary relaxation. To acknowledge this classic innovation, we call them as Johari–Goldstein (JG) secondary relaxation.[67,96,128] In 1979, K.L Ngai came up with a theoretical model citing about a primitive relaxation being the precursor of the α–relaxation.[99] On comparing with the resolved inter molecular secondary relaxation, he found that τ_{JG} (T, P) = τ_{CM} (T, P), i.e. the primitive relaxation is equal to the JG relaxation. His model can be represented with the following equation called Coupling model equation given by[98-99]

$$\tau_{CM} = (t_c)^n(\tau_\alpha)^{1-n} \qquad (21)$$

where τ_α is the structural relaxation time, t_c= 2 ps for molecular glass formers and 1– n = β_{KWW} is the stretched exponential parameter of KWW equation used to fit the structural relaxation process. Dielectric spectroscopy is attracting an increasing attention of characterization of pharmaceutical materials and is applied for investigating various types of glass forming liquids including ILs.[98-99] It can play a

significant influence on the crystallization processes and stability of pharmaceuticals.[98-99]

3.5. LIQUID–LIQUID EXTRACTION METHOD

Dyes are organic compounds which delivers colour to that material. The colour of a dye is due to the existence of a major structure element chromophore group. They are widely used to colour the materials as textile fibre, paper, leather, hair, fur, plastic material, wax, as cosmetic base and food stuff. Based on chemical structure of chromophore, there are 20–30 diverse collections of dyes.[33-40]They commonly contain a minimum of one nitrogen–nitrogen (N=N) double bond. They are widely used in various industries such as textiles, paper, carpet, leather, plastics, rubber, pharmaceutical, food and cosmetics. Textile and other industries produce huge amounts of dyes annually in worldwide and are discharged in to soil as liquid wastes that contain organic and inorganic compounds. The discharge of polluted, toxic, carcinogenic dyes and their metabolites into the environment affect the aquatic biota and human health. The release of coloured wastewater from textile industry may cause many significant problems, such as contamination of soil, ground water and surface water, increase in toxicity and chemical oxygen demand (COD) of the effluent and also decrease of light penetration, which has a derogatory effect on photosynthetic phenomenon. In this condition, removal of dyes from aqueous effluents is essential. Developing an efficient methodology for extracting these toxic dyes from aqueous discharge has been a herculean task for the industry.[33-40,131-133] Different technologies have been established for the removal of dyes from water and wastewaters, including biological wastewater treatment, physical (membrane filtration, adsorption, coagulation, flocculation, precipitation, reverse osmosis, ion exchange, etc.) and chemical (oxidation, ozonation, etc.) processes. However, most of these techniques have advantages and also demonstrate major drawbacks which have been widely reviewed.[33-40,131-133]

Among the oxidation process, UV/ozone or UV/H_2O_2 is one of the best method for the total removal of dye from wastewater and these processes are only effective for low concentrations of organic matter present in water. The separation

of dyes based on adsorption method on peat, wood, silica, bagasse pith, activated carbon & slag and bagasse fly ash have been suggested for removing the dyes from concentrated wastewater. But, rejuvenation of most of the adsorbents is difficult except for activated carbon. The factors affecting in dye adsorption are: dye/adsorbent interaction, adsorbent surface area, particle size, temperature, pH, and contact time. Adsorbents which enclose amino nitrogen tend to have a considerably larger adsorption capacity in acid dyes.[33-40]

In the flocculation precipitation process, the dye forms a complex with the flocculants; hence, the reuse of dye is not possible. The physical techniques are non–destructive and merely transfer the pollutants from one medium to another, thus giving subordinate method. Due to high dosage and production of a large quantity of sludge, chemical methods are not economically feasible. Precaution is needed to avoid membrane fouling in ultrafiltration (UF) and nanofiltration (NF) which can be used for complete removal of all classes of dyes. The conventional biological wastewater treatment process is not very proficient in treating wastewater having dye due to low biodegradability of dyes.[33-40, 131-133]

In recent years, solvent extraction or liquid–liquid extraction has often been a preferred choice in separation processes.[33-40,131] From various methods to remove the dyes from the aqueous solution, liquid–liquid extraction/adsorption of textile dyes is the more effective, economic and eco–friendly process to extract and recover dyes from wastewaters.[33-40,131] In technological front, the ILs showed potential ability for the removal of dyes owing to their hydrophobic nature on investigating *via* liquid–liquid extraction method. [33-40,131] The removal of different ionic dyes (e.g., methylene blue, malachite green, methyl orange, orange G, congo red, alizarin red S and rhodamine B) was possible by liquid–liquid extraction or adsorption process. Dye removal percentage from aqueous phase increases with the decrease in dye concentration or with the increase in surfactants concentration. Methylene blue is one of the most generally used dye for cotton, wood and silk. It can cause some harmful effects such as increased heart rate, vomiting, shock, cyanosis, jaundice, and quadriplegia and tissue necrosis in humans.[33-40]

ILs have extended an increasing attention in industry and academia. ILs are reflected as highly effective environmentally friendly solvents for liquid−liquid extraction and adsorption of organic dyes and heavy metals due to their unique physicochemical properties like hydrophobicity, low volatility, non–flammability, high thermal and oxidative stability, tunable viscosity and high solubility. Moreover, the physicochemical properties of ILs can be tailored by the proper choice of their cation/anion combinations which allows them to be tuned for specific applications, such as in extraction processes that can replace conventional volatile solvents and where the recovery of solvent and reuse of dyes are required features.[33]

3.5.1. Removal of toxic textile dyes

The adsorption/extraction of dyes *viz.* rhodamine B, methylene blue, methyl orange, alizarin red S, malachite green and congo red with phosphonium based hydrophobic ILs $[P_{14,6,6,6}][NTf_2]$, $[P_{14,6,6,6}][N(CN)_2]$, $[P_{14,6,6,6}][Cl]$ and their binary mixtures $[P_{14,6,6,6}][NTf_2][Cl]$, $[P_{14,6,6,6}][N(CN)_2][Cl]$, PVA–$[P_{14,6,6,6}][NTf_2]$ ionogel and PVA–$[P_{14,6,6,6}][N(CN)_2]$ ionogel were investigated. A stock solution of the dyes containing 47, 31 and 32 ppm respectively were prepared by dissolving the dyes in distilled water (DI). For adsorption kinetics studies, the dye solutions of 10 mL were added to different 50 mL conical flasks and 1.5 mL of the IL was injected into each dye solution using a syringe, and consequently, a cloudy solution was obtained. The flasks were kept on an orbital shaker and stirred for 15 min at a fixed rpm to ensure that the dyes were extracted into fine droplets of ILs. The DI water from each dye solution was separated out using a syringe. UV−vis absorption spectra were recorded for finding the concentration of dye solution before and after adsorption of the dyes, and the efficiency of adsorption was calculated. The reuse of ILs and given dyes is also possible by proper methods using suitable solvents[131] The extrac tion/adsorption efficiency (E) can be calculated by the equation[33-37]

$$E = \frac{C_i - C_f}{C_i} \times 100 \qquad (22)$$

where C_i and C_f represent initial and final concentrations of the dye in the aqueous solution respectively. It can be shown that the adsorption process is affected by the

amount and type of ILs used and the type of dyes as well as initial concentration of the dye solutions. The partition coefficient of the dyes concerning IL was calculated by[33-37, 131-133]

$$P = \left[\frac{C_i - C_f}{C_i}\right]\frac{V_{aq}}{V_{IL}} \qquad (23)$$

V_{aq} is the volume of aqueous dye solution and V_{IL} is the volume of ILs.

3.5.2. Extraction of heavy metals and phenolic compounds

The extraction of heavy metals (arsenic, chromium, cadmium, mercury, lead, zinc and copper) from their standard solutions AS $(NO_3)_3$, Cr (NO_3), Cd $(NO_3)_2$, Hg $(NO_3)_2$, Pb $(NO_3)_2$, Zn $(NO_3)_2$, and Cu $(NO_3)_2$ and phenolic compounds from rice and cashew industrial waste waters with phosphonium based hydrophobic ILs $[P_{14,6,6,6}][NTf_2]$, $[P_{14,6,6,6}][N(CN)_2]$ and $[P_{14,6,6,6}][Cl]$ were investigated. For extraction studies of heavy metals, 50 mL of standard solution of each heavy metal (arsenic, chromium, cadmium, copper, zinc, lead, mercury) was added with 0.25 g of the three ILs in separated conical flasks. The flasks were kept on an orbital shaker stirred for 5 minutes at a fixed rpm. Consequently, the ILs adsorbs the heavy metals and pure water is separated with a syringe. ICPMS (Inductive coupled plasma mass spectroscopy) method is used to find the outcome concentration and the efficiency of adsorption.[33-40]

For extraction studies of phenolic compounds, the polluted rice and cashew waste waters of 50 mL were added to different 100 mL conical flasks and 0.125 g of the ILs were injected into each waste water using a syringe. The flasks were kept on an orbital shaker stirred for 5 minutes at a fixed rpm. Consequently, the ILs adsorbs the phenolic contents and after filtering, pure water is separated. UV−VIS quantification method is used for finding the concentration of phenolic compounds adsorbed and the efficiency of adsorption is calculated.[33-40]

3.6. *IN SILICO* ANALYSIS OF DRUG LIKENESS & TOXICITY STUDIES

In silico studies are the first stage of drug discovery and further studies of them can be done after getting lead molecules. The pharmacokinetic profile (i.e.,

absorption, distribution, metabolism, excretion and toxicity (ADMET)) and topological polar surface area (TPSA), clogP, fragment-based drug likeness, drug score values, etc. with phosphonium based hydrophobic ILs $[P_{14,6,6,6}][NTf_2]$, $[P_{14,6,6,6}][N(CN)_2]$ and $[P_{14,6,6,6}][Cl]$ were predicted using POM (Petra, Osiris and Molinspiration) analysis, admetSAR and ADME tools. Comparison of the parameters is done with their standard drugs used for different pathogens.[134-137]

3.7. BIOLOGICAL ACTIVITIES

Currently, the pharmaceutical industry is facing several problems and challenges in the discovery of innovative and effective drugs and their subsequent applications. Approximately 50% of the available drugs are directed as salts. This can have many disadvantages, some of which is related to low solubility, low bioavailability, low thermal stability, low chemical stability and the polymorphism of drugs. The advances of strategies using ILs are, therefore, a promising avenue for the pharmaceutical industry. Conversion of the crystalline drugs into IL is, therefore, a promising avenue for bypassing the above shortcomings.[138-146]

The bacterial resistance to antibiotics show a serious public health threat and needs novel and urgent actions. Anti–oxidant substance has the ability to neutralise and reduce the concentration of free radicals which may prevent oxidation. This pathology requires innovative therapies that can minimize or eliminate the side effects currently associated with conventional therapies. ILs are attracted due to their biological properties such as anti–cancer activities, anti–microbial agents, anti–oxidants, and local anaesthetic and are a promising compound. Consequently, tunable properties and toxicities of ILs could potentially be designed to impart maximum efficacy with minimal toxicity as anti–cancer, anti–microbial, anti–oxidants, anti–viral and other therapeutic agents. Several studies have reported the use of ILs in biomedical applications against tumors, and as anti–bacterial and anti–oxidant agents. Arising from these, we studied different biological properties of the three phosphonium based hydrophobic ILs $[P_{14,6,6,6}][NTf_2]$, $[P_{14,6,6,6}][N(CN)_2]$ and $[P_{14,6,6,6}][Cl]$.[138-146]

Cell lines and cell culture

Four cancer cell lines: A549 (Human lung cancer), K562 (chronic myelogenous leukemia), Jurkat E6–1 (leukemic T cell lymphoblast) and HCT 116 (colorectal carcinoma) were obtained from National Centre for Cell Science (NCCS), Pune, India. HCT 116 was cultured in Dulbecco's modified Eagles medium, while K562 and Jurkat E6–1 were maintained in RPMI-1640. Both Dulbecco's modified Eagles medium and RPMI media were supplemented with 10% fetal bovine serum, streptomycin (100 µg/mL) and penicillin (50 IU/mL). A549 was maintained with 2 mM L-glutamine and Earle's basal salt solution adjusted to contain 1.5 g/L Na bicarbonate, 0.1 mM non essential amino acids, and 1.0 mM of Na pyruate. Cells were cultured in a humidified atmosphere containing 5% CO_2 at 37°C.[138]

3.7.1. Cell viability assay (MTT assay)

The effect of three phosphonium based hydrophobic ILs $[P_{14,6,6,6}][NTf_2]$, $[P_{14,6,6,6}][N(CN)_2]$ and $[P_{14,6,6,6}][Cl]$ on cell viability was determined using MTT assay. Briefly, 10,000 cells/well were seeded into a 96 well tissue culture plate (shown in figure 3.15) and incubated overnight in CO_2 incubator at 37°C in 5% CO_2 atmosphere under humidified condition. Subsequently, fresh medium containing varying concentrations of the three ILs used were added to each well and incubated for 48 h. After incubation, the media was aspirated and replaced with fresh medium. MTT (5 mg/mL) dissolved in phosphate-buffered saline (PBS) was added to each well, and the plates were incubated for further 4 h at 37°C in dark. After removing the medium, the formazan crystals formed were dissolved in DMSO and the cell growth condition was reflected by the color intensity of the formazan solution. Absorbance at 570 nm was taken on a 96-well microplate reader (MD VERSA max). The half maximal inhibitory concentration of proliferation (IC_{50}) values for samples on each cancer cell line was calculated as the average of three independent experiments. The OD (optical density) value was used to calculate the percentage of viability using the formula[138-146]

$$\% \text{ of cell viability} = \frac{OD\ value\ of\ experimental\ sample}{OD\ value\ of\ experimental\ control} \text{ x } 100 \quad (24)$$

Morphological observation

A549 cells were grown ($1x10^5$/cover slip) and incubated with the three phosphonium ILs at their IC_{50} concentrations, and then, they were fixed in methanol: acetic acid (3:1, v/v). The cover slip was gently mounted on glass slide for the morphometric analysis. Morphological changes of the A549 cells were analyzed under Nikon (Japan) bright field inverted light microscope at 40X magnification.[140]

DAPI staining for nuclear morphology study

For visualization of A549 cells, the nuclei of the cells were stained with DAPI. The efficiency of ILs were tested through apoptosis study. For this purpose, A549 cells were treated with ILs at their IC_{25} and IC_{50} concentrations for 24 h at 37 °C. Then, cells were fixed with 4% paraformaldehyde for 15 min, permeabilized with 0.1% Triton X-100, and stained with 1 mg/mL DAPI for 10 min. The cells were then rinsed with PBS and morphological changes were analyzed under fluorescence microscope (Nikon Eclipse, Inc., Japan) at 400X magnification with excitation filter at 510–590 nm.[140]

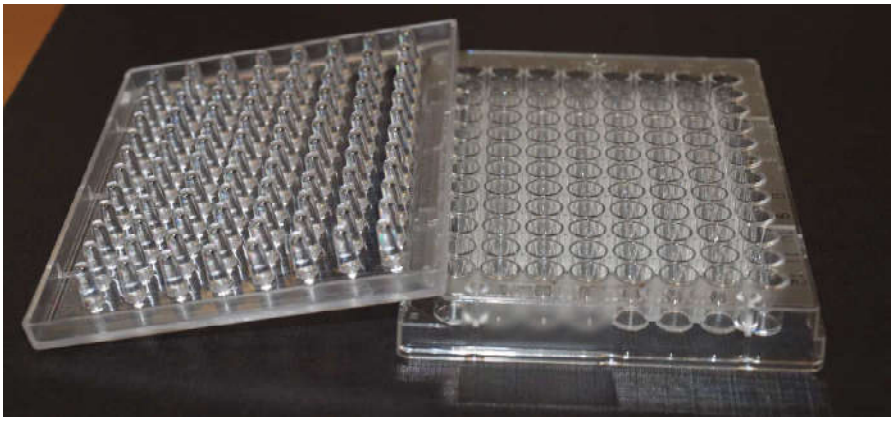

Figure 3.15. Commercially available cell viability assay tissue culture plate.

3.7.2. Anti–bacterial activity

The *in vitro* anti–bacterial activity of the three phosphonium based hydrophobic ILs $[P_{14,6,6,6}][NTf_2]$, $[P_{14,6,6,6}][N(CN)_2]$ and $[P_{14,6,6,6}][Cl]$ ILs were

tested against two bacterial strains *viz. E. coli* and *S. aureus* by the agar disc diffusion method. The inocula of the selected bacterial species were prepared from fresh overnight broth cultures (Tripton soy broth with 0.6% yeast extract-Torlak, Serbia) which were incubated at 37°C at constant stirring and used for diffusion studies. The diffusion technique was carried out by pouring agar into Petri dishes to form 4 mm thick layers and adding dense inocula of the test organisms of two bacterial strains in order to obtain better growth. Petri plates were left for 10 min in a laminar air flow and discs (6 mm) were prepared from Whatman no. 3 filter paper, immersed into different volumes (0, 2.5, 5.0, 7.5 (µg/mL) of samples, placed at equal distances and then incubated at 37°C for overnight in a bacteriological incubator. The results were obtained by measuring the width of the zone of inhibition in millimeter around the disc which was produced by the samples against the two bacterial strains.[147-160]

3.7.3. Anti–oxidant assay (DPPH free radical scavenging assay)

The DPPH (1,1-diphenyl–2-picryl hydrazyl) radical scavenging activity of three phosphonium based hydrophobic ILs $[P_{14,6,6,6}][NTf_2]$, $[P_{14,6,6,6}][N(CN)_2]$ and $[P_{14,6,6,6}][Cl]$ were carried out as per Brand–Williams *et al.* protocol with slight modifications. Different concentrations of samples were prepared in methanol. 0.1 mM methanolic solution of DPPH was added to these concentrations and absorbance was measured at 517 nm after 30 minutes incubation in the dark. Ascorbic acid was used as standard. All measures were done in triplicate. The DPPH scavenging activity was calculated as[151-161]

$$\% \text{ DPPH scavenging activity } = \frac{\text{A control} - \text{A sample}}{\text{A control}} \text{ X } 100 \qquad (25)$$

The IC_{50} concentration which is required to obtain a 50% antioxidant effect was determined.

3.8. ELECTROCHEMICAL CHARACTERISATION OF SUPERCAPACITOR

The main bottleneck in fabricating a supercapacitor for high voltage applications is the difficulties involved in improving the operational voltage

window. The conventional electrolyte can provide a voltage in the range of 0–1 V. To overcome this, a better electrolyte with high ionic conductivity, improved electrode-electrolyte interaction, better electrochemi cal and thermal stability had to be selected. In addition to these, the selected ionic liquids are non–flammable (essential to have good electrolyte for practical application), have low melting point, low volatility, and have better solubility with many organic compounds by virtue of their ionic liquid nature. Thus, we fabricated double layer supercapacitor (EDLC) with graphene/activated carbon as working electrode and the ILs $[P_{14,6,6,6}][NTf_2]$, $[P_{14,6,6,6}][(NCN)_2]$, $[P_{14,6,6,6}][Cl]$ and their polymer composite as the electrolytes. Subsequ ently, we carried out electrochemical measurements using cyclic voltammetry, impedance spectroscopy and charge–discharge measurements for comparing their electrochemical perfor mance.[27,130,165-167]

3.8.1. Fabrication of supercapacitor cells:

The ionic liquid electrolyte was first impregnated in a filter paper (Whatman filter paper) for about 10 minutes to get the IL absorbed completely in the paper. The grapheme/activated carbon electrodes were fabricated on a copper foil in the standard procedure as given in our previous publications from our laboratory. Thus deposited active layer mass was noted down for the estimation of specific capacitance and energy density by a sensitive weighing balance. Both symmetric electrodes were then placed face to face by keeping the filter paper in between and slightly pressed to form a complete cell.[27,130,165-167]

3.8.2. Electrochemical measurements of supercapacitor:

Electrochemical characterization of thus formed supercapacitor was carried out with an electrochemical work station (Bio–Logic electrochemical work station): cyclic voltammetry (CV) over a voltage range from -3.5 V to 3.5 V at scan rate of 50 mV/s, electrochemical impedance spectroscopy (EIS) over a frequency range from 1MHz to 1mHz with alternating current amplitude of 20 mV, and charge discharge measurements from -3.5 V to 3.5 V. The specific capacitance, operational voltage and energy density were calculated from the obtained values.[27,130,165-167]

CHAPTER 4

THERMAL, SPECTROSCOPIC & ELECTROCHEMICAL INVESTIGATIONS ON IONIC LIQUIDS

4.1. THERMAL ANALYSIS AND BROADBAND DIELECTRIC MEASUREMENTS

4.1.1. Thermal and broadband dielectric spectroscopic analysis of $[P_{14,6,6,6}][NTf_2]$ IL

4.1.1.1 Thermogravimetric analysis (TGA)

To study the thermal stability of the IL $[P_{14,6,6,6}][NTf_2]$, TGA measurements are taken within an interval of 300 K– 900 K. The mass loss curve of the IL is presented in figure 4.1. The decomposition temperatures (Td) were obtained over the TG curves and reveals that the IL has good thermal stability, i.e., exposed good obstruction to thermal decomposition, up to 573 K and began to decay gradually above this temperature.

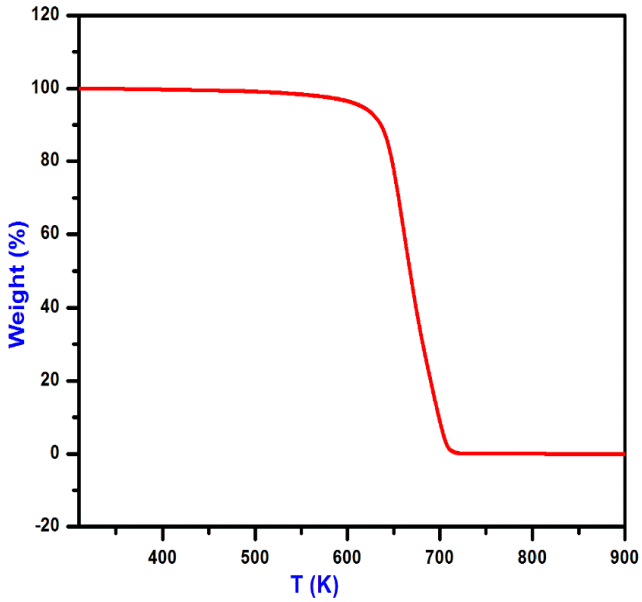

Figure 4.1. TGA plot of $[P_{14,6,6,6}][NTf_2]$ IL.

4.1.1.2. Differential scanning calorimetry (DSC) analysis

DSC plot of $[P_{14,6,6,6}][NTf_2]$ at a heating rate of 10 K /min from 123 K to 300 K is shown in figure. 4.2. The slight deviation in the DSC slops are due to the base line mismatch and does not in any way affect the transition temperatures.

$[P_{14,6,6,6}][NTf_2]$ IL could be super cooled at a normal cooling rate of 10 K/min without any indications of crystallization. The cooling curve showed a step–like change indicating a glass transition of 193.02 K.

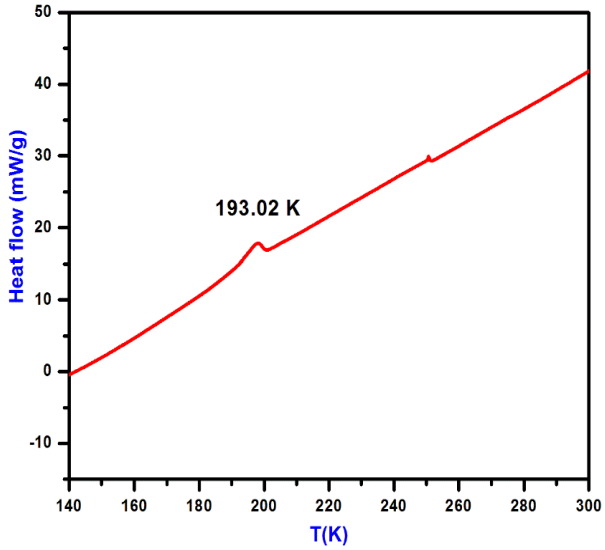

Figure 4.2. DSC plot of $[P_{14,6,6,6}][NTf_2]$ IL.

4.1.1.3. Broadband dielectric spectroscopy (BDS) analysis

In this current work, we report the dielectric relaxation dynamics of phosphonium based IL $[P_{14,6,6,6}][NTf_2]$, from deep glassy state to room temperature at ambient pressure over a wide frequency (10^{-2} to 10^{7} Hz) and temperature range (123 K to 300 K) by broadband dielectric spectroscopy (BDS) and the dielectric spectra of permittivity, conductivity and modulus representations in real and imaginary part above and below T_g were plotted as a function of frequency at various temperatures. Molecular dynamics study has a vital role to explain the stability, reactivity and physicochemical properties of amorphous materials. For monitoring the molecular dynamics, many experimental techniques were used taking advantage of the molecular mobility in both super cooled and glassy states.[13,27,162] Dielectric spectroscopy hails to be the best among other techniques, where minute molecular information can be extracted by applying a small AC electric field using highly refined and specialized electrical techniques over a wide frequency range.

BDS measures the complex impedance of a sample, $z^*(\omega) = z'(\omega) - j\,z''(\omega)$ and the results can be exemplified in three equivalent representations, *viz*. permittivity ($\varepsilon^*(\omega) = \varepsilon'(\omega) - j\,\varepsilon''(\omega)$), conductivity ($\sigma^*(\omega) = \sigma'(\omega) + j\,\sigma''(\omega)$) and electric modulus ($M^*(\omega) = M'(\omega) + j\,M''(\omega)$).[13,27,162]

Molecular dynamics study of $[P_{14,6,6,6}][NTf_2]$ IL from 123 K to room temperature at ambient pressure over a frequency of 10^{-2} to 10^{7} Hz were studied by BDS and the real and imaginary part of the dielectric spectra above and below T_g in permittivity, conductivity and modulus representations were plotted as a function of frequency in figure 4.3 (a & b), 4.4 (a & b), 4.5 (a & b) and 4.6 (a & b) respectively. From the figure 4.3 (a & b), the top panels correspond to the real and the imaginary parts of the permittivity $\varepsilon'(\omega)$ and $\varepsilon''(\omega)$. The real and imaginary parts of the permittivity $\varepsilon'(\omega)$ and $\varepsilon''(\omega)$ show up a steep increase at lower frequencies due to the blocking of charges resulting from the electrode polarization and this should not be interpreted as the energy stored in the system. From the imaginary part $\varepsilon''(\omega)$, we are unable to resolve the peak loss due to the masking of DC conductivity contribution originating from translational motion of ions. The peaks of $\varepsilon''(\omega)$ shift into higher frequen cies with increase in temperature individually.[130,105]

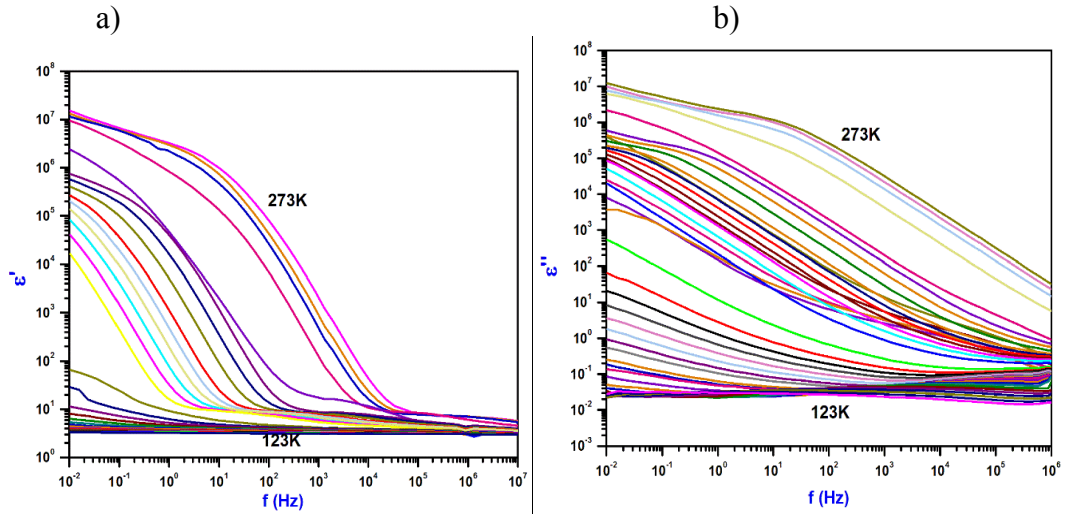

Figure 4.3. Frequency dependence of **(a)** real part $\varepsilon'(\omega)$ and **(b)** imaginary part $\varepsilon''(\omega)$ for $[P_{14,6,6,6}][NTf_2]$ IL.

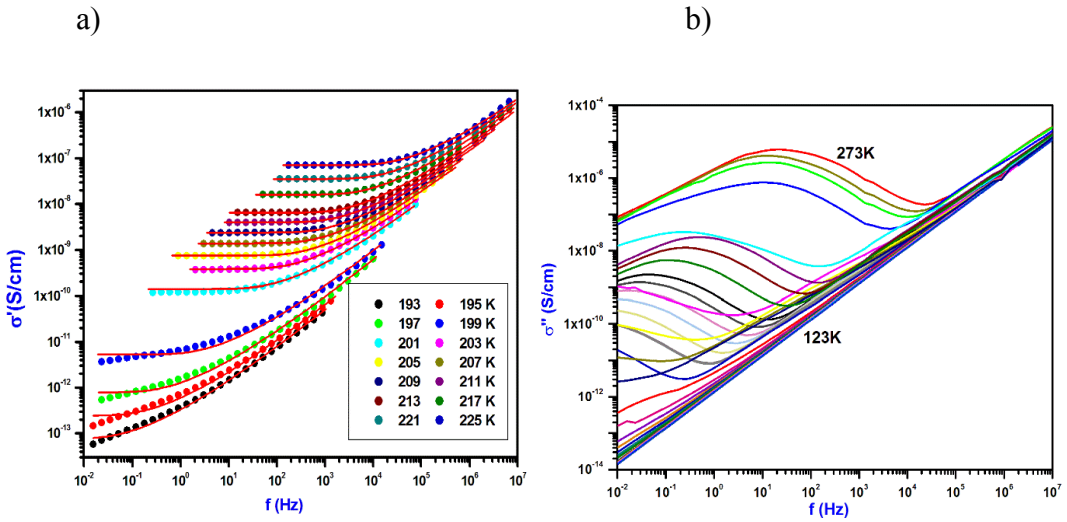

Figure 4.4. Frequency dependence of **(a)** real part σ′ (ω) and **(b)** imaginary part σ″ (ω) for $[P_{14,6,6,6}][NTf_2]$ IL.

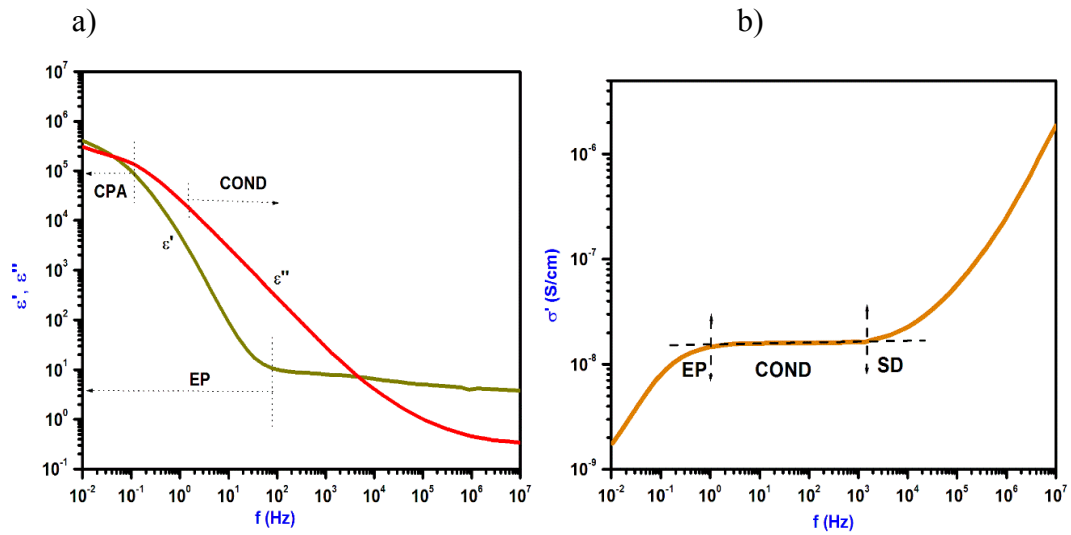

Figure 4.5. Frequency dependence of (a) ε′ (ω), ε″ (ω) and (b) σ′ (ω) of $[P_{14,6,6,6}][NTf_2]$ IL at 217K.

From figure 4.4 (a) the conductivity plots are evident that the ac conductivity plateau corresponds to the long range DC conductivity σ_0 due to random diffusion of ionic charge carriers *via* activated hopping. The conductivity drop observed in the lower frequency side of the plateau is due to the blocking of ionic carriers at the electrodes. This phenomenon is the characteristic of ionic charge transport and would be absent in electronically conducting solids. On moving towards higher frequencies, the conductivity becomes frequency dependent showing a positive slope (power law) and the plateau crosses over to a dispersive regime from

correlated forward–backward motion of ions.[112-118] This frequency dependence of the conductivity can be explained by Jonscher's universal power law ($\sigma_{AC} = \sigma_0 + A\omega^s$),[112-118] where, σ_0 is the DC conductivity, A is a temperature dependent parameter and s is the frequency exponent having its value within $0 < s < 1$ for ion conducting materials. As one can see in figure 4.4 (a), when the temperature increases, σ_0 also increases and the power law region moves out of the experimental window. In figure 4.4 (b), σ′′ (ω) shows a power law behaviour at higher frequency region and it vanishes at lower frequency side due to electrode polarisation effect.

The real part of permittivity ε′ (ω) in figure 4.5 (a) represented an EP (electrode polaris ation) region and a CPA (constant phase angle) region at lower frequencies. The imaginary part ε′′ (ω) shows a (Cond) d c conductivity region at lower frequency side showing a straight line with slope of -1.[83,105] The real part of conductivity σ′ (ω) offers an EP region at lower frequency side then shows a straight line (Cond) d c conductivity region or frequency independent region and at high frequency side existing a SD (sub diffusive conductivity) region exhibited in figure 4.5 (b).[83,105]

a) b)

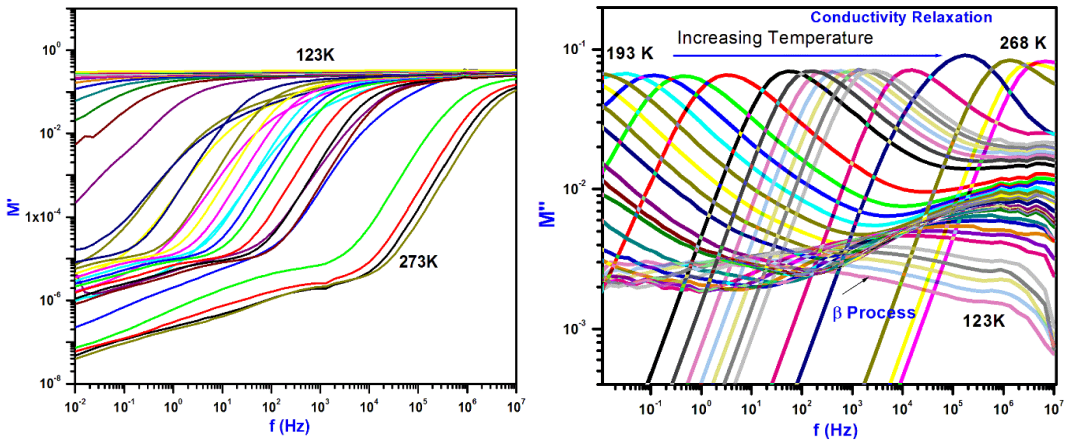

Figure 4.6. Frequency dependence of **(a)** the real part M′ (ω) and **(b)** the imaginary part M′′ (ω) of the electric modulus function M^*, at different temperatures for $[P_{14,6,6,6}][NTf_2]$ IL. .

The real and imaginary parts of the electric modulus are also shown in figure 4.6 (a & b). The characteristic relaxation time of the conductivity process can be

extracted from the imaginary part M″ (ω) by taking its inverse of the crossover frequency, which is nothing but the maxima of the modulus loss peaks. Thus the crossover manifests as a relaxation in the imaginary part and a step in the real part M′ (ω) in the modulus representation.[81-86,121]

The dielectric response of the sample was further examined in detail by the J. Dyre's random barrier model. The charge transport in disordered systems may be explained in terms of hopping of charge carriers in spatially varying random energy landscape within the framework of this model. Fit parameters of $[P_{14,6,6,6}][NTf_2]$ above T_g by Dyre equation (equation 9) are shown in table 4.1, are the parameters σ_0 and τ_e were obtained. From Dyre fit, it can be revealed that the DC conductivity σ_0 increases with increase in temperature, but the electrical relaxation time τ_e decreases.[81-86,121] Fit parameters of $[P_{14,6,6,6}][NTf_2]$ by Dyre equation shows a good agreement results with fit parameters by HN function. Below the glass transition temperature (τ_β) 123 K to 190 K, dielectric data were fitted with Cole–Cole function and the Arrhenius dependence was obtained. To explore the temperature dependence of charge transport quantities σ_0 and the conductivity relaxation time τ_e, we have plotted them in figure. 4.7 (a & b).

Table 4.1. *Fit parameters of $[P_{14,6,6,6}][NTf_2]$ to Dyre model.*

T (K)	σ_0 (S/cm)	τ_e (s)	ε_∞
1.93E+02	1.03E-13	7.17E+00	3.24E+00
1.95E+02	2.44E-13	2.60E+00	3.15E+00
1.97E+02	9.40E-13	9.36E-01	2.94E+00
1.99E+02	5.14E-12	1.50E-01	2.94E+00
2.01E+02	1.42E-10	5.73E-03	2.88E+00
2.03E+02	3.81E-10	2.16E-03	2.85E+00
2.05E+02	7.50E-10	1.17E-03	2.80E+00
2.07E+02	1.38E-09	6.51E-04	2.77E+00
2.09E+02	2.37E-09	4.02E-04	2.70E+00
2.11E+02	3.98E-09	2.45E-04	2.67E+00
2.13E+02	6.40E-09	1.64E-04	2.65E+00
2.17E+02	1.59E-08	6.49E-05	2.54E+00
2.21E+02	3.51E-08	2.88E-05	2.53E+00
2.25E+02	7.03E-08	1.38E-05	2.52E+00

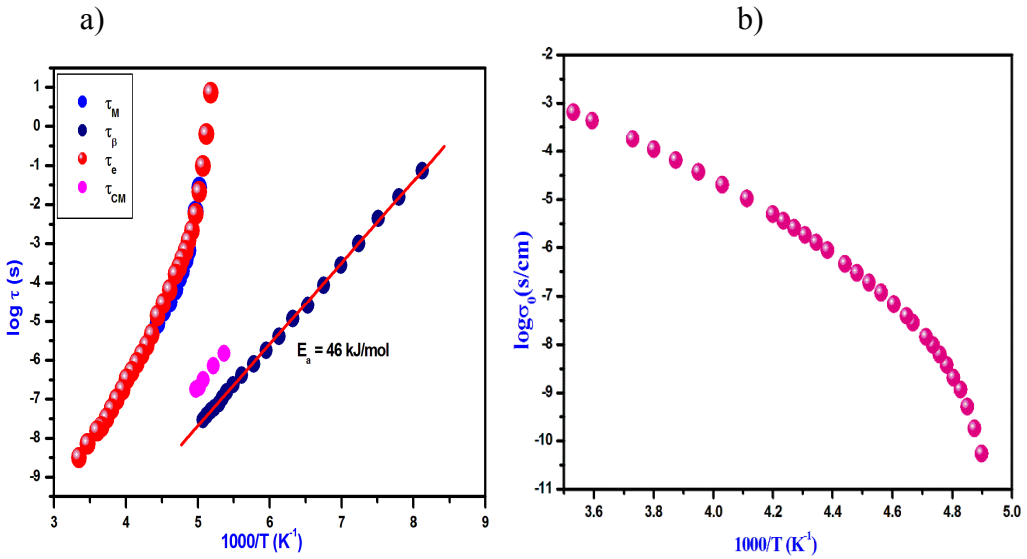

Figure 4.7. a) Plot of log τ (s) vs 1000/T and (b) Plot of log σ_0 (S/cm) vs 1000/T of $[P_{14,6,6,6}]$ $[NTf_2]$. (τ_e –Dyre fit data, τ_M – HN fit, τ_β - Cole–Cole fit and τ_{CM}- coupling model).

At temperatures above Tg, both the quantities followed time honoured VFT behaviour. From figure. 4.7 (a & b), it shows that the conductivity relaxation time τ_e, increases with decrease in temperature and the DC conductivity σ_0 is a thermally activated process, it increases with increase in temperature. The VFT fitting parameters of the IL is shown in table 4.2, the glass transition temperatures were spotted similarity with the T_g obtained from DSC measurement. E_β is the activation energy of the IL.

Table 4.2. *The fit parameters of $[P_{14,6,6,6}][NTf_2]$ IL to VFT and KWW functions.*

Sample	log τ_0 (s)	B (K)	T_0 (K)	T_g (BDS) (K)	T_g (DSC) (K)	Fragility (m)	E_β (kJ/mol)	β_{KWW}
$[P_{14,6,6,6}]$ $[NTf_2]$	9.00± 0.12	585± 0.97	165± 0.68	185	193	113± 0.32	46±0.2	0.5

The fragility plot of the IL is shown in figure 4.8. On the basis of above discussion, the IL is a fragile system showing considerable deviation from the

Arrhenius behaviour. From figure 4.8 and table 4.2, the fragility of the IL shows the value of m is 113.

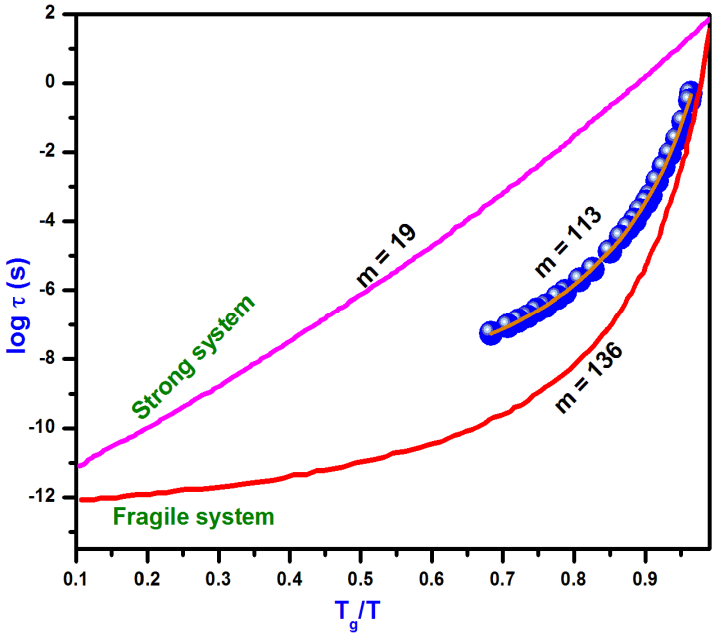

Figure 4.8. Angell plot (log τ (s) vs Tg/T) of $[P_{14,6,6,6}][NTf_2]$ IL.

Frequency dependence of imaginary part $M''(\omega)$ of $[P_{14,6,6,6}][NTf_2]$ for various temperatures are presented in figure 4.9. It is found that the value of β_{KWW} is 0.50 at 193 K from equation 20. The value of β_{KWW} provides the non–exponential character of the relaxation function in time domain.[95-99] K. L. Ngai's coupling model prediction (equation 21) is commonly applied to check the true nature of the secondary relaxation, whether it is JG type or non–JG type.[95-99] The analogy between the primitive relaxation time and the JG β–relaxation leads to their approximate relation, $\tau_\beta \approx \tau_0$.This approximate relation is another criterion to verify if the secondary relaxation is the JG β–relaxation or not. The coupling model predicts the probable secondary relaxation peak with approximate agreement between τ_0 and τ_β. since, there is a good agreement between τ_0 and τ_β and the secondary relaxations can be called as Johari Goldstein β relaxation. The primitive and the β relaxation processes are not identical in $[P_{14,6,6,6}][NTf_2]$, but they are

closely related. $i.e.$ $\tau_\beta \approx \tau_0 = (t_c)^n(\tau_\alpha)^{1-n}$.This approximate relation has been proved for various glass forming systems. [95-99, 121]

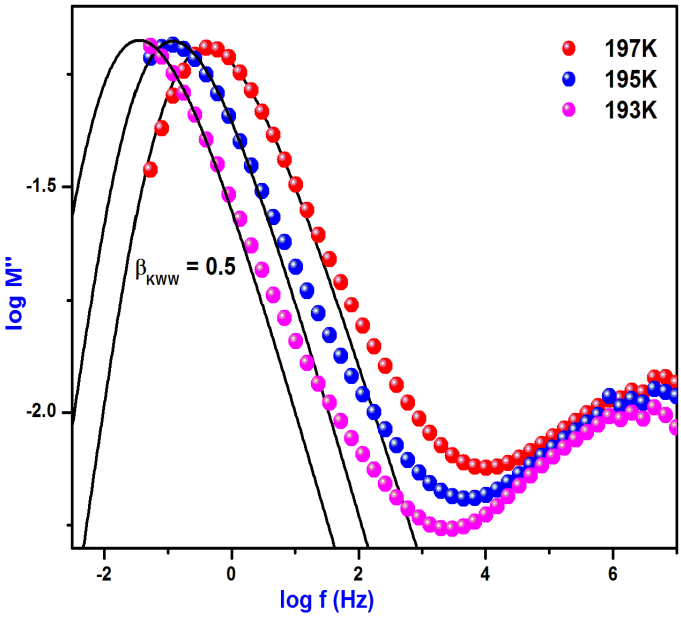

Figure 4.9. Frequency dependence of imaginary part M ″ (ω) for $[P_{14,6,6,6}][NTf_2]$ IL. The solid line is a KWW function with β_{KWW} = 0.5 at 193 K.

The temperature dependence of σ_0 and ω_e, the two observable quantities describing charge transport by Dyre approach are shown in figure 4.10 (a & b). The temperature dependence of the σ_0 and ω_e detected the VFT behavior. The two parameters can be easily coincided. This states the well-known relation BNN from equation 11, $\sigma_0 \sim 1/\tau_e$. [162-163] Figure 4.10 (a) shows that the d c conductivity σ_0 and the characteristic frequency ω_e are well reputable by BNN relation which shows an Arrhenius behavior. It indicates that D C and A C conductions are created on the same mechanism of charge transport. It connects the dielectric loss peak frequency, dielectric loss strength $\Delta\varepsilon$ and the D C conductivity, $\sigma_0 = P\Delta\varepsilon\varepsilon_0\omega_e$, where P is a numerical constant of order 1. BNN relation is explained within the frame work of Einstein and Einstein–Smoluchowski relations.[162-163] From Einstein and Einstein–Smol uchowski relations,

$$\sigma_0 = nq\mu = n\frac{q^2D}{KT} \qquad 26$$

Here, n is the effective number density of ions, D is the diffusion coefficient and μ refers to the mobility of charge carriers, where $D = \frac{\lambda^2\ \omega_e}{2}$, λ is the hopping length of charge carriers. Therefore $\sigma_0 = n\frac{q^2}{KT}\frac{\lambda^2\ \omega_e}{2}$. Hence it can be resolved that $\sigma_0 \propto \omega_e$ or $\sigma_0 \approx \omega_e$.[81,83,162-163]

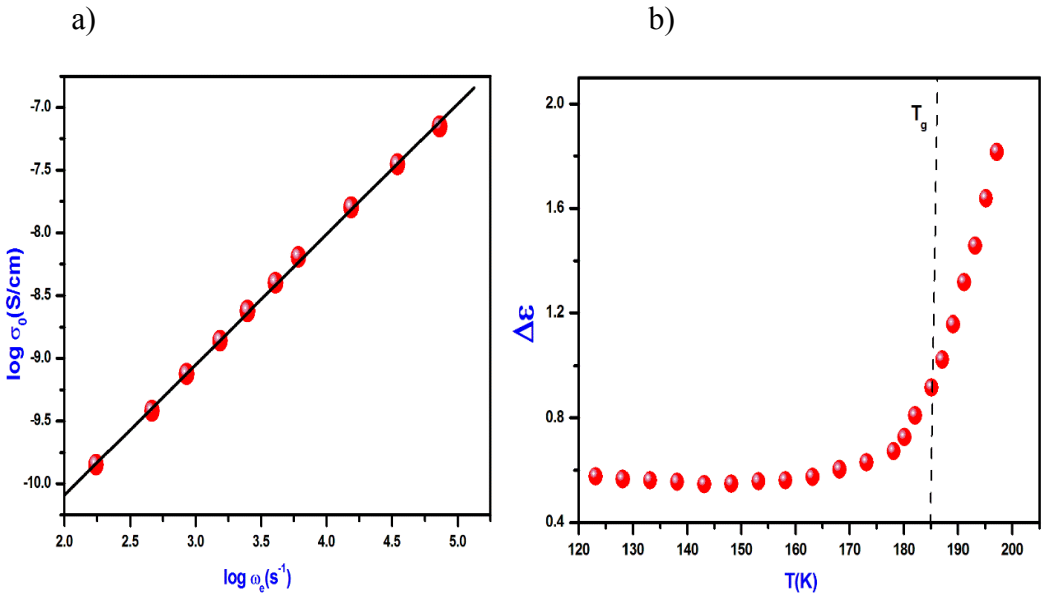

Figure 4.10. (a) BNN plot and (b) temperature vs Δε of $[P_{14,6,6,6}][NTf_2]$ IL.

The increase in the ε' (ω) is related to the increase in $\Delta\varepsilon$, ie, $\Delta\varepsilon = \varepsilon_s - \varepsilon_\infty$, where ε_s , ε_∞ are the low and high frequency limits of the real part of permittivity respectively. Temperature vs $\Delta\varepsilon$ graph is indicated in figure 4.10 (b). It shows that dielectric loss strength $\Delta\varepsilon$ is weakly dependent on the temperature for β relaxation process. But above T_g (185 K) Δε increases with increase in temperature. The Kirkwood–Frohlich–Onsager approach describes the dielectric strength as[81,83,162-163]

$$\Delta\varepsilon = \frac{1}{3\varepsilon_0}\, g_k F \frac{\mu^2}{k_B T}\frac{N}{V} \qquad (27)$$

Where $\Delta\varepsilon$ is the dielectric strength, ε_0 is the permitivity constant, μ^2 is the mean square dipole moment , the dipolemoment of $[P_{14,6,6,6}][Tf_2N]$ was calculated by DFT is 13.8930 D. F ≈ 1 is the onsager factor, $g_k = 1+\left[\langle\sum_{i=1}^{N}\sum i<j\,\mu_i\mu_j\rangle\right]/(\overline{N}\,\mu^2)$ the Kirkwood–Frohlich correlation factor, which indicates the short range intermolecular interactions that led to the specific static dipole–dipole orientations. K_B is the Boltzmann factor, T is the temperature and $\left(\frac{N}{V}\right)$ the number density of dipoles. Mostly, the parallel or antiparallel correlations between neighbouring dipoles are $g_k > 1$ or $0 < g_k < 1$ respectively while for a random orientation of dipoles $g_k = 1$ embraces. High values of the dielectric strength are detected when $g_k > 1$ while low values of $\Delta\varepsilon$ relates to $g_k < 1$. The Kirkwood–Frohlich–Onsager approach correspondingly describes that dielectric loss strength $\Delta\varepsilon$ is weakly dependent on the temperature for secondary process (low temperature).[87]

4.1.2. Thermal and broadb and dielectric spectroscopic analysis of $[P_{14,6,6,6}][N(CN)_2]$ IL

4.1.2.1. Thermogravimetric analysis

To study the thermal stability of the IL $[P_{14,6,6,6}][N(CN)_2]$, TGA measurement is taken in an interval of 300 K–900 K. The mass loss curve of the IL was presented in figure 4.11. The decomposition temperatures (Td) is found over the TG curves and reveals that the IL has good thermal stability, up to 573 K and began to decay above this temperature.

4.1.2.2. Differential scanning calorimetry analysis

DSC plot of $[P_{14,6,6,6}][N(CN)_2]$ IL at a heating rate of 10 K /min. from 123 K to 300 K is shown in figure 4.12. IL could be super cooled at a normal cooling rate of 10 K/min without any signals of crystallization. The heating curve showed a step–like change representing glass transition as a value of 195.99 K. No melting peak is obtained in this DSC response graph.

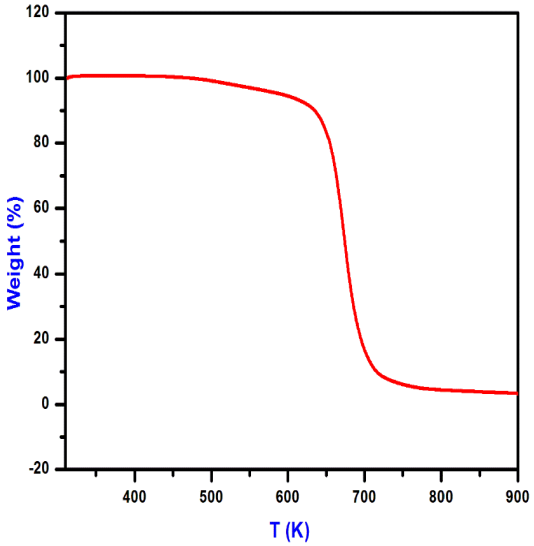

Figure 4.11. TGA plot of $[P_{14,6,6,6}][N(CN)_2]$ IL

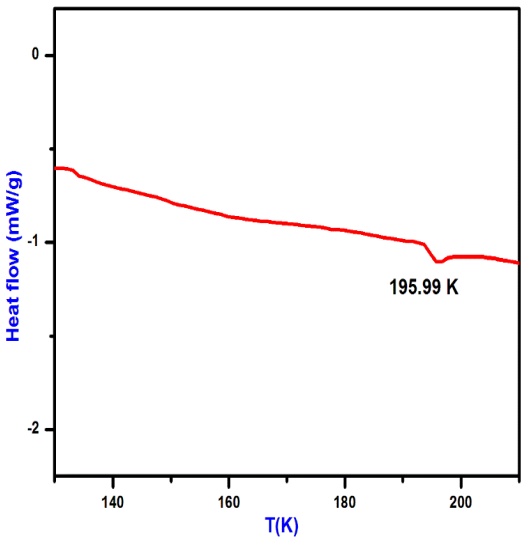

Figure 4.12. DSC plot of $[P_{14,6,6,6}][N(CN)_2]$.

4.1.2.3. Broadband dielectric spectroscopic analysis

Dielectric spectroscopy offers a rotational dynamic component and a translational component in the presence of an electric field over a broad frequency range. The rotational dynamic (dielectric orientational relaxation) component includes conductivity relaxation time τ_α and the translational component DC conductivity - σ_{dc}, which is found at lower frequ encies or higher temperatures. Below T_g, the sample $[P_{14,6,6,6}][N(CN)_2]$ was in glassy state, thus the movement of molecules were some what restricted and secondary relaxation is observed similar to the so called JG relaxation, i.e., inter molecular relaxation, originate from rotation of the whole molecule that is typically observed in molecular glasses. JG relaxation has been viewed as the precursor of the cooperative conductive relaxation.[67,96] The response of $[P_{14,6,6,6}][N(CN)_2]$ has been characterized with real & imaginary parts of complex dielectric permittivity $\varepsilon^*(\omega)$, real & imaginary parts of complex conductivity $\sigma^*(\omega)$ and real & imaginary parts of complex electrical modulus $M^*(\omega)$, at different temperatures are presented in figure 4.13 (a & b), 4.14 (a & b) and 4.15 (a & b) respectively.

Figures 4.13 (a & b) show the variation of real and imaginary part of dielectric permittivity with frequency for different temperatures. It can be found that ε' (ω) decreases with the increase in frequency and a huge increase and a plateau region at lower frequencies is due to electrode polarization. At lower frequencies ε'' (ω) is higher due to electrode polarisation effects on the electrode and movement of free charge carrier in the system is strongly related to the conductivity of the IL. The peaks of ε'' (ω) shift into higher frequ encies with increasing temperature consistently in modulus representation. But the value of frequency express higher in permittivity representation (five decades) associated to modulus representation.[81,83] The peaks are not observed clearly in conductivity relaxation and secon dary relaxation due large contribution of DC conductivity.

a) b)

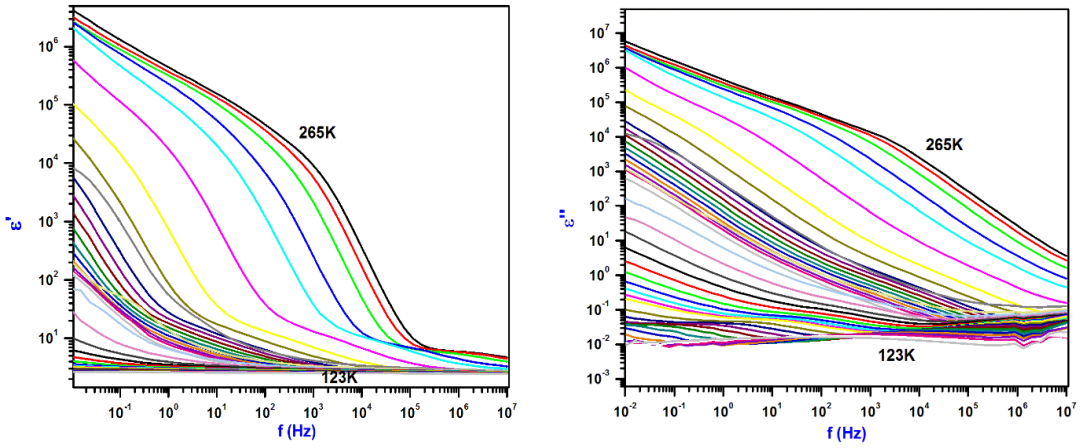

Figure 4.13. Frequency dependence of **(a)** real part ε' (ω) and **(b)** imaginary part ε'' (ω) of permittivity representation for $[P_{14,6,6,6}][N(CN)_2]$ IL.

The real part of the conductivity σ' (ω) demonstrating the charge transport can be recognized as a plateau on the low-frequency side in σ' (ω) vs frequency graph (figure 4.14 (a), the dispersion sets in and turns into a power law towards higher frequency side. A correlation is found with temperature. At low temperature, DC conductivity term vanishes and power law behaviour appears in lower frequency side.[112-114] σ'' (ω) vs frequency in figure 4.14 (b) spectra have not clearly identified due to electrode polarisation effect in this IL.

The real part M′ (ω) reaches a maximum value at high frequency region and obtain a low value region at lower frequency, ie it shows a step like arrangement. M″ (ω) shows a steep decrease at lower frequencies due to electrode polarisation effects. M′′ (ω) spectra which have an ability to mask the conductivity contribution show the spectra clearly with different peaks for different temperatures. The conductivity-relaxation peak M′′ (ω) is endorsed to the translational ionic motions.[90,130] In figures 4.15 (a & b) it is shown that as temperature decreases as the relaxation peak is moving toward lower frequency side. ie, The peak in modulus representation shifts into higher temperatures with the increase in frequency and relaxation time decreases. The characteristic time (τ) is proportional to the inverse of the angular frequency (ω_M). i.e., $\tau_M = 1/2\pi\omega_{max}$. When τ_M increases toward 100 s, the glass transition temperature (T_g) from dielectric measurements are obtained.[90,98-99] Secondary relaxation (β process) is clearly visible at temperatures from 123 K to 183 K.

a) b)

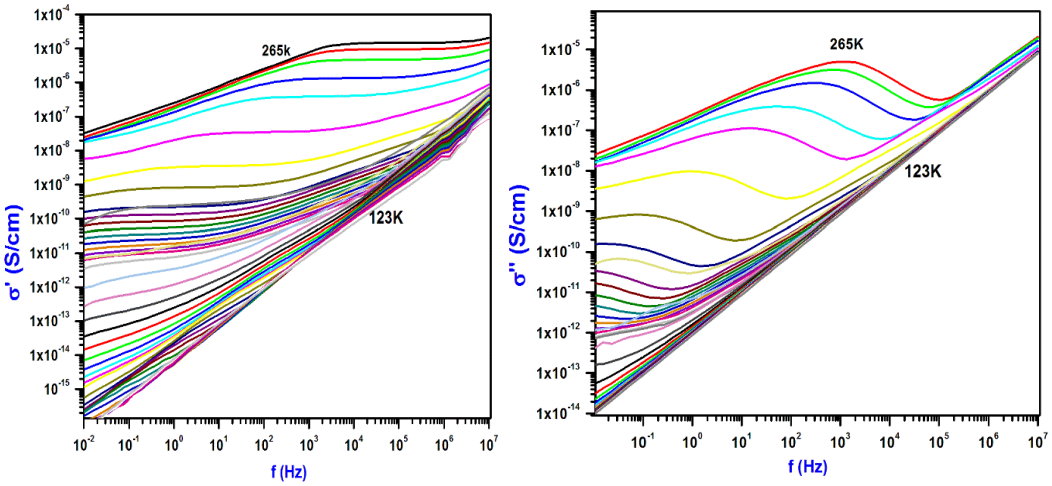

Figure 4.14. Frequency dependence of **(a)** the real part σ′ (ω) & **(b)** imaginary part σ′′ (ω) of conductivity formalism for the sample $[P_{14,6,6,6}][N(CN)_2]$ IL.

a) b)

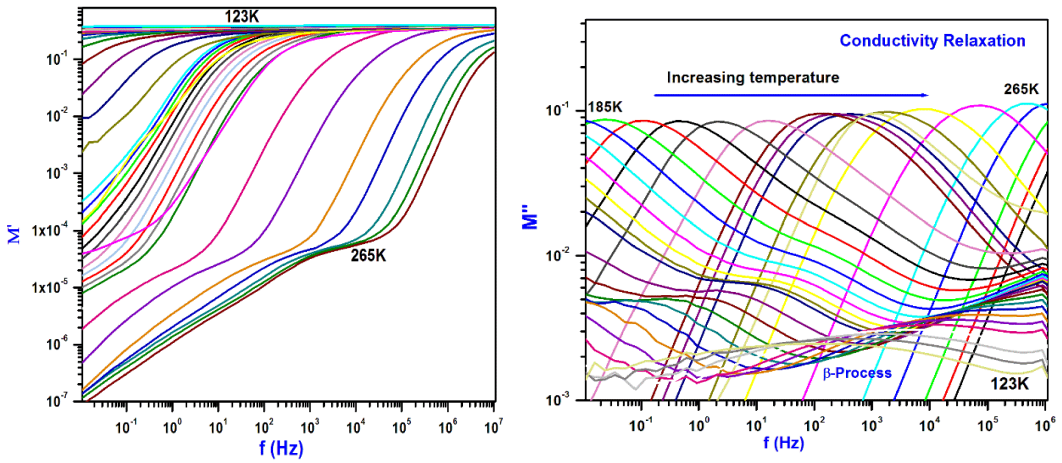

Figure 4.15. Frequency dependence of **(a)** the real part M' (ω) and **(b)** the imaginary part M'' (ω) at different temperatures for $[P_{14,6,6,6}][N(CN)_2]$ IL.

The dielectric response of the sample was further scrutinized in detail by the J. Dyre's random barrier model. Fit parameters of $[P_{14,6,6,6}][N(CN)_2]$ by Dyre equation were shown in table 4.3, from which it can be revealed that the d c conductivity σ_0 increases with increase in temperature, but the electrical relaxation time τ_e decreases.[88,92,94,163]

Table 4.3. *Fit parameters of $[P_{14,6,6,6}][N(CN)_2]$ to Dyre function.*

T (K)	σ_0 (S/cm)	τ_e (s)	ε_∞
1.95E+02	4.62E-12	9.80E+00	2.61E+00
1.99E+02	*8.87E-11*	*5.18E-01*	*2.70E+00*
2.05E+02	3.11E-08	1.91E-03	1.94E+00
2.09E+02	2.63E-07	1.90E-04	2.15E+00
2.13E+02	1.20E-09	1.60E-02	2.11E+00
2.17E+02	1.88E-09	1.27E-02	2.16E+00
2.21E+02	3.52E-09	8.19E-03	2.11E+00
2.25E+02	7.46E-09	4.50E-03	2.07E+00
2.29E+02	1.82E-08	2.03E-03	2.05E+00
2.31E+02	3.02E-08	1.25E-03	2.04E+00
2.39E+02	4.33E-07	1.50E-04	1.90E+00
2.43E+02	4.27E-06	1.51E-05	1.76E+00
2.51E+02	1.43E-04	4.98E-07	1.32E+00

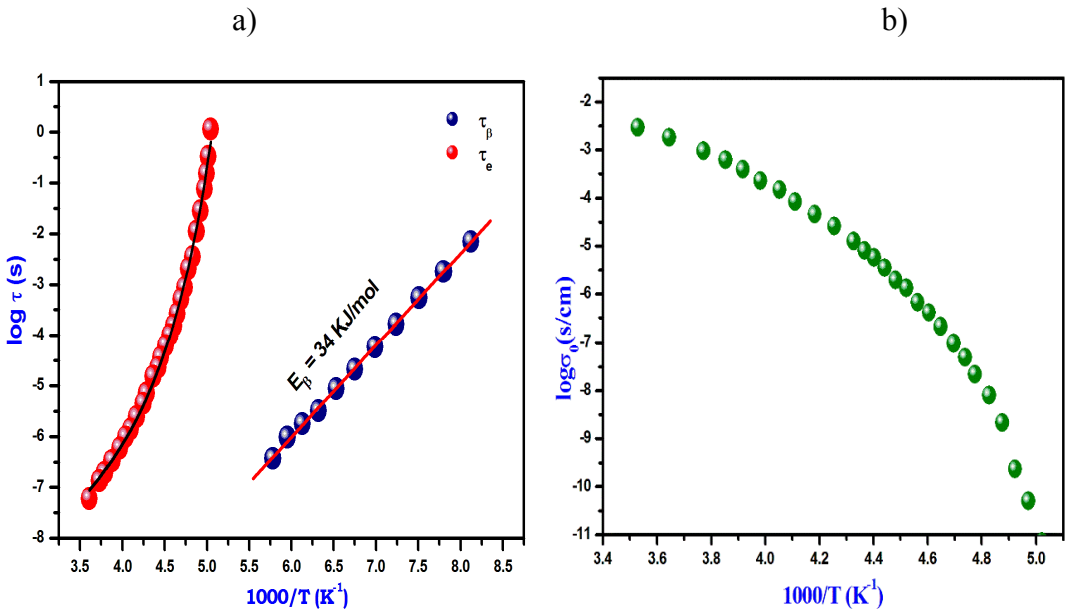

Figure 4.16. Plots of (**a)** log τ (s) vs 1000/T and **(b)** log σ (S/cm) vs 1000/T of $[P_{14,6,6,6}]$ $[N(CN)_2]$ IL.

In $[P_{14,6,6,6}][N(CN)_2]$ IL, the conductivity relaxation (above T_g) shows non Arrhenius VFT behaviour whereas the secondary relaxation obtained by an Arrhenius temperature dependence. The VFT equation is widely used to fit the conductivity data to get the quantitative information about the glass forming behavior of the ILs. The temperature dependence for the conductivity relaxation time (τ_e), DC conductivity (σ_0) are shown in figure 4.16 (a & b) and it shows that the conductivity relaxation time τ_e, increases with the decrease in temperature. The temperature dependence of the β relaxation (secondary relaxation) time (τ_β) exhibits a linear dependence. VFT fitting parameters are shown in table 4.4 below.

Table 4.4. *The fit parameters of $[P_{14,6,6,6}][N(CN)_2]$ IL to VFT and KWW functions.*

Sample	log τ_0 (s)	B (K)	T_0 (K)	T_g (BDS) (K)	T_g (DSC) (K)	Fragility (m)	E_β (kJ/mol)	β_{KWW}
$[P_{14,6,6,6}][N(CN)_2]$	9±0.2	708± 0.11	166± 0.41	190	195	98	34±0.32	0.45

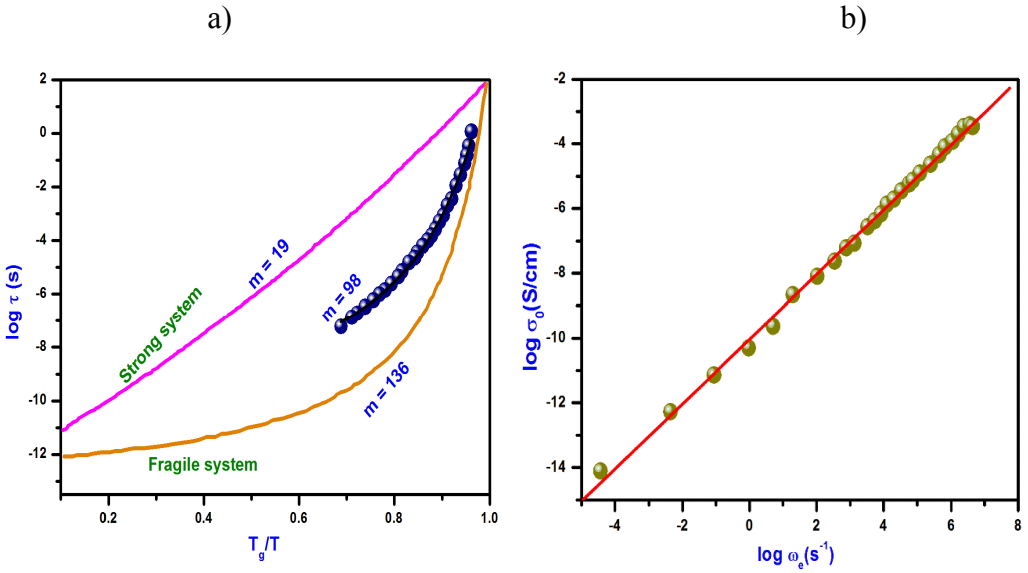

Figure 4.17. (a) log τ (s) vs Tg/T plot and (b) BNN plot of $[P_{14,6,6,6}][N(CN)_2]$ IL.

VFT fitting parameters of $[P_{14,6,6,6}][N(CN)_2]$ IL shows the value of m is 98 and the fragility plot is represented in figure 4.17 (a). The temperature dependence of the two observable quantities σ_0 and ω_e describing charge transport by Dyre approach are shown in figures 4.16 (a & b). The temperature dependence of the σ_0 and ω_e identified the VFT behavior. But plotting ω_e on X axis and σ_0 on Y axis, the two parameters can be easily overlapped and got an Arrhenius dependence. Figure 4.17 (b) shows that the DC conductivity σ_0 and the characteristic frequency ω_e are well defined by the relation BNN, $\sigma_0 \sim 1/\tau_e \sim \omega_e$. It specifies that DC and AC conduction are formed on the same mechanism of charge transport.

Frequency dependence of imaginary part M″ (ω) of $[P_{14,6,6,6}][N(CN)_2]$ are shown in figure 4.18 with β_{KWW} of 0.45. The value of β_{KWW} offers the non–exponential character of the relaxation function in time domain. Debye type relaxation indicates β =1 which is narrow and symmetric and the values of β < 1 indicates the non-Debye relaxation.

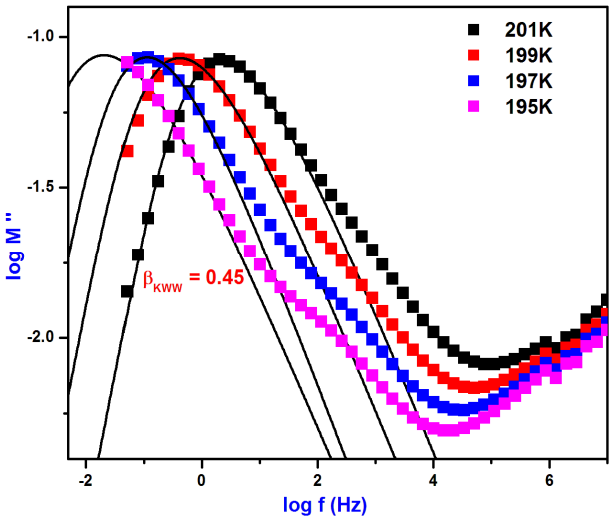

Figure 4.18. Frequency dependence of imaginary part M ″ (ω) of $[P_{14,6,6,6}][N(CN)_2]$ at different temperatures above and below T_g. The black solid line represents the KWW fit with β_{KWW} = 0.45 for the temperature 201 K.

4.1.3. Thermal and broadband dielectric spectroscopic analysis of $[P_{14,6,6,6}][Cl]$ IL

4.1.3.1. Thermogravimetric analysis

Thermal analysis of the IL $[P_{14,6,6,6}][Cl]$ is studied with TGA in an interval of 300 K– 900 K and the weight loss curve of the IL was presented in figure 4.19. The decomposition temperatures (Td) is obtained over the TG curves and exposes that up to 573 K the sample is thermally stable and began to fall off above this temperature. Due to high thermal stability of the sample, it can prefer for various high temperature technological applications.

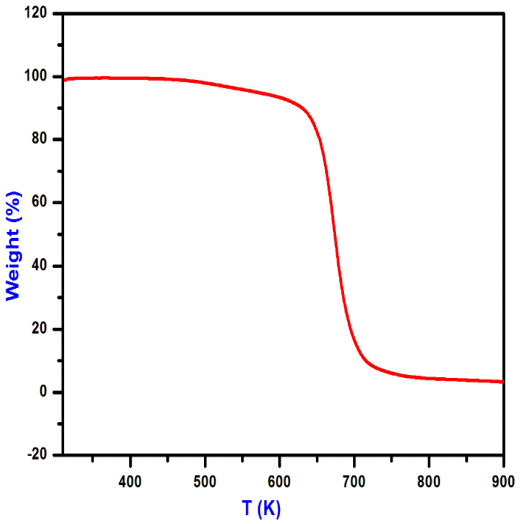

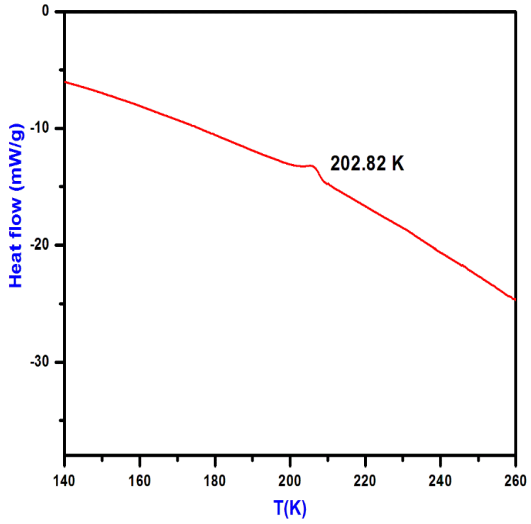

Figure 4.19. TGA plot of $[P_{14,6,6,6}]Cl]$ IL. **Figure 4.20.** DSC plot of $[P_{14,6,6,6}][Cl]$ IL.

4.1.3.2. Differential scanning calorimetry analysis

DSC plot of $[P_{14,6,6,6}][Cl]$ at a heating rate of 10 K /min. from 123 K to 300 K is presented in figure. 4.20 and the transition showed a glass transition temperature of 202.82 K.

4.1.3.3. Broadband dielectric spectroscopic analysis

The response of $[P_{14,6,6,6}][Cl]$ has been represented with different formalisms as follows. Real & imaginary parts of complex dielectric permittivity $\varepsilon^*(\omega)$, real & imaginary parts of complex conductivity $\sigma^*(\omega)$ and real & imaginary parts of complex electrical modulus $M^*(\omega)$ are presented in figures 4.21 (a & b), 4.22 (a & b) and 4.23 (a & b) respectively. Figures 4.21 (a & b) show the variation of real and imaginary part of dielectric permittivity with frequency for different temperature. It can be found that $\varepsilon'(\omega)$ decreases with increase in frequency and the steep increase and a plateau region at lower frequencies is due to electrode polarisation. At lower frequencies $\varepsilon''(\omega)$ are higher due to electrode polarisation effects on the electrode and movement of free charge carrier in the system is intensely connected to the conductivity of the ionic liquid. The peaks of $\varepsilon''(\omega)$ shift into higher frequencies with increasing temperature correspondingly in modulus representation. But the

value of frequency shows higher in permittivity representation compared to modulus representation.[90,105]

a) b)

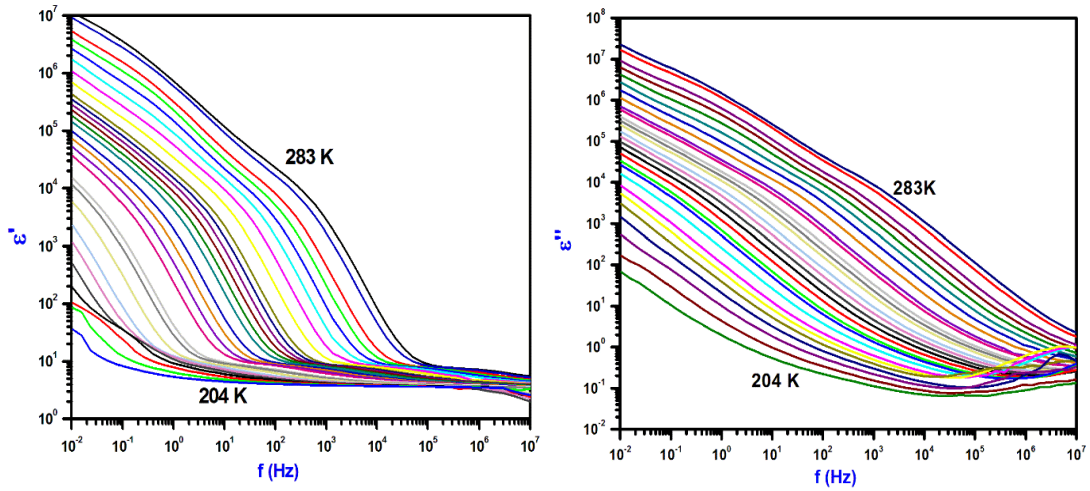

Figure 4.21. Frequency dependence of **(a)** real part ε′ (ω) and (b) imaginary part ε′′ (ω) of permittivity representation at different temperatures for the sample $[P_{14,6,6,6}][Cl]$ IL.

a) b)

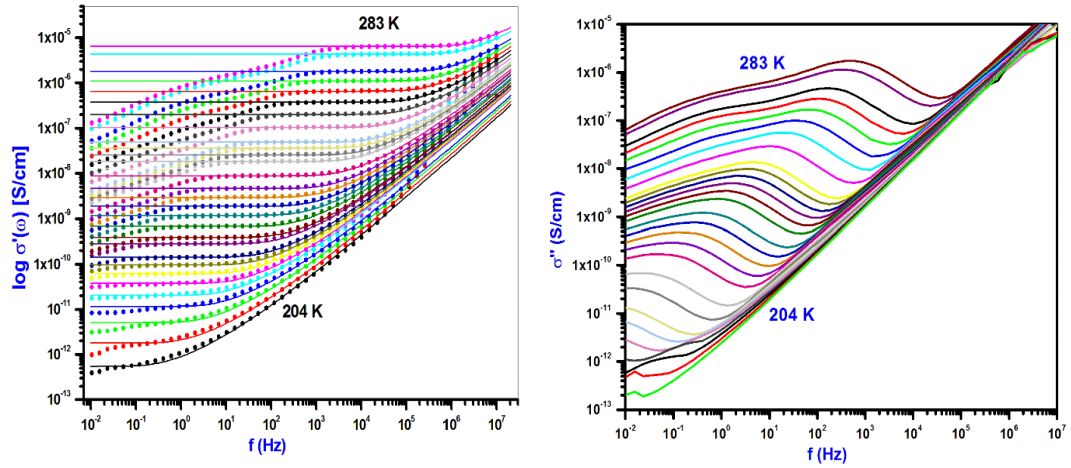

Figure 4.22. Frequency dependence of (a) the real part σ′ (ω) (b) imaginary part σ′′ (ω) of conductivity formalism at different temperatures for the sample $[P_{14,6,6,6}][Cl]$ IL.

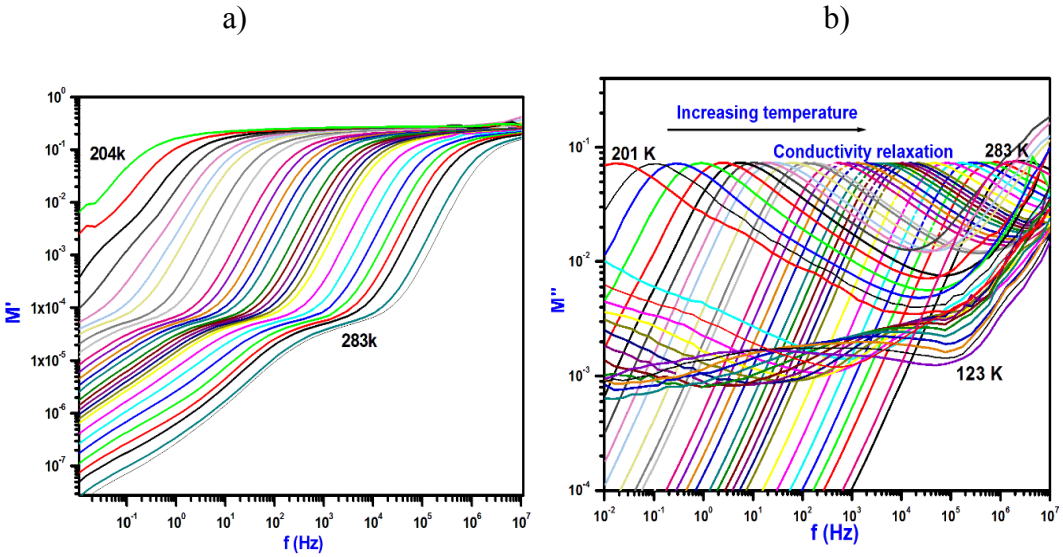

Figure 4.23. Frequency dependence of (a) the real part M′ (ω) and (b) the imaginary part M″ (ω) of the electric modulus function M^*, at different temperatures for $[P_{14,6,6,6}][Cl]$ IL.

The real part of the conductivity σ′ (ω) representing the charge transport can be recognized as a plateau on the low-frequency side in σ′ (ω) vs frequency graph 4.22 (a & b) at elevated temperatures at the characteristic radial frequency, ω_e, the dispersion sets in and turns into a power law towards higher frequency side as well as a strong increase in ε″ (ω) vs frequency graph are observed, which mark the onset of the power law. The fits to the data with the equation is shown as dashed lines in figure 4.22 (a). As depicted in the figure.4.22 (a), at lower frequencies, σ' (ω) decreases from σ_0 and this is due to electrode polarization that results from blocking of charge carriers at the electrodes.[88,92,105]

The real part M′ (ω) reaches a maximum value at high frequency region and obtain a low value at lower frequency as in figure (4.23 (a)). The main peak in M″ (ω) (the conductivity-relaxation peak shown in figure 4.23 (b)) is attributed to the translational ionic motions and τ_σ is determined from the peak frequency ν_σ *via* $\tau_\sigma = 1 / (2\pi\nu_\sigma)$.[90,121] The modulus representation suppresses the effects of blocking electrodes showing up at low frequencies. Any appreciable charge transport in a sample generates a prominent peak in M″ (ω).

The dielectric response of the sample was further investigated in detail by the J. Dyre's random barrier model. Within the framework of this model, the charge transport in disordered systems may be explained in terms of hopping of charge carriers in spatially varying random energy landscape. Fit parameters of $[P_{14,6,6,6}][Cl]$ to Dyre equation were shown in table 4.5. It is seen that the DC conductivity σ_0 increases with increase in temperature, but the electrical relaxation time τ_e decreases with increase in temperature.

Table 4.5. *Fit parameters of $[P_{14,6,6,6}][Cl]$ to Dyre equation.*[88,92]

T (K)	σ_0 (S/cm)	τ_e (s)	ε_∞
208.15	2.04E-9	0.04159	3.184
219.15	1.175E-7	6.903E-4	2.869
228.15	8.829E-7	1.03E-4	2.832
238.15	4.929E-6	1.786E-5	2.681
248.15	2.01E-5	4.435E-6	2.615
258.15	6.599E-5	1.372E-6	2.508
268.15	1.791E-4	5.229E-7	2.419
278.15	4.326E-4	2.165E-7	2.426
283.15	6.413E-4	1.469E-7	2.384

Temperature dependence of the conductivity relaxation process at different time scales of $[P_{14,6,6,6}][Cl]$ was investigated by fitting the data corresponding to different isotherms with Dyre equation. We have further fitted the spectra with HN function to check that the time scales measured by either method yields same result. Dielectric data were fitted with Cole–Cole function and the Arrhenius dependence was obtained below the glass transition temperature, 123 K to 188 K. The temperature dependence for the conductivity relaxation time (τ_e), DC conductivity (σ_0) are shown in figure 4.24 (a & b) and it shows that the conductivity relaxation time τ_e, increases with the decrease in temperature.

The conductivity relaxation process shows a non–Arrhenius behaviour and was fitted to the time honored VFT, the fitting parameters of the sample were obtained as τ_∞= 9 s, B = 718 K and T_0=169 K. From the VFT fits the glass transition temperature was estimated as T_g = 195 K, which was observed within a difference of 3–4 K with the T_g obtained from DSC measurement (192 K). The dielectric spectra of $[P_{14,6,6,6}][Cl]$ reveals that a well resolved secondary or β–relaxation, which survives even below T_g, and can be fitted very well with the Arrhenius equation. From the Arrhenius fits the activation energy (E_β) was estimated as 15 kJ/mol.

a) b)

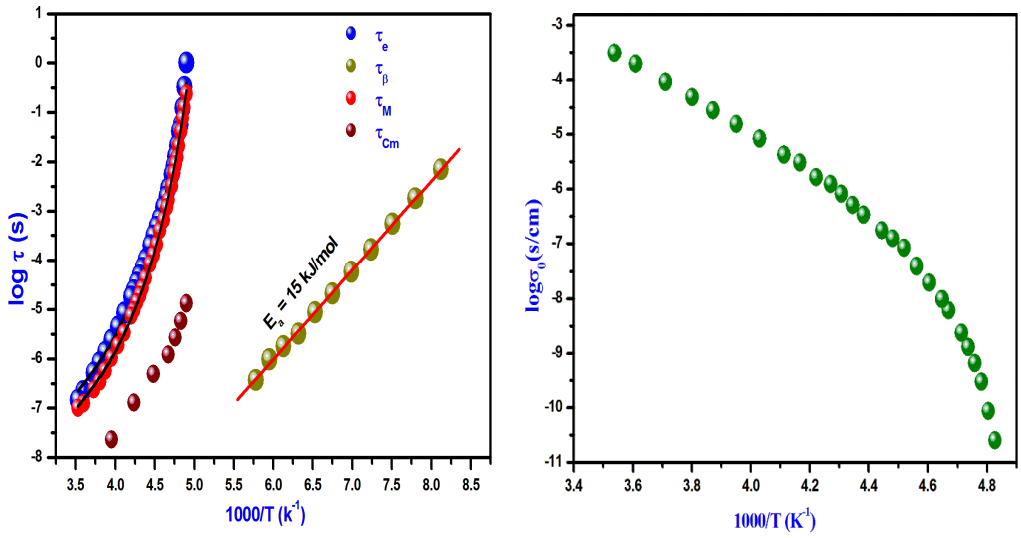

Figure 4.24. Plot of **(a)** log τ (s) vs 1000/T & **(b)** log σ (S/cm) vs 1000/T of $[P_{14,6,6,6}]$ [Cl] IL.

Getting insights about the origin and significance of the slowest resolved secondary relaxation is very much appealing to the researchers working in different classes of glass formers. Subsequent investigations on glass formers of all kind reveals the presence of this secondary relaxation, which possess non trivial coupling with the primary relaxation.[98-99] To acknowledge this classic discovery, we call them as JG secondary relaxation. K.L Ngai's relation[99] found that $\tau_{JG}(T,P) = \tau_{CM}(T,P)$, i.e.

the primitive relaxation is nothing but the JG relaxation. On calculating the separation of the JG and the conductivity relaxation process using CM equation, we can conclude that the JG process is hidden under the intense primary relaxation process and the resolved secondary relaxation is arising due to intramolecular origin.[96,105]

Charge transport mechanisms and its role to the glassy dynamics in ionic liquids had been one of the hot topics among the researchers. BNN relation found that DC conductivities σ_0 and ω_e were correlated. In the case of $[P_{14,6,6,6}][Cl]$, an excellent correlation was observed as depicted in figure 4.25, where approximate equality holds good over wide temperature and a frequency window spanning over 7 decades.

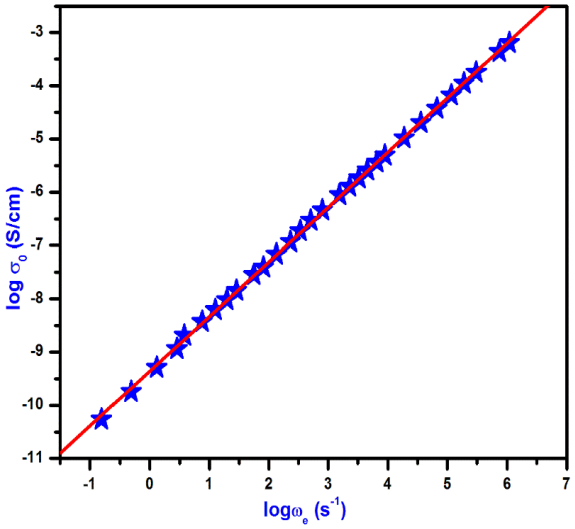

Figure 4.25. DC conductivity σ_0 versus the characteristic frequency, ω_e of $[P_{14,6,6,6}][Cl]$ IL

The fragility m is a useful measure to characterize the strength parameter of the sample, smaller values of m (m < 20) represents an Arrhenius dependence in the temperature dependence and classified as strong glass formers, while systems with m > 120 are categori zed as fragile systems.[125-127] From the figure 4.26 (a), the sample $[P_{14,6,6,6}][Cl]$ IL belongs to medium fragile system with m = 92. Bohmer *et al.,* proposed a linear relationship between the fragility index (m) and β_{KWW} , m = 250 ($\pm$ 30) − 320 β_{KWW}. [17] The correlation between m and β_{KWW} is confirmed for

$[P_{14,6,6,6}][Cl]$ using β_{KWW} =0.50, it gives m = 90 ± 30 being identical to the m obtained from the above equation.[125-127]

a) b)

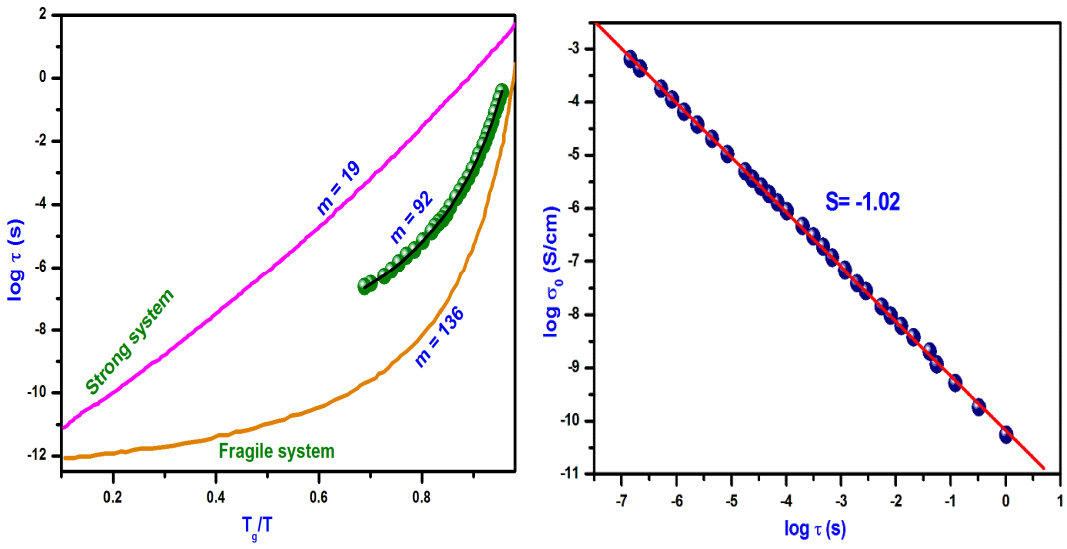

Figure 4.26. Plot of (a) log τ (s) vs T_g/T and (b) representation of log σ_{dc} versus log τ_α for temperatures close to T_g of $[P_{14,6,6,6}][Cl]$ IL.

Dielectric spectroscopy deals with the rotational dynamics part (α–relaxation time τ_α) and the translational part (DC conductivity-σ_{dc}) in presence of an electric field. The DC conductivity was observed at lower frequencies prior to α relaxation. It is further motivating to probe the coupling between the rotational dynamics and the translational part exemplified by conductivity relaxation and structural relaxations respectively. In order to check the decoupling between the two, a relationship known as Fractional-Debye-Stokes-Einstein (FDSE) equation given by $\sigma_{dc}(T)\,\tau_\alpha(T)^s = a\ constant$[87] is used where s is the fractional exponent show the degree of decoupling. Plot of log σ_{dc} against log τ_α is shown in figure 4.26 (b). The value of s thus obtained for $[P_{14,6,6,6}][Cl]$ is -1.02, which shows that the ionic conductivity is very well coupled to the structural relaxation in the super cooled state of the IL.

Frequency dependence of imaginary part $M''(\omega)$ of $[P_{14,6,6,6}][Cl]$ are shown in figure 4.27. On fitting the data with KWW, we got a value of n of KWW to be 0.51 for conductivity relaxation process around the glass transition temperature corresponding to tau = 100 s.

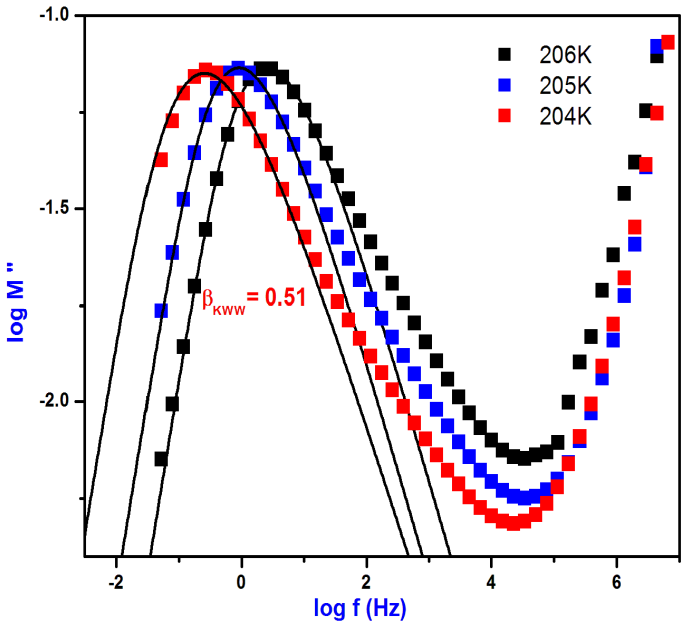

Figure 4.27. Frequency dependence of imaginary part M $''$ (ω) for $[P_{14,6,6,6}][Cl]$ IL. The solid line is a KWW function with β_{KWW} = 0.51 for the temperature 204 K.

4.1.4. Thermal and broadband dielectric spectroscopic analysis of $[P_{14,6,6,6}][NTf_2][Cl]$ IL

4.1.4.1. Thermogravimetric analysis

Thermal analysis of the IL $[P_{14,6,6,6}][NTf_2][Cl]$ is calculated with TGA in an interval of 300 K–900 K and the weight loss curve of the IL is obtained from the figure 4.28. It is revealed that up to 573 K the sample is thermally stable and began to decrease above this temperature. Parent ILs also shows the same thermal stability.

4.1.4.2. Differential scanning calorimetry analysis

DSC plot of $[P_{14,6,6,6}][NTf_2][Cl]$ at a heating rate of 10 K /min. from 123 K to 300 K is exhibited in figure. 4.29 and the transition displayed a glass transition temperature of 190.11 K. There is a melting peak observed at a temperature of 206.27 K in this DSC response curve.

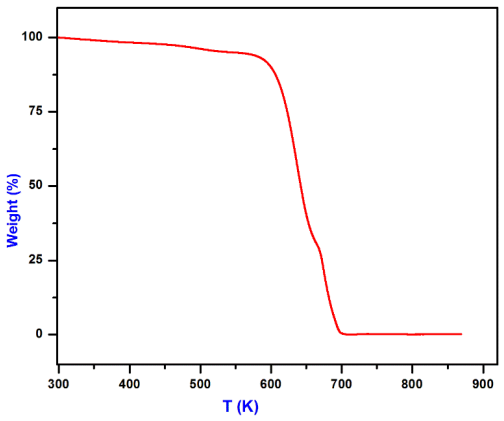

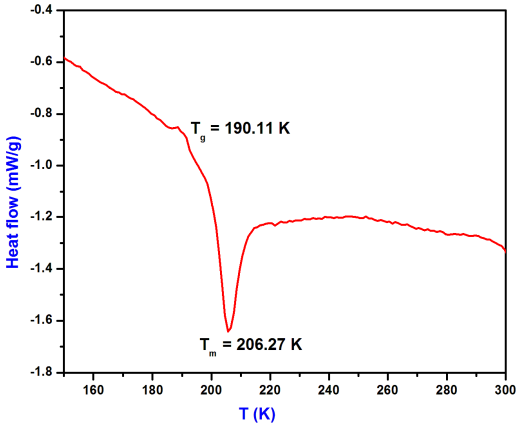

Figure 4.28. TGA plot of $[P_{14,6,6,6}][NTf_2][Cl]$. **Figure 4.29.** DSC plot of $[P_{14,6,6,6}][NTf_2][Cl]$.

4.1.4.3. Broadband dielectric spectroscopic analysis

We have determined the dielectric response of a mixing of two ILs $[P_{14,6,6,6}][NTf_2]$ and $[P_{14,6,6,6}][Cl]$ form an IL $[P_{14,6,6,6}][NTf_2]_x[Cl]_{1-x}$ with x =0.5. The dynamics of charge transport and the dielectric response of the IL $[P_{14,6,6,6}][NTf_2][Cl]$, were studied using broadband dielectric spectroscopy in a broad frequency range from 10^{-2} to 10^7 Hz and a wide temperature range between 123 K to 298 K. The technique was useful for investigating charge transport, dipolar fluctuations and the interaction of electromagnetic waves with matter in glassy and liquid phases of both mixtures. The dielectric properties of $[P_{14,6,6,6}][NTf_2][Cl]$ was analysed by impedance spectroscopy on application of a small AC signal across the sample cell with blocking electrode. Modulus representation was used to draw the dielectric spectra which display the dielectric peak which does not display from permitti vity representation due to the signature of DC conductivity and it is a direct method for measuring the orientational polarization and ionic conductivity. It is the

reciprocal of the permittivity, which characterize the dielectric properties of the liquid and quantifies the relaxation of the electric field at constant charge conditions.[86,121]

Figures 4.30 (a & b), 4.31 (a & b), 4.32 (a & b) and 4.33 (a & b) show the dielectric spectra of $[P_{14,6,6,6}][NTf_2][Cl]$. The spectra determine the comparison of the experimental data of dielectric permittivity, conductivity and modulus functions which are useful to distinguish a long–range conduction process from the localized dielectric relaxation. The peak in ε'' (ω) spectra is due to the reorientation process of dipoles of the dielectric relaxation. The increase in ε' (ω) is affected by the electrode polarization and the resultant peak in ε′′ (ω) shift to higher frequencies with the increase in temperatures. The value of σ' (ω) shows a frequency independent region yields the DC conductivity (σ_0) in the lower frequency and exhibits a power law behaviour in higher frequencies. The power law expressed as $\sigma(\omega) = \sigma_0 + A\,\omega^n$, where σ_0 is the DC conductivity, A is the pre-exponential factor and n is the fractional exponent between 0 and 1. The deviation of DC conductivity in the lower frequency region is due to electrode polarization. Electrode polarization is prominent to blocking electrodes investigating with dielectric spectroscopy. The charge transport takes place due to hopping conduction supplemented by the electrical relaxation which increases with decrease in frequency.

a) b

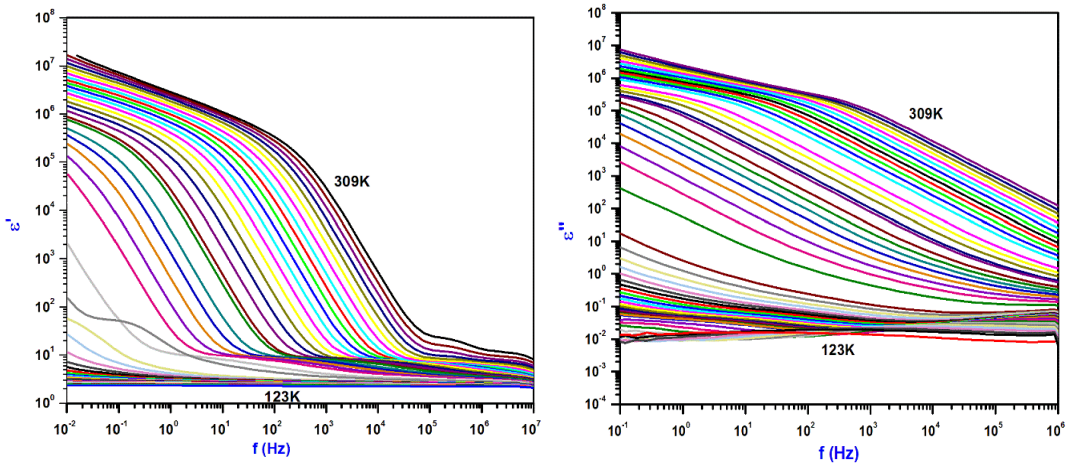

Figure 4.30. Frequency dependence of **(a)** real part ε′ (ω) and (b) imaginary part ε′′ (ω) of $[P_{14,6,6,6}][NTf_2][Cl]$ IL.

From figure 4.30 (a), it is seen that a huge increase in $\varepsilon'(\omega)$ and a decrease in $M'(\omega)$ happens with the decrease in frequencies, which is typically found in many ionic liquids.[81-86] This is due to the reorientation of dipoles at higher frequencies and translational motion of charge carriers at lower frequencies. The plot display in figures 4.32 (a & b) & 4.33 (a & b), the dielectric peak comparing to $\varepsilon''(\omega)$ which has a slope of -1 are found. Secondary relaxations are clearly visible in log M" vs log f (ω) in figure 4.23 (g & h). The dielectric response of $[P_{14,6,6,6}][NTf_2][Cl]$ was further explored in detail by the J. Dyre's random barrier model and the fit parameters are shown in table 4.6. It is revealed that σ_0 (the d c conductivity) increases with increase in temperature, but τ_e (the conductivity relaxation time) offered an anti–correlation with temperature.

a) b)

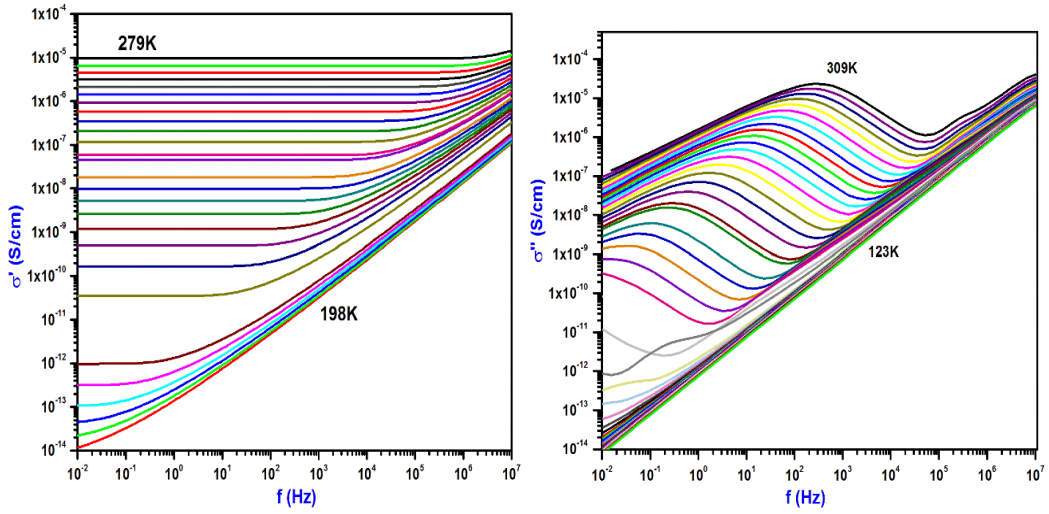

Figure 4.31. Frequency dependence of (a) the real part $\sigma'(\omega)$ and (b) imaginary part $\sigma''(\omega)$ of $[P_{14,6,6,6}][NTf_2][Cl]$ IL at different temperatures.

a) b)

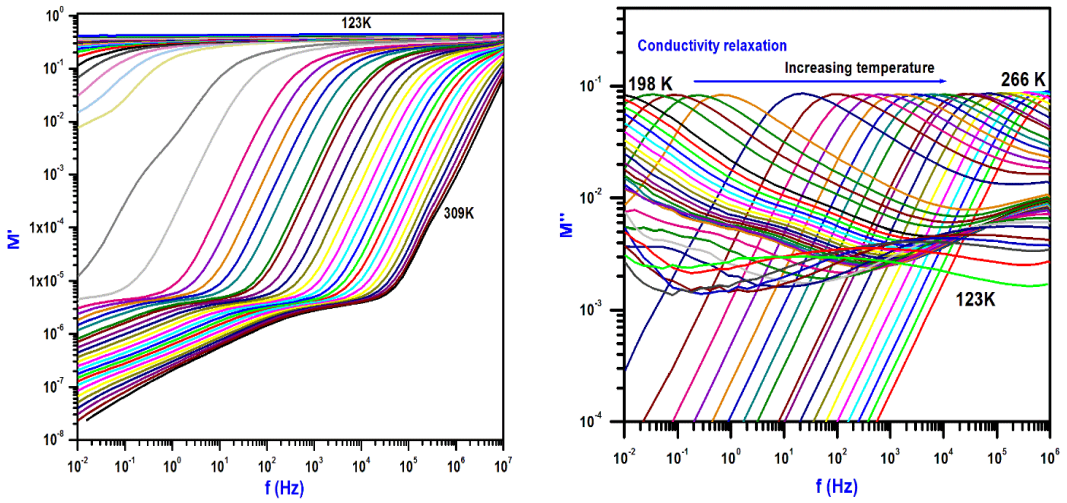

Figure 4.32. Frequency dependence of (a) the real part M′ (ω) and (b) the imaginary part M′′ (ω) of the electric modulus function of $[P_{14,6,6,6}][NTf_2][Cl]$ IL for various temperatures.

a) b)

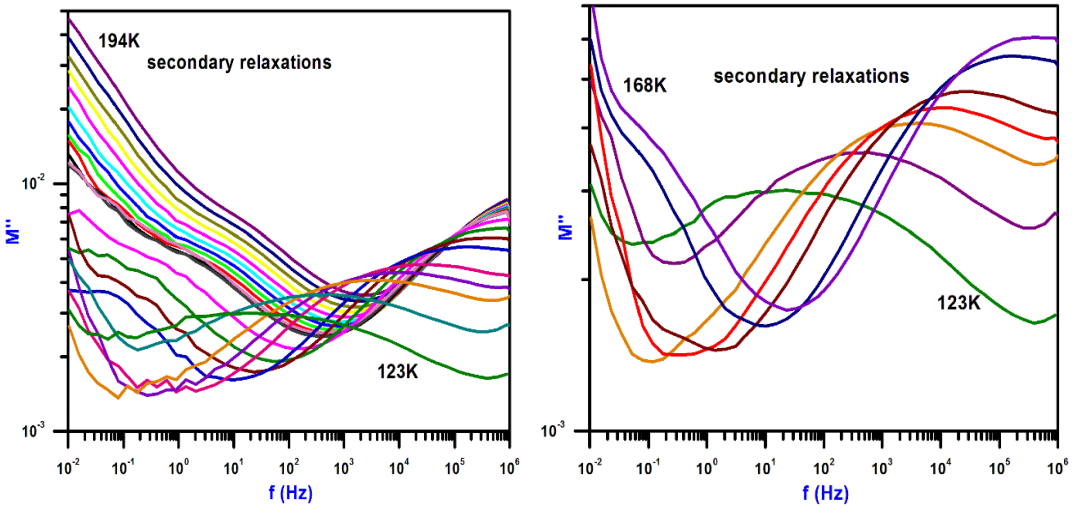

Figure 4.33. Frequency dependence of (a) the real part M′ (ω) and (b) the imaginary part M′′ (ω) of $[P_{14,6,6,6}][NTf_2][Cl]$ IL at temperatures 123 K to 194 K.

Table 4.6. *Fit parameters of* $[P_{14,6,6,6}][NTf_2][Cl]$ *to Dyre equation*.

T (K)	σ_0 (S/cm)	τ_e (s)	ε_∞
1.98E+02	8.15E-15	6.80E+01	1.00E+00
2.01E+02	1.06E-13	5.25E+00	1.00E+00
2.02E+02	3.16E-13	1.74E+00	1.00E+00
2.09E+02	1.67E-10	4.27E-03	1.00E+00
2.12E+02	4.90E-10	1.50E-03	1.00E+00
2.21E+02	5.20E-09	1.45E-04	2.18E+00
2.24E+02	9.92E-09	7.67E-05	2.18E+00
2.34E+02	5.80E-08	1.33E-05	2.18E+00
2.38E+02	1.16E-07	6.53E-06	2.18E+00
2.50E+02	5.76E-07	1.31E-06	2.18E+00
2.62E+02	2.15E-06	3.78E-07	1.80E+00
2.66E+02	3.16E-06	2.57E-07	1.74E+00
2.74E+02	6.43E-06	1.24E-07	1.30E+00
2.79E+02	9.61E-06	8.02E-08	1.02E+00

The Arrhenius plot for the conductivity relaxation and secondary relaxation of $[P_{14,6,6,6}][NTf_2][Cl]$ are shown in figure 4.34 (a). The temperature dependence of the conductivity relaxation time τ_e and the DC conductivity (σ_0) shown in figure 4.34 (b) indicate a non–Arrhenius VFT behaviour whereas the secondary relaxation obtained by an Arrhenius temperature dependence. VFT fitting parameters of $[P_{14,6,6,6}][NTf_2][Cl]$ are given in table 4.7.

a) b)

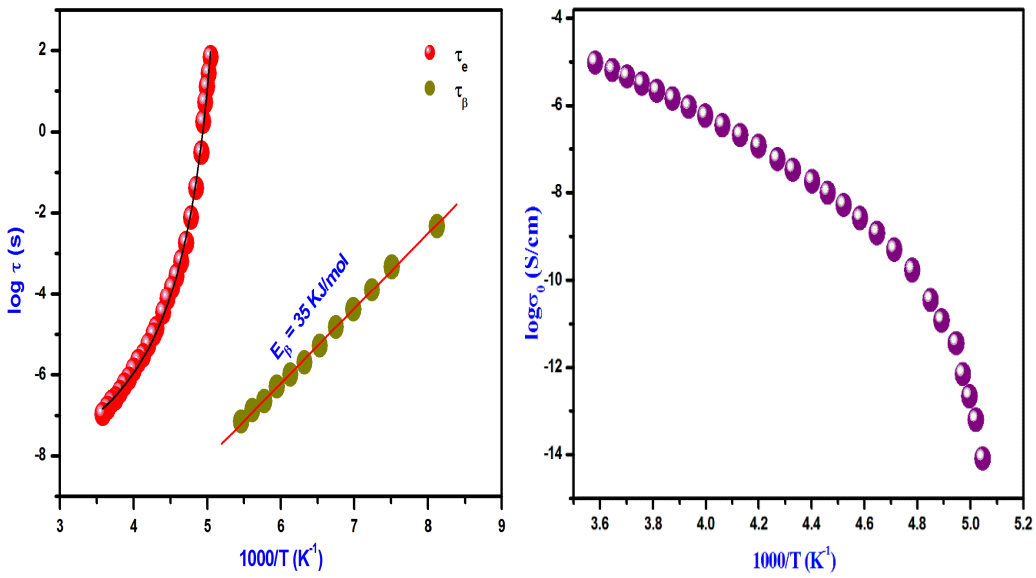

Figure 4.34. Plot of (**a**) log τ (s) vs 1000/T and (b) log σ (S/cm) vs 1000/T of $[P_{14,6,6,6}][NTf_2][Cl]$.

Table 4.7. *The fit parameters of $[P_{14,6,6,6}][NTf_2][Cl]$ IL to VFT and KWW functions.*

Sample	log τ_0 (s)	B (K)	T_0 (K)	T_g (BDS) (K)	T_g (DSC) (K)	Fragility (m)	E_β (kJ/mol)	β_{KWW}
$[P_{14,6,6,6}]$ $[NTf_2][Cl]$	9.00± 0.12	504± 0.14	178± 0.24	196	190	125	35± 0.45	0.51

The deviation from the Arrhenius nature near the glass transition is revealed at the slope of log (τ) vs T_g/T plot as shown in figure 4.35 and is termed as the steepness index (m). The value of the fragility index m of $[P_{14,6,6,6}][NTf_2][Cl]$ is given as 125. It indicates that the fragility of binary mixing ILs was higher than their parent ionic liquids. It can be found that the typical values of m are between 16 –45 ("strong" glass formers, m $<$ 45) and 75–200 ("fragile" ones).[125-127] Fragility

expresses how the relaxation time changes as T_g is approached. The slope of the Angell plot (log (τ), log σ_0 vs (T_g/T)) shows the fragility behaviour of the sample. For a strong glass former the plot shows straight line behaviour. The fragility behaviour of the sample can also be calculated by using the value of melting temperature and glass transition temperature. If T_m/T_g (in K) > 1.5 creates the strong glass former and T_m/T_g (in K) < 1.5 generate a fragile glass former.[105,125]

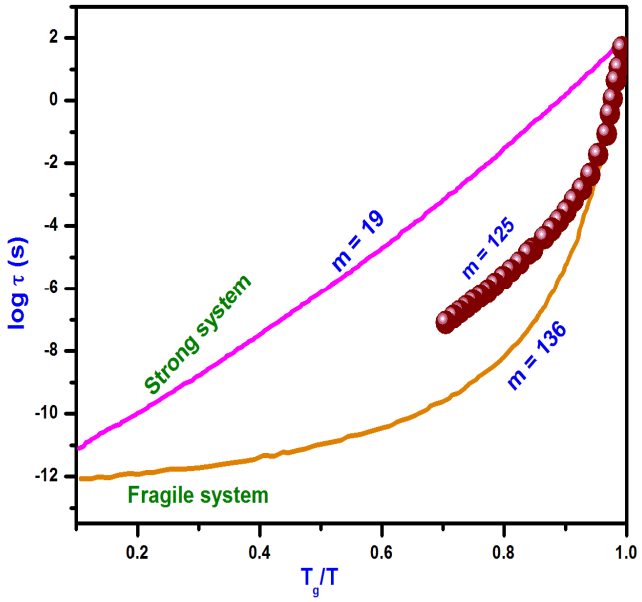

Figure 4.35. Plot of log τ (s) vs T_g/T of $[P_{14,6,6,6}][NTf_2][Cl]$.

The temperature dependence of σ_0 and ω_e , the two observable quantities describing charge transport by Dyre approach are shown in fig 4.36 (a). The temperature dependence of the σ_0 and ω_e detected the VFT behaviour, but the two parameters can be easily coincided and log σ_0 vs log ω_e is identified as straight line behaviour. This states the well-known BNN relation, $\sigma_0 \sim 1/\tau_e$.[83,162] The Frequency dependence of imaginary part M′ (ω) of $[P_{14,6,6,6}][NTf_2][Cl]$ are shown in figure 4.36 (b). On fitting the data, we got a value of n of KWW to be 0.51 for conductivity relaxation process around the glass transition temperature corresponding to tau = 100 s. It can be anticipated that the value of $\beta_{KWW} = 0.51$ is less than 1 and the relaxation process seems to be non–Debye type relaxation.

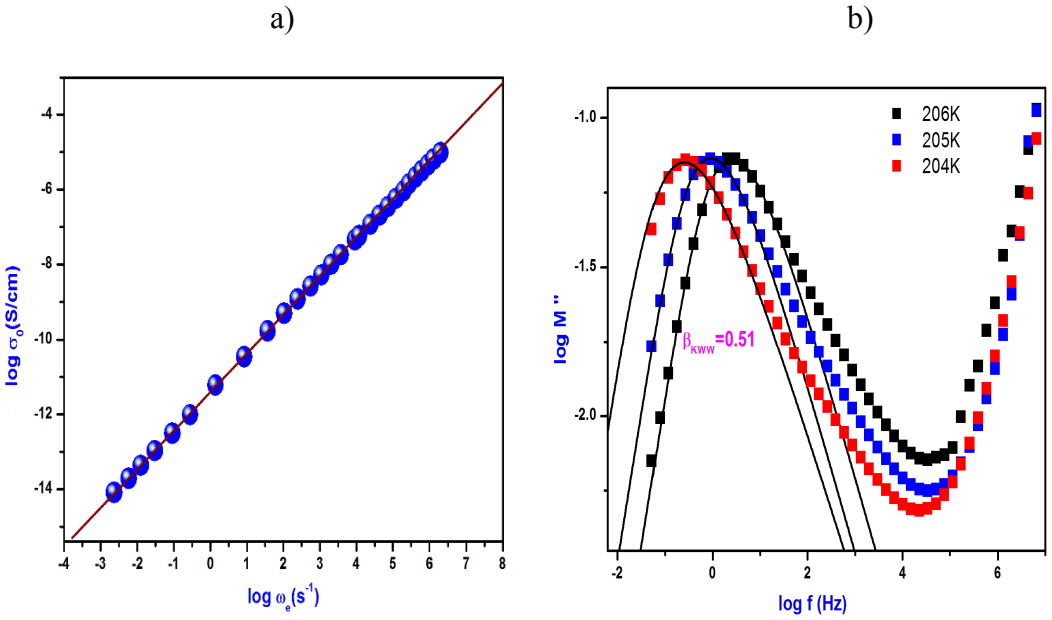

Figure 4.36. (a) DC conductivity σ_0 versus the characteristic frequency, ω_e and b) Frequency dependence of log M′′ (ω) of $[P_{14,6,6,6}][NTf_2][Cl]$. The black solid line represents the KWW fit with $\beta_{KWW} = 0.51$.

4.1.5. Thermal and broadband dielectric spectroscopic analysis of $[P_{14,6,6,6}][N(CN)_2][Cl]$

4.1.5.1. Thermogravimetric analysis

Thermal stability of the IL $[P_{14,6,6,6}][N(CN)_2][Cl]$ is measured with TGA in an interval of 300 K–900 K and the weight loss curve of the IL was obtained in figure 4.37. It is revealed that up to 573 K the sample is thermally stable and began to decrease above this temperature. Nearly same thermal stability is observed with their parent ILs.

4.1.5.2. Differential scanning calorimetry analysis

DSC response of $[P_{14,6,6,6}][N(CN)_2][Cl]$ at a heating rate of 10 K /min. from 123 K to 300 K is represented in Figure. 4.28. The transition displayed a glass transition temperature of 196.01 K. The glass forming ability of the sample is

identified with the value of glass transition temperature. There is no crystallisation peak is observed in this sample, but a melting peak is found at 208.72 K.

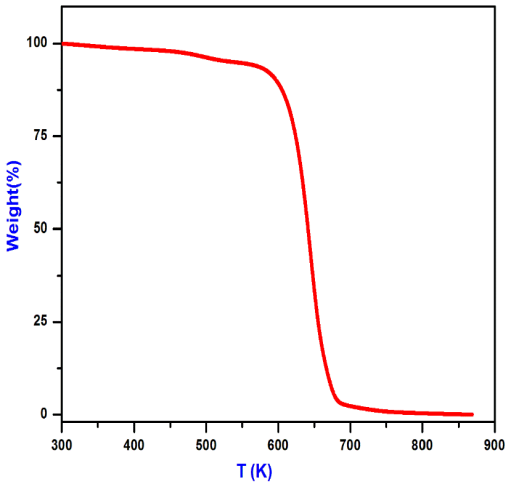

Figure 4.37. TGA plot of $[P_{14,6,6,6}][N(CN)_2][Cl]$.

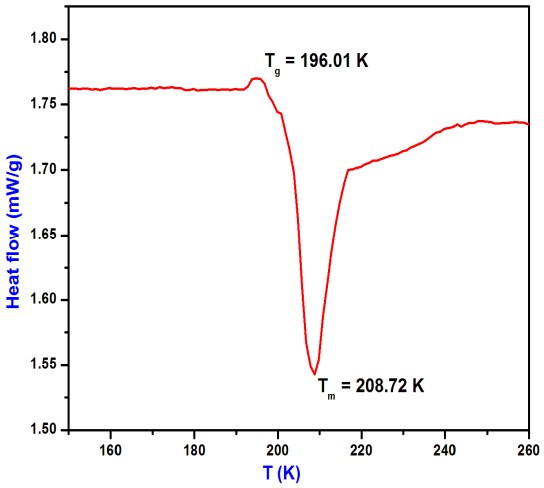

Figure 4.38. DSC plot of $[P_{14,6,6,6}][N(CN)_2][Cl]$.

4.1.5.3. Broadband dielectric spectroscopic analysis

We have determined the dielectric response of a mixing of two ILs $[P_{14,6,6,6}][N(CN)_2]$ and $[P_{14,6,6,6}][Cl]$ form an IL $[P_{14,6,6,6}][N(CN)_2]_x[Cl]_{1-x}$ with x =0.5. The dielectric properties of $[P_{14,6,6,6}][N(CN)_2][Cl]$ was analysed by impedance spectroscopy on application of a small a.c signal across the sample cell with blocking electrode. The real and imaginary parts of dielectric permittivity, conductivity and modulus functions of $[P_{14,6,6,6}][N(CN)_2][Cl]$, as a function of frequency at temperatures from 123 K to 313 K were presented in figures 4.39 (a & b), 4.40 (a & b), 4.41 (a & b) and 4.42. The real part of permittivity ε' is dominated by electrode polarization at lower frequencies. The strong increase flats off after the small peak in the imaginary part ε", starts a region where the phase angle is nearly constant (CPA). Modulus representation was used to draw the dielectric spectra which display the dielectric peak which does not display from permittivity representation due to the signature of DC conductivity and it is a direct method for measuring the orientational polarization and ionic conductivity. The peak in ε" (ω) spectra is due to the reorientation process of dipoles of the dielectric relaxation. The increase in ε' (ω) is affected by the electrode polarization and the resultant peak in ε″ shift to higher frequencies with increasing temperatures. The prominent peaks are

not seen due to conductivity contribution for this sample. The value of σ' (ω) shows a frequency independent plateau region yields the DC conductivity (σ_0) in the lower frequency and exhibits dispersive region in higher frequencies. The abnormality of DC conductivity in the lower frequency region is due to electrode polarization. Log M" (ω) vs log f plot display the broad non Debye type dielectric peak. Secondary relaxations are clearly visible in log f vs log M" (ω).[81-121]

a) b)

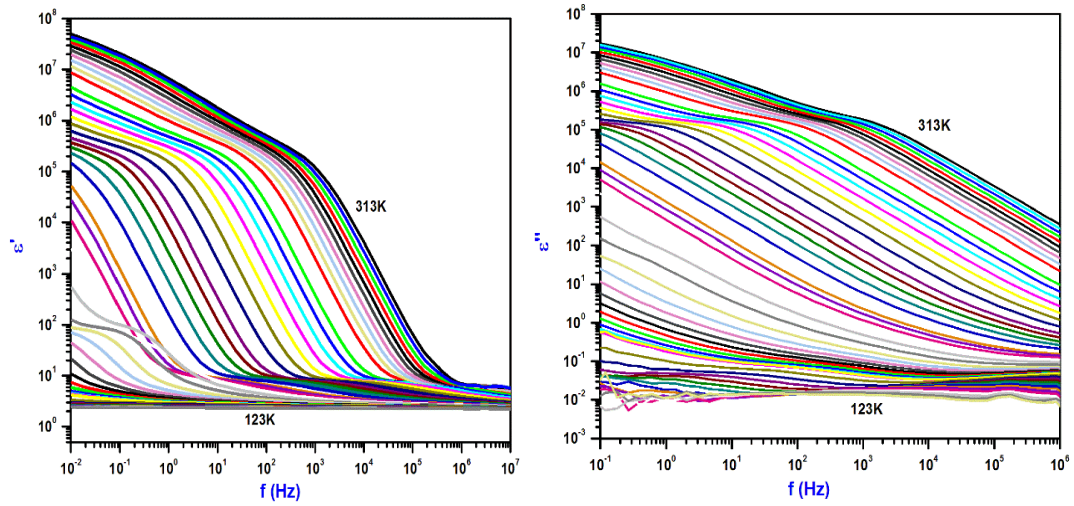

Figure 4.39. Frequency dependence of **(a)** real part ε′ (ω) and (b) imaginary part ε″ (ω) for $[P_{14,6,6,6}][N(CN)_2][Cl]$ IL.

a) b)

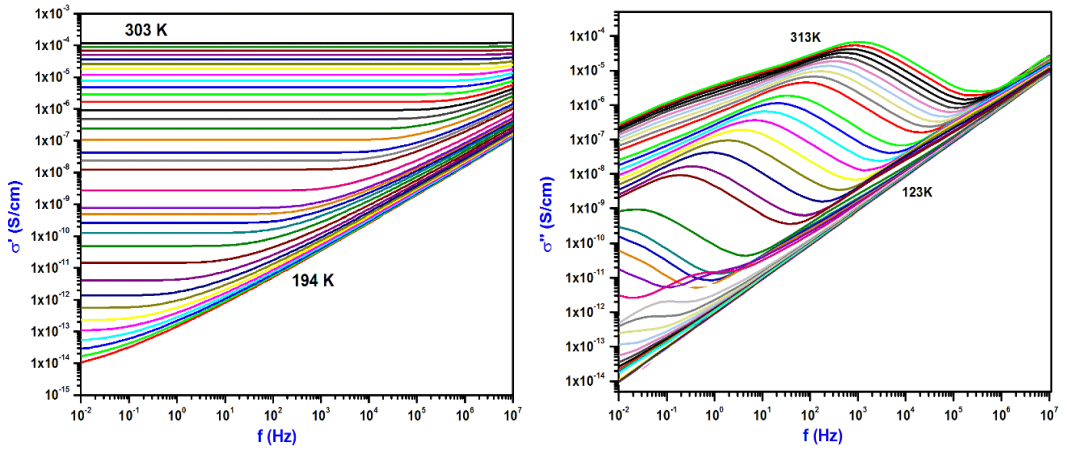

Figure 4.40. Frequency dependence of (a) the real part σ′ (ω), (b) imaginary part σ″ (ω) at different temperatures for the sample $[P_{14,6,6,6}][N(CN)_2][Cl]$ IL.

a) b)

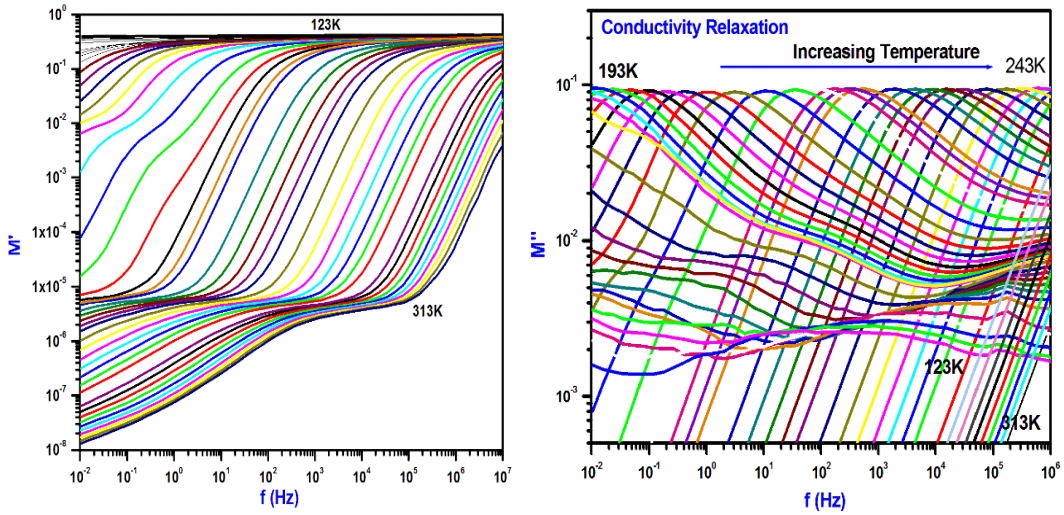

Figure 4.41. Frequency dependence of (a) the real part M′ (ω) and (b) the imaginary part M″ (ω) at different temperatures for the sample $[P_{14,6,6,6}][N(CN)_2][Cl]$ IL.

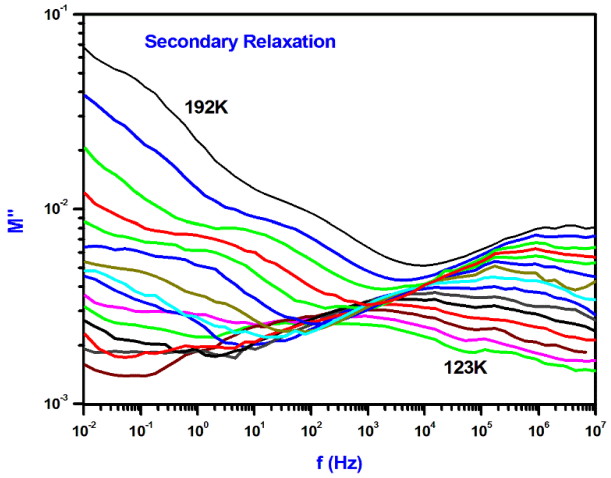

Figure 4.42. Frequency dependence of M″ (ω) at temperatures 123 K to 192 K for $[P_{14,6,6,6}][N(CN)_2][Cl]$ IL.

The dielectric response of $[P_{14,6,6,6}][N(CN)_2][Cl]$ in the charge transport dominated regime was further discovered in detail by the random barrier model of J. Dyre and the fit parameters are shown in table 4.8. It is exposed that σ_0 (the DC conductivity) increases with the increase in temperature, but τ_e (the conductivity relaxation time) existing a decrease with the increase in temperature. The thermal

activation plots in figure 4.43 (a & b) of conductivity relaxation time (τ_e) and DC conductivity(σ_0) exhibits a VFT-type of thermal behaviour above T_g and the τ_e shows transitions to Arrhenius-type of temperature dependence below T_g. The VFT parameters are shown in table 4.9 below.

Table 4.8. *Fit parameters of $[P_{14,6,6,6}][N(CN)_2][Cl]$ IL to Dyre equation..*

T (K)	σ_0 (S/cm)	τ_e (s)
1.94E+02	6.56E-15	9.73E+01
1.98E+02	1.08E-13	5.59E+00
2.04E+02	4.93E-11	1.23E-02
2.07E+02	4.84E-10	1.32E-03
2.14E+02	6.09E-09	1.17E-04
2.23E+02	4.23E-08	1.79E-05
2.38E+02	4.85E-07	1.70E-06
2.53E+02	2.90E-06	3.06E-07
2.68E+02	1.19E-05	8.15E-08
2.83E+02	3.67E-05	3.01E-08
2.98E+02	9.03E-05	1.58E-08

a) b)

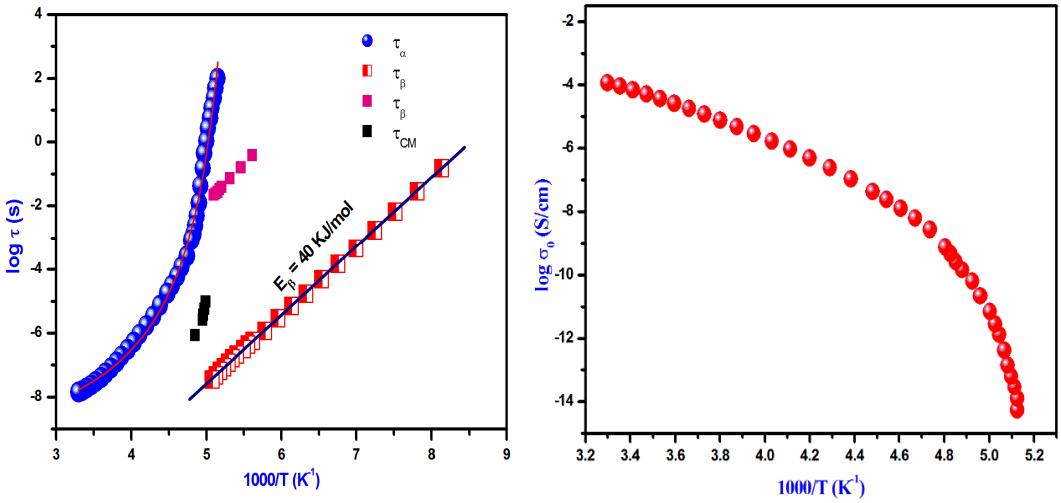

Figure 4.43. Thermal activation plot of (a) conductivity relaxation time (τ_e) above T_g and below T_g (τ_γ),(τ_{cm} is the coupling model data) and b) d c conductivity (σ_0) of the sample $[P_{14,6,6,6}][N(CN)_2][Cl]$ IL.

The glass forming ILs classified in terms of the way of vitrification as strong ILs whose viscosity follows the Arrhenius law and the other is fragile liquids whose viscosity obeys the non-Arrhenius VFT equation. A quantitative measure of the fragility of $[P_{14,6,6,6}][N(CN)_2][Cl]$ can be obtained from the value m of the sample. The fragile systems express a deviation from Arrhenius behaviour. Plot of log τ (s) vs T_g/T of $[P_{14,6,6,6}][N(CN)_2][Cl]$ are shown in figure 4.44 (a). The VFT fitting parameters are shown in table 4.9**.** E_β is the activation energy of the IL. The figure 4.44 (b) represents that the sample $[P_{14,6,6,6}][N(CN)_2][Cl]$ follows the BNN relation properly. i.e. $\sigma_0=1/\tau_e$.

Table 4.9. *The fit parameters of $[P_{14,6,6,6}][N(CN)_2][Cl]$ IL to VFT and KWW functions.*

Sample	log τ_0 (s)	B (K)	T_0 (K)	T_g (BDS) (K)	T_g (DSC) (K)	Fragility (m)	E_β (kJ/mol)	β_{KWW}
$[P_{14,6,6,6}]$ $[N(CN)_2][Cl]$	9.00 ± 0.30	516 ± 0.4	175 ± 0.1	193	196	131	40 ± 0.5	0.59

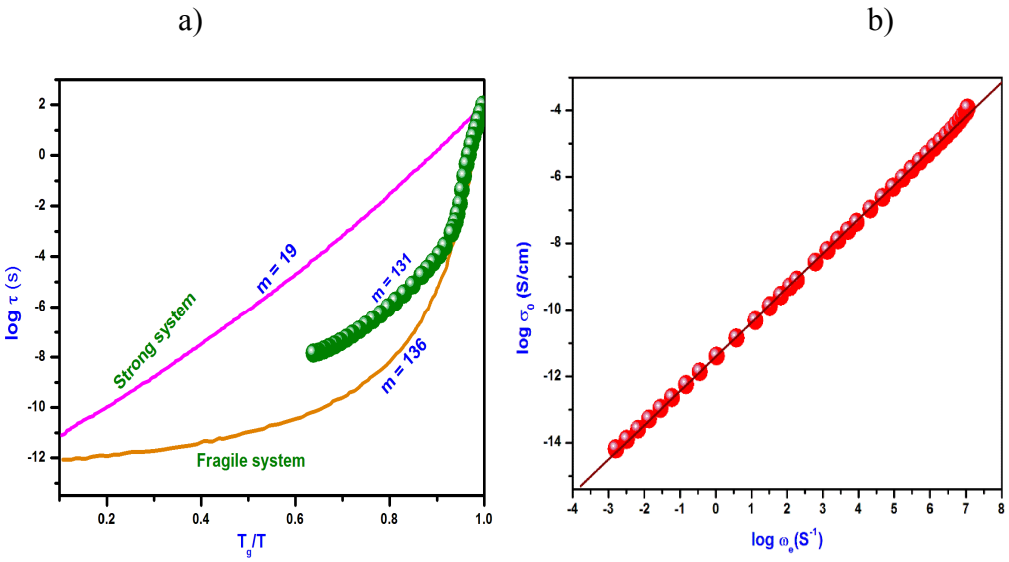

Figure 4.44. Plot of (a) log τ (s) vs T_g/T and b) d c conductivity σ_0 versus the characteristic frequency, ω_e of $[P_{14,6,6,6}][N(CN)_2][Cl]$ IL.

Frequency dependence of the imaginary part of the modulus representation for $[P_{14,6,6,6}][N(CN)_2][Cl]$ at different temperatures are shown in figure 4.45. The solid line is a KWW function with $\beta_{KWW} = 0.59$. The stretching parameter β_{KWW} which explains the asymmetric delivery of relaxation time has very important role in expecting the stability of an amorphous system, as β_{KWW} decreases stability also decreases.

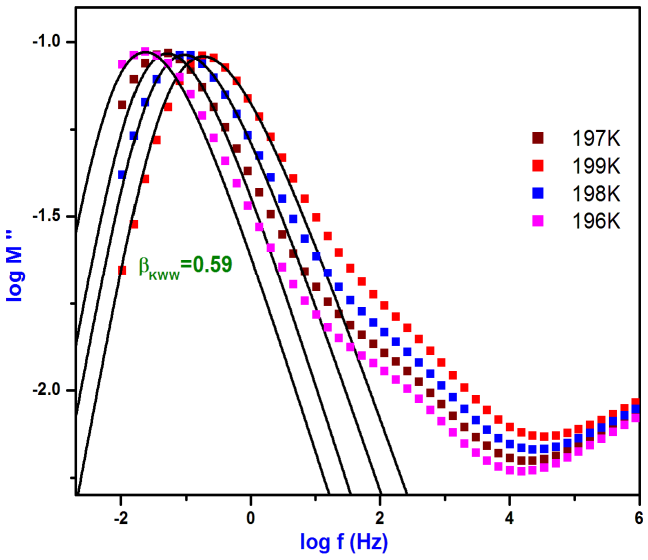

Figure 4.45. Frequency dependence of log M′′ (ω) of $[P_{14,6,6,6}][N(CN)_2][Cl]$ with $\beta_{KWW} = 0.59$.

4.1.6. Thermal and broadband dielectric spectroscopic analysis of PVA–$[P_{14,6,6,6}][NTf_2]$ ionogel

4.1.6.1. Thermogravimetric analysis

Thermal stability of the IL PVA–$[P_{14,6,6,6}][NTf_2]$ ionogel is measured with TGA in an interval of 300 K–900 K and the weight loss curve of the IL was obtained in figure 4.46 (a). It is revealed that up to 323 K the sample is thermally stable and hence this sample is not suitable for high temperature applications.

4.1.6.2. Differential scanning calorimetry analysis

DSC plot of PVA–$[P_{14,6,6,6}][NTf_2]$ ionogel at a heating rate of 10 K /min. from 123 K to 300K is presented in figure. 4.46 (b). The transition displayed a glass

transition temperature of 226.26 K and a melting temperature of 275.87 K. The glass forming ability of the sample is identified with the value of glass transition temperature.

a) b)

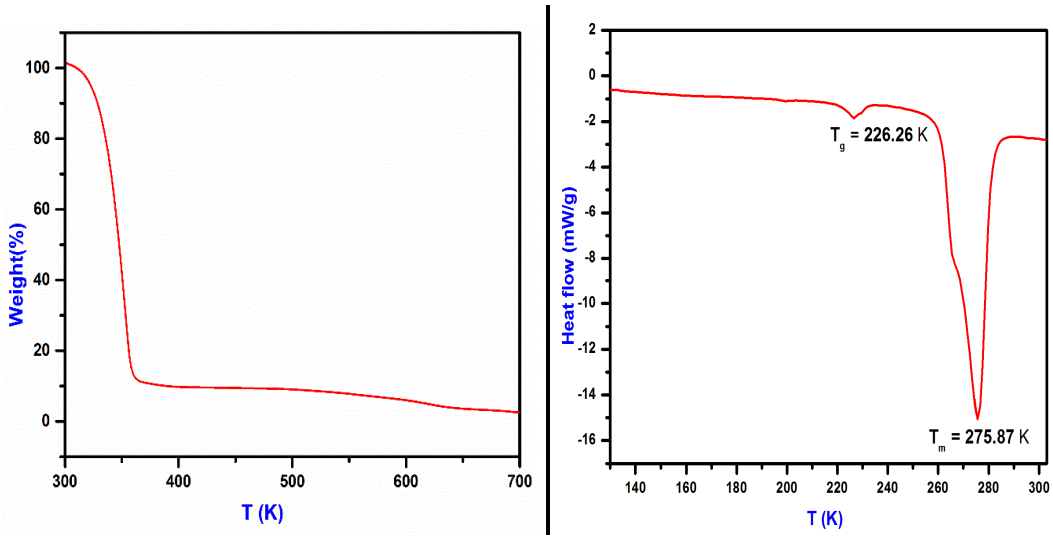

Figure 4.46. (a) TGA plot & (b) DSC plot of PVA– $[P_{14,6,6,6}][NTf_2]$ IL.

4.1.6.3. Broadband dielectric spectroscopic analysis

Figures 4.47 (a & b), 4.48 (a & b), 4.49 (a & b), 4.50 (a & b) and 4.51 (a & b) show the permittivity, conductivity and modulus spectra of PVA–$[P_{14,6,6,6}][NTf_2]$ ionogel. The data cover from 10^{-2} to 10^{7} Hz frequency range and a temperature from 123 K to 322 K. There is no relevant relaxation peaks observed in permittivity and conductivity spectra due to electrode polarisation, but in modulus spectra, it suppresses the conductivity contribution and well peaks are observed $\omega\tau = 1$ with non-Debye behaviour. A conductivity plateau observed in plots of the figure 4.49 (a) corresponds to a DC conductivity. At low frequency side the conductivity is dropped due to the blocking of ionic charges. At higher frequency, there is a dispersive region shown in certain temperatures only. We should note that the peaks at 123 K–133 K, which are appear to be in glassy state, to be somewhat distorted as compared to higher temperatures. When temperature increases, the relaxation peaks shift into

higher frequency side. The peaks at higher frequencies may be rather flat, i.e, frequency independent. From 153 K to 250 K some relaxation process observed in ε′ (ω), ε″ (ω), σ′ (ω) and M″ (ω).

a) b)

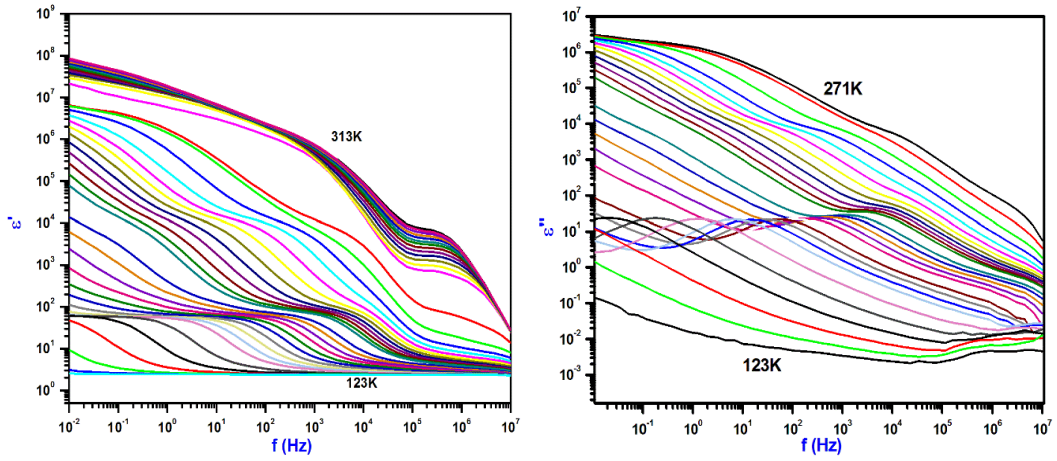

Figure 4.47. Frequency dependence of **(a)** ε′ (ω) and (b) ε″ (ω) of PVA–$[P_{14,6,6,6}][NTf_2]$ ionogel.

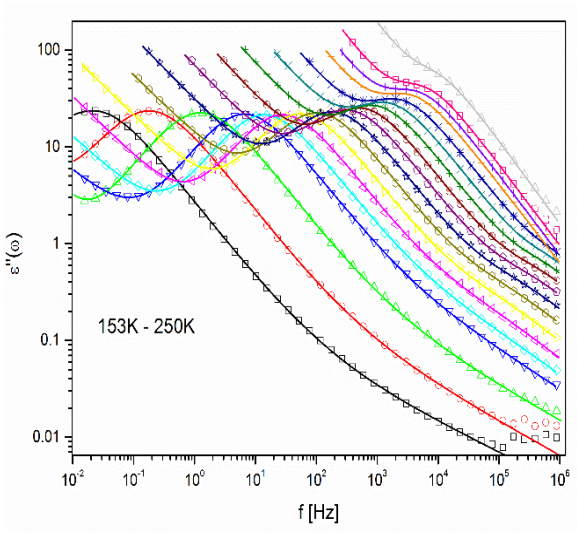

Figure 4.48. Frequency dependence of ε″ (ω) of PVA–$[P_{14,6,6,6}][NTf_2]$ ionogel at temperatures 153 K–250 K.

a) b)

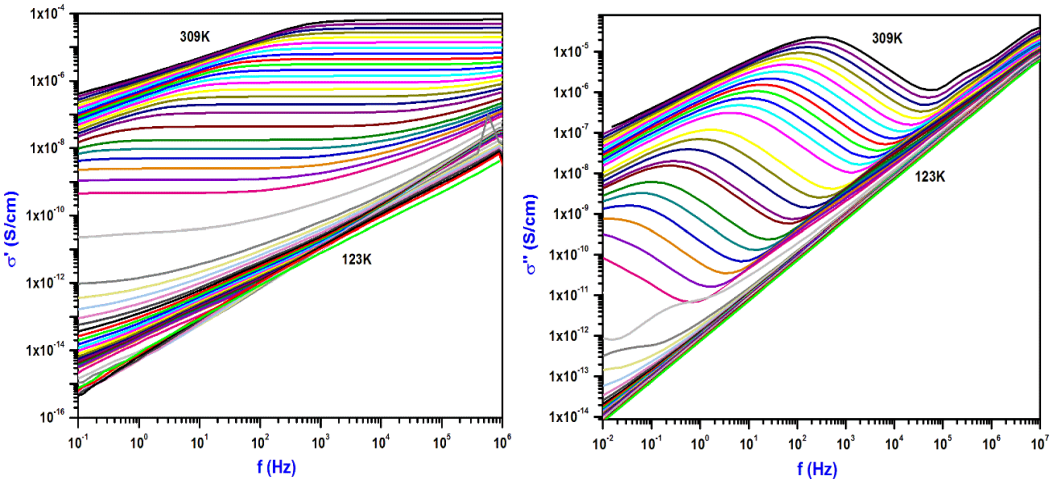

Figure 4.49. Frequency dependence (a) the real part σ' (ω) and (b) imaginary part σ'' (ω) at different temperatures for the sample PVA–$[P_{14,6,6,6}][NTf_2]$ ionogel.

a) b)

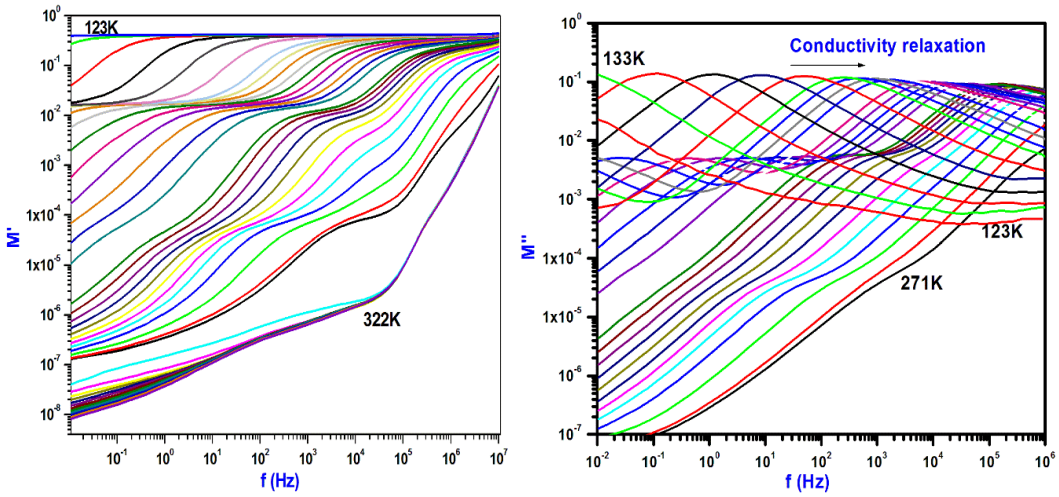

Figure 4.50. Frequency dependence of (a) the real part M′ (ω) and (b) the imaginary part M′′ (ω) at different temperatures for the sample PVA–$[P_{14,6,6,6}][NTf_2]$ ionogel.

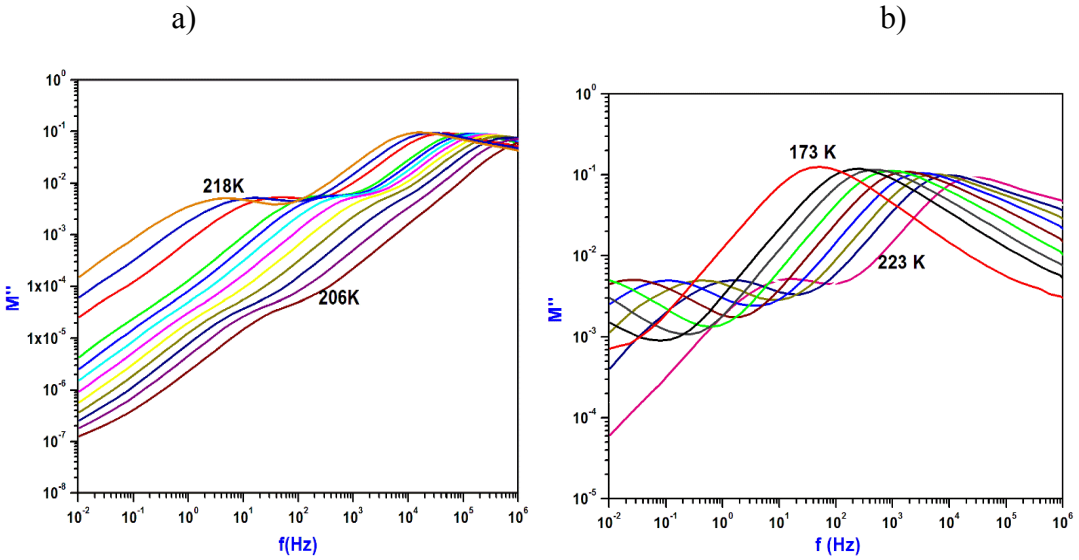

Figure 4.51. Frequency dependence of (a) M″ (ω) at temperatures 206 K–218 K for PVA–$[P_{14,6,6,6}][NTf_2]$ ionogel.

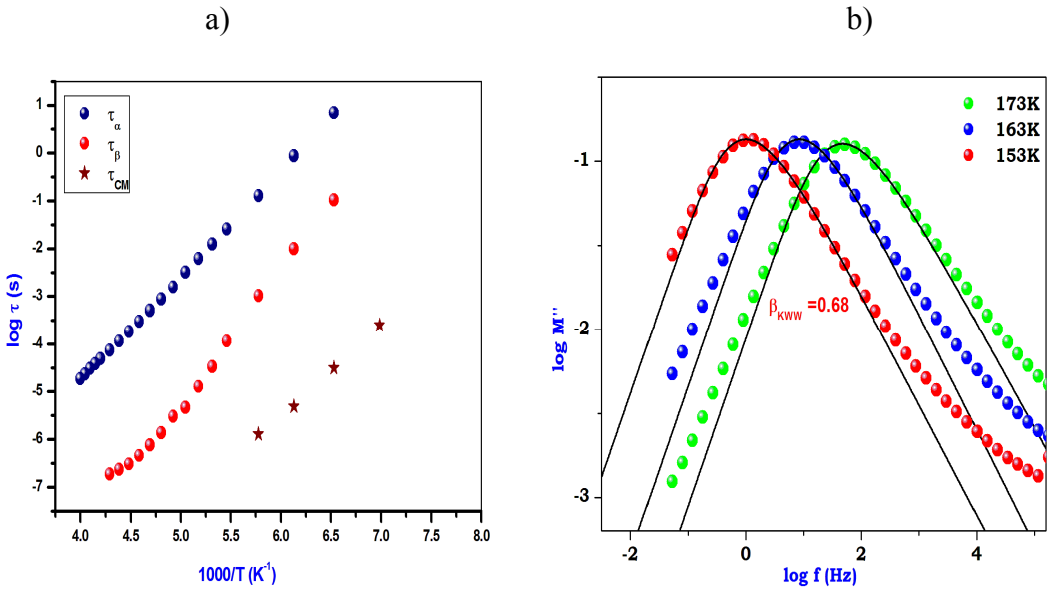

Figure 4.52. (a) Thermal activation plots above T_g and below T_g and (b) dielectric loss spectra of PVA–$[P_{14,6,6,6}][NTf_2]$ ionogel with $\beta_{KWW} = 0.68$.

Figure 4.52 (a) represents the Arrhenius plot of the IL. In this figure, both the conductivity relaxation and the secondary relaxation show Arrhenius behaviour. There is no VFT behaviour observed in conductivity relaxation. Frequency dependence of the imaginary part of the modulus representation for PVA–

$[P_{14,6,6,6}][NTf_2]$ at different temperatures are shown in figure 4.52 (b). The solid line is a KWW function with β_{KWW}=0.68.

4.1.7. Thermal and broadband dielectric spectroscopic analysis of PVA–$[P_{14,6,6,6}]$ $[N(CN)_2]$ ionogel.

4.1.7.1. Thermogravimetric analysis

Thermal stability of the IL PVA–$[P_{14,6,6,6}][N(CN)_2]$ ionogel is measured with TGA in an interval of 300 K–900 K and the weight loss curve of the IL was obtained in figure 4.53 (a). It reveals that up to 500 K, the sample is thermally stable.

4.1.7.2. Differential scanning calorimetry analysis

DSC response of PVA–$[P_{14,6,6,6}][N(CN)_2]$ ionogel at a heating rate of 10 K /min. from 123 K to 300 K is presented in figure. 4.53 (b). The transition displayed a glass transition temperature of 169.05 K and a melting temperature of 206.15 K. The glass forming ability of the sample is recognized with the value of glass transition temperature.

a) b)

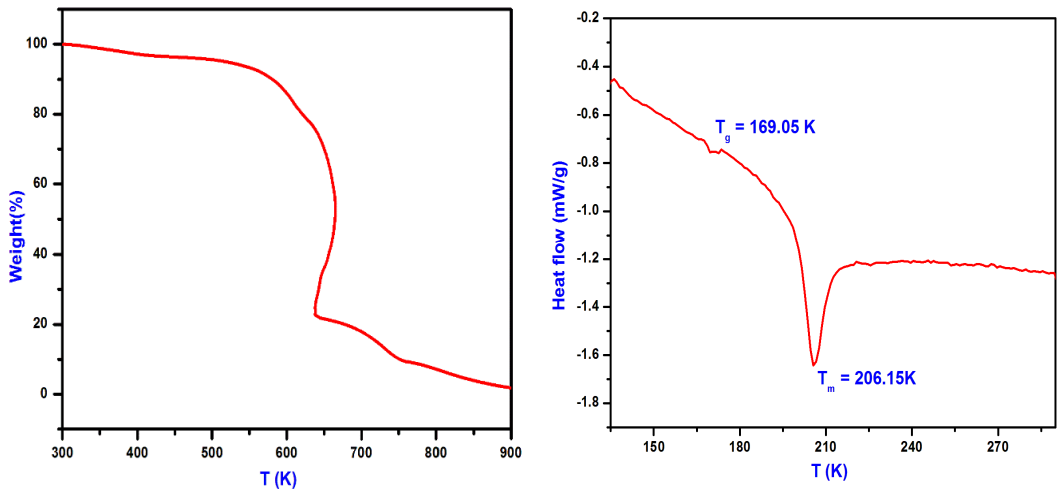

Figure 4.53. (a) TGA plot & **(b)** DSC response of PVA–$[P_{14,6,6,6}][N(CN)_2]$ ionogel

4.1.7.3. Broadband dielectric spectroscopic analysis

Figures 4.54 (a & b), 4.55 (a & b), 4.56 (a & b) and 4.57 (a & b) show the frequency dependence of the real part of the ε′ (ω), imaginary part ε″ (ω) of permittivity representation, the real part σ′ (ω) & imaginary part σ″ (ω) of conductivity formalism and the real part M′ (ω) & the imaginary part M″(ω) of the electric modulus function M^*, at different temperatures for the sample PVA–$[P_{14,6,6,6}][N(CN)_2]$ ionogel. From 179 K to 245 K some relaxation process observed in ε′ (ω), ε″ (ω), σ′ (ω) and M″ (ω). The plot of modulus M″ (ω) show asymmetric behaviour with respect to peak maxima whose positions are frequency and temperature dependent. The conductivity representation is the most prominent formalism to transmit the macroscopic measurement to the microscopic movement of the ions. The frequency dependent conductivity spectrum displays a low frequency plateau and high frequency dispersive regions usually. But here, the high frequency dispersive region is not seen. The frequency independent DC conductivity displays in some temperature only. Figure 4.59 represents the temperature dependence of the PVA–$[P_{14,6,6,6}][N(CN)_2]$ ionogel, which shows Arrhenius behaviour for both conductivity relaxation and secondary relaxation. There is no VFT behaviour observed in conductivity relaxation for this sample.

a) b)

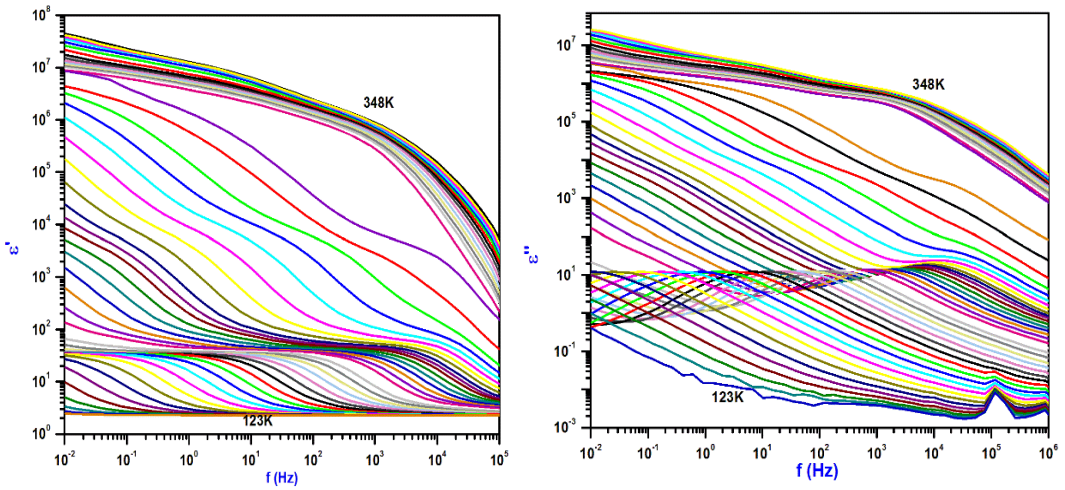

Figure 4.54. Frequency dependence of **(a)** real part ε′ (ω) and (b) imaginary part ε″ (ω) at different temperatures for the sample PVA–$[P_{14,6,6,6}][N(CN)_2]$ ionogel.

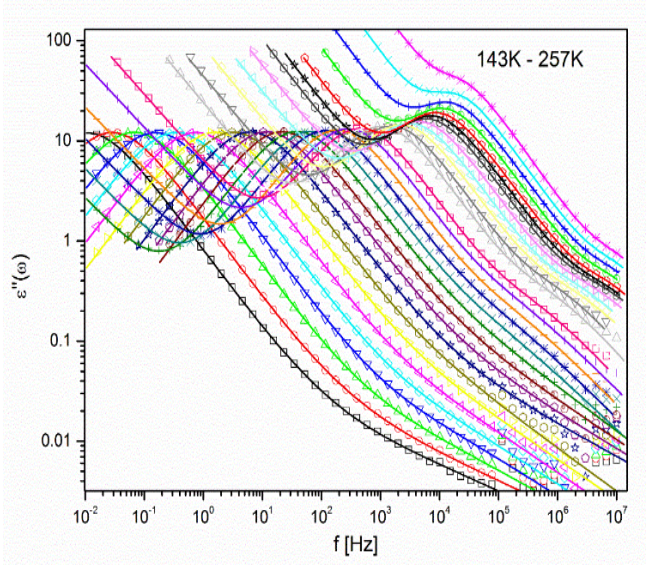

Figure 4.55. Frequency dependence of **(a)** imaginary part $\varepsilon''(\omega)$ at temperatures 143 K−257 K for the sample PVA−$[P_{14,6,6,6}][N(CN)_2]$ ionogel.

a) b)

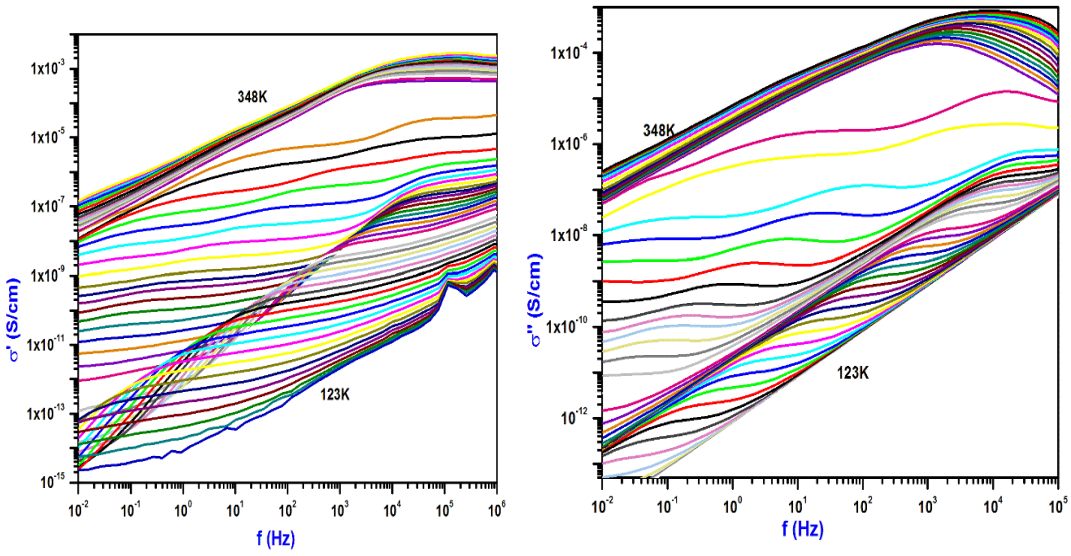

Figure 4.56. Frequency dependence of (a) the real part $\sigma'(\omega)$ and (b) imaginary part $\sigma''(\omega)$ at different temperatures for the sample PVA−$[P_{14,6,6,6}][N(CN)_2]$ ionogel.

a) b)

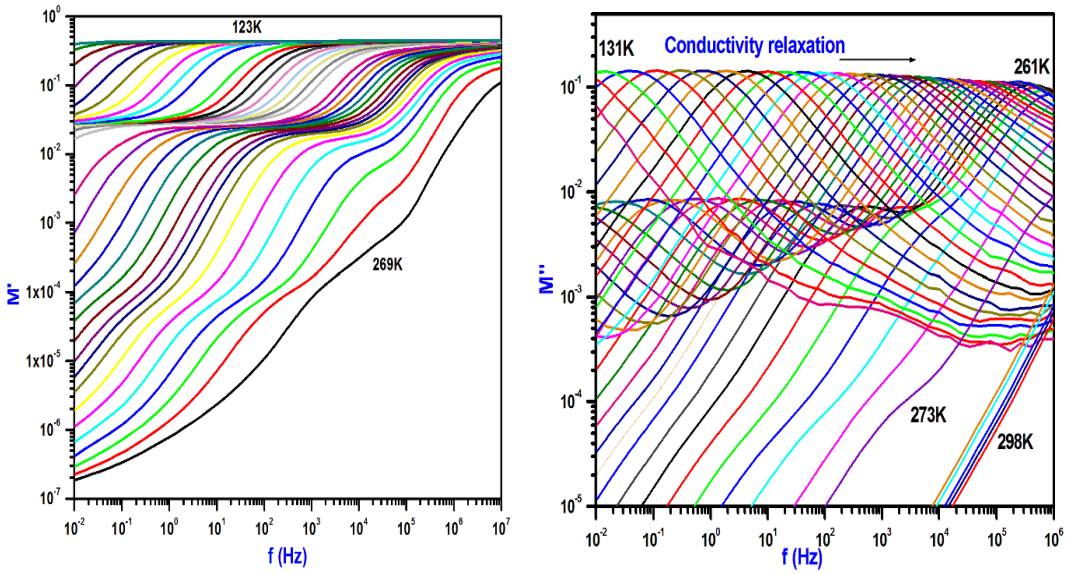

Figure 4.57. Frequency dependence of (a) M′ (ω) and (b) M″ (ω) at different temperatures for the sample PVA−$[P_{14,6,6,6}][N(CN)_2]$ ionogel.

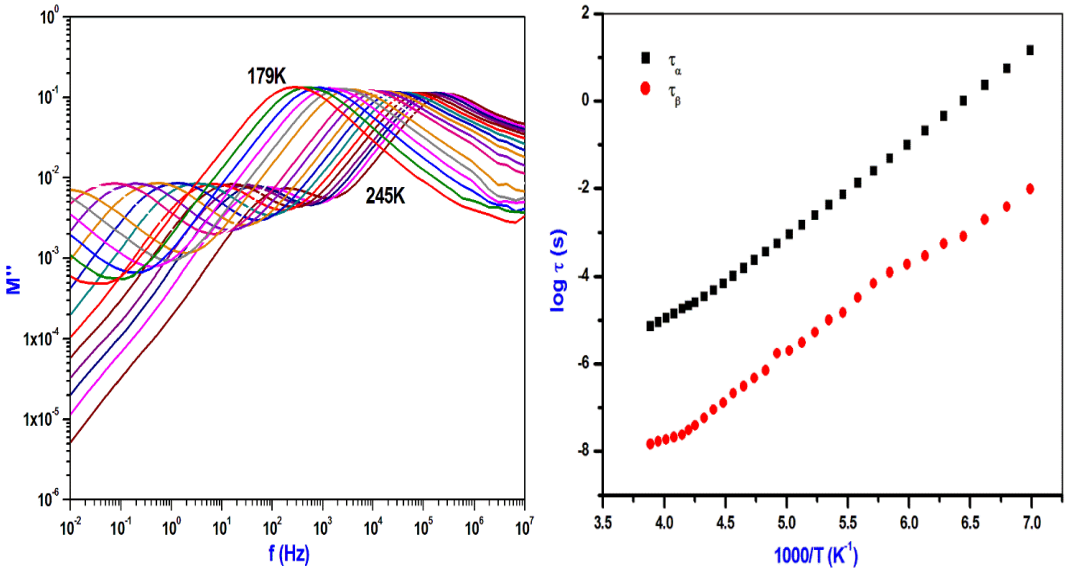

Figure 4.58. Frequency dependence of M″ (ω) at temperatures 179 K−245 K and **Figure 4.59.** Temperature dependence of PVA−$[P_{14,6,6,6}][N(CN)_2]$ ionogel.

a) b)

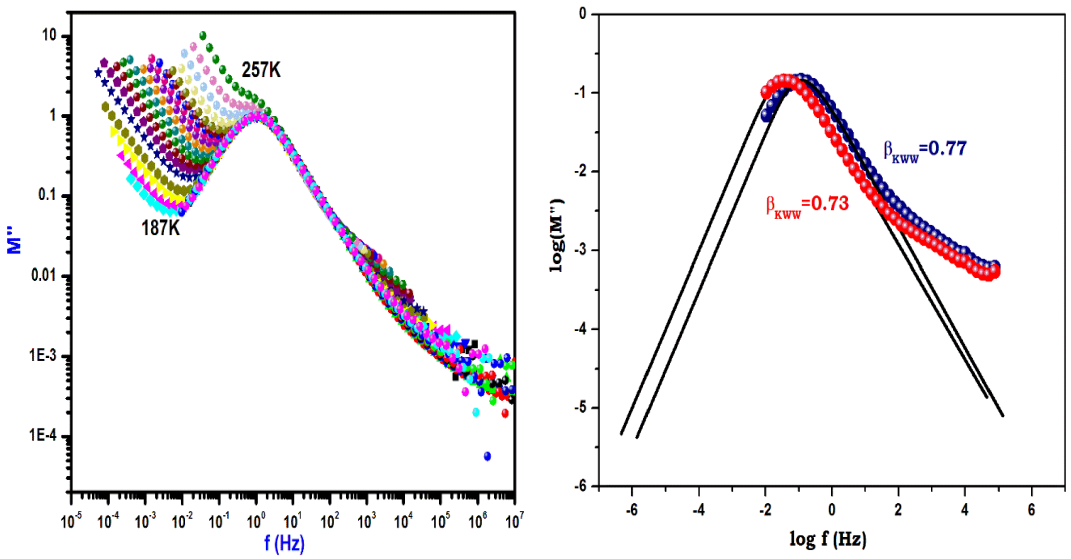

Figure 4.60. (a) Superimposed dielectric spectra of PVA−$[P_{14,6,6,6}][N(CN)_2]$ ionogel taken at temperatures 187 K−267 K and **(b)** dielectric loss spectra in modulus formalism of PVA− $[P_{14,6,6,6}][N(CN)_2]$ at temperatures above and below T_g. The black solid line represents the KWW fit with β_{KWW}=0.73**.**

Superimposed dielectric spectra of PVA−$[P_{14,6,6,6}][N(CN)_2]$ ionogel taken at different temperatures are presented in figure 4.60 (a). Frequency dependence of the imaginary part of the modulus representation for PVA−$[P_{14,6,6,6}][N(CN)_2]$ ionogel at different temperatures are shown in the figure 4.60(b). The solid line is a KWW function with β_{KWW}=0.73.

4.1.8. Thermal and broadband dielectric spectroscopic analysis of ranitidine docusate

4.1.8.1. Thermogravimetric analysis

Thermal stability of the IL ranitidine docusate is measured with TGA with in an interval of 300 K−900 K and the weight loss of the IL is shown in figure 4.61 (a). It is revealed that the sample is thermally stable up to 373 K.

4.1.8.2. Differential scanning calorimetry analysis

DSC response of ranitidine docusate at a heating rate of 10 K /min. from 123 K to 300 K is presented in Figure. 4.61 (b) and the transition displayed a glass transition temperature of 209.31 K. The glass forming ability of the sample is predictable with the value of glass transition temperature. There is no crystallisation and melting peaks observed in this sample.

a) b)

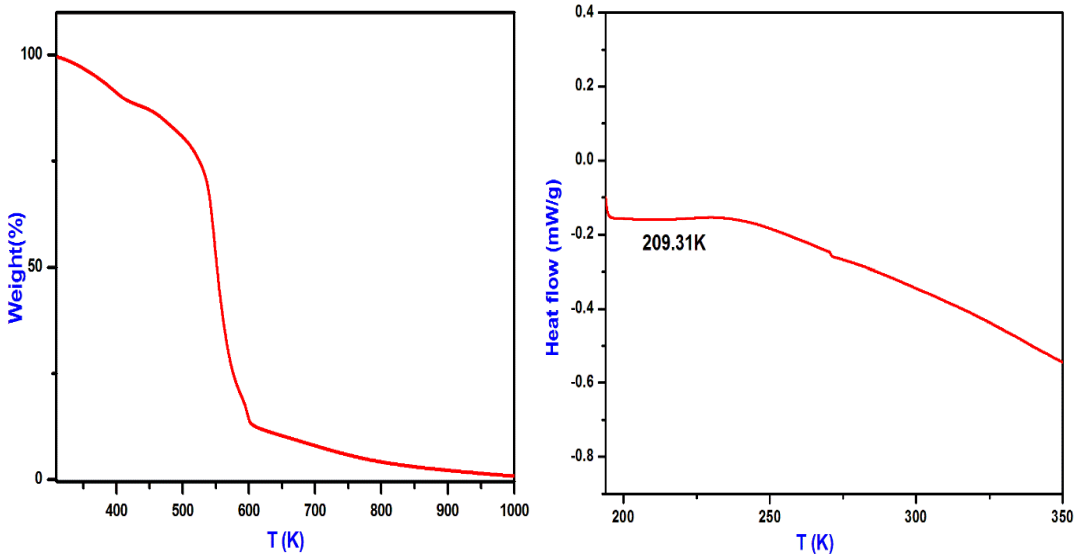

Figure 4.61. (a) TGA plot & (b) DSC plot of ranitidine docusate

4.1.8.3. Broadband dielectric spectroscopic analysis

Normally, dielectric spectra in glassy dynamics represent by three relaxation process: DC conductivity, conductivity relaxation (structural relaxation or α relaxation) and secondary relaxation (β, γ etc). DC conductivity is due to translational motion of mobile ions present in the sample while conductivity relaxation and secondary relaxation are related to rotational molecular motion (reorientation of molecules) above T_g and below T_g respectively.[13,58] T_g describes the time scale of the characteristic relaxation larger than ~100 s or the viscosity about 10^{12} Pa. Conductivity relaxation spectra of ranitidine docusate above the glass

transition temperature (T_g) in permittivity representation,conductivity and modulus representation are pronounced from 123 K to 309 K in the figures 4.62 (a & b), 4.63 (a & b) and 4.64 (a & b) respectively.

The strong increase of the $\varepsilon'(\omega)$ & $\varepsilon''(\omega)$ at lower frequencies are added by the DC conductivity (figures 4.62 (a & b)). The conductivity relaxation peaks in the dielectric permittivity loss spectra masks by the strong d c ionic conductivity due to ion hopping. This difficulty can be overcome by analysing the data in modulus representation and the loss peaks are clearly visible in modulus spectra (figures 4.64 (a & b) and 4.65). The f_{max} of M" (ω) peaks were higher in several decades than the real and imaginary components of the dielectric permittivity. It can be seen that the spectra ($M''(\omega)$) above T_g reveal a prominent conductivity relaxation peak which moves towards higher frequencies with the increase in temperature and at lower frequencies the peaks due to translational motion of mobile ions were observed similar to most of the molecular liquids. The relaxation peak breadth increases with increase in temperature. An asymmetric and broader relaxation peaks than the classical Debye shape were found.[105-106]

Secondary relaxation spectra (β) of ranitidine docusate below the glass transition temperature (T_g) in permittivity representation and modulus representation were observed from 123 K to 309 K in the figures 4.62 (b), 4.64 (b) and 4.65. Below T_g, this relaxation process is clearly visible both in ε'' and M''. Below T_g the sample turn into glassy state where the translational motions of ions become low and the peaks move toward low frequencies with decrease in temperature, but its breadth become high for highest temperature. The real part of the conductivity $\sigma'(\omega)$ signifying the charge transport can be documented as a plateau on the low-frequency side in $\sigma'(\omega)$ vs frequency graph (Figure 4.63 (a)) , the dispersion sets in and turns into a power law towards higher frequency side. $\sigma''(\omega)$ as shown in figure 4.63 (b) observed no relevant information. The dielectric response of the IL was further investigated in detail by the J. Dyre's random barrier model and the fit parameters are shown in table 4.10.[94,163]

a) b)

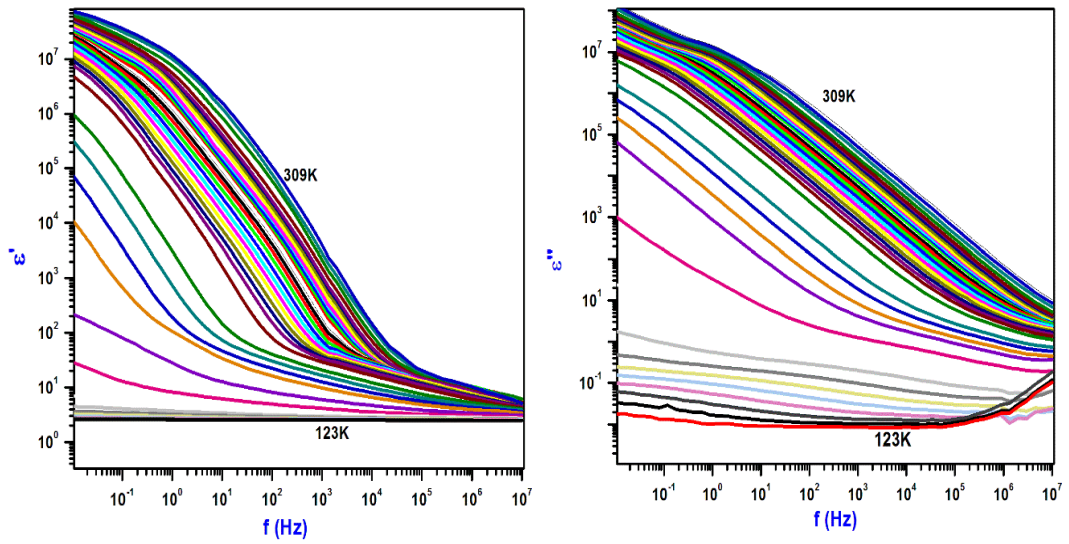

Figure 4.62. Frequency dependence of real part **(a)** ε′ (ω) and **(b)** imaginary part ε′′ (ω) at different temperatures for the sample ranitidine docusate IL.

a) b)

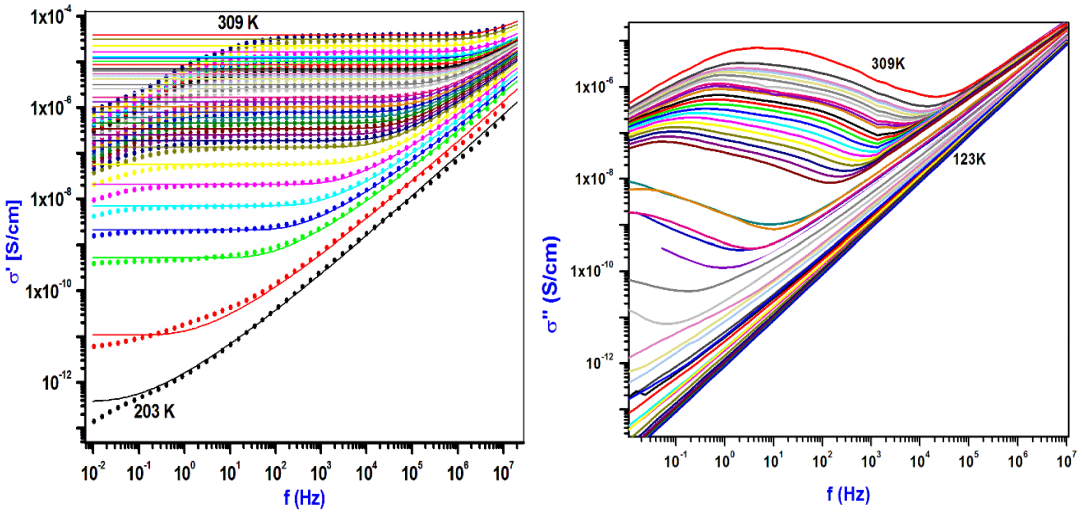

Figure 4.63. Frequency dependence of **(a)** the real part σ′ (ω) and **(b)** imaginary part σ′′ (ω) at different temperatures for the sample ranitidine docusate IL.

a) b)

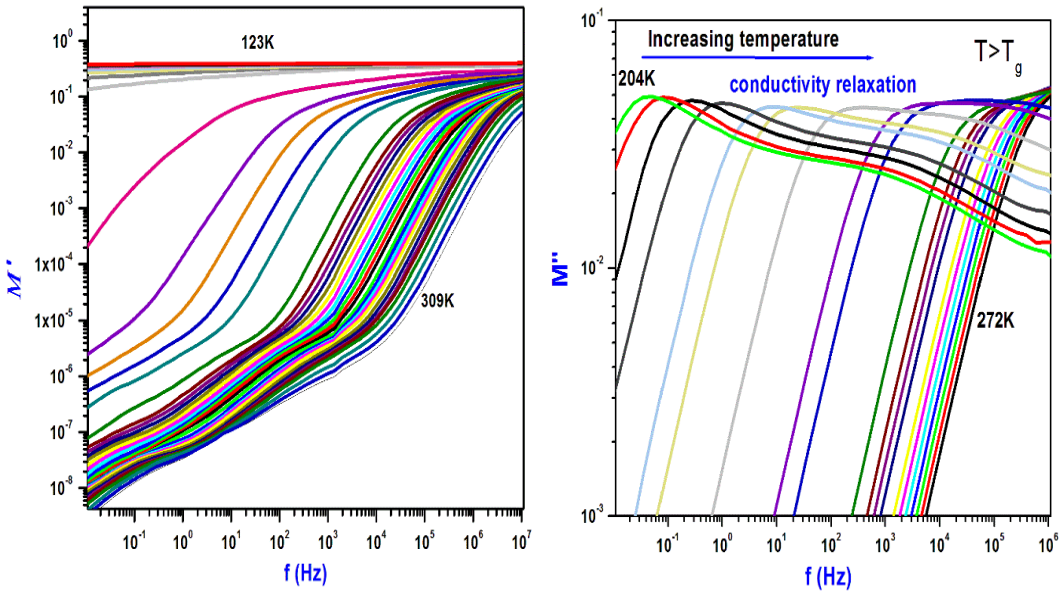

Figure 4.64. Frequency dependence of (a) the real part M′ (ω) and (b) the imaginary part M′′ (ω) at different temperatures for the sample ranitidine docusate IL.

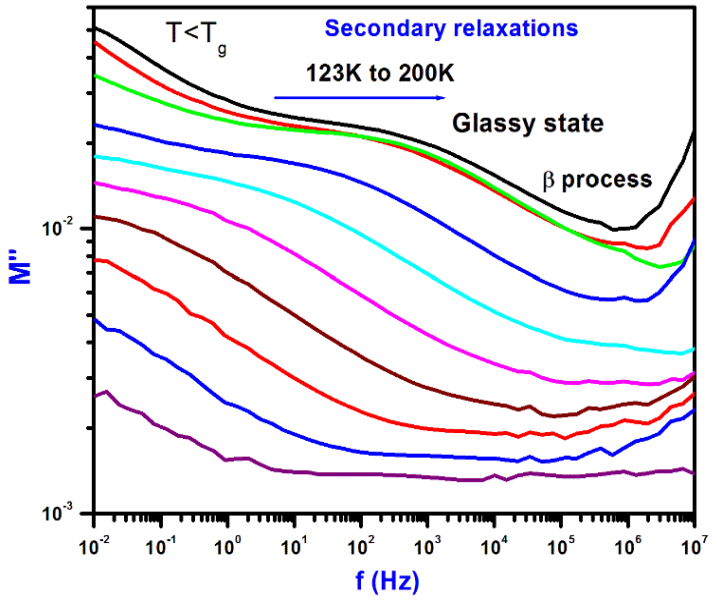

Figure 4.65. F vs M′′ (ω) at temperatures 123 K to 200 K for ranitidine docusate IL.

Table 4.10. *Fit parameters of ranitidine docusate to Dyre equation.*

T (K)	σ_0 (S/cm)	τ_e (s)
2.03E+02	3.82E-13	7.42E+00
2.28E+02	2.08E-09	1.75E-03
2.43E+02	5.75E-08	6.27E-05
2.52E+02	2.56E-07	1.38E-05
2.58E+02	6.11E-07	6.03E-06
2.64E+02	1.32E-06	2.78E-06
2.70E+02	2.58E-06	1.33E-06
2.77E+02	4.89E-06	6.24E-07
2.83E+02	7.00E-06	3.69E-07
2.92E+02	1.20E-05	1.85E-07
2.94E+02	1.30E-05	1.62E-07

From table. 4.10, it can be noted that σ_0 (the d c conductivity) increases with increase in temperature, but τ_e (the electrical relaxation time) decreases with increase in temperature.[2] Temperature dependence data represent a VFT behaviour to (τ_e), (τ_M) and a good resemblance found to Dyre fit data (τ_e) and HN equation fit data (τ_M) above T_g as shown in figure 4.66 (a). Below the glass transition temperature, 123 K to 200 K dielectric data were fitted with Cole–Cole function and the Arrhenius dependence was attained. The temperature dependence of the secondary relaxations (below T_g,), log τ vs 1000/T was plotted and with temperature dependent activation energy was obtained by fitted with Arrhenius law. The VFT fitting parameters of ranitidine docusate are given in table 4.11. E_β is the activation energy of the IL. Plot of log σ (S/cm) vs 1000/T of ranitidine docusate is shown with a slight non Arrhenius behaviour. As we can see in figure 4.66 (b) that conductivity relaxation time (τ_σ) increases with lowering temperature towards T_g and an anti-correlation was observed for DC conductivity ($\sigma_{d\ c}$). The type of secondary relaxation in ranitidine docusate is identified by K.L Ngai's coupling

model, he found that τ_{JG} (T,P) = τ_{CM} (T,P), i.e. the primitive relaxation is nothing but the JG relaxation. In ranitidine docusate τ_{JG} and τ_{CM} were nearly same.[98-99]

Table 4.11. *The fit parameters of ranitidine docusate to VFT and KWW functions.*

Sample	log τ_0 (s)	D	T_0 (K)	T_g (BDS) (K)	Fragility (m)	E_β (kJ/mol)	β_{KWW}
Ranitidine docusate	11 ±0.81	11± 0.41	145± 0.28	196	56	71± 0.02	0.43

a) b)

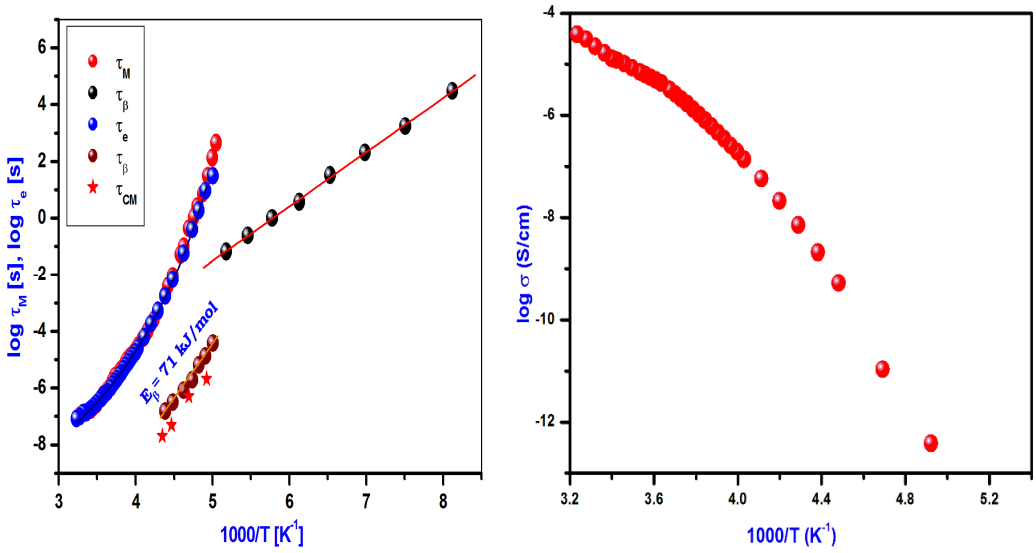

Figure 4.66. (a). Plot of log τ (s) vs 1000/T of ranitidine docusate. (τ_M as obtained from the maximum in $M''(\omega)$, τ_e as taken from Dyre equation.) & **(b)** plot of log σ (S/cm) vs 1000/T.

Materials were classified as 'fragile glass former' if their temperature dependence of τ_σ obviously deviates from the Arrhenius behaviour characterized by temperature-dependent activation energy and 'strong glass former' if it indicates Arrhenius type of relationship, with activation energy independent of temperature. The degree of deviation from Arrhenius-type temperature dependence near the glass

transition is apparent at the slope of log (τ) vs T_g/T plot. The Angell plot log (τ) vs (T_g/T) for two ILs were drawn as shown in figure 4.67 (a). For a strong glass former the plot shows Arrhenius behavior. To anticipate the recrystallization tendency of the amorphous drug and reflecting the stability of a liquid structure to temperature changes in the supercooled state, it is beneficial to calculate the value of the steepness index (m). Fragile glass formers considered as less stable than strong one, along with fragile antibiotics should reveal great ease of crystallization. Hereafter, fragility has a key aspect in choosing the best temperature condition for storing amorphous pharmaceutical. From the results ranitidine docusate categorise as a strong glass former.[74-75, 105,125]

a) b)

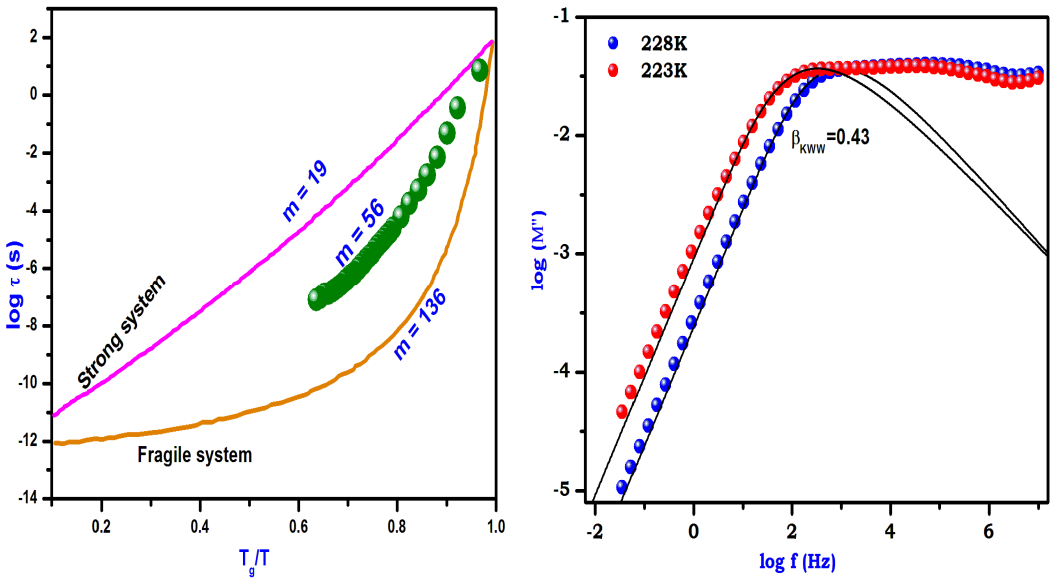

Figure 4.67 (a). Plot of log τ(s) vs T_g/T of ranitidine docusate and **(b)** frequency dependence of the dielectric loss spectra of ranitidine docusate. The black solid line represents the KWW fit with $\beta_{KWW} = 0.43$**.**

Frequency dependence of imaginary part M'' (ω) of ranitidine docusate is shown in figure 4.67 (b). On fitting the data of ranitidine docusate, we got a value of n of KWW to be 0.45 for conductivity relaxation process around the glass transition temperature corresponding to tau = 100 s.

4.1.9. Thermal and broadband dielectric spectroscopic analysis of lidocaine docusate

4.1.9.1. Thermogravimetric analysis

Thermal stability of the IL lidocaine docusate is measured with TGA in an interval of 300 K–900 K and the weight loss of the IL was shown in figure 4.68 (a). It can be found that up to 373 K the IL is thermally stable. Hence, the pharmaceutical sample is efficient for drug delivery system.

4.1.9.2. Differential scanning calorimetry analysis

DSC response of lidocaine docusate at a heating rate of 10 K /min. from 123 K to 300 K is offered in figure. 4.68 (b) and the transition displayed a glass transition temperature of 199.41 K. There is no crystallisation and hence melting peaks are observed in this IL.

a) b)

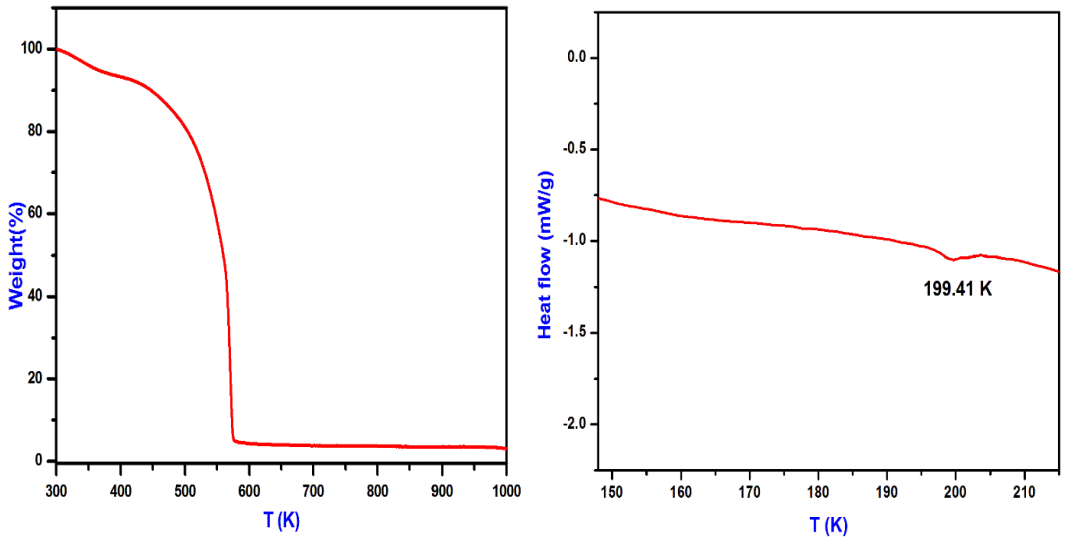

Figure 4.68. (a) TGA plot & (b) DSC curve of lidocaine docusate

4.1.9.3. Broadband dielectric spectroscopic analysis

Dielectric spectra of lidocaine docusate from deep glassy state to the room temperature is collected and presented in permittivity representation, conductivity

representation and modulus representation at ambient pressure as a function of frequency over a range of temperatures 123.15 K to 309.15 K are shown in the figures 4.69 (a & b), 4.70 (a & b), 4.71 (a & b) and 4.72 (a & b) in two panels (above T_g) and (below T_g). The electric modulus formalism permitted to resolve the relaxation process intensely masked by DC conductivity in permittivity representation in the figures 4.71 (a & b) and 4.72. Data depicted in figure describes a well pronounced conductivity relaxation peak in modulus representation above T_g, which moves towards low frequencies with decreasing temperature. Conductivity relaxation peaks found were broader than the classical Debye response. Below T_g conductivity relaxation became too slow and secondary relaxations were clearly visible. Besides conductivity relaxation and multiple relaxation process (two secondary relaxation process β relaxation and γ relaxation) were observed in lidocaine docusate spectra (permittivity and modulus formalism). The slowest one was labelled as β, which is broad and well defined below T_g and its amplitude increased with increase in temperature. The new additional secondary relaxation process is appeared at the lowest temperatures and herein was labelled as γ process. Similar relaxation mode was observed for Tramadol monohydrate, lidocaine HCl water mixtures and Telmisartan.[65,104]

Particular information on the ion dynamics from the plot of frequency vs σ' of lidocaine docusate are presented in figure 4.70 (a). Ionic conductivity can be expressed as $\sigma = \omega\varepsilon_0\,\varepsilon''(\omega)$, where ε_0 denotes the permittivity of vacuum. The frequency independent parameter DC conductivity (σ_0) represented by a plateau at lower frequencies and a power law behaviour shown at higher frequencies. At higher temperatures power law behaviour vanishes for the IL. At low temperatures, the high-frequency conductivity σ'' (ω) can be approached to a straight line (in figure 4.70 (b)). The dielectric response of lidocaine docusate was further explored in detail by the J. Dyre's random barrier model and the fit parameters are shown in table 4.12. It is revealed that σ_0 (the DC conductivity) increases with increase in temperature, but τ_e (the conductivity relaxation time) presented an anti-correlation with temperature.

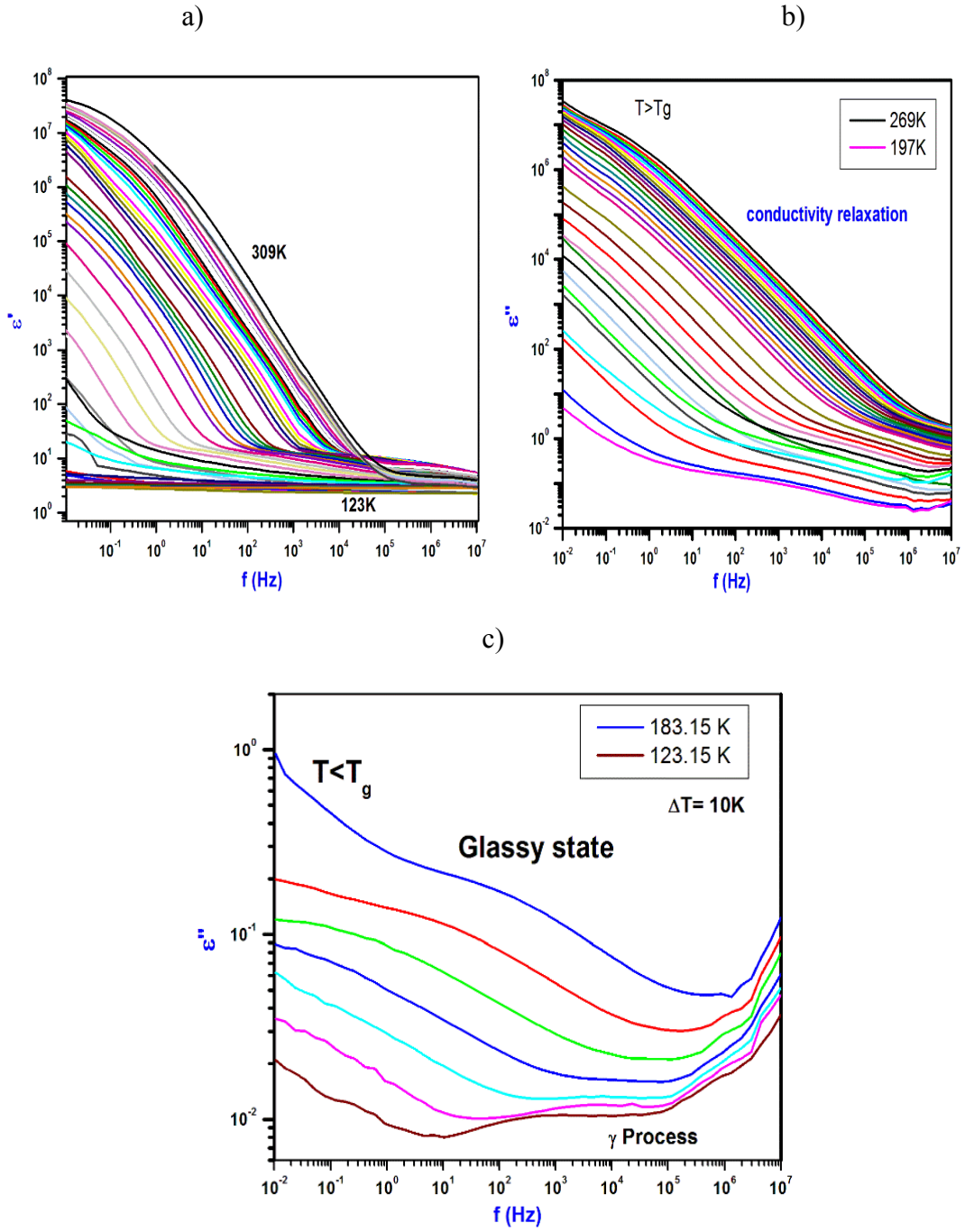

Figure 4.69. Frequency dependence of **(a)** real part ε′ (ω) and (b, c) represents the imaginary part ε′′ (ω) at different temperatures for the sample lidocaine docusate IL.

a) b)

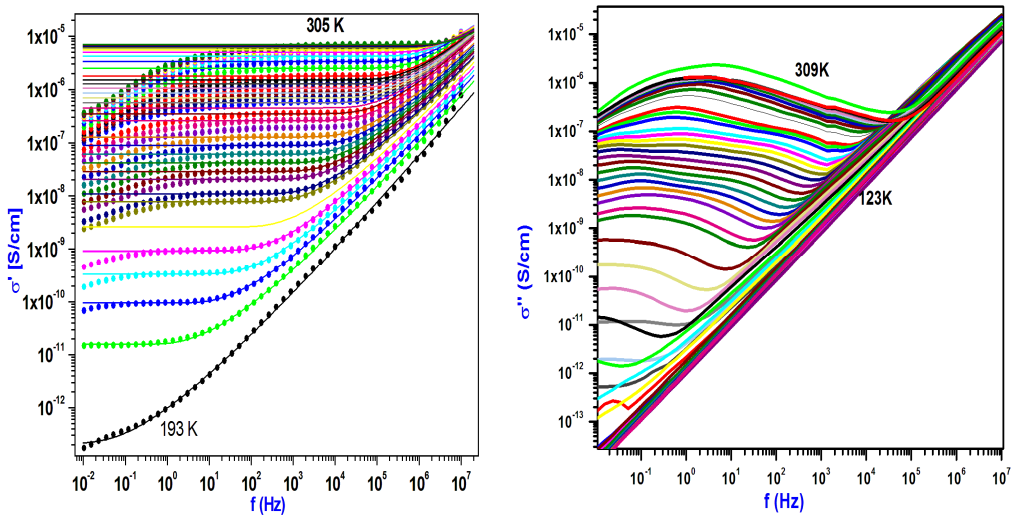

Figure 4.70. Frequency dependence of (a) the real part σ′ (ω) and (b) represents the imaginary part σ′′ (ω) at different temperatures for the sample lidocaine docusate IL.

a) b)

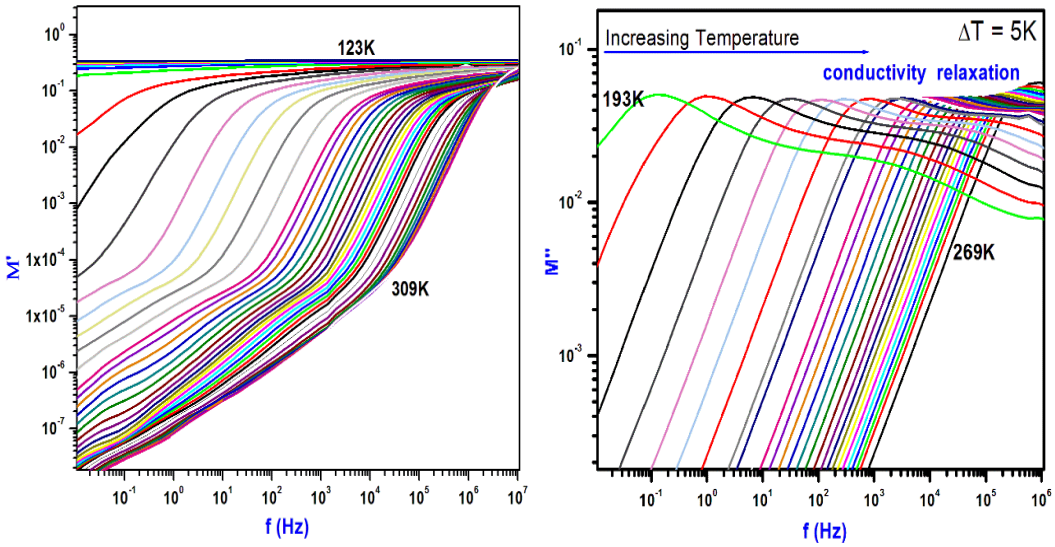

Figure 4.71. Frequency dependence of (a) the real part M′ (ω) and (b) the imaginary part M′′ (ω) at different temperatures for the sample lidocaine docusate IL.

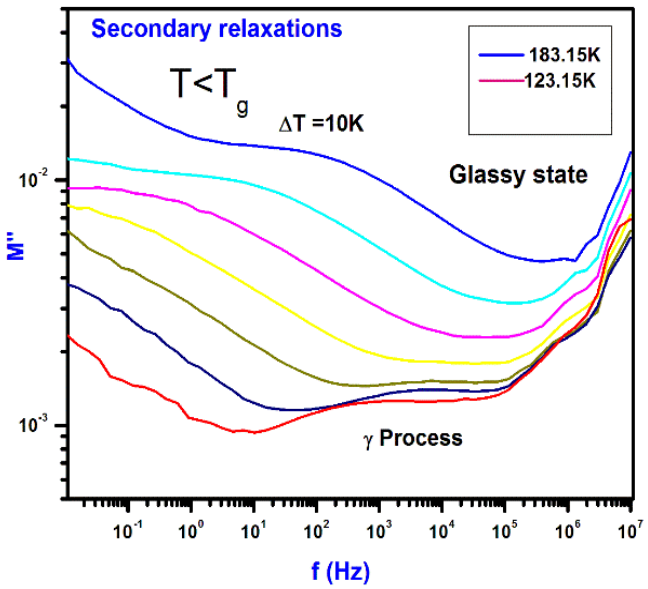

Figure 4.72. Frequency dependence of the imaginary part M′′ (ω) at temperatures 123 K to 183 K for the sample lidocaine docusate IL.

***Table 4.12**. Fit parameters of lidocaine docusate to Dyre equation.*

T (K)	σ_0 (S/cm)	τ_e (s)
2.08E+02	9.49E-11	2.16E-02
2.23E+02	2.62E-09	8.41E-04
2.33E+02	2.04E-08	1.11E-04
2.39E+02	6.10E-08	3.75E-05
2.45E+02	1.84E-07	1.28E-05
2.51E+02	4.51E-07	5.13E-06
2.57E+02	8.63E-07	2.48E-06
2.63E+02	1.52E-06	1.25E-06
2.73E+02	3.33E-06	4.40E-07
2.85E+02	5.57E-06	1.56E-07
2.97E+02	6.76E-06	7.40E-08
3.05E+02	7.02E-06	5.21E-08

The temperature dependence of the relaxation time for conductivity relaxation of lidocaine docusate shows deviation from the Arrhenius behaviour being explained by VFT equation, which is widely used to fit the conductivity data

of the glass-forming ionic liquids. The VFT fitting parameters of lidocaine docusate IL are given in table 4.13. E_β and $E\gamma$ are the activation energies of the IL. The results are shown in figure 4.73 (a). The data from Dyre fit (τ_e) and HN equation fit (τ_M) show good agreement results above T_g. The temperature dependence of the secondary relaxations (below T_g,) of two ILs reveal a linear dependence with temperature dependent activation energy when log τ vs 1000/T was plotted and it can be fitted with Arrhenius law.

a) b)

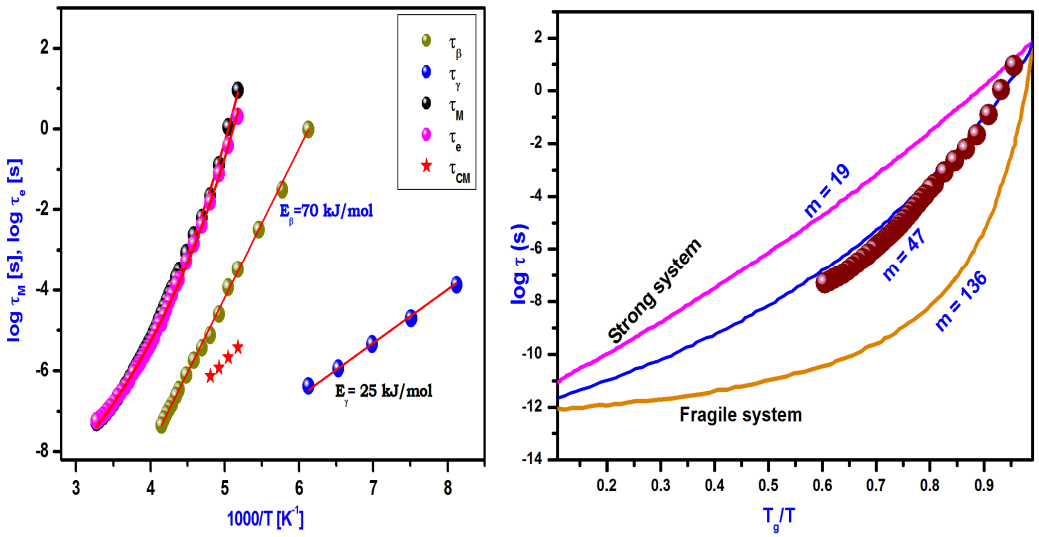

Figure 4.73. (a) The temperature dependence of the conductivity relaxation time and β relaxation time of lidocaine docusate. (τ_M as obtained from the maximum in M'' (ω), τ_e as taken from Dyre equation.) and **b**) Angell plot (log (τ) vs T_g/T) - the relaxation times of lidocaine docusate as a function of normalized temperature above T_g.

Table 4.13. *The fit parameters of lidocaine HCl and lidocaine docusate to VFT and KWW functions.*[89]

Sample	log τ_0 (s)	D	T_0 (K)	T_g (BDS) (K)	Fragility (m)	E_β (kJ/mol)	$E\gamma$ (kJ/mol)	β_{KWW}
Lidocaine Hcl	15± 0.45	13± 1.26	218± 3.86	307	51	58±3.2	22±0.23	0.64
Lidocaine docusate	12± 0.11	16± 0.03	124± 0.54	184	47	70±0.13	25±0.81	0.45

The Angell plot log (τ) vs (T_g/T) for lidocaine docusate is drawn as shown in figure 4.73 (b). For a strong glass former the plot shows Arrhenius behaviour. To anticipate the recrystallization tendency of the amorphous drug and reflecting the stability of a liquid structure to temperature changes in the super cooled state, it is beneficial to calculate the value of the steepness index (m). Fragile glass formers are considered as less stable than strong one, along with fragile antibiotics should reveal great ease of crystallization. Hereafter, fragility has a key aspect in choosing the best temperature condition for storing amorphous pharmaceutical. For the pharmaceutical field the value of m concerns the stability of amorphous drug. Strong glass formers are expected to be more physically stable than fragile with stability against temperature fluctuations.[105,125]

To perspective, the whole set of measured data within one figure dielectric data are presented as ‘‘master plot” in which a number of dielectric curves measured at different temperatures (both above and below Tg) have been superimposed. The master plot obtained is presented in figure 4.74 (a). Frequency dependence of imaginary part M'' (ω) of lidocaine docusate is shown in figure 4.74 (b). On fitting the data, we got a value of n of KWW to be 0.45 for conductivity relaxation process around the glass transition temperature corresponding to tau = 100 s. It can be anticipated that the value of $\beta_{KWW} = 0.45$ is less than 1 for lidocaine docusate. Hence the relaxation process seems to be non–Debye type relaxation.

a) b)

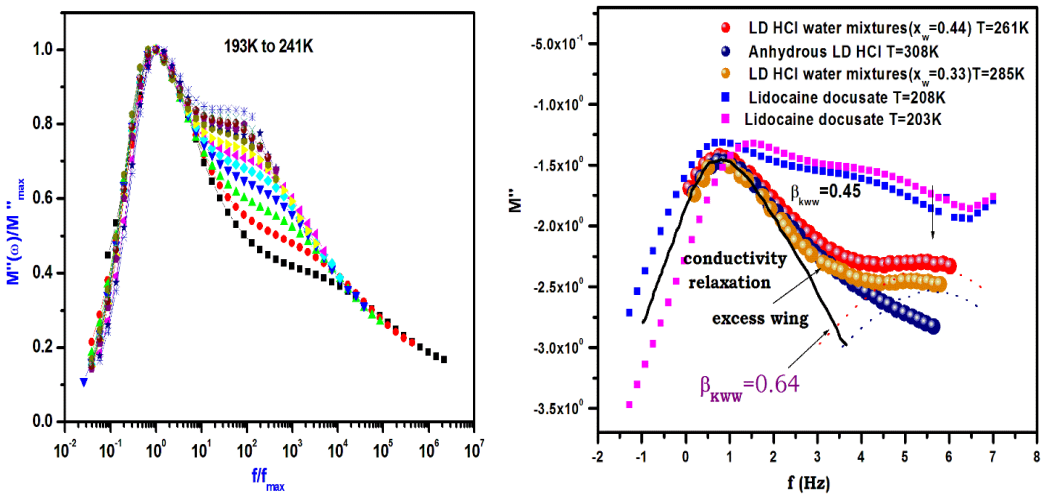

Figure 4.74. (a) Superimposed imaginary spectra in modulus formalism and **(b)** frequency dependence of $M''(\omega)$ of lidocaine docusate.[89]

4.2. VIBRATIONAL ANALYSIS

4.2.1. Experimental characterisation

4.2.1.1. Fourier transform Infrared spectroscopy (FT−IR)

The observed experimental FT–IR spectra of $[P_{14,6,6,6}][NTf_2][Cl]$, $[P_{14,6,6,6}]$ [N(CN)2] [Cl], PVA $[P_{14,6,6,6}]$[NTf2] ionogel and PVA $[P_{14,6,6,6}][N(CN)_2]$ ionogel are shown in figure 4.75 (a) & (b) and 4.76 (a) & (b) respectively. The results are listed in tables 4.14 & 4.15 respectively. Figure 4.77 (a & b) represent the experimental FT–IR spectra of ranitidine docusate and lidocaine docusate respectively. The resulting experimental vibrational frequencies of ranitidine docusate and lidocaine docusate for IR intensities are presented in table 4.16. The peak values are in agreement with the literature data in all ionic liquids used in the present study.

a) b)

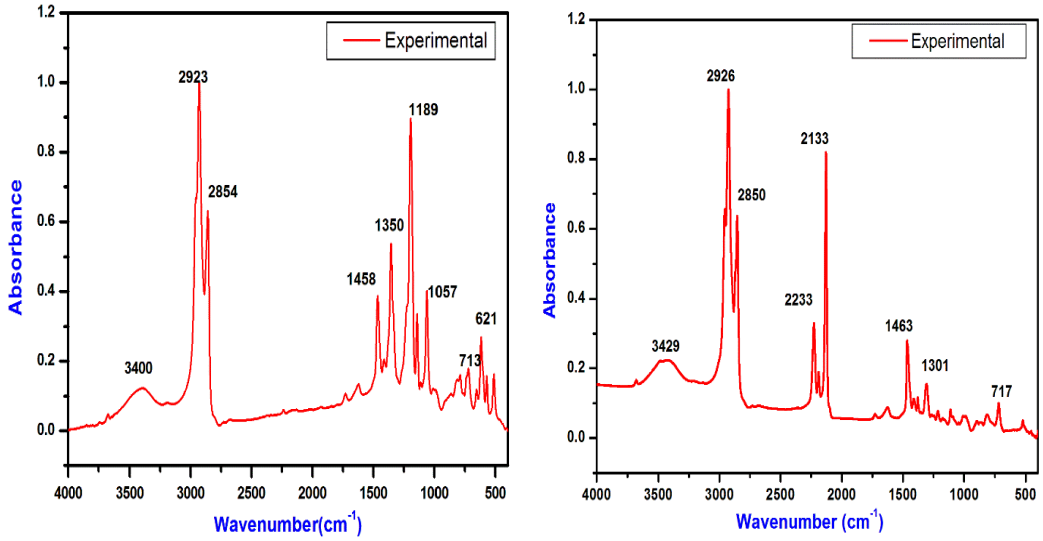

Figure 4.75. Experimental FT–IR spectra of **(a)** $[P_{14,6,6,6}][NTf_2][Cl]$ **(b)** $[P_{14,6,6,6}][N(CN)_2][Cl]$.

Table 4.14. *Experimental values of FT–IR spectra of* $[P_{14,6,6,6}][NTf_2][Cl]$ *&* $[P_{14,6,6,6}][N(CN)_2][Cl]$.

Spectra	Sample	Experimental value (cm^{-1})	Bond assigned
IR	$[P_{14,6,6,6}][NTf_2][Cl]$	3407	O-H stretching
		2923	C-H stretching
		2854	C-H stretching
		1458	C-H bending
		1350	C-H bending
		1189	C-C stretching
		1057	C-C stretching
	$[P_{14,6,6,6}][N(CN)_2][Cl]$	3429	O-H stretching
		2926	C-H stretching
		2850	C-H stretching
		2233	C-N stretching
		2133	C=C stretching
		1463	C-H bending
		1301	C-C stretching

a) b)

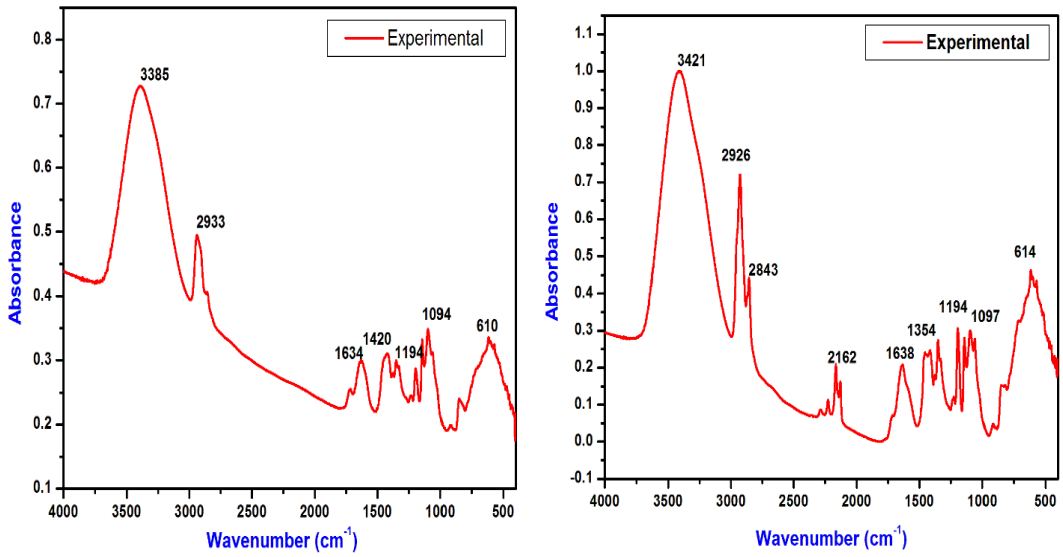

Figure 4.76. Experimental FT–IR spectra of **(a)** PVA– $[P_{14,6,6,6}][NTf_2]$ ionogel (**b)** PVA– $[P_{14,6,6,6}][N(CN)_2]$ **)** ionogel.

Table 4.15. *Experimental values of FT –IR spectra of PVA– $[P_{14,6,6,6}][NTf_2]$ and PVA– $[P_{14,6,6,6}][N(CN)_2]$.*

Spectra	Sample	Experimental value (cm^{-1})	Bond assigned
IR	**PVA–$[P_{14,6,6,6}][NTf_2]$**	3385	O-H stretching
		2933	C-H stretching
		1634	C=O stretching
		1420	C-H bending
		1194	C-C stretching
		1094	C-C stretching
	PVA–$[P_{14,6,6,6}][N(CN)_2]$	3421	O-H stretching
		2926	C-H stretching
		2162	C-N stretching
		1638	C=O stretching
		1354	C-H bending
		1194	C-C stretching
		1097	C-O stretching

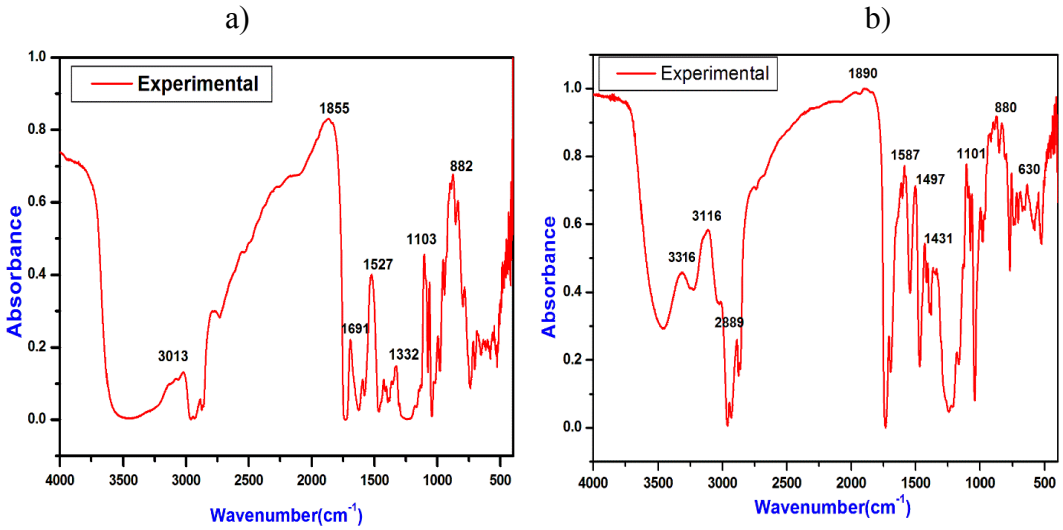

Figure 4.77. FT–IR spectra of **(a)** ranitidine docusate IL and **(b)** lidocaine docusate IL

Table 4.16. *Experimental values of FT–IR spectra of* ranitidine docusate and lidocaine docusate.

Spectra	Sample	Experimental value (cm^{-1})	Bond assigned
IR	**Ranitidine docusate**	3013	N-H stretching
		1855	C=O stretching
		1691	C=C stretching
		1527	C=O stretching
		1332	C-H bending
		1103	C-C stretching
		882	C-C stretching
	Lidocaine docusate	3317	N-H stretching
		3116	C-H stretching
		2889	C-H stretching
		2771	C-H stretching
		1890	C=O stretching
		1587	C=O stretching
		1497	C-H bending
		1431	C-H bending
		1101	C-C stretching
		880	C-C stretching

4.2.1.2 Fourier transform Raman spectroscopy (FT–Raman)

The observed experimental FT–Raman spectra of $[P_{14,6,6,6}][NTf_2][Cl]$ and $[P_{14,6,6,6}][N(CN)_2][Cl]$ ionogels are shown in figure 4.78 (a & b) respectively. The

results are listed in table 4.17. The figure 4.79 (a & b) represent the experimental FT –Raman spectra of PVA–$[P_{14,6,6,6}][NTf_2]$ and PVA–$[P_{14,6,6,6}][N(CN)_2]$ respectively. The resulting experimental vibrational frequencies of PVA–$[P_{14,6,6,6}][NTf_2]$ and PVA–$[P_{14,6,6,6}][N(CN)_2]$ for IR intensities are presented in table 4.18.

a) b)

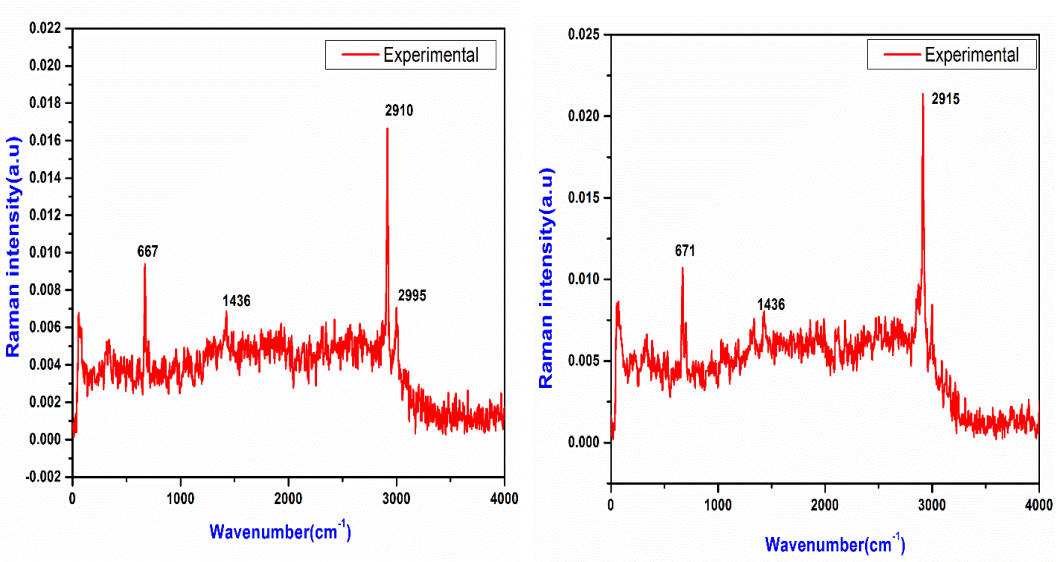

Figure 4.78. Experimental FT–Raman spectra of (a) $[P_{14,6,6,6}][NTf_2][Cl]$ & **(b)** $[P_{14,6,6,6}][N(CN)_2][Cl]$

Table 4.17. *Experimental values of FT –Raman spectra of* $[P_{14,6,6,6}][NTf_2][Cl]$ *and* $[P_{14,6,6,6}][N(CN)_2][Cl]$.

Spectra	Sample	Experimental value (cm^{-1})	Bond assigned
Raman	**$[P_{14,6,6,6}][NTf_2][Cl]$**	2995	C-H stretching
		2910	C-H stretching
		1436	C-H bending
	$[P_{14,6,6,6}][N(CN)_2][Cl]$	2915	C-H stretching
		1436	C-H bending

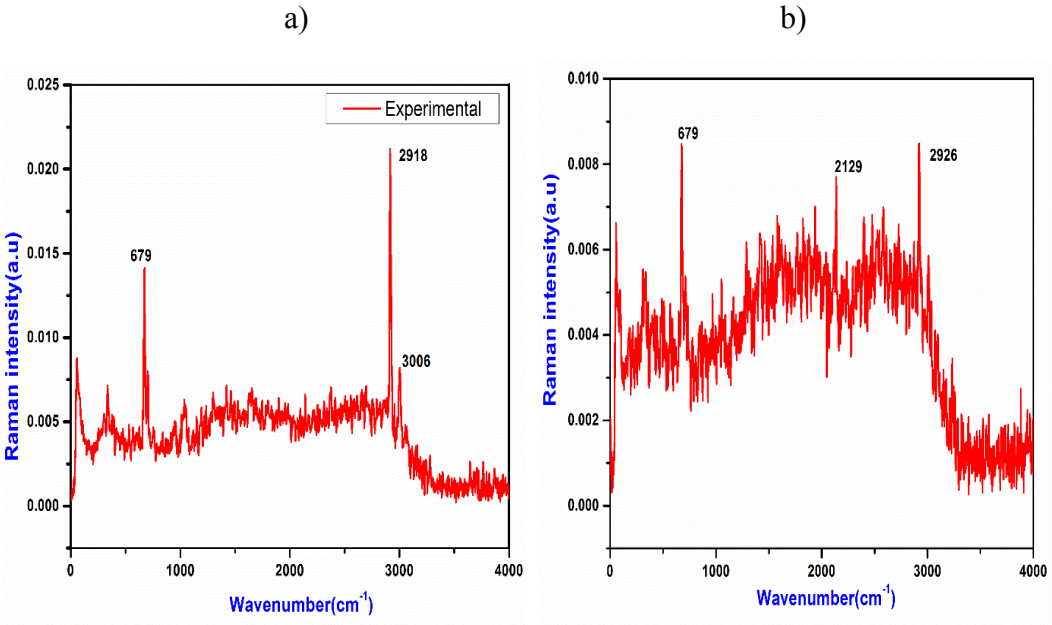

Figure 4.79. (a) Experimental FT–Raman spectra of PVA– $[P_{14,6,6,6}][NTf_2]$ and **(b)** PVA– $[P_{14,6,6,6}][N(CN)_2]$ ionogel.

Table 4.18. *Experimental values of FT –Raman spectra of PVA– $[P_{14,6,6,6}][NTf_2]$ and PVA– $[P_{14,6,6,6}][N(CN)_2]$.*

Spectra	Sample	Experimental value (cm^{-1})	Bond assigned
Raman	**PVA– $[P_{14,6,6,6}][NTf_2]$**	3006	C-H stretching
		2916	C-H stretching
	PVA–$[P_{14,6,6,6}][N(CN)_2]$	2926	C-H stretching
		2129	C-N stretching

FT–Raman spectra of ranitidine docusate and lidocaine docusate allowed us to detect the changes in the structural properties of the samples. The figures 4.80 (a &b) represent the experimental FT–Raman spectra of ranitidine docusate and lidocaine docusate respectively. The resulting experimental vibrational frequencies

of ranitidine docusate and lidocaine docusate for Raman intensities are presented in table 4.19.

a) b)

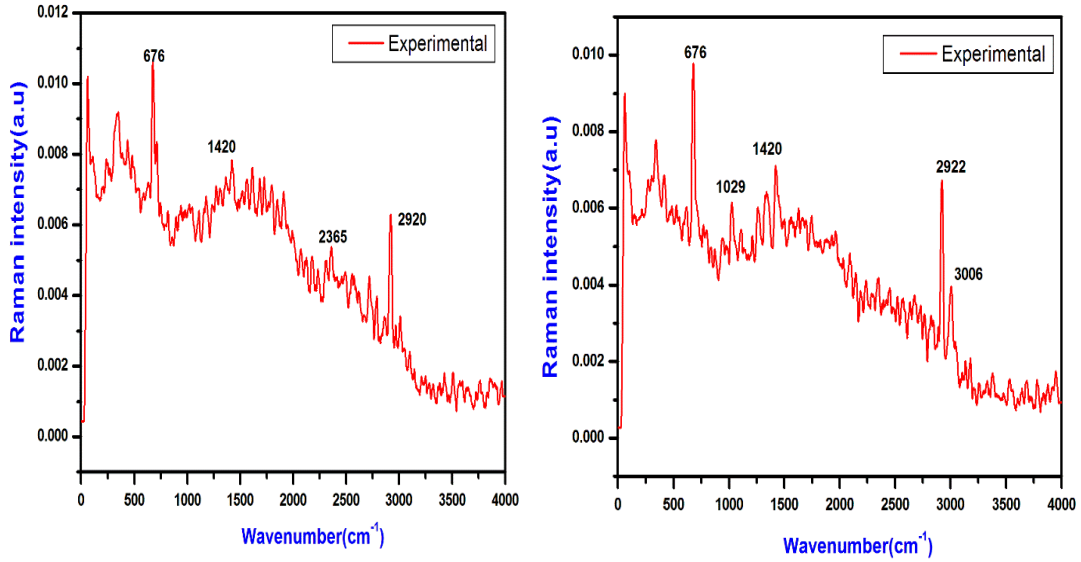

Figure 4.80. FT–Raman spectra of **(a)** ranitidine docusate and (**b)** lidocaine docusate.

Table 4.19. *FT –Raman spectra results of ranitidine docusate and lidocaine docusate*.

Spectra	Samples	Experimental value (cm^{-1})	Bond assigned
		2920	C-H stretching
	ranitidine	2365	C-H stretching
	docusate	1420	C-H bending
Raman		3006	C-H stretching
		2922	C-H stretching
	lidocaine	1420	C-H bending
	docusate	1029	C-O stretching

4.2.2. Computational characterization

4.2.2.1. Fourier transform Infrared (FT−IR) spectroscopy

Figures 4.81 (a), (b) and (c) and 4.82 (a & b) show the FT−IR (theoretical) spectra of $[P_{14,6,6,6}][NTf_2]$ IL, $[P_{14,6,6,6}][N(CN)_2]$, $[P_{14,6,6,6}][Cl]$, ranitidine docusate and lidocaine docusate in the range from 400 to 3500 cm^{-1} and the peaks are presented in table 4.20 and 4.21. The results show that theoretical value and experimental value got a good agreement result.

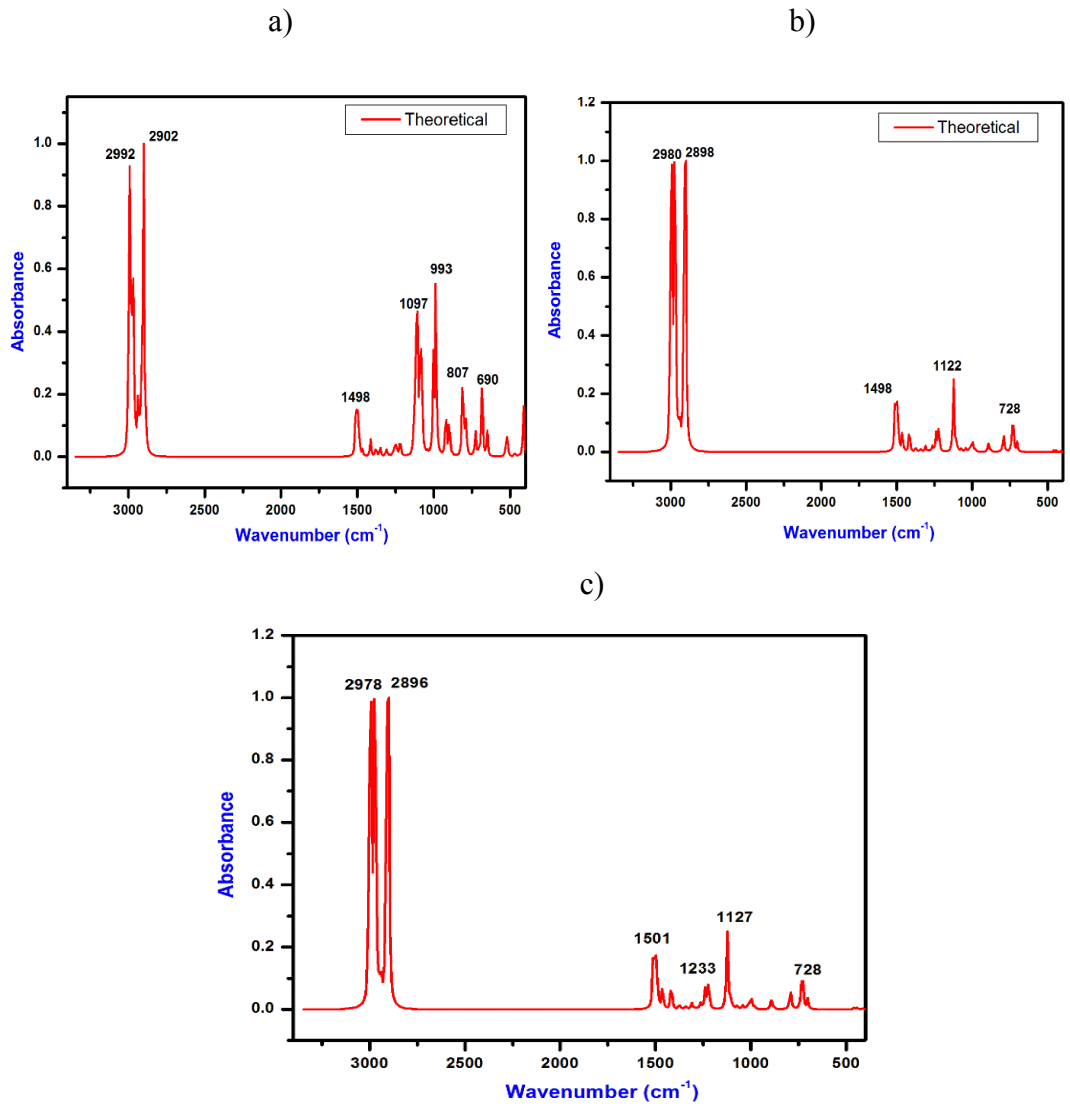

Figure 4.81. Theoretical FT−IR spectra of **(a)** $[P_{14,6,6,6}][NTf_2][Cl]$, **(b)** $[P_{14,6,6,6}][N(CN)_2][Cl]$ and $[P_{14,6,6,6}][Cl]$ IL.

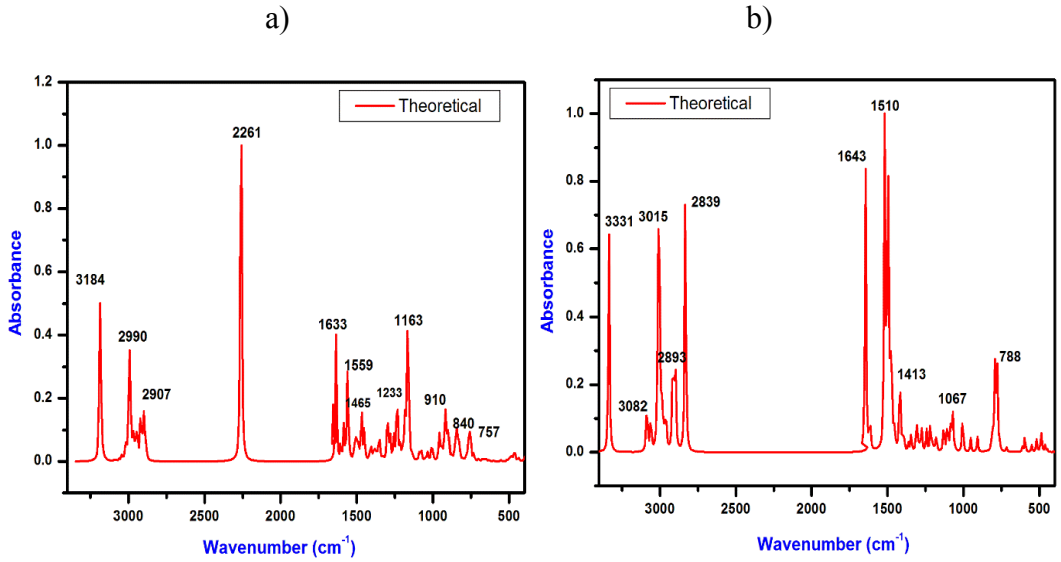

Figure 4.82. Theoretical FT–IR spectra of **(a)** ranitidine docusate, (**b**) lidocaine docusate.

Table 4.20. *Theoretical values of FT–IR spectra of* $[P_{14,6,6,6}][NTf_2][Cl]$, $[P_{14,6,6,6}][N(CN)_2][Cl]$, and $[P_{14,6,6,6}][Cl]$ ILs.

Spectra	Sample	Theoretical value (cm^{-1})	bond assigned
IR	**$[P_{14,6,6,6}][NTf_2][Cl]$**	2992	C-H stretching
		2902	C-H stretching
		1498	C-H bending
		1104	C-C stretching
		993	C-C stretching
		807	P-C stretching
	$[P_{14,6,6,6}][N(CN)_2][Cl]$	2980	C-H stretching
		2898	C-H stretching
		1498	C-H bending
		1122	C-C stretching
		728	P-C stretching
	$[P_{14,6,6,6}][Cl]$	2978	C-H stretching
		2896	C-H stretching
		1501	C-H bending
		1233	C-C stretching
		1127	C-C stretching
		728	P-C stretching

Table 4.21. *Theoretical values of FT–IR spectra of ranitidine docusate and lidocaine docusate.*

Spectra	Sample	Theoretical value (cm^{-1})	Bond assigned
IR	ranitidine docusate	3184	C-H stretching
		2990	C-H stretching
		2907	C-H stretching
		2261	C≡C stretching
		1633	C=O stretching
		1559	C=O stretching
		1465	C-H bending
		1233	C-C stretching
		1163	C-C stretching
	lidocaine docusate	3331	O-H stretching
		3082	C-H stretching
		3015	C-H stretching
		2893	C-H stretching
		2839	C-H stretching
		1643	C=O stretching
		1510	C-H bending
		1413	C-H bending
		1067	C-O stretching

4.2.2.2. Fourier transform Raman spectroscopy (FT–Raman).

Theoretical FT–Raman spectra of $[P_{14,6,6,6}][NTf_2][Cl]$, $[P_{14,6,6,6}][N(CN)_2][Cl]$ and $[P_{14,6,6,6}][Cl]$ are shown in figure 4.83 (a, b & c) and the results are presented in table 4.22. The results show that theoretical value and experimental value attained a good promising result.

a) b)

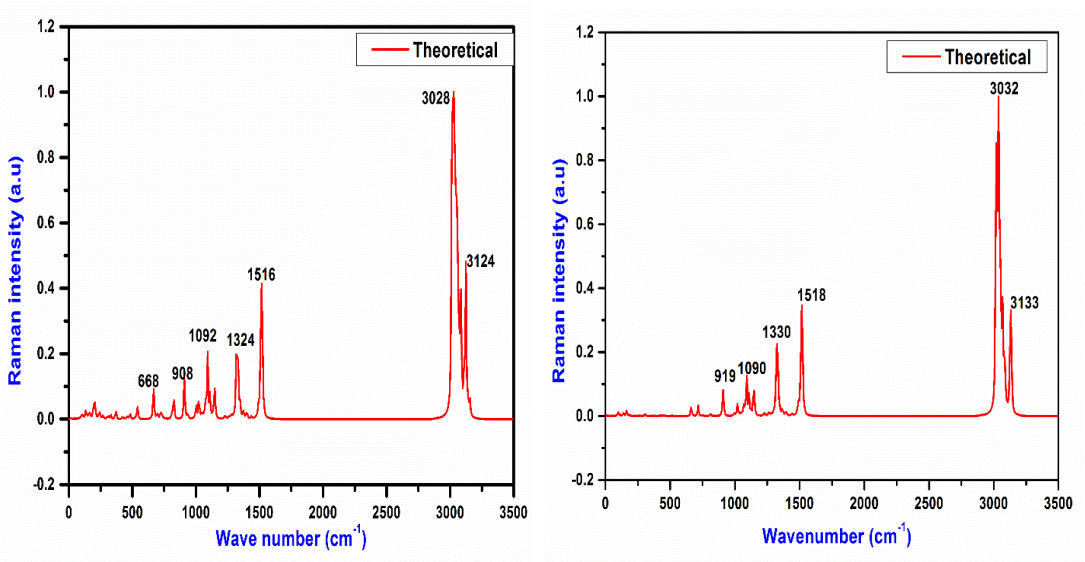

c)

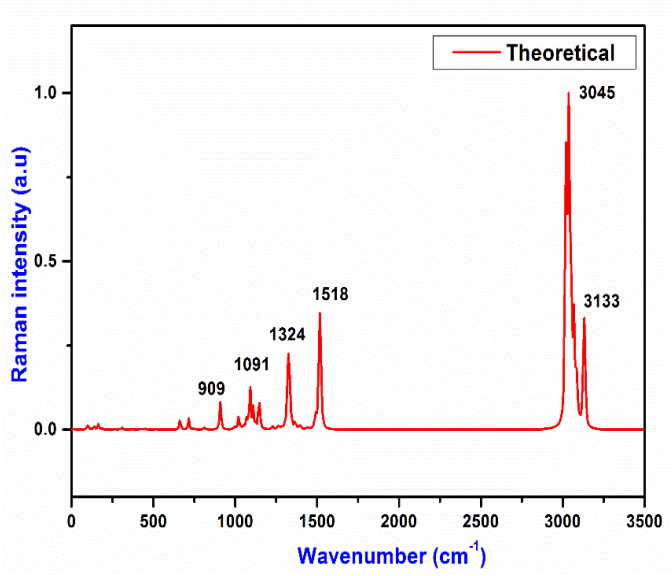

Figure 4.83. Theoretical FT−Raman spectra of **(a)** $[P_{14,6,6,6}][NTf_2][Cl]$, **(b)** $[P_{14,6,6,6}][N(CN)_2][Cl]$ and (c) $[P_{14,6,6,6}][Cl]$ IL.

Table 4.22. *Theoretical values of FT –Raman spectra of* $[P_{14,6,6,6}][NTf_2][Cl]$, $[P_{14,6,6,6}][N(CN)_2][Cl]$ *and* $[P_{14,6,6,6}][Cl]$.

Spectra	Sample	Theoretical value (cm^{-1})	Bond assigned
Raman	$[P_{14,6,6,6}][NTf_2][Cl]$	3124	C-H stretching
		3028	C-H stretching
		1516	C-H bending
		1324	C-C stretching
		1092	C-F stretching
	$[P_{14,6,6,6}][N(CN)_2][Cl]$	3133	C-H stretching
		3032	C-H bending
		1518	C-H bending
		1330	C-C stretching
		1090	C-F stretching
	$[P_{14,6,6,6}][Cl]$	3133	C-H stretching
		3045	C-H bending
		1518	C-H bending
		1324	C-C stretching
		1091	C-F stretching

a) b)

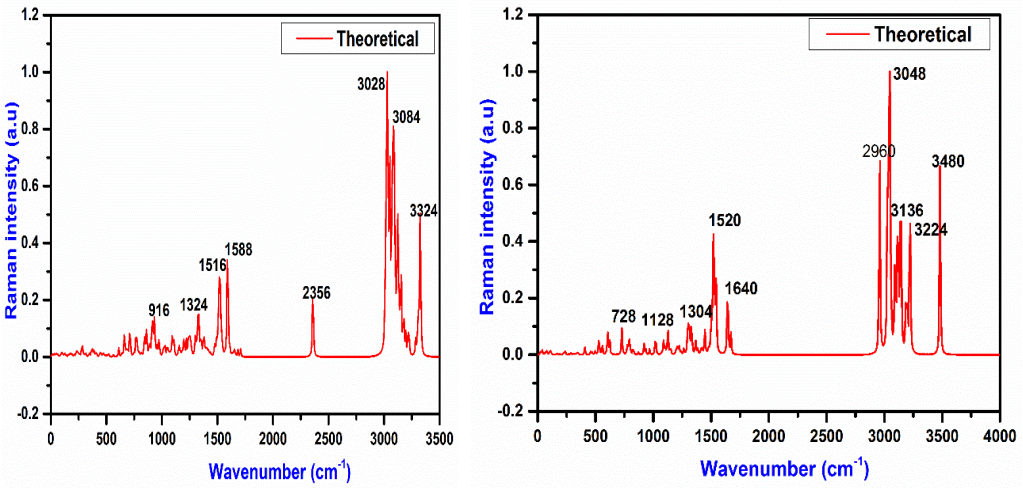

Figure 4.84 Theoretical FT–Raman spectra of **(a)** ranitidine docusate, (b) lidocaine docusate

Table 4.23. *Theoretical FT –Raman spectra of ranitidine docusate and lidocaine docusate.*

Spectra	Sample	Theoretical value (cm^{-1})	Bond assigned
RAMAN	**ranitidine docusate**	1324	C-C stretching
		1516	C-H bending
		1588	C=O stretching
		3028	C-H stretching
		3084	C-H stretching
		3324	N-H stretching
	lidocaine docusate	1128	C-C stretching
		1520	C=O stretching
		1640	C=C stretching
		2960	C-H stretching
		3048	C-H stretching
		3136	C-H stretching
		3224	N-H stretching
		3480	N-H stretching
			O-H stretching

Figures 4.84 (a & b) represent the theoretical FT–Raman spectra of ranitidine docusate and lidocaine docusate respectively. The resulting experimental vibrational frequencies of ranitidine docusate and lidocaine docusate are presented in table 4.23. The comparison study of experimental and theoretical studies of FT–IR and FT-Raman spectroscopy calculated to obtain vibrational frequencies of ionic

clusters of ILs have shown a good agreement result closely in all samples. Computational calculations of FT−IR and FT-Raman spectra of the above samples give a complete description of Molecular geometry and molecular vibrations.

4.3. ELECTROCHEMICAL ANALYSIS OF SUPERCAPACITOR

Electrochemical measurements of the fabricated supercapacitor with graphene/activated carbon as working electrode and the ILs $P_{14,6,6,6}][NTf_2]$, $[P_{14,6,6,6}][N(CN)_2]$, $[P_{14,6,6,6}][Cl]$ and their polymer composite as the electrolytes for turning the properties to have superior conductivity, improved thermal stability and better electrode−electrolyte interaction. The obtained electrochemical results are tabulated in the table 4.24, given below.[27,165-167]

Table 4.24. *Electrochemical performance of ILs in various electrodes.*[27,165-167]

Electrolyte	Active electrode	Operation voltage window (V)	Specific capacitance (Fg^{-1})	Energy density (KWh/Kg)
$[P_{14,6,6,6}][Cl]$	Graphene	3.5	370	33.0
PVA−$[P_{14,6,6,6}]$ $[N(CN)_2]$	Graphene	3.0	876	37.1
$[P_{14,6,6,6}]$ $[NTf_2]$	Activated carbon	3.5	300	11.0
PVA−$[P_{14,6,6,6}]$ $[NTf_2]$	Graphene	4.0	495	11.5

From the table 4.24, the introduction of IL as electrolyte results in achieving higher specific capacitance with improved rate scalability and increased operation voltage window as against the conventional electrolytes. It is worth mentioning that all the phosphonium based ILs can give a voltage window in the range of 3–4 V. Addition of PVA in IL facilitates for developing flexible supercapacitor to overcome the leakage issues and having all the other advantages of IL based supercapacitors.

The other important aspect is that, the addition of PVA in $[P_{14,6,6,6}][NTf_2]$ enhances the operating voltages further along with improved electrochemical parameters. This is because of the ability of the IL to solvate PVA easily without altering its chemical properties, while constraining the mobility of electrolyte. Moreover, the presence of oxygen atoms in the hydroxyl group of PVA enhances conductivity further.[27, 165-167]

CHAPTER 5

IONIC LIQUIDS IN SEPARATION TECHNOLOGY

5.1. LIQUID–LIQUID EXTRACTION METHOD

5.1.1 Removal of toxic textile dyes with phosphonium ILs

In this study, extraction of six harmful textile industry used dyes (rhodamine B, methylene blue, methyl orange, malachite green, alizarin red S and congo red) from aqueous solutions have been investigated with hydrophobic phosphonium based ILs $[P_{14,6,6,6}][NTf_2]$, $[P_{14,6,6,6}][N(CN)_2]$, $[P_{14,6,6,6}][Cl]$, $[P_{14,6,6,6}][NTf_2][Cl]$, $[P_{14,6,6,6}][N(CN)_2][Cl]$ IL mixtures, PVA–$[P_{14,6,6,6}][NTf_2]$ and PVA–$[P_{14,6,6,6}][N(CN)_2]$ ionogels as extractant/adsorbent. The dyes adsorbed by the ILs were precipitated in the conical flasks of each dye solution after 15 min stir in the dark. The DI water was removed by injecting with a syringe from the dye solution after complete adsorption of dyes from the conical flasks. To determine the percentage of dye adsorption efficiency, the studied dyes in the aqueous solution before and after adsorption /extraction process was analysed using a UV-Vis spectrometer.

5.1.1.1. Extraction of rhodamine B dye

Rhodamine B is one of the organic dyes which dissolve in water easily and commonly used in textile, pharmaceutical and food products. It causes allergy to the respiratory system, skin and eyes. It is a very well-familiar water tracer fluorescent dye.[131] The hydrophobic phosphonium based ILs $[P_{14,6,6,6}][NTf_2]$, $[P_{14,6,6,6}][N(CN)_2]$, $[P_{14,6,6,6}][Cl]$, $[P_{14,6,6,6}][NTf_2][Cl]$, $[P_{14,6,6,6}][N(CN)_2][Cl]$, PVA–$[P_{14,6,6,6}][NTf_2]$ ionogel and PVA–$[P_{14,6,6,6}]$ $[N(CN)_2]$ ionogel were used as extractant /adsorbent from aqueous solution of Rhodamine B dye. It was found that, in rhodamine B dye solution after 15 min stir in dark, $[P_{14,6,6,6}][NTf_2]$ IL showed 100% extraction efficiency, $[P_{14,6,6,6}][N(CN)_2]$ IL showed partial adsorption and no adsorption was found in $[P_{14,6,6,6}][Cl]$ IL, but a cloudy solution with a dark pink colour was obtained. In $[P_{14,6,6,6}][NTf_2][Cl]$ and $[P_{14,6,6,6}][N(CN)_2][Cl]$, adsorption of dye was not occurred, but a slight colour change as pale pink was acquired. It is found due to the fluorescence of the dye. The hydrophobicity of IL is the major property for the adsorption or seperation of the dyes from dye solutions. In $[P_{14,6,6,6}][NTf_2][Cl]$ and $[P_{14,6,6,6}][N(CN)_2][Cl]$, the influence of anion [Cl] may lead rather than the parent compound anions $[NTf_2]$ and $[N(CN)_2]$.

In PVA−$[P_{14,6,6,6}][NTf_2]$ ionogel and PVA−$[P_{14,6,6,6}]$ $[N(CN)_2]$ ionogel also, adsorption of dye was not occurred, but a slight colour change as pale pink was acquired. The partition coefficient of the dye for IL $[P_{14,6,6,6}][NTf_2]$ (shows 100% absorption of dye) was calculated to be 6.667. Figure 5.1 and table 5.1 shows the adsorption of the given ILs in rhodamine B aqueous solution.

Figure 5.1. Extraction of rhodamine B dye by hydrophobic ILs (1) $[P_{14,6,6,6}][NTf_2]$, (2) $[P_{14,6,6,6}][N(CN)_2]$, (3) $[P_{14,6,6,6}][Cl]$, (4) $[P_{14,6,6,6}][NTf_2][Cl]$, (5) $[P_{14,6,6,6}]$ $[N(CN)_2][Cl]$, (6) PVA−$[P_{14,6,6,6}][NTf_2]$, (7)) PVA−$[P_{14,6,6,6}][N(CN)_2]$ & (8) dye solution without treating IL.

Table 5.1. *The efficiency of rhodamine B dye in the ILs*

Ionic liquid	**Efficiency of dye adsorption**
	Rhodamine B
$[P_{14,6,6,6}][NTf_2]$	100%
$[P_{14,6,6,6}][N(CN)_2]$	Partial adsorption
$[P_{14,6,6,6}][Cl]$	No adsorption
$[P_{14,6,6,6}][NTf_2][Cl]$	No adsorption
$[P_{14,6,6,6}][N(CN)_2][Cl]$	No adsorption
PVA −$[P_{14,6,6,6}][NTf_2]$ ionogel	No adsorption
PVA −$[P_{14,6,6,6}][N(CN)_2]$ ionogel	No adsorption

5.1.1.2 Extraction of methylene blue dye

Methylene blue is a hydrophilic cationic dye often used in the textile industry.[145] It is one of the most commonly used dyes in cotton, wood and silk. It can cause some harmful effects with acute exposure as increased heart rate, vomiting, shock, cyanosis, jaundice, and quadriplegia and tissue necrosis in humans.[38] It is essential to remove the dye from waste water to minimize the damage to the environment.[38] The hydrophobic phosphonium based ILs $[P_{14,6,6,6}][NTf_2]$, $[P_{14,6,6,6}][N(CN)_2]$, $[P_{14,6,6,6}][Cl]$, $[P_{14,6,6,6}][NTf_2][Cl]$ ionogel, $[P_{14,6,6,6}][N(CN)_2][Cl]$ ionogel, PVA−$[P_{14,6,6,6}][NTf_2]$ ionogel and PVA−$[P_{14,6,6,6}]$ $[N(CN)_2]$ ionogel were used as extractant/adsorbent to remove methylene blue dye from its aqueous solution. It was found that, ILs $[P_{14,6,6,6}][NTf_2]$, $[P_{14,6,6,6}][N(CN)_2]$, $[P_{14,6,6,6}][Cl]$ showed 100% extraction efficiency in methylene blue dye solution after 15 min stir in dark.

In $[P_{14,6,6,6}][NTf_2][Cl]$ and $[P_{14,6,6,6}][N(CN)_2][Cl]$, adsorption of dye was not occurred, but a slight colour change as pale blue was attained. It is due to the fluorescence of the dye observed. In PVA−$[P_{14,6,6,6}][NTf_2]$ ionogel and PVA−$[P_{14,6,6,6}]$ $[N(CN)_2]$ ionogel also, adsorption of dye was not occurred, but a slight colour change as pale blue was acquired. In all studied ILs, the hydrophobicity is responsible for the adsorption or seperation of the dyes from aqueous dye solutions. Additionally, the fluorescence of the dye is quenched and leads to change in colour. Figure 5.2 and table 5.2 shows the adsorption of the ILs in aqueous solution of methylene blue dye.

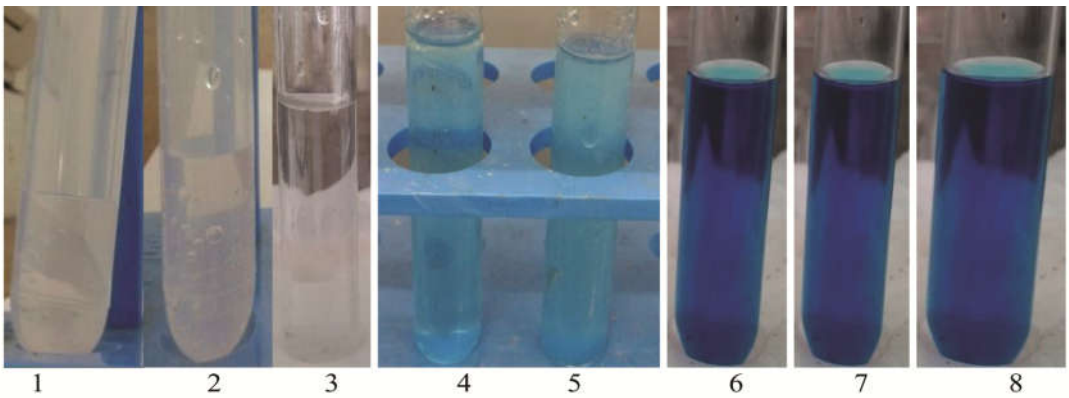

Figure 5.2. Extraction of methylene blue dye by hydrophobic ILs (1) $[P_{14,6,6,6}][NTf_2]$, (2) $[P_{14,6,6,6}][N(CN)_2]$, (3) $[P_{14,6,6,6}][Cl]$, (4) $[P_{14,6,6,6}][NTf_2][Cl]$, (5) $[P_{14,6,6,6}]$ $[N(CN)_2][Cl]$, (6) PVA−$[P_{14,6,6,6}][NTf_2]$, (7)) PVA−$[P_{14,6,6,6}][N(CN)_2]$ & (8) dye solution without treating IL.

***Table 5.2**. The efficiency of methylene blue dye in the ILs*

Ionic liquid	Efficiency of dye adsorption
	Methylene blue
$[P_{14,6,6,6}][NTf_2]$	100%
$[P_{14,6,6,6}][N(CN)_2]$	100%
$[P_{14,6,6,6}][Cl]$	100%
$[P_{14,6,6,6}][NTf_2][Cl]$	Partial adsorption
$[P_{14,6,6,6}][N(CN)_2][Cl]$	Partial adsorption
PVA –$[P_{14,6,6,6}][NTf_2]$ ionogel	No adsorption
PVA –$[P_{14,6,6,6}]$ $[N(CN)_2]$ ionogel	No adsorption

5.1.1.3. Extraction of methyl orange dye

The hydrophobic phosphonium based ILs $[P_{14,6,6,6}][NTf_2]$, $[P_{14,6,6,6}][N(CN)_2]$, $[P_{14,6,6,6}][Cl]$, $[P_{14,6,6,6}][NTf_2][Cl]$, $[P_{14,6,6,6}][N(CN)_2][Cl]$, PVA–$[P_{14,6,6,6}][NTf_2]$ ionogel and PVA–$[P_{14,6,6,6}]$ $[N(CN)_2]$ ionogel were used as extractant /adsorbent to remove methyl orange dye from its aqueous solution. In methyl orange dye solution, $[P_{14,6,6,6}][NTf_2]$ IL remains in the bottom of the test tube. There was no dye adsorption occurred; only a colour change from orange to dark red was acquired. The adsorption maximum (λ_{max}) of methyl orange dye solution after addition of IL $[P_{14,6,6,6}][NTf_2]$ was improved from 464 nm into 503 nm after 15 min stirred in the dark. The pH of the dye was changed from 4.69 into 3.65 after 15 min stirred in the dark with IL. It indicates the hydrophobic nature of the mentioned ILs used. In addition to this, the fluorescence of the dye is quenched and leads to change in colour. But $[P_{14,6,6,6}][N(CN)_2]$ and $[P_{14,6,6,6}][Cl]$ ILs were separated on upper surface of the test tube by adsorbing the methyl orange dye and DI water was separated as a clear solution. The UV absorption spectra clearly showed the 100% adsorption efficiency in above two ILs.

In $[P_{14,6,6,6}][NTf_2][Cl]$ and $[P_{14,6,6,6}]N[(CN)_2][Cl]$, methyl orange was adsorbed completely after 30 minute stir in dark and a separate layer of water and IL with dye was formed above the flask or test tube. It indicates the hydrophobic nature of the mentioned ILs used. In addition to this, the fluorescence of the dye is quenched and leads to change in colour. It was found that the influence of anion [Cl] affect the adsorption of the anionic dye in $[P_{14,6,6,6}][NTf_2][Cl]$ than the parent anion $[NTf_2]$. In PVA–$[P_{14,6,6,6}][NTf_2]$ ionogel, there was no dye adsorption occurred, only a colour change from dark orange to pale orange was observed. This is due to the fluorescence of the dye focussed. PVA–$[P_{14,6,6,6}][N(CN)_2]$ ionogel was separated on upper surface of the test tube by adsorbing the methyl orange dye and DI water was detached as a clear solution. The UV absorption spectra clearly indicate the 100% adsorption efficiency.

The reuse of the ILs were shown of great significance to meet the economy of the process when using ILs as an adsorbent for liquid –liquid extraction method. The retrieval of each dye from IL was finally separated after filtration. After filtration, the ILs also were recovered and reused in a new one. Figure 5.3 and table 5.3 shows the adsorption of the ILs in methyl orange aqueous dye solution.

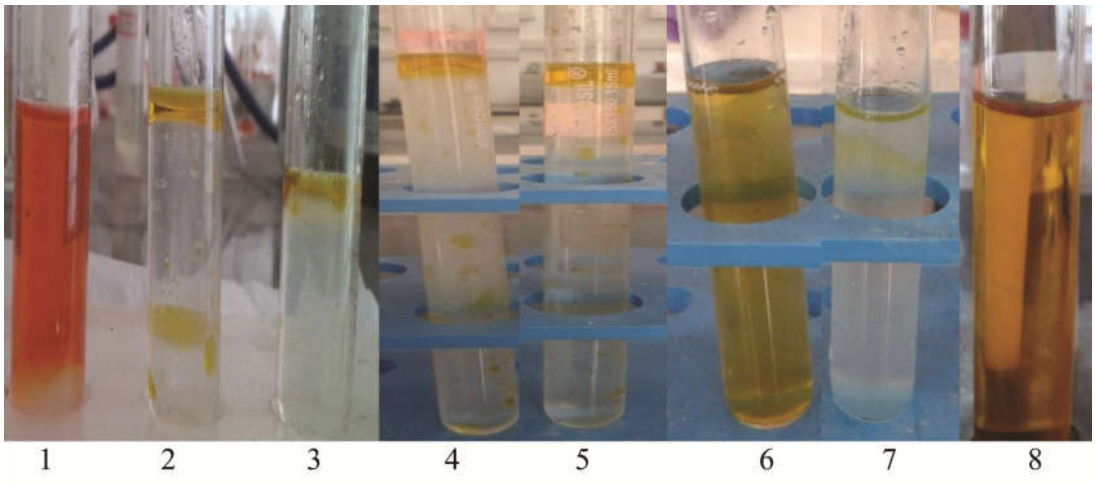

Figure 5.3. Extraction of methyl orange dye by hydrophobic ILs (1) $[P_{14,6,6,6}][NTf_2]$, (2) $[P_{14,6,6,6}][N(CN)_2]$, (3) $[P_{14,6,6,6}][Cl]$, (4) $[P_{14,6,6,6}][NTf_2][Cl]$, (5) $[P_{14,6,6,6}][N(CN)_2][Cl]$, (6) PVA–$[P_{14,6,6,6}][NTf_2]$, (7)) PVA–$[P_{14,6,6,6}][N(CN)_2]$ & (8) dye solution without treating IL.

***Table 5.3**. The efficiency of methyl orange dye in the ILs*

Ionic liquid	Efficiency of dye adsorption
	Methyl Orange
$[P_{14,6,6,6}][NTf_2]$	No adsorption
$[P_{14,6,6,6}][N(CN)_2]$	100%
$[P_{14,6,6,6}][Cl]$	100%
$[P_{14,6,6,6}][NTf_2][Cl]$	100%
$[P_{14,6,6,6}][N(CN)_2][Cl]$	100%
PVA -$[P_{14,6,6,6}][NTf_2]$ ionogel	Partial adsorption
PVA - $[P_{14,6,6,6}][N(CN)_2]$ ionogel	100%

5.1.1.4 Extraction of malachite green dye

The hydrophobic phosphonium based ILs $[P_{14,6,6,6}][NTf_2]$, $[P_{14,6,6,6}][N(CN)_2]$ and $[P_{14,6,6,6}][Cl]$ were used as extractant/adsorbent to extract malachite green dye from its aqueous solution. It was found that $[P_{14,6,6,6}][NTf_2]$ shows 100% extraction efficiency in malachite green dye solution after 15 min stir in dark. No adsorption took place for malachite green in $[P_{14,6,6,6}][N(CN)_2]$ and $[P_{14,6,6,6}][Cl]$ ILs. Figure 5.4 and table 5.4 show the adsorption of the ILs in malachite green aqueous dye solution.

***Table 5.4**. The efficiency of malachite green dye in the ILs*

Ionic liquid	Efficiency of dye adsorption
	Malachite green
$[P_{14,6,6,6}][NTf_2]$	100%
$[P_{14,6,6,6}][N(CN)_2]$	No adsorption
$[P_{14,6,6,6}][Cl]$	No adsorption

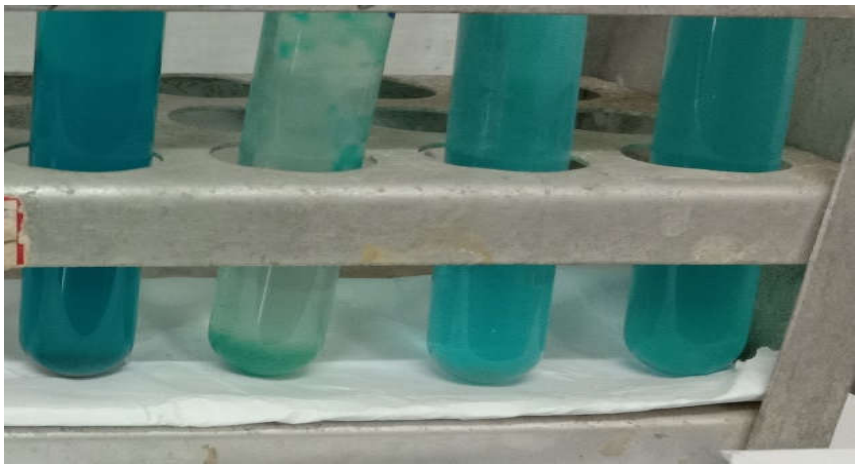

1 **2** **3** **4**

Figure 5.4. Extraction of malachite green dye with hydrophobic phophonium ILs (1) without treating IL, (2) $[P_{14,6,6,6}][NTf_2]$ IL, (3) $[P_{14,6,6,6}][N(CN)_2]$ IL & (4) $[P_{14,6,6,6}][Cl]$ IL.

5.1.1.5 Extraction of alizarin red S dye

The hydrophobic phosphonium based ILs $[P_{14,6,6,6}][NTf_2]$, $[P_{14,6,6,6}][N(CN)_2]$ and $[P_{14,6,6,6}][Cl]$ were used as extractant /adsorbent to extract alizarin red S from its aqueous solution. It was found that $[P_{14,6,6,6}][N(CN)_2]$ shows 100% extraction efficiency in malachite green dye solution after 15 min stir in dark. No adsorption took place for alizarin red S in $[P_{14,6,6,6}][NTf_2]$ and $[P_{14,6,6,6}][Cl]$ ILs. Figure 5.5 and table 5.5 show the adsorption of the ILs in alizarin red S aqueous dye solution.

***Table 5.5**. The efficiency of alizarin red S dye in the ILs*

Ionic liquid	**Efficiency of dye adsorption**
	Alizarin red S
$[P_{14,6,6,6}][NTf_2]$	No adsorption
$[P_{14,6,6,6}][N(CN)_2]$	100%
$[P_{14,6,6,6}][Cl]$	No adsorption

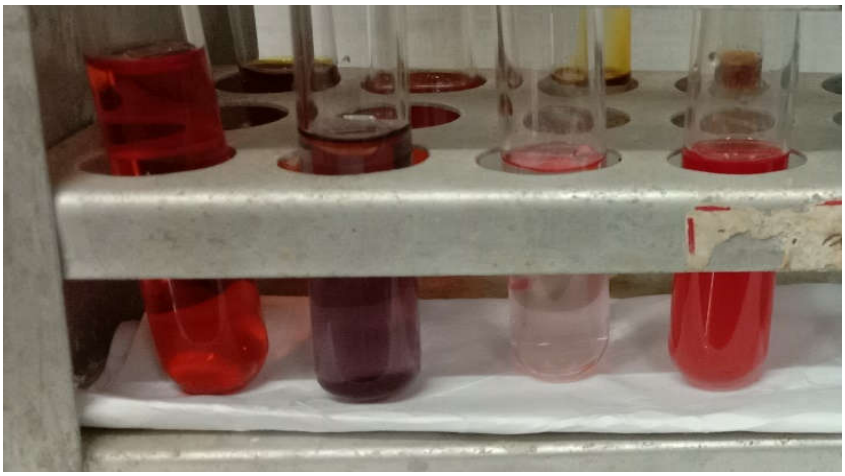

1 2 3 4

Figure 5.5. Extraction of alizarin red S dye with hydrophobic ILs (1) without treating IL, (2) $[P_{14,6,6,6}][NTf_2]$ IL, (3) $[P_{14,6,6,6}][N(CN)_2]$ IL & (4) $[P_{14,6,6,6}][Cl]$ IL.

5.1.1.6 Extraction of congo red dye

The hydrophobic phosphonium based ILs $[P_{14,6,6,6}][NTf_2]$, $[P_{14,6,6,6}][N(CN)_2]$ and $[P_{14,6,6,6}][Cl]$ were used as extractant/adsorbent to extract congo red from its aqueous solution. It was found that $[P_{14,6,6,6}][N(CN)_2]$ and $[P_{14,6,6,6}][Cl]$ show 100% extraction efficiency in congo red dye solution after 15 min stir in dark. No adsorption took place for congo red in $[P_{14,6,6,6}][NTf_2]$ IL. Figure 5.6 and table 5.6 show the adsorption of the ILs in congo red aqueous dye solution.

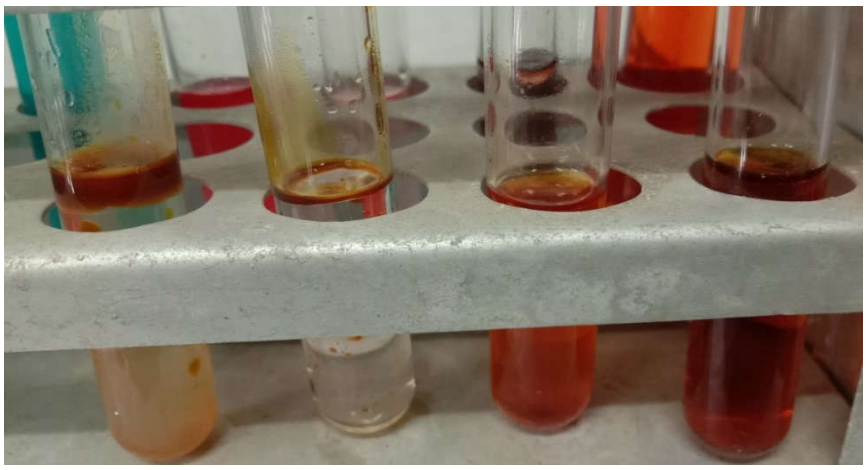

1 2 3 4

Figure 5.6. Extraction of congo red dye with hydrophobic ILs (1) $[P_{14,6,6,6}][Cl]$ IL, (2) $[P_{14,6,6,6}][N(CN)_2]$ IL, (3) $[P_{14,6,6,6}][NTf_2]$ IL & (4) without treating IL

***Table 5.6**. The efficiency of congo red dye in the ILs*

Ionic liquid	Efficiency of dye adsorption
	Congo red
$[P_{14,6,6,6}][Cl]$	100%
$[P_{14,6,6,6}][N(CN)_2]$	100%
$[P_{14,6,6,6}][NTf_2]$	No adsorption

5.1.2. Removal of harmful metal oxides with phosphonium ILs

Water in urban areas has been completely polluted by heavy metals. Their toxicity, persistence, and accumulation in living organisms have negative environmental and health effects and its contamination in the water environment has attracted great concern owing to its environmental toxicity and persistence. Use of ILs has been predicted as a proficient approach for removing the harmful seven heavy metals (arsenic, chromium, cadmium, copper, zinc, lead and mercury) by liquid–liquid extraction method by using three hydrophobic ILs $[P_{14,6,6,6}][NTf_2]$, $[P_{14,6,6,6}][N(CN)_2]$ and $[P_{14,6,6,6}][Cl]$ from its standard solutions AS $(NO_3)_3$, Cr (NO_3), Cd $(NO_3)_2$, Hg $(NO_3)_2$, Pb $(NO_3)_2$, Zn $(NO_3)_2$, and Cu $(NO_3)_2$. Here, we report the extraction of the heavy metals from their standard solutions using the three hydrophobic phosphonium ILs as extractant/adsorbent. The ILs were added to the standard solution of each metal defined in the experimental section and the extraction/adsorption kinetics were revealed by evaluating the heavy metal concentration before and after the addition of ILs from ICPMS (inductive coupled plasma mass spectrometry) and observed the efficiency of the adsorption. The results are tabulated in table 5.7.

Table 5.7*. The efficiency of heavy metals by extraction of ILs*

Ionic liquid	Concentration of extraction of heavy metals						
	As (20ppm)	**Cr (20ppm)**	**Cd (20ppm)**	**Cu (20ppm)**	**Zn (20ppm)**	**Pb (20ppm)**	**Hg (20ppm)**
$[P_{14,6,6,6}][NTf_2]$	2.17	3.35	2.37	1.37	5.32	0.34	0.26
$[P_{14,6,6,6}][N(CN)_2]$	3.52	5.86	6.47	2.25	7.17	0.82	0.37
$[P_{14,6,6,6}][Cl]$	1.34	2.32	0.34	0.14	0.54	0.24	0.34

5.1.3. Removal of phenolic compounds with phosphonium ILs

A lot of industrial developments produce huge amount of wastewater polluted with different organic and inorganic substances. Due to their industrial relevance, phenolic compounds are amongst the most common organic pollutants seen in many industrial waste waters. Developing an effective method for extracting these phenolic compounds from industrial waste waters has been a Herculean task for the industry. Use of hydrophobic ILs has been envisaged as an efficient strategy for removing them by liquid–liquid extraction. Here, we report the extraction pathway of phenolic compounds from rice and cashew industrial waste waters using the three hydrophobic phosphonium ILs as extractant/adsorbent. The ILs were added to both waste waters as defined in the experimental section and the extraction/adsorption kinetics were explored by evaluating the phenolic concentration before and after the addition of ILs from UV−Vis quantification followed by assessing the efficiency of the adsorption.

We got a moving result from UV–Visible spectroscopy that the IL $[P_{14,6,6,6}][Cl]$ could completely be separated out (100%) of the phenolic compounds that contains in cashew waste water with the initial concentration of 96 mg/L reduced to 0.4mg/L. But, in rice waste water, the former phenolic compounds concentration of 32 mg/L was diminished to 4 mg/L (88%) after adding

$[P_{14,6,6,6}][Cl]$. No effects were seen with other two ILs in both waste waters. The results are shown in figure 5.7 & 5.8 and the values are tabulated in the table 5.8.

1 2 3 4

Figure 5.7. Extraction of phenolic compounds from cashew industrial waste water with three phosphonium ILs : 1) waste water of cashew with 96 mg/L phenolic contents, (2) after adding with the IL $[P_{14,6,6,6}][Cl]$, (3) after treating with the IL $[P_{6,6,6,14}][N(CN)_2]$) and (4) after treating with the IL $[P_{6,6,6,14}][NTf_2]$.

1 2 3 4

Figure 5.8. Extraction of phenolic compounds from rice industrial waste water with three phosphonium ILs : 1) waste water of rice industry with 32 mg/L phenolic contents, (2) after adding with the IL $[P_{14,6,6,6}][Cl]$, (3) after treating with the IL $[P_{6,6,6,14}][N(CN)_2]$) and (4) after treating with the IL $[P_{6,6,6,14}][NTf_2]$.

Table 5.8. The *efficiency of phenolic compounds extraction* calculated for the *three phosphonium based ILs in rice and cashew industrial waste waters.*

Ionic liquid	Efficiency of phenolic compounds in industrial waste waters	
	Cashew	Rice
$[P_{14,6,6,6}][NTf_2]$	No adsorption	No adsorption
$[P_{14,6,6,6}][N(CN)_2]$	No adsorption	Partial adsorption
$[P_{14,6,6,6}][Cl]$	100%	88%

On exploring the origin of adsorption, the hydrophobicity of ILs are liable for the adsorption /seperation of phenolic compounds from the industrial waste waters. The retrieval of the IL was in conclusion done by filtration followed by the recovery of IL for reuse by appropriate solvents. The provision for the reuse of ILs after the extraction has a better significance from the economic side, since it reduces the total cost of ILs and diminishes problem to the environment.

CHAPTER 6

DRUG LIKENESS PROPERTY AND BIOLOGICAL ACTIVITIES OF PHOSPHONIUM IONIC LIQUIDS

6.1. DRUG LIKENESS PROPERTY AND TOXICITY CALCULATION OF ILS BY *IN SILICO* ANALYSIS

A compound to be a potential drug, it must have a good pharmacokinetic properties as well as having a good biological activity. To access the pharmacokinetic profile of the ILs, we have used a well validated *in silico* ADMET (absorption, distribution, metabolism, excretion and toxicity) prediction tools. In 1997, Lipinski et al. reported a simple rule of thumb that allowed in silico prediction of solubility and bioavailability are likely to allow oral absorption. An analysis of small drug-like molecules (MW < 450) suggested that for better brain permeation and to have a good oral absorption. Lipinski's rule of five is commonly used by pharmaceutical chemists in drug design and predicts the pharmacokinetic parameters and toxicity potential of the selected drug molecules.[31,134-136]

High oral bioavailability, molecular hydrophobicity or lipophilicity, (commonly estimated by a calculated log *P*) and molecular mass are the important attention for the progress of bioactive molecules as therapeutic agents. *In silico* techniques are able to identify the ability to guide drug design and to select the best candidates for the drug development based on a set of six fundamental physicochemical parameters: lipophilicity, partition coefficient (log P), distribution coefficient (log D), molecular weight (MW), topological polar surface area (TPSA) and number of hydrogen bond donors (HBD). An analysis of drug-like molecules (MW < 450) suggested for better brain permeation and to have a good oral absorption. Lipinski's rule of five is commonly used by pharmaceutical chemists in drug design and predicts the pharmacokinetic parameters and toxicity potential of the selected drug molecules. Lipinski's 'rule of five', suggests that a candidate molecule will possible to be orally active, if the molecular weight must be a value of (MW) ≤ 500 (g/mol), the calculated octanol/water partition coefficient (Log P) ≤ 5 and ≥ 0, the hydrogen bond donors (OH and NH groups) ≤ 5 and hydrogen bond acceptors (notably N and O)) < 10. For suitable oral bioavailability, the topological polar surface (TPSA) should be ≤ 140 $Å^2$ and the number of rotatable bonds (nrotbs ≤ 10–20).[31,134-136]

The molecular properties of the ILs and their parent drugs were calculated using Osiris, Molinspiration and admetSAR softwares and are tabulated in table 6.1, table 6.2 and table 6.3 respectively. Physico chemical properties and toxicity parameters of all ILs & their parent drugs were compared with that of standard drugs as Norfloxacin, Erythromycin and Pencillin G. From this, it is revealed that all ILs and their parent compounds showed a promising bioactivity score for drug targets by Molinspiration software and were predicted to have very low toxicity risk by OSIRIS online software. Drug likeness analysis was also within the required limits and the results are shown in table 6.1. An evaluation of toxicity risk parameters is required to asses a drug candidate during the development of a new drug for any disease. Consequently, *in silico* toxicity analysis was performed and the results were shown in table 6.2 & 6.3 respectively. AMES toxicity analysis shows that the ILs were non toxic. For further investigation, the computed LD_{50} calculated in rat acute toxicity models and the compounds seem to be relatively safe.[31,134-136]

Table 6.1. *In silico prediction of physicochemical calculations and drug likeness property of the ILs & their parent drugs.*[31,134-136]

Compound	MW	Physicochemical properties					Drug likeness					
		TPSA	OH/ NH	N rotb	VOL	n ON	GPC	ICM	KI	NRL	PI	EI
Lidocaine HCl	270	32	2	5	245	3	-0.43	-0.39	-0.49	-0.68	-0.65	-0.34
Ranitidine HCl	350	86	3	10	289	7	-0.01	-0.59	-0.51	-1.01	-0.21	0.29
lidocaine docusate	657	107	1	18	410	7	-0.05	-0.23	-0.38	-0.03	0.20	0.09
Ranitidine docusate	737	106	1	17	409	7	-0.00	-0.11	-0.27	-0.07	0.16	0.02
Norfloxacin	419	120	2	6	359	9	0.22	-0.13	-0.14	0.02	-0.11	0.17
Erythromycin	733	193	5	7	709	14	-0.50	-1.31	-.25	-1.12	-0.18	-0.60
Pencillin G	334	87	2	4	287	6	0.01	-0.42	-0.71	-0.37	-0.86	0.30
$[P_{14,6,6,6}][NTf_2]$	764	72	0	20	715	0	-0.25	-0.95	-0.77	-0.69	0.05	-0.52
$[P_{14,6,6,6}][N(CN)_2]$	550	51	0	22	623	0	0.14	0.07	0.01	-0.04	0.30	0.23
$[P_{14,6,6,6}][Cl]$	519	0	0	24	590	0	0.33	0.15	0.00	0.01	0.20	0.17

TPSA (total polar surface area), OH/NH (OH–HN interaction), nrotb (number of rotable bond), VOL (volume), nON(number of hydrogen bond acceptors O and N) GPC (GPCR ligand), ICM (ion channel modulator), KI (kinase inhibitor), NRL (nuclear receptor ligand), PI (protease inhibitor), EI (enzyme inhibitor).

Log P values of lidocaine docusate, ranitidine docusate and their parent drugs were seen to be less than 5 and they obeyed Lipinski's rule of five, suggesting good permeability across cell membrane. But, the three Phosphonium ILs were in violation to Lipinski's rule of five. Molecular weight of lidocaine docusate, ranitidine docusate and the three phosphonium ILs were found to be $<$ 500 which violated Lipinski's rule of five. In all ILs, number of hydrogen bond acceptors (O and N atoms) and number of hydrogen bond donors (NH and OH) were in agreement with the Lipinski's rule of five i.e. less than 10 and 5 respectively. It can be predicted that all ILs were likely to be orally active as they obeyed Lipinski's rule of five. Topological polar surface area was very much correlated with the hydrogen bonding of a molecule and was a very good indicator of the bioavailability of drug molecule. TPSA of the ILs and their parent drugs were observed less than 140 $Å^2$ and indicated good oral bioavailability. [31,134-136]

Toxicity studies show that lidocaine HCl shows a slightly toxic in carcinogenicity, highly mutagenic, highly irritant and shows highly reproductive effect. But all other ILs found to be non toxic in AMES toxicity, carcinogenicity, Irritant, mutagenic and reproductive effective.

Table 6.2. *In silico screening of toxicity and bioavailability score of the ILs & parent drugs.* [31,134-136]

Compound	AMES Toxicity	Carcinogenecity	Rat acute toxicity LD_{50} (mol/kg)	Bioavailability score
Lidocain HCl			2.75	0.55
Ranitidine HCl			2.24	0.17
lidocaine docusate			2.55	0.55
Ranitidine Doculate			2.24	0.55
$P_{14,6,6,6}][NTf_2]$			2.81	0.17
$[P_{14,6,6,6}][N(CN)_2]$			2.26	0.55
$[P_{14,6,6,6}][Cl]$			2.33	0.17
Norfloxacin			1.87	0.55
Erythromycin			2.22	0.17
Pencillin G			1.65	0.56

:nontoxic , : toxic

Table 6.3. *Osiris calculations of toxicity parameters and drug-score of the ILs & parent drugs.* [31,134-136]

Compound	Toxicity calculation				Drug score			
	MUT	TUMO	IRRI	REP	CLP	S	DL	DS
Lidocaine HCl					2.16	-2.37	9.01	0.2
Ranitidine HCl					-2.02	-3.52	-0.5	0.59
lidocaine docusate					3.63	-3.5	-5.7	0.1
Ranitidine Docusate					3.18	-3.23	-11.3	0.11
Norfloxacin					0.36	-2.79	4.39	0.81
Erythromycin					1.67	-3.64	11.29	0.47
Pencillin G					1.54	-2.04	11.28	0.33
$P_{14,6,6,6}][NTf_2]$					10.27	-7.79	-29.7	0.12
$[P_{14,6,6,6}][N(CN)_2]$					12.1	-8.2	-13.5	0.1
$[P_{14,6,6,6}][Cl]$					13.4	-9.67	-32.6	0.1

MUT (mutagenic),TUMO (tumorigenic), IRRI (irritant), REP (reproductive effective), CLP (cLogP), S (solubility), DL(drug likeness), DS (drug-score), non toxic, slightly toxic, highly toxic.

6.2. BIOLOGICAL ACTIVITIES OF PHOSPHONIUM BASED ILS

Now a day the pharmaceutical industry is facing many challenges in the discovery of novel and effective drugs for various therapeutic applications. Approximately 50% of available drugs are administered as crystalline salts, which can have many disadvantages such as low bioavailability, low solubility, low thermal stability, low chemical stability and polymorphism. Conversion of the crystalline drugs into ILs is therefore a promising avenue for the pharmaceutical industry. ILs propose a suitable technique to investigate the properties of alterations in the structures on the resultant physical and chemical properties and they can be designed to be non-toxic, non-flammable, non-corrosive, with a wide range of hydrophobicity/hydrophilicity, acidity/basicity, viscosities, high thermal and chemical stability by mixtures of diverse cations and anions.[138-148] Possessing a combination of favourable biological properties, ILs are being studied and assessed for their applications in various fields. Several studies have reported the use of ILs in biomedical applications as anti−tumour agents, anti−bacterial and anti−oxidant agents. Arising from the impressive drug likeness properties and toxicity studies by Molinspiration, AdmetSAR and OSIRIS softwares shown by ionic liquids, we decided to study the biological properties of the typical ILs. In this study we present the different biological properties as anti−cancer activity, anti−bacterial activity and anti−oxidant properties of the three phosphonium ILs $[P_{14,6,6,6}][Tf_2N]$, $[P_{14,6,6,6}][(CN)_2N]$ and $[P_{14,6,6,6}][Cl]$.

6.2.1 Anti−cancer activity (MTT assay) of three phosphonium based ILs

Human Cancer is a primary cause of death in economically rising countries and the second leading cause of death and burden in developing countries.[142,149] Numerous studies on cytotoxicity of ionic liquids towards various cells, both normal and cancerous cells of humans have been reported.[47] In the fight to synthesize new pharmceutical drugs, ILs have attracted a great consideration amongst in the scientific community due to their variety of potential pharmaceutical applications.[150] Understanding and managing the toxicity of small molecule toxins is a most important task in the innovation and growth of new drugs. Therefore, advance of

new anti-cancer agents that reduce the toxicity associated with existing chemotherapies and those targeted at avoiding tumour resistance mechanism is a major work of drug discovery efforts.[47] In the present study, the anticancer activity of three phosphonium based ILs $[P_{14,6,6,6}][NTf_2]$, $[P_{14,6,6,6}][N(CN)_2]$ and $[P_{14,6,6,6}][Cl]$ ILs against A549 (human lung cancer), K562 (chronic myelogenous leukemia) , Jurkat E6-1 (leukemic T cell lymphoblast) , HCT 116 (colorectal carcinoma) and HEK 293 (human embryonic kidney 293 cells) cancer cell lines were evaluated using a standard 3−(4, 5−dimethylthiazol−2−yl)−2, 5−dipheny ltetrazolium bromide (MTT) assay. The obtained results with ILs against A549, K562, Jurkat E6-1 and HCT 116 human cancer cells were compared with HEK 293 normal cells.

6.2.1.1 In vitro cytotoxic activity against human lung cancer A549 cell line.

The cytotoxicity of representative compounds $[P_{14,6,6,6}][NTf_2]$, $[P_{14,6,6,6}][N(CN)_2]$ and $[P_{14,6,6,6}][Cl]$ ILs against human lung cancer cell line A549 were evaluated using a standard 3− (4, 5-dimethylthiazol−2−yl)−2, 5−diphenyltetrazolium bromide (MTT) assay. Figures 6.1 (a & b), 6.2 (a & b) and figures 6.3 (a & b) show the MTT assay results confirming the in vitro cytotoxicity effect of $[P_{14,6,6,6}][NTf_2]$, $[P_{14,6,6,6}][Cl]$ and$[P_{14,6,6,6}][N(CN)_2]$ ILs against the human lung cancer cell line A549. The Fifty percent cell death, which determine the inhibitory concentration (IC_{50}) concentration detected were 40 μM/Ml, 36 μM/Ml and 25 μM/Ml respectively and which can analyse the magnitude of cytotoxic effect of the samples. The lower the IC_{50} value, the more cytotoxic is the ILs used. From the results it shows that $[P_{14,6,6,6}][N(CN)_2]$ shows lower IC_{50} than other two ILs. The cytotoxicity evaluation results are promising and point to the possibilities of these ILs as potential inhibitors of human lung cancer cell line A549. The results attained with ILs against A549 human cancer cells were compared with HEK non-malignant cells. The HEK cell line got IC_{50} values of 218.78 ± 3.9 μM/Ml, 57.5 ± 2.8 μM/Ml and 175± 2.3 μM/Ml for three studied samples respectively which show the higher value of IC_{50} concentration comparing to A549cell line in three ILs studied. These ILs were more efficient on A549 cancer cells and less toxic to HEK cells at same concentrations.[138-147]

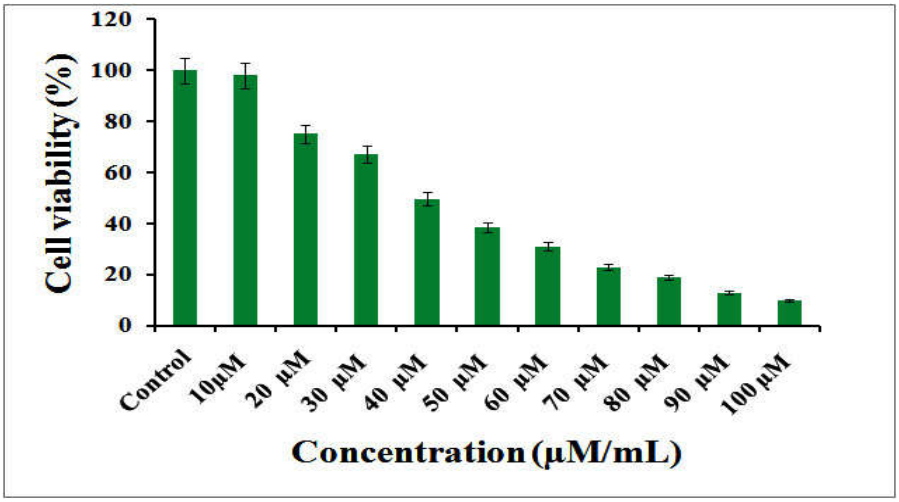

Figure 6.1. (a) In vitro cytotoxicity effect of $[P_{14,6,6,6}][NTf_2]$ IL against A549 cell line. The detected IC_{50} concentration was found to be 40 µM/Ml.

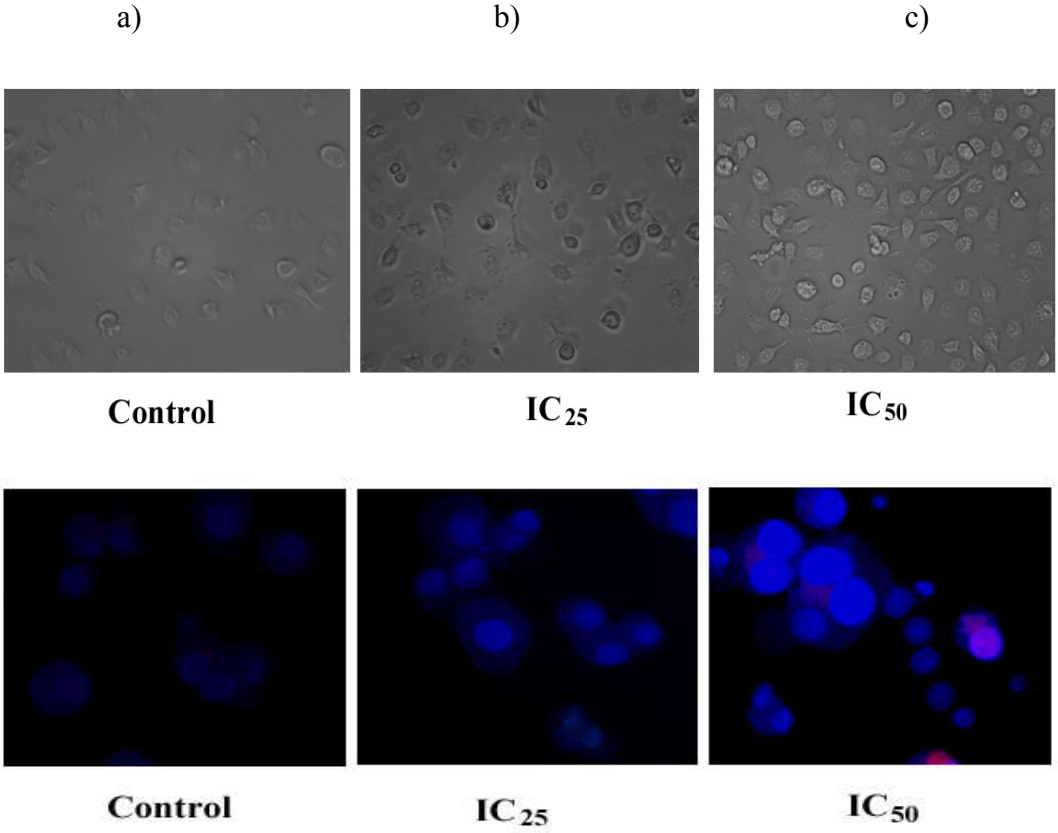

Figure 6.1 (b). Bright field inverted light microscopy images and fluorescence microscopy images of A549 cell line (a) control, (b) IC_{25} and (c) IC_{50} concentration of $[P_{14,6,6,6}][NTf_2]$.

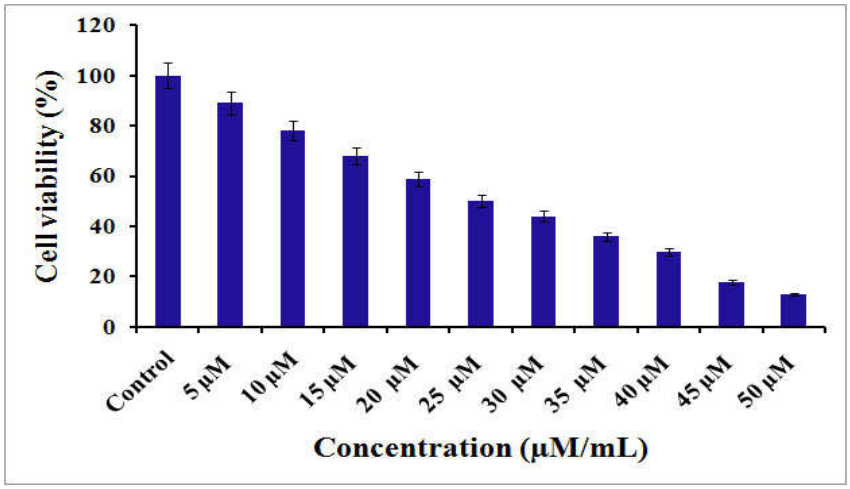

Figure 6.2 (a). The in vitro cytotoxicity effect of $[P_{14,6,6,6}][N(CN)_2]$ IL against A549 cell line. The detected IC_{50} concentration was obtained as 25 µM/Ml.

a) b) c)

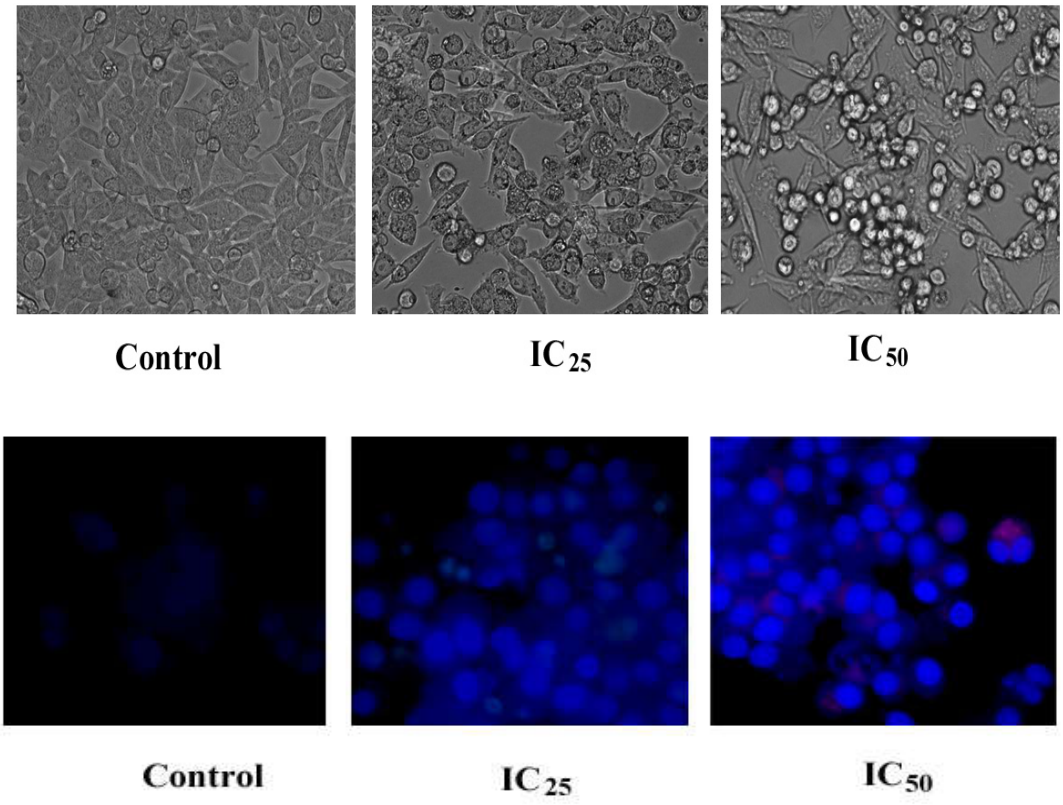

Figure 6.2 (b). Bright field inverted light microscopy images and fluorescence microscopy images of A549 cell line. (a) control (untreated IL), (b) IC_{25} and (c) IC_{50} of$[P_{14,6,6,6}][N(CN)_2]$.

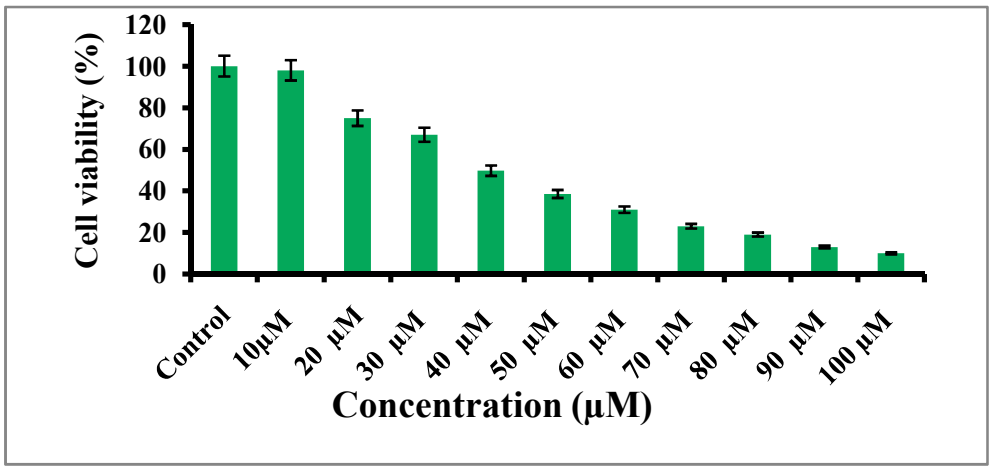

Figure 6.3 (a). The in vitro cytotoxicity effect of $[P_{14,6,6,6}][Cl]$, against the human lung cancer cell line A549. The detected IC_{50} concentration was found to be 36 µM/Ml.

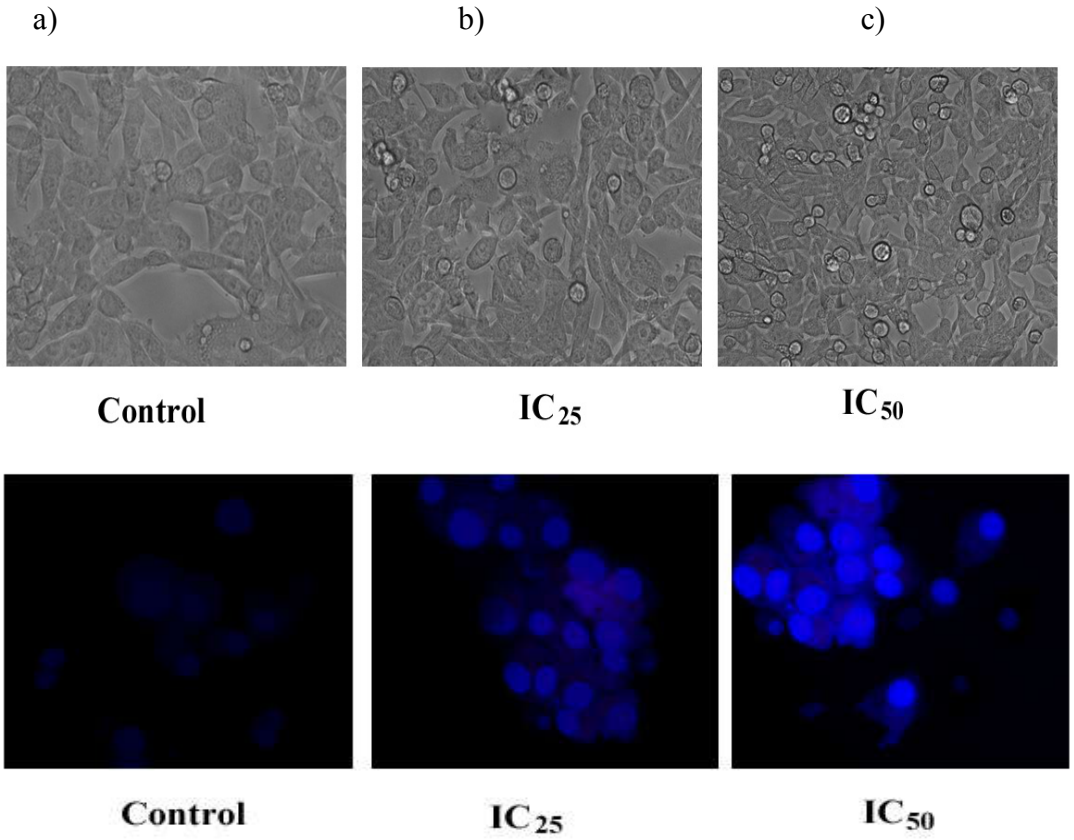

Figure 6.3 (b). Bright field inverted light microscopy images and fluorescence microscopy images of A549 cell line (a) control (without IL), (b) IC_{25} and (c) IC_{50} of $[P_{14,6,6,6}][Cl]$ IL.

6.2.1.2 In vitro cytotoxic activity against K562 (Chronic myelogenous leukemia) cell line.

An in vitro anticancer effect of the three phosphonium ILs $[P_{14,6,6,6}][NTf_2]$, $[P_{14,6,6,6}][N(CN)_2]$ and $[P_{14,6,6,6}][Cl]$ were employed using MTT assay. The dose dependent cytotoxicity was observed in three ILs treated K562 (chronic myelogenous leukemia) cells and were depicted in the figures 6.4 (a & b), 6.5 (a & b) and 6.6 (a & b) respectively. From the figure, it can be found that the fifty percent cell death, which determines the inhibitory concentration (IC_{50}) concentration detected were 241.9 ±2.4, 175 ± 6.2 and 40 ±5.3 at 24 h incubation respectively. The lower the IC_{50} value, the more cytotoxic is found to be the ILs used. Bright field inverted light microscopy images of control (untreated IL) and IC_{50} of three ILs are tabulated in the figures 6.4 (b), 6.5 (b) and 6.6 (b) respectively. From the above results, it can be analysed that $[P_{14,6,6,6}][Cl]$ shows lower IC_{50} value , higher cytotoxicity than other two ILs. It is evident from the results that the biocompatibility of the IL is affected by the anion [Cl]. These results support the anti–cancer property of the above mentioned ILs against K562 cell lines. The results attained with ILs against the K562 cells are compared with HEK non–malignant cells. The HEK cell line got a IC_{50} values of 218.78 ± 3.9 µM/Ml, 57.5 ± 2.8 µM/Ml and 175± 2.3 µM/Ml for three samples and which shows the higher value of IC_{50} concentration comparing to K562 cell line in three ILs studied. These ILs were more efficient on K562 cancer cells and less toxic to HEK cells at same concentrations.[147-151]

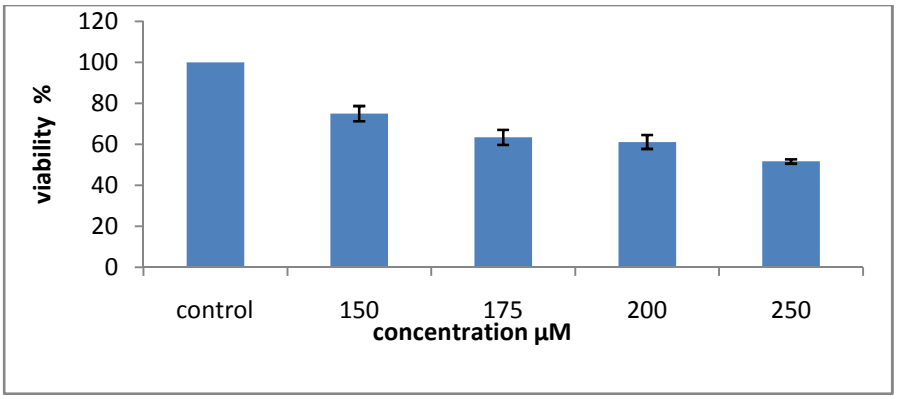

Figure 6.4 (a). In vitro cytotoxicity effect of $[P_{14,6,6,6}][NTf_2]$ against K562 (chronic myelogenous leukemia) cell line. The detected IC_{50} concentration was 241.9 ±2.3 µM/Ml .

a) b)

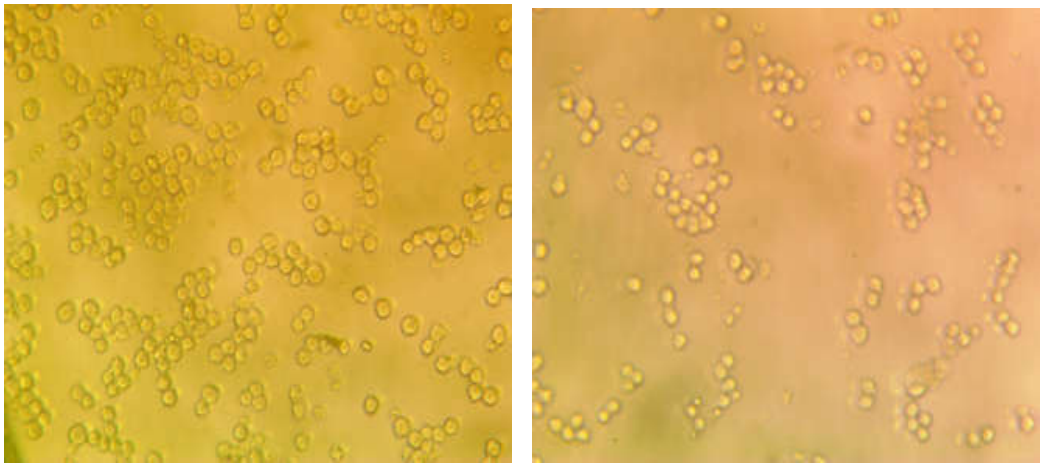

Figure 6.4 (b). Bright field inverted light microscopy images of K562 (chronic myelogenous leukemia) cell line (a) control (without treated IL), (b) IC_{50} concentration of $[P_{14,6,6,6}][NTf_2]$.

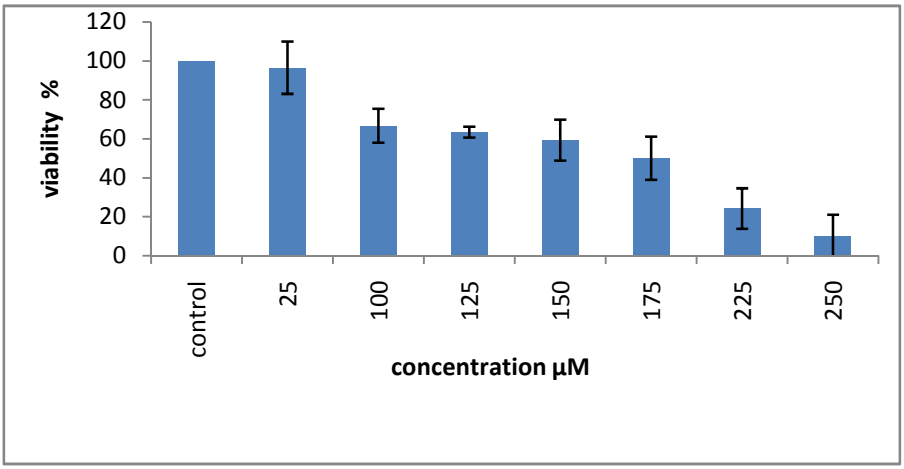

Figure 6.5 (a). In vitro cytotoxicity effect of $[P_{14,6,6,6}][N(CN)_2]$ against K562 (chronic myelogenous leukemia) cell line . The detected IC_{50} concentration was 175 ± 6.2 µM/Ml

a) b)

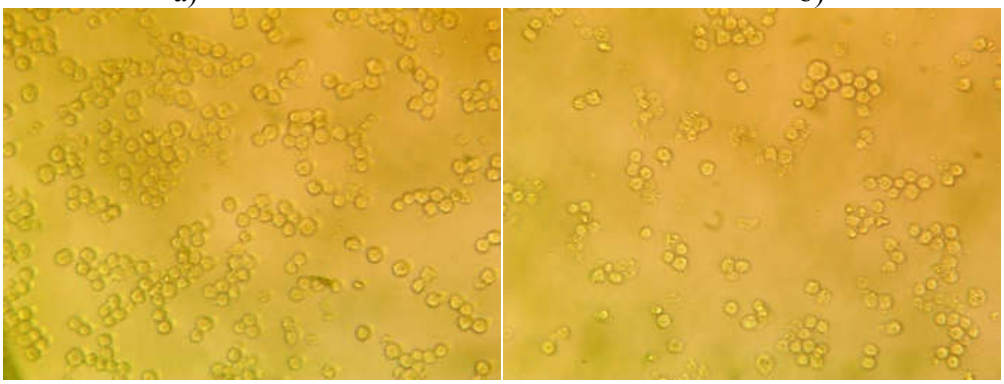

Figure 6.5 (b). Bright field inverted light microscopy images of K562 (chronic myelogenous leukemia) cell line (a) control (without treated IL) (b) IC_{50} concentration of $[P_{14,6,6,6}][N(CN)_2]$

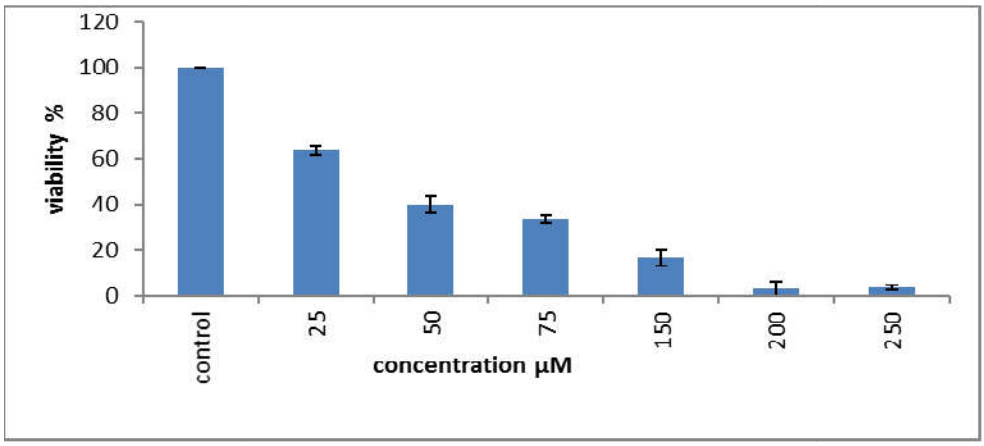

Figure 6.6 (a). In vitro cytotoxicity effect of $[P_{14,6,6,6}][Cl]$ against K562 (chronic myelogenous leukemia) cell line . The detected IC_{50} concentration was 40 ±5.3 µM/Ml .

a) b)

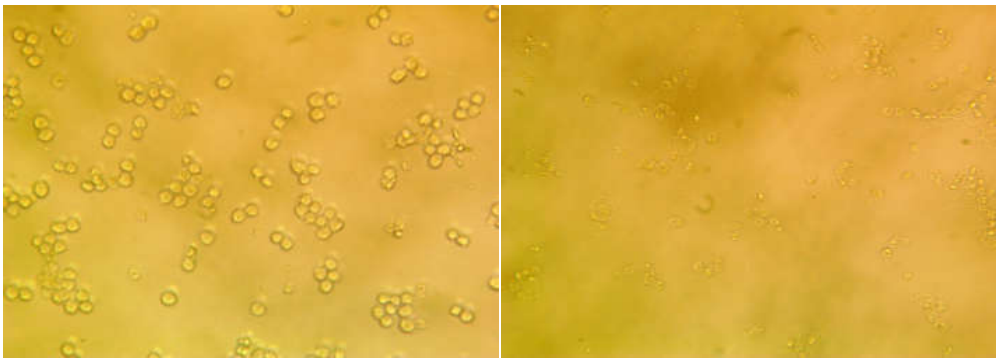

Figure 6.6 (b). Bright field inverted light microscopy images of K562 (chronic myelogenous leukemia) cell line (a) control (without treated IL), (b) IC_{50} concentration.

6.2.1.3 In vitro cytotoxic activity against Jurkat E6-1 (leukemic T cell lymphoblast) cell line.

In vitro cytotoxicity assay for hydrophobic phosphonium based ILs, $[P_{14,6,6,6}][NTf_2]$, $[P_{14,6,6,6}][N(CN)_2]$ and $[P_{14,6,6,6}][Cl]$ ILs against Jurkat E6-1 (leukemic T cell lymphoblast) cell line were conducted using a standard 3–(4,5–dimethylthiazol–2–yl)–2,5– diphenyltetrazolium bromide (MTT) reduction assay. The percentage cell viability of the above mentioned ILs were calculated with respect to the control for 1 day and the results are shown as bar diagram in the figures 6.7 (a & b), 6.8 (a & b) and 6.9 (a & b) respectively. The fifty percent cell death, which determines the inhibitory concentration (IC_{50}) concentration noticed were 168.8 ±5.2, 146.25 ± 7.2 and 23.75 ±2.4 µM/Ml respectively. The lower the IC_{50} value, the more cytotoxic is the ILs used. Bright field inverted light microscopy images of control (without treating IL) and IC_{50} of three ILs are charted in figure 6.7 (b), 6.8 (b) and 6.9 (b) respectively. From the results it shows that $[P_{14,6,6,6}][Cl]$ shows lower IC_{50} than other two ILs. The cytotoxicity evaluation results of the ILs are promising point to reduce the proliferation of cancerous cells of Jurkat E6-1. The results attained with ILs against Jurkat E6-1 cells were compared with HEK non-malignant cells. The HEK cell line got a IC_{50} values of 218.78 ± 3.9 µM/Ml, 57.5 ± 2.8 µM/Ml and 175± 2.3 µM/Ml for three studied samples respectively and which shows the higher value of IC_{50} concentration comparing to Jurkat E6-1 cell line in three ILs studied. These ILs were more proficient on Jurkat E6-1 cancer cells and less harmful to HEK cells at same concentrations.[138-147]

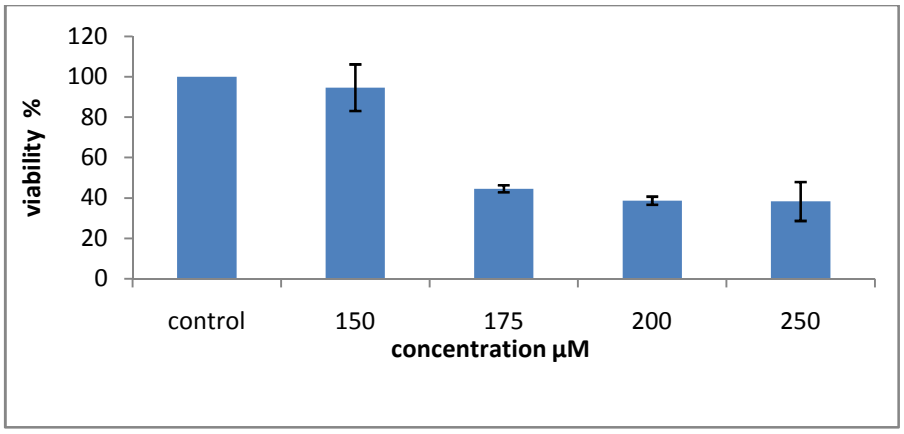

Figure 6.7 (a). In vitro cytotoxicity effect of $[P_{14,6,6,6}][NTf_2]$ against Jurkat E6-1 (leukemic T cell lymphoblast) cell line. The detected IC_{50} concentration was 160.8 ±5.2 µM/Ml.

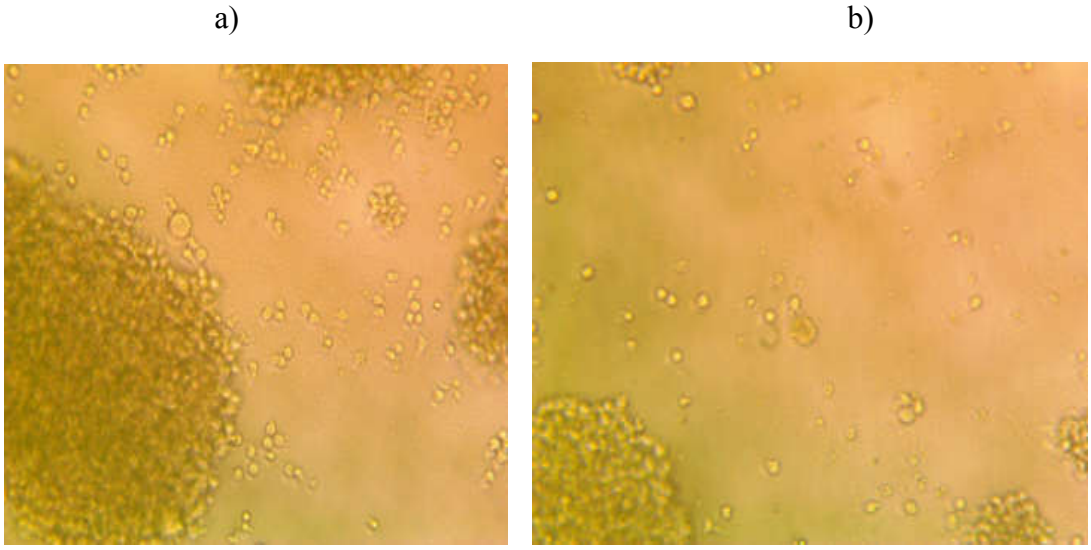

Figure 6.7 (b). Bright field inverted light microscopy images of Jurkat E6-1 (leukemic T cell lymphoblast)cell line (a) control (without treated IL) (b) IC_{50} concentration of $[P_{14,6,6,6}][NTf_2]$IL.

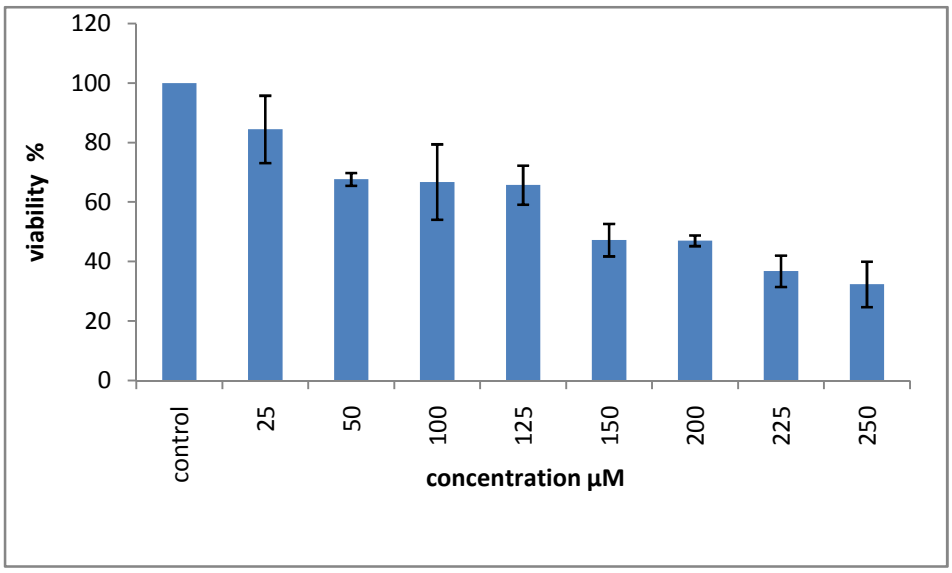

Figure 6.8 (a). In vitro cytotoxicity effect of $[P_{14,6,6,6}][N(CN)_2]$ against Jurkat E6-1 cell line. The detected IC_{50} concentration was 146.25 ±7.2 µM/Ml.

a) b)

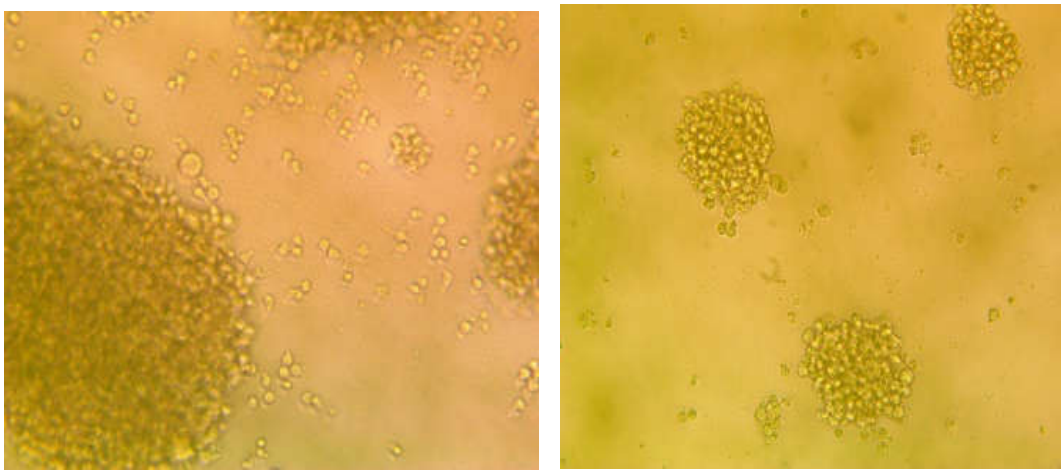

Figure 6.8 (b). Bright field inverted light microscopy images of Jurkat E6-1 cell line (a) control (without treated IL), (b) IC_{50} concentration of $[P_{14,6,6,6}][N(CN)_2]$ IL.

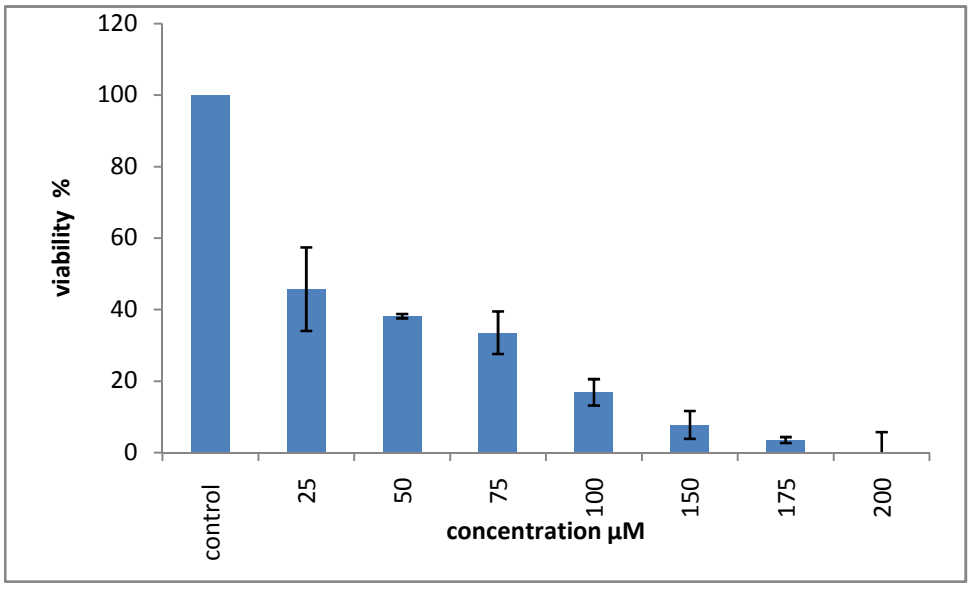

Figure 6.9 (a). In vitro cytotoxicity effect of $[P_{14,6,6,6}][Cl]$ against Jurkat E6-1 (leukemic T cell lymphoblast) cell line. The detected IC_{50} concentration was 23.75 ±2.4 µM/Ml.

a) b)

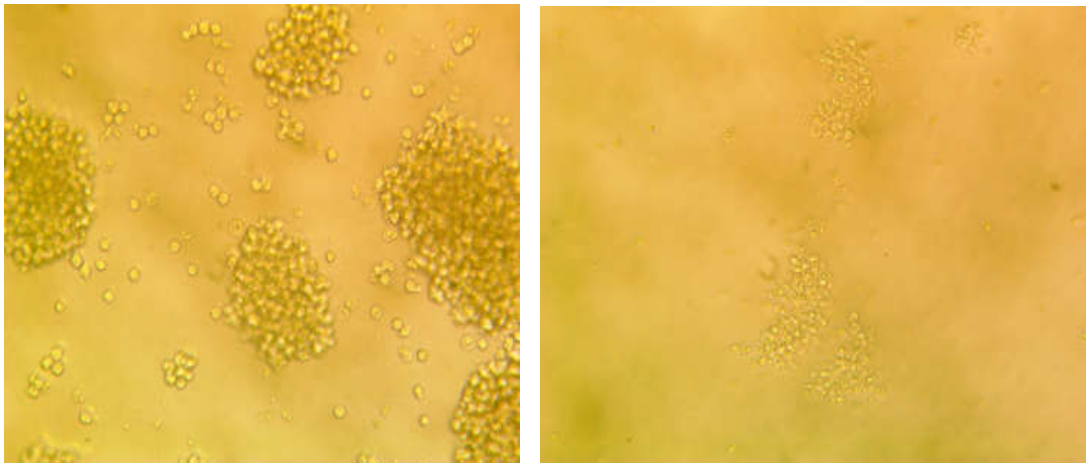

Figure 6.9 (b). Bright field inverted light microscopy images of Jurkat E6-1 cell line (a) control (without treated IL), (b) IC_{50} concentration of $[P_{14,6,6,6}]$ [Cl] IL.

6.2.1.4 In vitro cytotoxic activity against HCT 116 (colorectal carcinoma) cell line.

The antiproliferative effect of three phosphonium based ILs $[P_{14,6,6,6}][NTf_2]$, $[P_{14,6,6,6}]$ $[N(CN)_2]$ and $[P_{14,6,6,6}][Cl]$ against HCT 116 (colorectal carcinoma) cells were clearly demonstrated with MTT assay and microscopic images. To assess the cellular toxicity of the three ILs, we treated a number of HCT 116 cells in a culture medium with high and low concentration for 24 h and compared with control cells (untreated ILs). Toxicity has been generally found within 24 h and the results were tabulated as bar diagram. From the figure it can be observed that, the fifty percent cell death, which determines the inhibitory concentration (IC_{50}) concentration discovered were 503.11 ±2.6, 288 ± 4.8 and 107.5 ± 5.1 µM/Ml respectively. The lower the IC_{50} value, the more cytotoxic is the ILs used. The bright field inverted light microscopy images of control (without treating IL) and IC_{50} of three ILs are presented in the figures 6.10 (a & b), 6.11 (a & b) and 6.12 (a & b) respectively. From the results, it can be seen that $[P_{14,6,6,6}][N(CN)_2]$ shows lower IC_{50} than other two ILs. The results of ILs against HCT 116 cells were compared with HEK non-malignant cells. The HEK cell line got a IC_{50} values of 218.78 ± 3.9 µM/Ml, 57.5 ±

2.8 µM/Ml and 175± 2.3 µM/Ml for three studied samples respectively and it showed the higher value of IC_{50} concentration relating to HCT 116 cell line. The presence of strong electronegative or electron donating groups has a strong impact on the lipophilicity of molecules which can fluctuate the cytotoxicity of the drug candidates.[138-147]

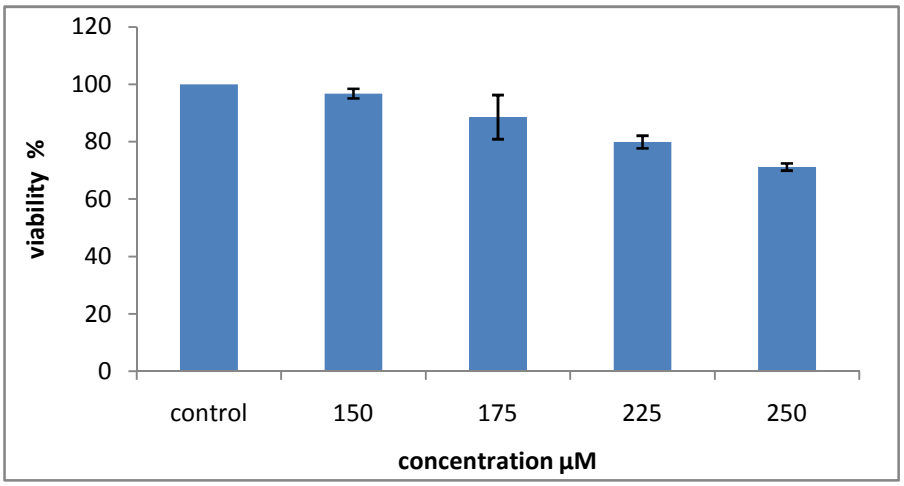

Figure 6.10 (a). In vitro cytotoxicity effect of $[P_{14,6,6,6}][NTf_2]$ against HCT 116 (colorectal carcinoma) cell line . The detected IC_{50} concentration was 503.11 ±2.5 µM/Ml.

a) b)

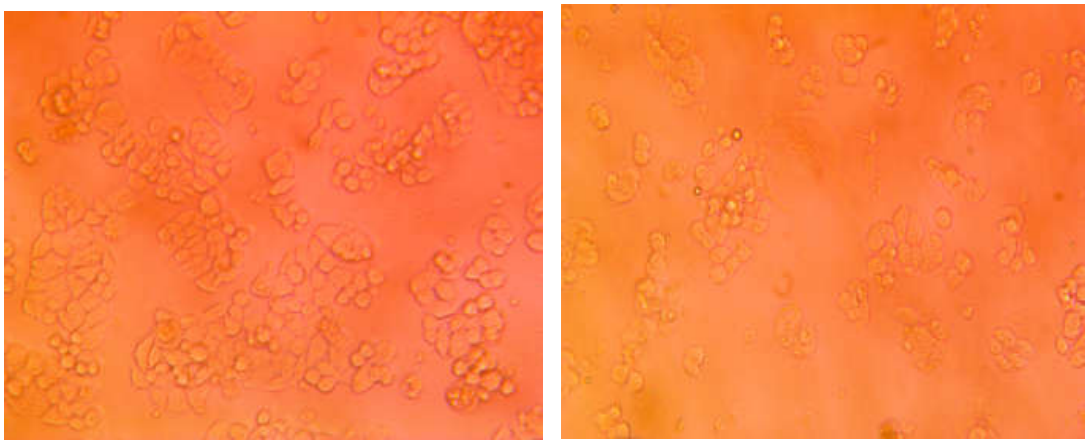

Figure 6.10 (b). Bright field inverted light microscopy images of HCT 116 (colorectal carcinoma) (a) control (without treated IL), (b) IC_{50} concentration of $[P_{14,6,6,6}]$ $[NTf_2]$ IL.

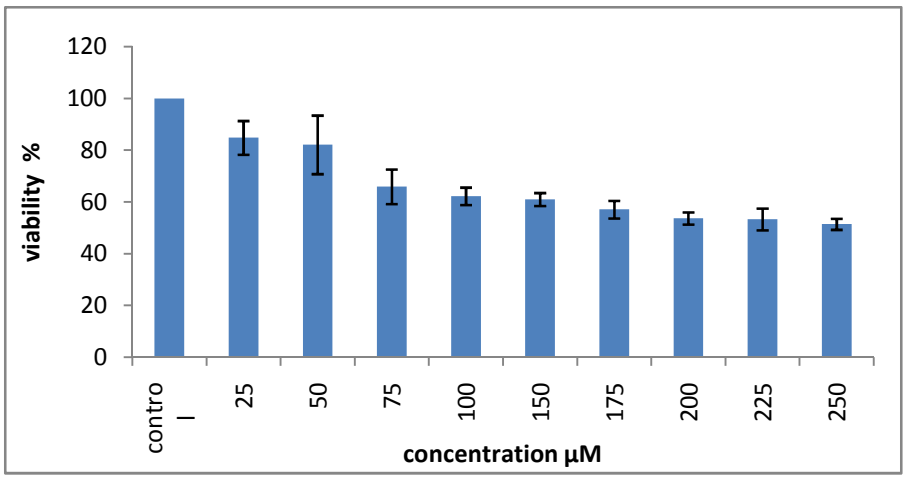

Figure 6.11 (a). In vitro cytotoxicity effect of $[P_{14,6,6,6}][N(CN)_2]$ against HCT 116 (colorectal carcinoma) cell line . The detected IC_{50} concentration was 288 ±4.8 µM/Ml .

a) b)

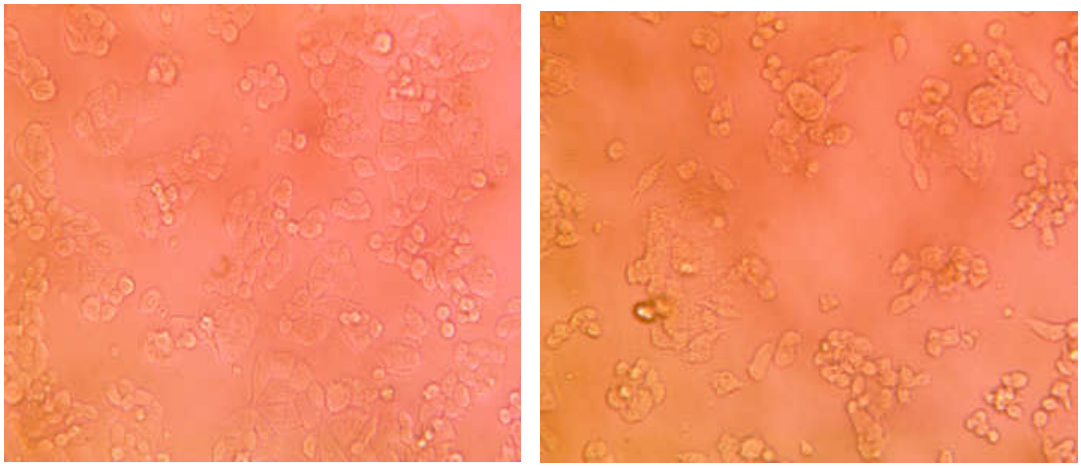

Figure 6.11 (b). Bright field inverted light microscopy images of HCT 116 (colorectal carcinoma) (a) control (without treated IL), (b) IC_{50} concentration of $[P_{14,6,6,6}][N(CN)_2]$ IL.

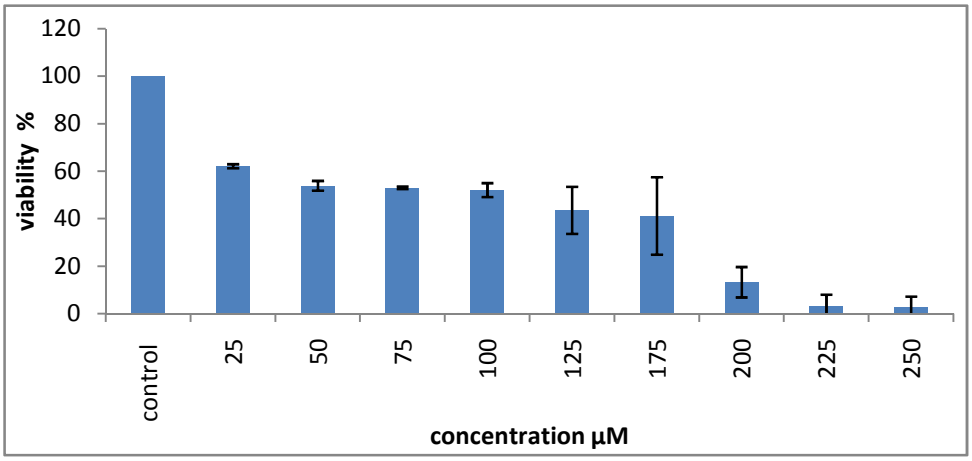

Figure 6.12 (a). In vitro cytotoxicity effect of $[P_{14,6,6,6}][Cl]$ against HCT 116 (colorectal carcinoma) cell line . The detected IC_{50} concentration was 107.5 ±5.1 µM/Ml.

a) b)

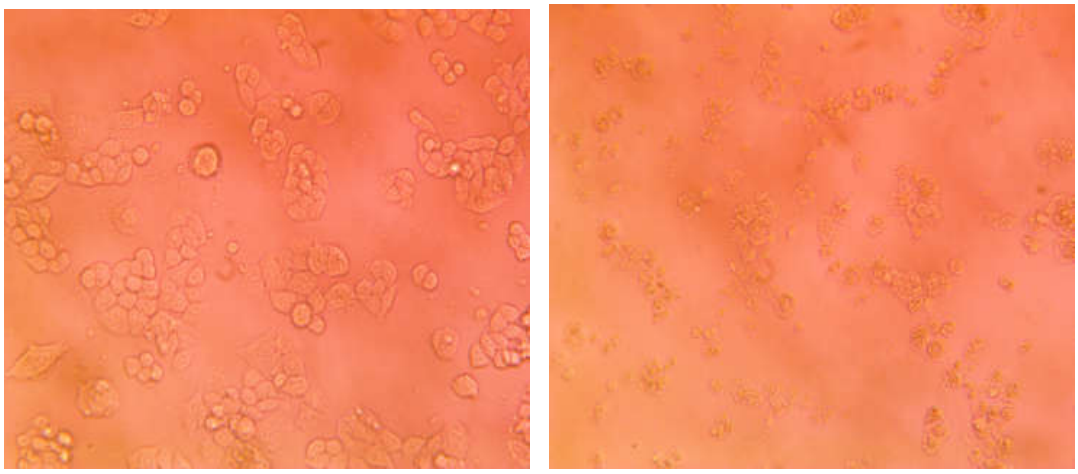

Figure 6.12 (b). Bright field inverted light microscopy images of HCT 116 (colorectal carcinoma) (a) control (without treated IL), (b) IC_{50} concentration of $[P_{14,6,6,6}][Cl]$ IL.

6.2.1.5 In vitro cytotoxic activity against HEK 293 (Human embryonic kidney) cell line.

The MTT cell proliferation assay is widely accepted as a reliable way to measure the cell proliferation rates and cell death. The data obtained by the MTT assay show that ILs $[P_{14,6,6,6}][NTf_2]$, $[P_{14,6,6,6}][N(CN)_2]$ and $[P_{14,6,6,6}][Cl]$ have

inhibitory effects on the growth of HEK cells in dosage-dependent manners shown in the figures 6.13 (a) , 6.14 (a) and 6.15 (a). Bright field inverted light microscopy images of control (without treating IL) and IC_{50} of three ILs are arranged in the figures 6.13 (b), 6.14 (b) and 6.15 (b). The results with ILs against all cell lines measured were compared with HEK non-malignant cells. The HEK cell line got IC_{50} values of 218.78 ± 3.9 µM/Ml, 57.5 ± 2.8 µM/Ml and 175± 2.3 µM/Ml for three studied samples respectively and that showed the higher value of IC_{50} concentration comparing to all cell lines used for the study in three ILs.[138-147]

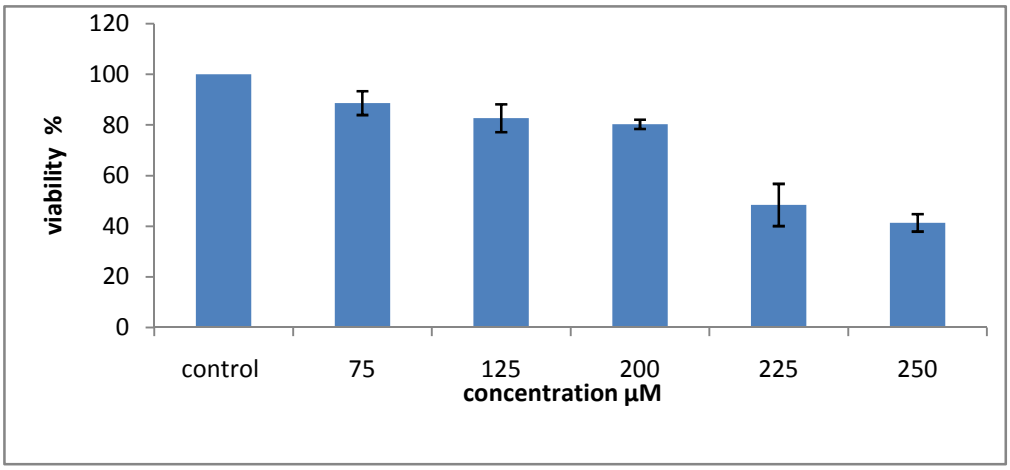

Figure 6.13 (a). In vitro cytotoxicity effect of $[P_{14,6,6,6}][NTf_2]$ against HEK 293 (Human embryonic kidney) cell line (normal). The detected IC_{50} concentration was 218.78 ± 3.9 µM/Ml.

a) b)

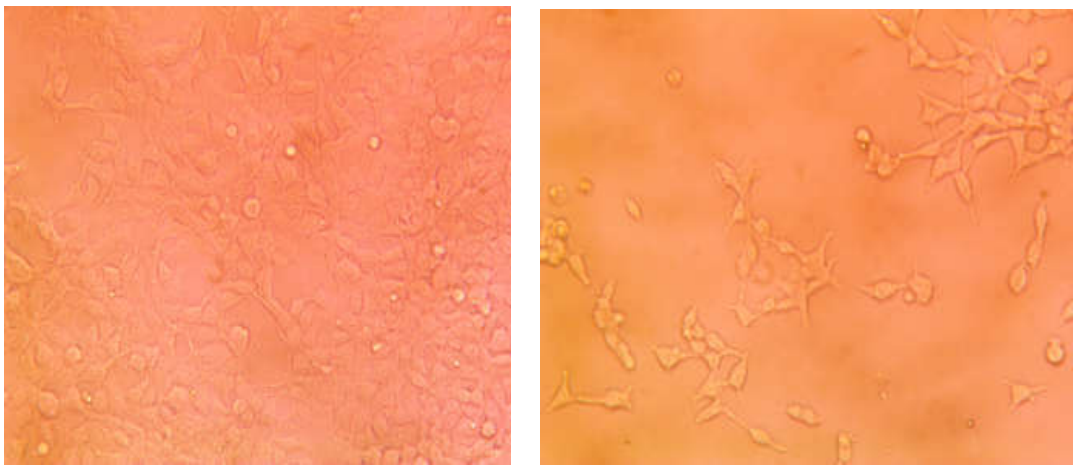

Figure 6.13 (b). Bright field inverted light microscopy images of HEK cell line (a) control (without treated IL) and (b) IC_{50} concentration of $[P_{14,6,6,6}][NTf_2]$ IL.

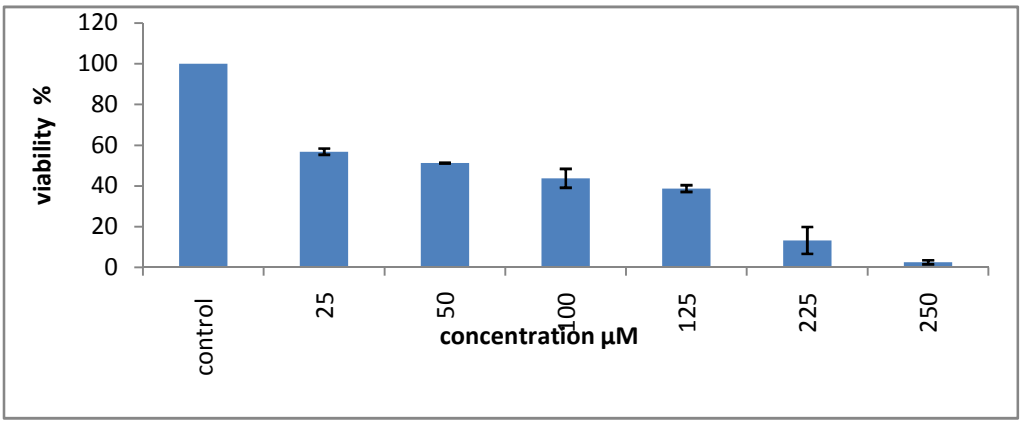

Figure 6.14 (a). In vitro cytotoxicity effect of $[P_{14,6,6,6}][N(CN)_2]$ against HEK cell line. The detected IC_{50} concentration was 57.5 ± 2.8 µM/Ml.

a) b)

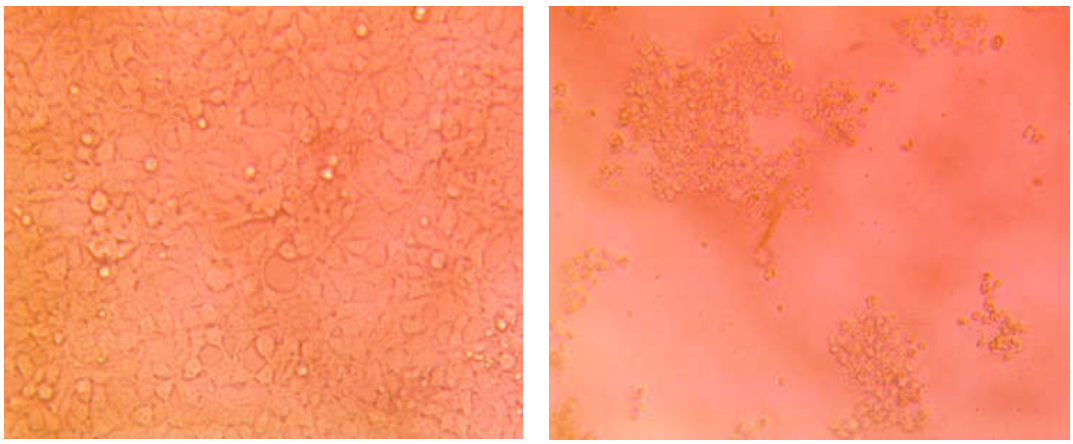

Figure 6.14 (b). Bright field inverted light microscopy images of HEK cell line (a) control (without IL) and (b) IC_{50} of $[P_{14,6,6,6}][N(CN)_2]$ IL.

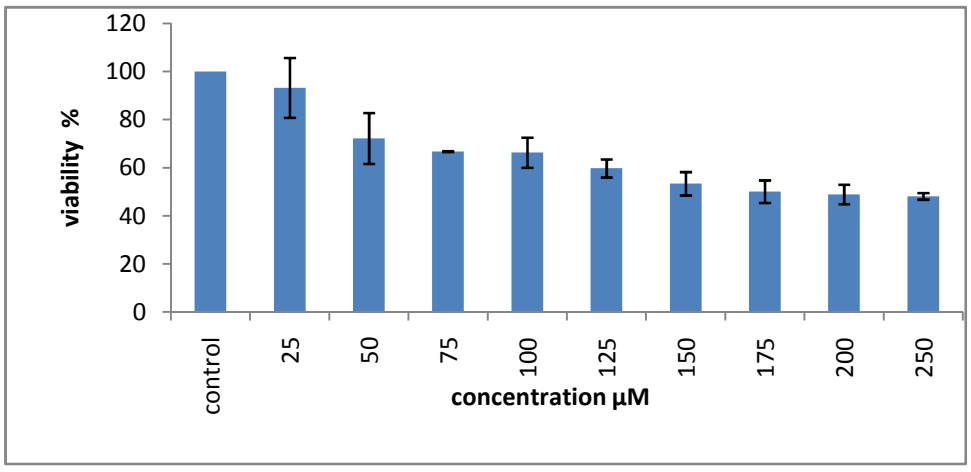

Figure 6.15 (a). In vitro cytotoxicity effect of $[P_{14,6,6,6}]$ [Cl] against HEK cell line. The detected IC_{50} concentration was 175 ± 2.3 µM/Ml.

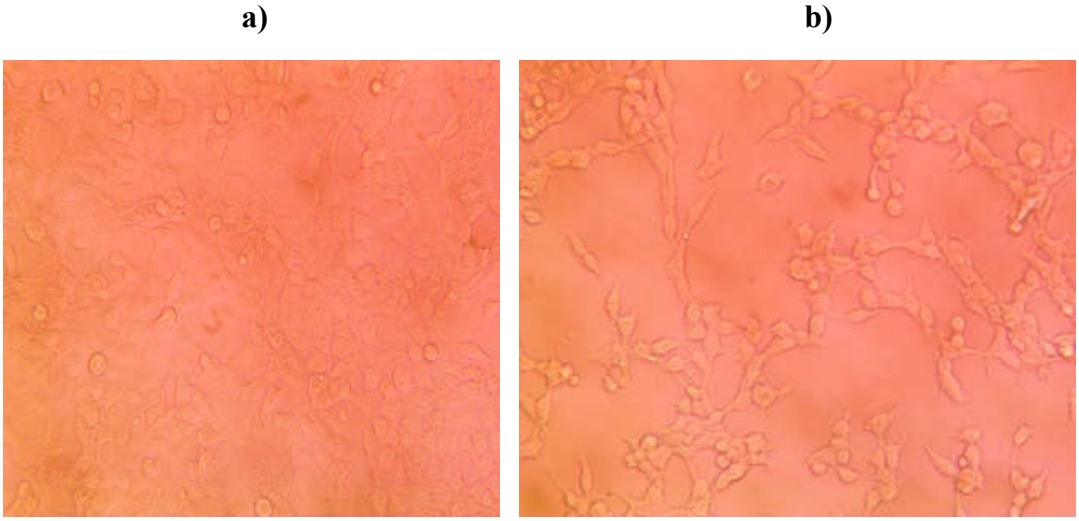

Figure 6.15 (b). Bright field inverted light microscopy images of HEK cell line (a) control (without IL) and (b) IC_{50} of $[P_{14,6,6,6}][Cl]$ IL.

In observance with above results, the anti-cancer activity of the given ILs depends up on the impact of anion used. In this study, the present three ILs are with same cation $[P_{14,6,6,6}]$ but anion is varying as $[NTf_2]^-$, $[(CN)_2N]^-$ and $[Cl]^-$ respectively. In the given three ILs $[P_{14,6,6,6}][N(CN)_2]$ in A549 cell line and $[P_{14,6,6,6}][Cl]$ in other three cell line show the highest anti–cancer activity. The entire results of anti–cancer activity of three ILs in five cell lines as K562, Jurkat E6-1, HCT 116 and HEK 293 (normal cells) are presented in table 6.4.

***Table 6.4**. The calculated IC_{50} values (MTT assay) of $[P_{14,6,6,6}][NTf_2]$, $[P_{14,6,6,6}][N(CN)_2]$ and $[P_{14,6,6,6}][Cl]$ ILs.*

Cell line	**IC_{50} value (µM/Ml)**		
	$[P_{14,6,6,6}][NTf_2]$	**$[P_{14,6,6,6}][N(CN)_2]$**	**$[P_{14,6,6,6}][Cl]$**
A549	40	25	36
K562	241.9 ± 2.4	175 ± 6.2	40 ± 5.3
Jurkat E6-1	160.8 ± 5.2	146.25 ± 7.2	23.75 ± 2.4
HCT 116	503.11 ± 2.6	288 ± 4.8	107.5 ± 5.1
HEK 293	218.78 ± 3.9	175± 2.3	57.5 ± 2.8

6.2.2. Anti–bacterial activity of phosphonium based ILs

Adhesion of bacteria on a surface can cause problems in healthcare, food and beverage storage, water treatment, and the shipping industry. The usage of antibiotics to bypass the difficulties mentioned here can be useless in many times due to antibacterial resistance. Thus, it is critical to generate new antibacterial alternatives against the general bacteria's that are found in skin infections of extreme importance.[147-150] The progress of animated antibiotics that do not trigger microbial resistance continues to be one of the major challenges faced by the pharmaceutical industry. ILs with their intrinsic antimicrobial potentials and highly tunable nature, are aspiring to address this requirement. IL cations (e.g., imidazolium, pyridinium, quaternary ammonium and phosphonium) can be combined with a diversity of anions to create a different set of compounds with properties that can be further tuned via functionalization of either ion. Previously, a systematic evaluation of several different cation/anion pairings was conducted with superior antimicrobial activity and low cytotoxicity to human cells. Hiring from the literature results, we suggest to test the potential application of the three phosphonium based ILs $[P_{14,6,6,6}][NTf_2]$, $[P_{14,6,6,6}][N(CN)_2]$ and $[P_{14,6,6,6}][Cl]$ as an anti–microbial agent to treat skin infection by determining its efficacy against escherichia coli (gram-negative) and the staphylococcus aureus (gram-positive). In the present study, the in vitro anti–bacterial activity of the given three ILs were observed against escherichia coli and the staphylococcus aureus.[46]

6.2.2.1 In vitro anti–bacterial activity of $[P_{14,6,6,6}][Tf_2N]$ IL

The anti–bacterial activity of $[P_{14,6,6,6}][NTf_2]$ was observed by measuring the width of the inhibitory zones against Escherichia coli and the staphylococcus aureus. S. aureus and E. coli are the general bacteria's that are found in the contaminated wound. The sample IL $[P_{14,6,6,6}][NTf_2]$ was tested against S. aureus and E. coli stains at different concentrations of IL as 2.5, 5.0, 7.5, 10.0 and 12.5 **(**μg/ml**)**. It was found that while increasing the concentration, the measured inhibition zone for E. coli and S. aureus were increasing. Figure 6.16 shows the anti–bacterial activity of the given IL. Relatively, the antibacterial activity of IL against E. coli is slightly

higher than that of S. aureus. The anti–bacterial activity results are well maintained by the zone of inhibition detected from figure 6.16 (c). The measured inhibition zones for the IL was found to be 0.2, 10.6, 14.3, 17.2, 19.5 and 21 mm for S. aureus, and 0.3, 13.5, 17.3, 20.4, 21.4 and 23.4 mm for E. coli respectively. From the results it is well striking that the IL not only hinders the bacterial adhesion, but also effectively kills the adhered bacteria suggesting effective and long lasting anti–bacterial activity against both E. coli and S. aureus.[46]

a) b)

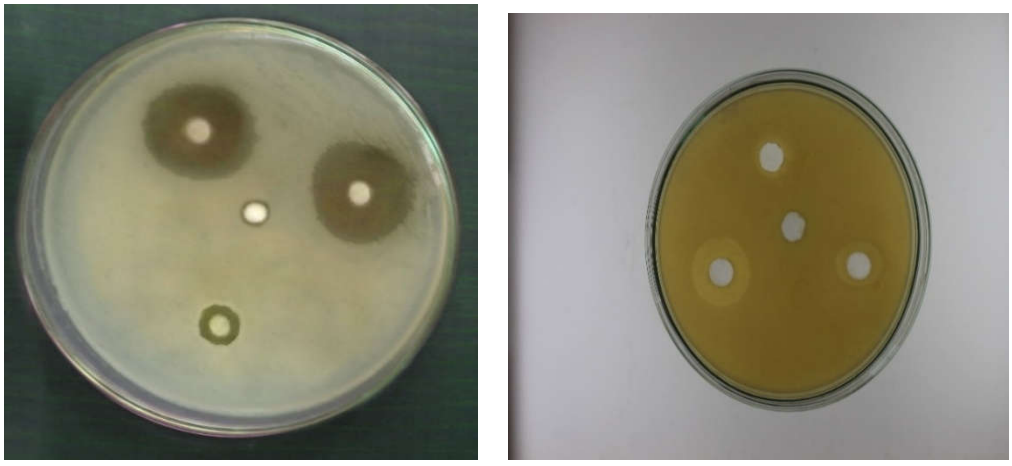

c)

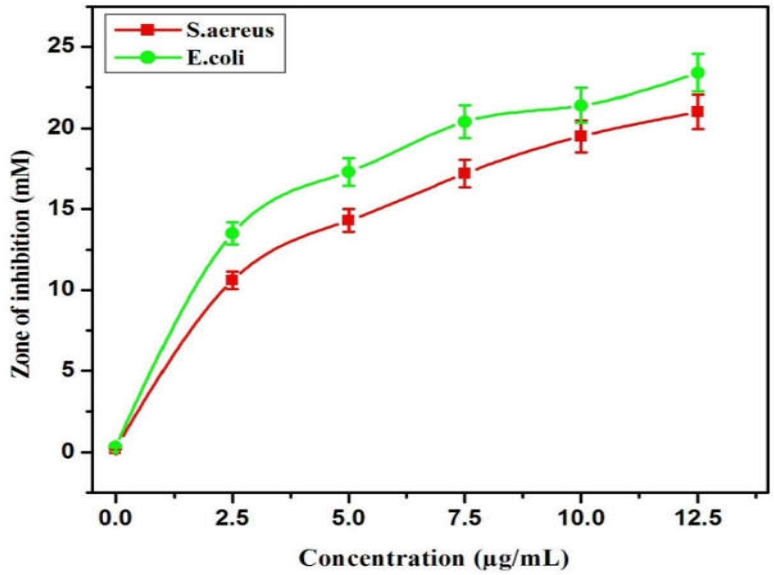

Fig. 6.16. Anti–bacterial activity of $[P_{14,6,6,6}][NTf_2]$ IL with different concentrations of 0,5.0, 7.5 , 10.0 and 12.5 (µg/ml) against (a) E. coli, (b) S. aureus and (c) photographs for the zone of inhibition of IL against S. aureus and E. coli.

6.2.2.2 In vitro anti−bacterial activity of $[P_{14,6,6,6}][N(CN)_2]$ IL.

The anti−bacterial activity of $[P_{14,6,6,6}][N(CN)_2]$ was detected by measuring the inhibitory zones against E. coli and the staphylococcus aureus at different concentrations of the given IL as 2, 4, 6, 8 and 10 **(**µg/ml**)** respectively. It was observed an inhibition of the bacterial viability in a dose-dependent manner that while increasing of IL concentration, the measured percentage of bacterial inhibition were also increasing for E. coli and S. aureus. Figure 6.17 shows the antibacterial activity of the given IL $[P_{14,6,6,6}]$ $[N(CN)_2]$ IL with different concentrations of 0, 5.0, 7.5, 10.0 and 12.5 (µg/ml) against (a), E. coli (b) S. aureus and (c) photographs for the zone of inhibition of IL against S. aureus and E. coli.

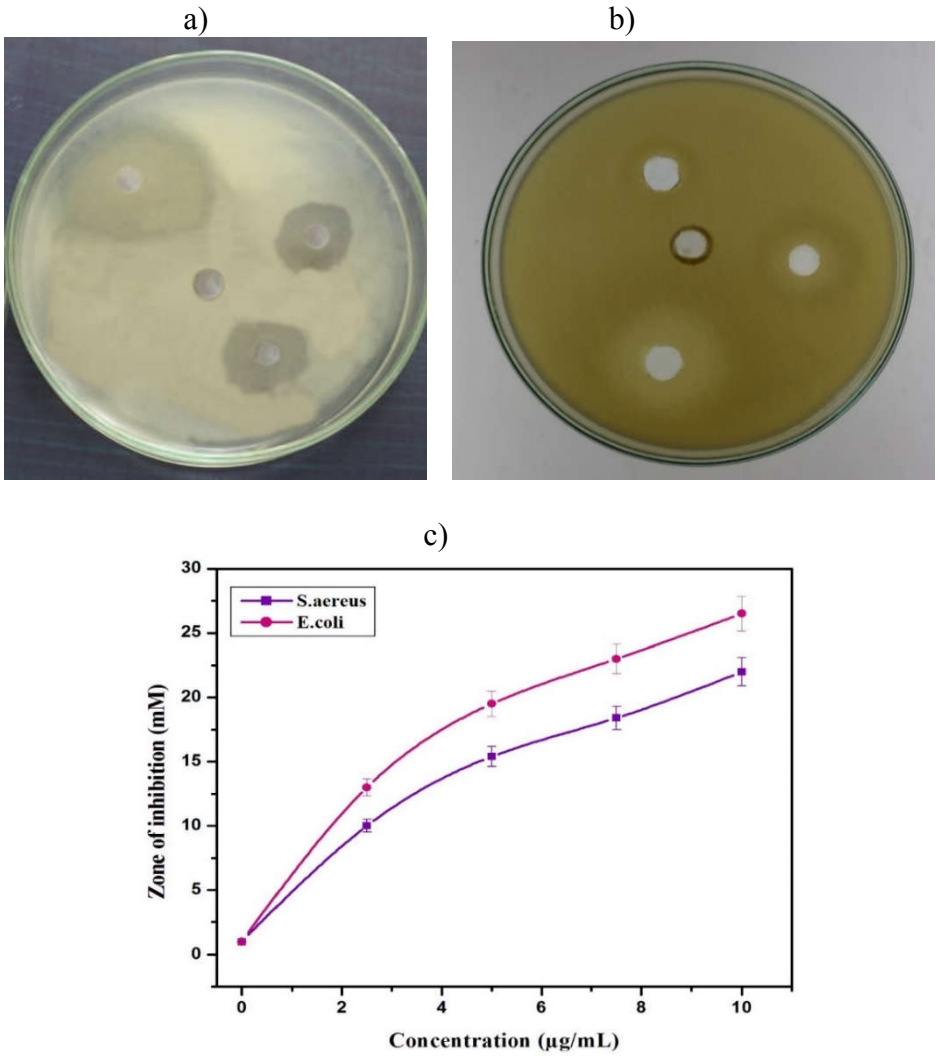

Figure 6.17. Anti−bacterial activity of $[P_{14,6,6,6}][N(CN)_2]$ IL against (a) E. coli (b), S. aureus and (c) photographs for the zone of inhibition of IL.

From the figures 6.17 (a, b & c) it is found that, E. coli is more sensitive for the given IL than that of S. aureus. The measured inhibition zones for the given IL was found to be 0.5, 12.6, 15.3, 19.4, 21.3 and 22.7 mm respectively for S. aureus and 0.5, 14.5, 17.4, 21, 23 and 25.4 mm respectively for E. coli.[46]

6.2.2.3 In vitro anti−bacterial activity of $[P_{14,6,6,6}][Cl]$ IL

The anti−bacterial sensitivity of $[P_{14,6,6,6}][Cl]$ was measured against escherichia coli and the staphylococcus aureus commonly cause skin infection in human body. The activity at different concentrations of IL was detected as 2, 4, 6, 8 and 10 **(**µg/ml**)**. It was observed that while increasing IL concentration, the measured percentage of bacterial inhibition was increasing for E. coli and S. aureus. Figure 6.18 shows the anti−bacterial activity of the given IL and found that, E. coli is more active for the given IL comparing that of S. aureus. The measured inhibition zones for the given IL was found to be 0.3, 9.8, 14.4, 19.4, and 21.2 mm for S. aureus, and 0.4, 12.6, 18.5, 22.1 and 25.2 mm for E. coli respectively.[46]

a) b)

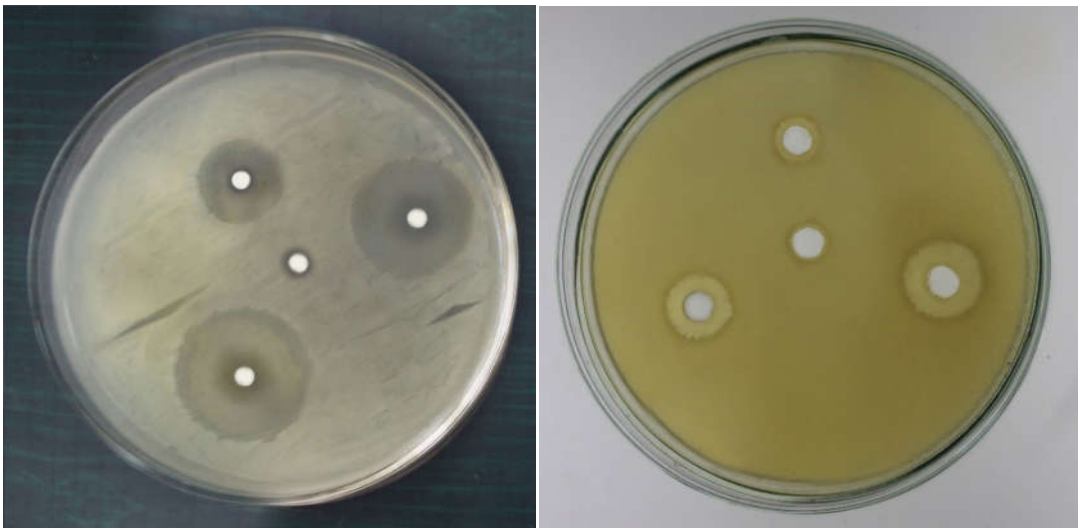

Figure 6.18. Anti−bacterial activity of $[P_{14,6,6,6}][Cl]$ IL with different concentrations of 0, 5.0, 7.5 and 10.0 against (a) E. coli and (b) S. aureus.

c)

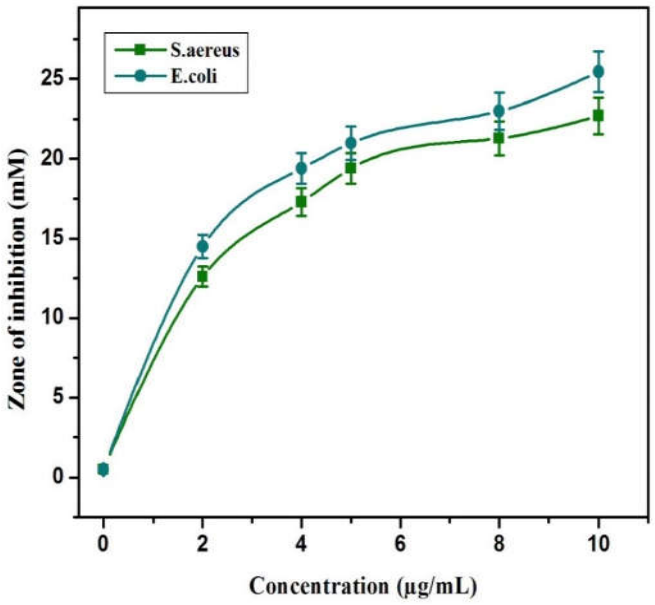

Figure 6.18. (c) photographs for the zone of inhibition of IL against S. aureus and E. coli.

Table 6.5. Bacterial growth inhibition of *three phosphonium based ILs with different concentration against* S. aureus and E. coli by the agar disc diffusion method.

Ionic liquid	Concentration (µg/ml)	E.Coli	S.Aureus
$[P_{14,6,6,6}][NTf_2]$	0	0.3	0.2
	2.5	13.5	10.6
	5	17.3	14.3
	7.5	20.4	17.2
	10	21.4	19.5
	12.5	23.4	21
$[P_{14,6,6,6}][N(CN)_2]$	0	0.5	0.5
	2	14.5	12.6
	4	17.4	15.3
	6	21	19.4
	8	23	21.3
	10	25.4	22.7
$[P_{14,6,6,6}][Cl]$	0	0.4	0.3
	2.5	12.6	9.8
	5	18.5	14.4
	7.5	22.1	19.4
	10	25.2	21.2

In keeping with the observations from our previous studies, the antimicrobial activity of the given ILs depends on the influence of anion used. In this study, the three ILs are with same cation but anion is varying. In the given three ILs $[P_{14,6,6,6}][N(CN)_2]$ IL shows highest anti−bacterial activity. The entire outcomes are tabulated in table 6.5. In all ILs it can be observed that E. coli is more sensitive than S. aureus.

6.2.3. Anti−oxidant activity - (DPPH free radical scavenging assay) of phosphonium based ILs

Neurodegenerative diseases, cancer and AIDS are the some disorders caused by the generation of Free radicals. Scavenging activity of antioxidants are useful for the controlling of those diseases.[151-158] Hence it is important to assess the anti-oxidant activity of various chemicals that are not well characterized and their mode of action is not well established. So research on ionic liquids is currently an area of intense effort. Anti−oxidants are that compounds which delay or inhibit the oxidation of lipids or other molecules by inhibiting the initiation or propagation of oxidative chain reactions and prevent the destruction done to the body's cells by oxygen. Various assays are used commonly to detect antioxidant activity and among which DPPH (2,2−diphenyl−1−picrylhydrazyl) stable free radical method is a sensitive way to regulate the antioxidant activity of different medicines. The DPPH radicals react with suitable reducing agents (anti−oxidant compound) and losing colour due to consumption of electrons was identified by the reduction (disappears) in its absorbance at 517nm.[151-160] The DPPH assay is a very simple method for screening even a small anti-oxidant molecules, due to its reaction and which can be analysed visually and intensity using common spectrophotometric assay. The efficiency of antioxidant activity was found as the IC_{50} value known as half maximal effective concentration of sample to scavenge 50% of free radicals. The lower IC_{50} value shows the higher antioxidant activity of the tested sample.[155-158] In the present study the in vitro antioxidant activity of the given three ILs $[P_{14,6,6,6}][NTf_2]$, $[P_{14,6,6,6}][N(CN)_2]$ and $[P_{14,6,6,6}][Cl]$ were observed with vitamin C/ascorbic acid as standard control.

6.2.3.1 In vitro anti−oxidant property of $[P_{14,6,6,6}][NTf_2]$ IL

DPPH free radical decolourization scavenging activities of $[P_{14,6,6,6}][NTf_2]$ IL was evaluated with vitamin C/ascorbic acid as standard control. Figures 6.19 (a & b) show the concentration required to obtain 50% radical inhibition of DPPH activity (IC_{50}) of the IL $[P_{14,6,6,6}][NTf_2]$ and vitamin C/ascorbic acid (standard/reference) as 0.28 mM and 0.023±0.31 mM respectively. The given IL showed a strong antioxidant activity by DPPH radical scavenging activity.[155-156] The result suggests that the given IL can propose as a source of antioxidant agent for pharmacological industry.[159]

6.2.3.2 In vitro anti−oxidant property of $[P_{14,6,6,6}][N(CN)_2]$ IL.

The DPPH free radical scavenging ability of $[P_{14,6,6,6}][N(CN)_2]$ IL was assessed with vitamin C/ascorbic acid as reference sample. Figure 6.20 (a) shows the potent anti-oxidant ability with inhibition of DPPH activity (IC_{50}) of the given IL and compared with Vitamin C/ascorbic acid (standard/reference) as 551.7 ± 14.5 and 0.0227 ± 0.31 mM respectively. The IC_{50} value of the given IL showed relatively poor free radical scavenging activity compared with the standard control.[159] It can be found that % inhibition of DPPH free radical, increased with the increase in the concentration of the IL used.[160]

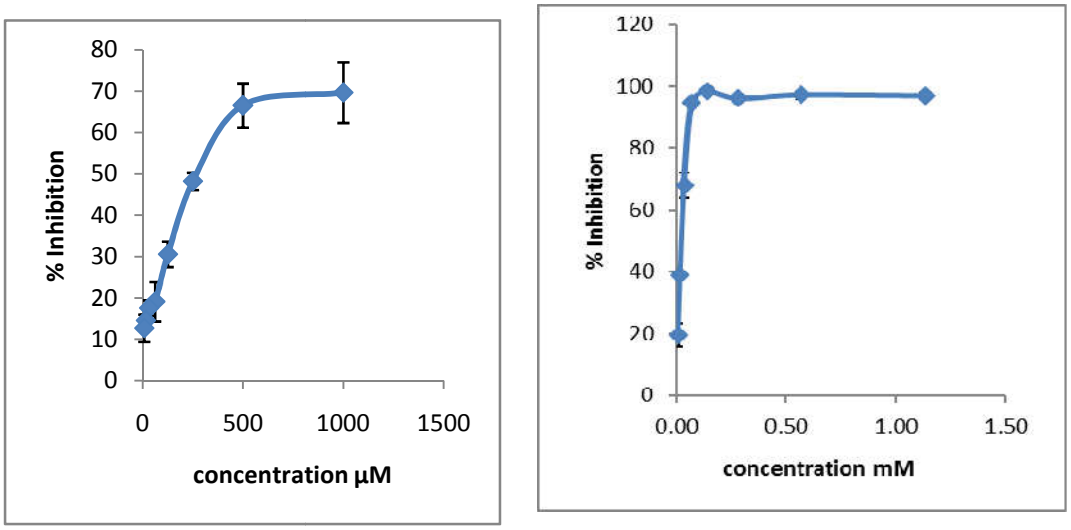

Figure. 6.19. Anti-oxidant property of (a) $[P_{14,6,6,6}][NTf_2]$ IL (b) ascorbic acid with IC_{50} value of 0.28 ± 6.93 and 0.023 ± 0.31 mM respectively.

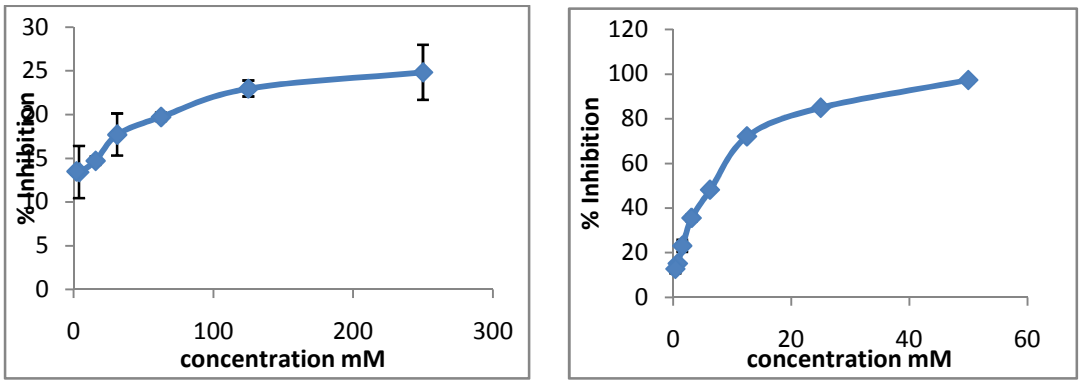

Figure. 6. 20 Antioxidant activity of (a) $[P_{14,6,6,6}][N(CN)_2]$ IL (b) $[P_{14,6,6,6}][Cl]$ IL measured using DPPH methods with ascorbic acid as reference.

6.2.3.3 In vitro anti−oxidant property of $[P_{14,6,6,6}][Cl]$ IL

The DPPH free radical scavenging method of $[P_{14,6,6,6}][Cl]$ IL was evaluated with vitamin C/ascorbic acid as reference sample. Figure 6.20 (b) shows the potent anti−oxidant ability with inhibition of DPPH activity (IC_{50}) of the given IL and compared with Vitamin C/Ascorbic acid (standard/reference) as 9.11 ± 0.15 and 0.023 ± 0.31 mM respectively. The IC_{50} value of the given IL showed relatively a moderate free radical scavenging activity compared with the reference control.[159-160] It can be identified that % inhibition increased with the increase in the concentration of the IL used.

The comparison study of anti−oxidant properties of the given three ILs were studied by DPPH assay. The order of scavenging activity was maximum in $[P_{14,6,6,6}][NTf_2]$ and followed by $[P_{14,6,6,6}][Cl]$. The $[P_{14,6,6,6}][N(CN)_2]$ IL exhibited poor free radical scavenging activity among three ILs. The values are also comparable with commercial antioxidant ascorbic acid.[159-160] Influence of anion is observed from the results tabulated in the table 6.6.

Table 6.6. *The calculated anti-oxidant IC_{50} values (mM) of $[P_{14,6,6,6}][NTf_2]$, $[P_{14,6,6,6}][N(CN)_2]$ and $[P_{14,6,6,6}][Cl]$ ILs*

Sample	IC $_{50}$ value (mM)
$[P_{14,6,6,6}][NTf_2]$	0.28 ± 6.93
$[P_{14,6,6,6}][N(CN)_2]$	552 ± 14.5
$[P_{14,6,6,6}][Cl]$	9 ± 0.15
Ascorbic acid/ vitamin C	0.02 ± 0.31

CHAPTER 7

CONCLUSIONS AND FUTURE PERSPECTIVES

CONCLUSIONS AND FUTURE PERSPECTIVES

In this concluding chapter, we summarize the contributions in the area of ionic liquids and ionogels and the potential influence of diverse technologies as we identify it. The literature review proposes the significant efforts have been made by researchers all over the world in applications of ILs with holding their unique properties. Here, we have make a challenge to explore the glass forming ability of the selected ILs and investigated their potential applications in the field of pharmaceutical, electrochemical, separation technology and biological activities.

Three phosphonium based ILs, trihexyl tetradecylphosphonium bis (trifluoromethyl sulfonyl) amide ($[P_{14,6,6,6}][NTf_2]$), trihexyl tetradecylphosphonium dicyanamide ($[P_{14,6,6,6}]$ $[N(CN)_2]$) and trihexyl tetradecyl phosphonium chloride ($[P_{14,6,6,6}][Cl]$), its binary mixtures with appropriate ILs and polymers ($[P_{14,6,6,6}][NTf_2][Cl]$, $[P_{14,6,6,6}][N(CN)_2][Cl]$, PVA– $[P_{14,6,6,6}][NTf_2]$ ionogel and PVA–$[P_{14,6,6,6}][N(CN)_2]$ ionogel) and two pharmaceutical samples (ranitidine docusate and lidocaine) with potential applications for industrial, pharmaceutical, biological and energy fronts, have been characterised with thermal, dielectric and other spectroscopic techniques were summarised. Thermal analysis were studied with thermogravimetry analysis (TGA) and differential scanning calorimetry DSC), from which, the glass transition temperature, melting temperature and decomposition temperatures were finalised. Dielectric measurements were done by broadband dielectric spectroscopy (BDS) and tested their applications with suitable methods as liquid–liquid extraction, biological activities (MTT assay, agar disc diffusion method and DPPH assay) and *in silico* analysis of drug likeness and toxicity studies by Molinspiration, admetSAR and OSIRIS softwares. The vibrational analysis (FT–IR and FT–RAMAN) were done to analyse the bond formation and structural confirmation of the samples.

Thermal analysis

TGA measurements of three phosphonium ILs $[P_{14,6,6,6}][NTf_2]$, $[P_{14,6,6,6}][N(CN)_2]$ and $[P_{14,6,6,6}][Cl]$ revealed that all ILs exhibited good stability up

to 573 K. TGA results were showing a good thermal stability for two pharmaceutical ILs ranitidine docusate and lidocaine docusate up to 373 K. For binary mixtures, $[P_{14,6,6,6}][NTf_2][Cl]$, $[P_{14,6,6,6}][N(CN)_2][Cl]$, PVA– $[P_{14,6,6,6}][NTf_2]$ ionogel and PVA –$[P_{14,6,6,6}][N(CN)_2]$ ionogel, thermal stabilities were found to be 600 K, 573 K, 303 K and 500 K respectively.

DSC response of $[P_{14,6,6,6}][NTf_2]$, $[P_{14,6,6,6}][N(CN)_2]$ and $[P_{14,6,6,6}][Cl]$ showed a glass transition temperatures 193 K, 195 K and 202 K respectively. Pharmaceutical samples, ranitidine docusate and lidocaine docusate displayed the glass transition temperatures of 209 K and 199 K respectively and that of binary mixtures $[P_{14,6,6,6}][NTf_2][Cl]$, $[P_{14,6,6,6}]$ $[N(CN)_2]$ [Cl], PVA–$[P_{14,6,6,6}][NTf_2]$ ionogel and PVA –$[P_{14,6,6,6}][N(CN)_2]$ ionogel recorded as 190 K, 196 K,226 K , 169 K and a melting peak observed in PVA ionogels as 275K and 206 K 206 K, constantly.

Broadband dielectric spectroscopy

Dielectric spectroscopy reviews polarity fluctuations due to the collective rotational dynamics of dipolar species, and in electrically conductive systems, an additional translational contribution due to charge transport was reported. The analysis of BDS results are summarised below. The conductivity relaxation, charge transport and dielectric studies of a phosphonium based ILs *viz*., $[P_{14,6,6,6}][NTf_2]$, $[P_{14,6,6,6}][N(CN)_2]$, $[P_{14,6,6,6}][Cl]$, that of binary mixtures $[P_{14,6,6,6}][NTf_2][Cl]$, $[P_{14,6,6,6}]$ $[N(CN)_2]$ [Cl], PVA–$[P_{14,6,6,6}][NTf_2]$ ionogel and PVA–$[P_{14,6,6,6}][N(CN)_2]$ ionogel and two pharmaceutical samples ranitidine docusate and lidocaine docusate were investigated using broadband dielectric spectro scopic studies. The comparison study of modulus formalism, conductivity and permittivity representation were used to evaluate the dielectric relaxation phenomena. The dielectric data could be described by J. Dyre's random barrier model in the entire temperature window above glass transition temperature. Below T_g, the secondary relaxation could be clarified by Cole–Cole equation and its T–dependence to Arrhenius law. The DC conductivity was matching with BNN relation, $\sigma \sim \omega$, which showed straight line behaviour. The conductivity relaxation was pronounced by VFT equation above glass transition temperature and T_g were estimated to be 185 K, 190 K, 195 K, 196

K, 193 K, 196 K and 184 K respectively. The fragility or steepness index (m) of ILs and binary mixtures were estimated to be 113, 98, 92, 125, 131, 56 and 47 respectively, which proved fragile behavior of the IL sample. The coupling model predictions (CM) was used to recognise the origin of the secondary (β) relaxation and it was found that there was no match observed with the CM on extending the secondary relaxation from low temperature regime.The β_{KWW} values are 0.5, 0.45, 0.51, 0.51, 0.59, 0.68,0.73, 0.43 and 0.45.

In (PVA−[$P_{14,6,6,6}$][NTf_2]) and (PVA−[$P_{14,6,6,6}$][$N(CN)_2$]), both conductivity relaxation and secondary relaxation showed Arrhenius behaviour. There was no VFT behaviour observed in conductivity relaxation. In the case of lidocaine docusate, two secondary relaxations (β and γ) were described. The additional relaxation (γ process) was not observable in ranitidine docusate. VFT fitting parameters of two ILs identified that the dynamics was more influenced by the anion. From the m value, two pharmaceutical ILs were classified as strong glass formers revealing the stability against temperature fluctuations.

Application in separation technology and biological activities

In technological front, the ILs showed potential ability for the removal of dyes owing to their hydrophobic nature on investigating *via* liquid–liquid extraction method. Toxic textile dyes (rhodamine B, methylene blue, methyl orange, malachite green, alizarin red S and congo red), harmful metal oxides AS $(NO_3)_3$, Cr (NO_3), Cd $(NO_3)_2$, Hg $(NO_3)_2$, Pb $(NO_3)_2$, Zn $(NO_3)_2$, and Cu $(NO_3)_2$ and phenolic compounds from rice and cashew industrial waste waters with ILs were investigated and could successfully removed with three hydrophobic phosph onium ILs. On preliminary exploration of biological activities, these ILs showed very good anti−cancer, anti−bacterial and anti−oxidant activities, highlighting their relevance and significance for pharmaceutical applications. Subsequently, the ILs fulfilled most of the requirements needed for pharmaceutical applications on evaluating pharmacokinetics, bioavailability and toxicity *via in silico* analysis.

FUTURE PERSPECTIVES

- The dielectric measurements with high frequency range can be done to get thorough information of wide relaxation process.
- Different combination of ILs can design various kinds of double active pharmaceutical ingredients, which can have low solubility and can improve the bioavailability and reduce the side effects by formation of Ionic liquid.
- Anti–cancer activity studies of ILs with polymer conjugation improve solubility and tumour targeting ability. In vivo studies of anti–cancer, anti –bacterial and anti–oxidant properties are significant in biological application of studied ILs.
- Phosphonium based ILs shows high operating voltages in super capacitor, hence, its relevance in batteries are a promising electrolyte.
- Ionogel possibilities open up in diverse technological applications, and can apply with different polymer composites, blends, nano composites etc.

REFERENCES

1. H.Weingartner, Understanding ionic liquids at the molecular level: facts, problems and controversies, Angew. Chem.Int.Ed. 47 (2008)654–670.

2. S.Sowmiah,V.Srinivasadesikan,T. Ming-Chung and C. Yen–Ho, On the chemical stabilities of ionic liquids, Molecules.14 (2009)3780–3813.

3. K.Fujita,D. R.MacFarlane and M. Forsyth, Protein solubilising and stabilising ionic liquids, Chem.Commun.(2005)4804–4806.

4. E.Frackowiak, G. Lota, and J.Pernak, Roomtemperature phosphonium ionic liquids for super capacitor applications, Appl. Phys. Lett. 86 (2005)164104-164107.

5. T. Welton, Ionic liquids in catalysis, Coord. Chem. Rev. 248 (2004) 2459–2477.

6. F.Hasan, P. Vidanapathirana, S. Das and V. E. Fernand, Ionic liquids as buffer additives in ionic liquidpolyacrylamide gel electrophoresis separation of mixtures of low and high molecular weight proteins, RSC Adv. 5 (2015) 69229–69237.

7. K. Ghandi, A review of ionic liquids, their limits and applications, G. S.Chem.4(2014) 44–53.

8. W.L Hough, *et al.* The third evolution of ionic liquids: Active pharmaceutical ingredients, New J. Chem.31(2007)1429–1436.

9. J. Liu, F. Wang, L. Zhang, F. Xiaoming and Z. Zhang, Thermodynamic properties and thermal stability of ionic liquid–based nanofluids containing graphene as advanced heat transfer fluids for medium–to–high-temperature applications, J. Renew.Energ. 63 (2014)519–523.

10. M.J. Earle, K.R. Seddon, Ionic liquids. Green solvents for the future, Pure Appl. Chem. 72 (2000) 1391–1398

11. Y. Fukayaab and H.Ohno, Hydrophobic and polar ionic liquids, J. Phys. Chem. Chem. Phys. 15 (2013)4066–4072.

12. E. W. Castner and J. F. Wishart, Spotlight on ionic liquids, J. Chem. Phy. 132(2010)120901-120909.

13. J. R. Sangoro and F. Kremer, Charge transport and glassy dynamics in ionic liquids, J. Acc. Chem. Res.4(2012)525–532.

14. A. S.Pospiech *et al.*,High pressure study of molecular dynamics of protic ionic liquid lidocaine hydrochloride,J. Chem. Phys. 136 (2012)224501-224510.

15. F. Endres and S. Z. Abedin, Air and water stable ionic liquids in physical chemistry,Phys. Chem. Chem. Phys.8 (2006)2101–2116.

16. P. Wasserscheid and W.Keim, Ionic liquids–new solutions for transition metal catalysis, Angew.Chem.Int.Ed.39 (2000)3772–3789.

17. T. Welton,Ionic liquids:a brief history,Bio.Phys. Rev. 10 (2018)691–706.

18. J. S.Wilkes,Ashort history of ionic liquids-from molten salts to neoteric solvents, Green Chem. 4 (2002)73–80.

19. Y. Fukaya *et al.*, Bio ionic liquids:room temperature ionic liquids composed wholly of biomaterials, Green. Chem. 9 (2007)1155–1157.

20. W. L. Hough and R. D. Rogers, Ionic liquids then and now: from solvents to materials to active pharmaceutical ingredients, Bull. Chem. Soc. Jpn.80(2007) 2262–2269.

21. T. Payagala and D. W. Armstrong, *Chiral Ionic liquids: A compendium of Synthesis and Applications*, (Wiley Online Library,New Jersey, 2011)https://doi.org/10.1002/chir.21975.

22. S. K. Riederer,B.Bechlars,W. A. Herrmann and F. E. Kuhn, Chiral *N*–heterocyclic biscarbenes based on 1,2,4-triazole as ligands for metalcatalyzed asymmetric synthesis, J. Dalton Trans.40(2011)41–43.

23. R. Ferraz, L. C. Branco, C. P. Tncio, J. P. Noronha, and Z.Petrovski,*Ionic liquids as Active Pharmaceutical Ingredients*,(Wiley Online Library,New Jersey, 2011)**https://doi.org /10. 1002/cmdc.201100082**.

24. X. Li, et al., Flexible all solid-state supercapacitors based on chemical vapor deposition derivedgraphenefibers, Phys. Chem. Chem. Phys. 15 (2013), 17752.

25. X. Zhang, H. Zhang, C. Li, K. Wang, X. Sun and Y. Ma, Recent advances in porous graphene materials for supercapacitor applications, RSC Adv. 4 (2014)45862–45884.

26. M. Watanabe,L. M. Thomas,S. Zhang,K. Ueno,T. Yasuda,and K.Dokko,Application of ionic liquids to energy storage and conversion materials and devices, J. Chem. Rev. 117 (2017) 7190–7239.

27. K. K. Thasneema, P. Shabeeba,M. Shahin Thayyil,M. Pillai,N. S. Krishna Kumar,G. Govindaraj,V.C. Saheer and M. P. Nighil Nath,Dielectric relaxation and electrochemical studies on trihexyl tetradecyl phosphonium chloride ionic liquid, J. Mol. Liq.252 (2018) 488–494.

28. Y. Miwa *et al*.,Lidocaine self sacrificially improves the skin permeation of the acidic and poorly water soluble drug etodolac via its transformation into an ionic liquid, Eur. J. Pharm. Biopharm.102 (2016) 92–100.

29. K. Adrjanowicz *et al*., Dielectric relaxation studies and dissolution behavior of amorphous verapamil hydrochloride, J.Pharm. Sci. 99 (2010) 828-838.

30. K. Kaminski*et al.*, Dielectric relaxation study on tramadol monohydrate and its hydrochloride salt*, J*.Pharm. Sci.99 (2010) 94-106.

31. C. A. Lipinski, Drug–like properties and the causes of poor solubility and poor permeability, J. Pharm. Technol. Method. 44(2000)235–249.

32. Z. Wojnarowska, C.M. Roland, A. S. Pospiech, K. Grzybowska and M. Paluch, Anomalous electrical conductivity behavior at elevated pressure in

the protic ionic liquid procainamide hydrochloride,Phys. Rev. Lett.108 (2012)015701-015704.

33. M. Gharehbaghi and F. Shemirani, A novel method for dye removal: Ionic liquid based dispersive liquid–liquid extraction, J. Clean-Soil, Air, Wat. 40(2012)290–297.

34. Y. C. Pei *et al.*, Factors affecting ionic liquids based removal of anionic dyes from water, J. Environ.Sci.Tech.41(2007)5090–5095.

35. G. Muthuraman and K. Palanivelu, Selective extraction and separation of textile anionic dyes from aqueous solution by tetrabutylammonium bromide. Dyes Pigm. 64 (2005)251-257.

36. L. Qi, J. Yu, M. Jaroniec,Enhanced and suppressed effects of ionic liquid on the photocatalytic activity of TiO_2,J. Adsorption.19(2013)557–561.

37. A. M. Ferreira, A. P. J. Coutinho, A. M. Fernandesand M. G. Freire, Complete removal of textile dyes from aqueous media using ionic-liquid-based aqueous two-phase systems, J. Separation and Purif. Tech.128(2014)58–66.

38. E. S.Z. El-Ashtoukhyand Y.O. Fouad, Liquid–liquid extraction of methylene blue dyefrom aqueous solutions using sodium dodecylbenzenesulfonate as an extractant, J. Alexa. Eng. 54(2015)77–81.

39. P.Pandit and S. Basu, Removal of ionic dyes from water by solvent extraction using reverse micelles, J. Environ. Sci. Technol. 38(2004)2435–2442.

40. R.Zambare,X. Song, S. Bhuvana,J. S. Antony Prince and P.Nemade,Ultrafast dye removal using ionic liquid−graphene oxide sponge, J. ACS Sustainable Chem. Eng. 5 (2017)6026−6035.

41. A. L. Blanchard, Z. Gu and J. F.Brennecke,High pressure phase behavior of ionic liquid/CO_2 systems, J.Phys.Chem.B. 105 (2001)2437–2444.

42. D. J. Oh and B. C. Lee, High pressure phase behavior of carbon dioxide in ionic liquid 1-butyl-3-methylimidazolium bis(trifluoromethylsulfonyl) amide,Korean J. Chem. Eng. 23(2006)800–805.

43. E. Ali,M. K. Hadj Kali and I. Alnashef,Modeling of CO_2 solubility in selected imidazolium based ionic liquids,J. Chem. Eng. Commun. 204(2017)205–215.

44. C. Yan and T. Mu,Investigation of ionic liquids for efficient removal and reliable storage of radioactive iodine:a halogen-bonding case, Phys. Chem. Chem. Phys. 16 (2014)5071–5075.

45. A. R. Dias,J. C. Rodrigues,M. H. Fernandes, R.Ferrazand C.Prudencio, The anti−cancer potential of ionic liquids, J. Chem. Med Chem.12(2017) 11–18.

46. K. N. Ibsen,H. Ma, A. Banerjee,E. L.Eden Tanner,S.Nangia,and S.Mitragotri, Mechanism of Anti−bacterial activity of choline−based ionic liquids (CAGE), ACS Biomater. Sci. Eng. 4(2018)2370−2379.

47. S.V.Malhotra,V. Kumar,A profile of the in vitro anti-tumor activity of imidazolium based ionic liquids, Bio.Medic. Chem. Lett. 20 (2010)581-585.

48. K. Czerniak and F.Walkiewicz, Synthesis and anti–oxidant properties of dicationic ionic liquids, New J. Chem. 41 (2017)530—539.

49. F Aqil, I Ahmed and ZMehmood, Antioxidant and free radical scavenging properties of twelve traditionally used Indian medicinal plants, Turk. J. Biol. 30 (2006) 177-183.

50. K. S. Egorova, G. E. Gordeevand V. P. Ananikov, Biological activity of ionic liquids and their application in pharmaceutics and medicine,Chem. Rev. 117 (2017)7132−7189.

51. N.K. Kaushik, Y.H. Kim, Y.G. Han and E.H. Choi, Effect of jet plasma on T98G human brain cancer cells, Curr. Appl. Phys. 13 (2013) 176–180.

52. Z. L. Xie *et al.*,Transparent flexible and paramagnetic ionogels based on PMMA and the iron based ionic liquid 1-Butyl 3-methyl imidazolium tetrachloroferrate(III)[Bmim][$FeCl_4$],J.Mater.Chem.20 (2010)9543-9549.

53. M. A. Bin Hasan Susan *etal.*,Ion gels prepared by in situ radical polymerization of vinyl monomers in an ionic liquid and their characterisation as polymer electrolytes, J.Chem.Soc.127 (2005)4976-4983.

54. O. W.Guirguis,Thermal and structural studies of poly(vinyl alcohol) and hydroxypropyl cellulose blends,Nat. Sci.4(2012)57-67.

55. P. Navia,J. Troncoso and L. Romani,Excess magnitudes for ionic liquid binary mixtures with a common ion, J.Chem.Eng.Data. 52(2007)1369-1374.

56. P. Navia, J. Troncoso and L. Romani,Viscosities for ionic liquid binary mixtures with a commmon ion, J . Sol. Chem. 37 (2008)677-688.

57. A. Vioux, L. Viau, S. Volland, J. Le Bideau, Use of ionic liquids in sol-gel, ionogels and applications, ComptesRendusChim. 13 (2010) 242–255.

58. J. Le Bideau, L. Viau and A. Vioux, Ionogels, ionic liquid based hybrid materials, Chem. Soc. Rev. 40 (2011) 907–925.

59. M. A. Bin Hasan Susan etal,Ion gels prepared by in situ radical polymerization of vinyl Monomers in an ionic liquid and their characterisation as polymer electrolytes, J.am.Chem.Soc.127(2005)4976-4983.

60. V.K Shalu and R.K Singh, Development of ion conducting polymer gel electrolyte membranes based on polymer PVdF-HFP, BMIMTFSI ionic liquid and the Li-salt with improved electrical, thermal and structural properties, J. Mater. Chem. 3 (2015) 7305–7318.

61. B. Schrader, *Infrared and Raman Spectroscopy* (*Wiley Online Library,*Weinheim, New York,1995).

62. C. Tabti, N. Benhalima, Molecular Structure, Vibrational Assignments and Non-Linear Optical Properties of by DFT and ab Initio HF Calculations, Adv. Mater. Phys. Chem. 5 (2015) 221–228.

63. E. R. Talaty, S. Raja, V. J. Storhaug, A.Dolle and W. Robert Carper,Raman and infrared spectra and ab initio calculations of $C_{2\text{-}4}$MIM imidazoliumhexafluorophosphate ionic liquids,J. Phys. Chem. B. 108(2004)13177-13184.

64. S. Vyas,C. Dreyer, J. Slingsby,D. Bicknase, J. M. Porter and C. M. Maupin, Electronic structure and spectroscopic analysis of 1□Ethyl-3 methylimidazoliumbis(trifluoromethylsulfonyl) imide ion pair, J. Phys. Chem. A. 118 (2014) 6873−6882.

65. Y. Jeon, J. Sung, C. Seo, H. Lim, H. Cheong, M. Kang, B. Moon, Y. Ouchi and D. Kim,Structures of ionic liquids with different anions studied by infrared vibration spectroscopy,J. Phys. Chem. B.112 (2008)4735-4740.

66. C. K. Z. Andrade, R. A. F. Matos,V. B. Oliveira,J. A. Duraes, M. J. A. Sales, Thermal study and evaluation of new menthol-based ionic liquids as polymeric additives, J. Therm. Anal Calorim. 99 (2010)539–543.

67. G. P. Johari, O. Andersson, On the nonlinear variation of dc conductivity with dielectric relaxation time, J. Chem. Phys. 125 (2006) 1–7.

68. D. Q.M. Craig, P. G. Royall, V. L. Kett, M. L. Hopton, The relevance of the amorphous state to pharmaceutical dosage forms: glassy drugs and freeze dried systems, Int. J. Pharm.179(1999)179–207.

69. B. C Hancock and S. L. Shamblin, Molecular mobility of amorphous pharmaceuticals determined using differential Scanning Calorimetry, Thermochem. Act. 380 (2001) 95-107.

70. L.Yu, Amorphous pharmaceutical solids: preparation, characterization and stabilization, Adv. Drug Deliv. Rev. 48 (2001)27–42.

71. L.M. Wang, C.A. Angell, Erratum: Response to "Comment on 'direct determination of the fragility indices of glassforming liquids by differential scanning calorimetry: Kinetic versus thermodynamic fragilities,'" J. Chem. Phys. 118 (2003) 10353–10355.

72. O.W. Guirguis, M.T.H. Moselhey, Thermal and structural studies of poly (vinyl alcohol) and hydroxypropyl cellulose blends, Nat. Sci. 4 (2012) 57–67.

73. T.H. Kim, T. Shibata, S. Kojima, D.M. Shin, Y.H. Hwang, J.H. Ko, Comparison of thermal and elastic properties of glassy racemic and enantiomorphic ibuprofen studied by Brillouin light scattering and modulated differential scanning calorimetry, Curr. Appl. Phys. 14(2014) 965–969.

74. C. A. Angell, A. Dworkin, P. Figuiere, A. Fuchs and H. Szwarc, Strong and fragile plastic crystals. J. Chem. Phys. 62 (1985)773-782.

75. L.M. Wang, C.A. Angell, R. Richert, Fragility and thermodynamics in nonpolymeric glass-forming liquids, J. Chem. Phys. 125 (2006) 1–8.

76. D. Q. M. Craig, M. Barsnes, P. G. Royall and V. L. Kett, An evaluation of the use of modulated temperature DSC as a means of assessing the relaxation behaviour of amorphous lactose,Pharm. Res.17 (2000)6-14.

77. H. McPhillips, D.Q. M. Craig, P.G. Royall, V.L. Hill, Characterisation of the glass transition of HPMC using modulated temperature differential scanning calorimetry, J. Pharm. Sci. 180(1999)83–90.

78. P. Debye, *Polar Molecules*, (The Chemical Catalog Company, New York,1929).

79. A. M. Kaushal, P. Gupta and A. K. Bansal, Amorphous drug delivery systems: molecular aspects,design, and performance, Crit. Rev.Therap. Drug Carrier. Sys.21(2004)133-193.

80. J. Leys *et al.,* Influence of the anion on the electrical conductivity and glass formation of 1-butyl-3-methylimidazolium ionic liquids. J. Chem. Phys.133(2010)034503-034513.

81. K. Adrjanowicz *et al.,* Molecular dynamics in supercooled liquid and glassy states of antibiotics: Azithromycin, clarithromycin and roxithromycin studied by dielectric spectroscopy. Advantages given by the amorphous state. Mol. Pharm.9(2012)1748–1763.

82. J. Leys,M. Wübbenhorst, C. P. Menon, R. Rajesh, J. Thoen and C.Glorieux, Temperature dependence of the electrical conductivity of imidazolium ionic liquids,J. Chem. Phys. 128 (2008)064509-064516.

83. C. Krause, J. R. Sangoro, C. Iacob, and F. Kremer, Charge transport and dipolar relaxations in imidazolium−based ionic liquids,J. Phys. Chem. B. 114 (2010) 382–386.

84. D. W Davidson and R. H. Cole. Dielectric relaxation in glycerine. J. Chem.Phys. 8(1950)141-149.

85. R. Richert, H. Wagner, The dielectric modulus: relaxation versus retardation, Solid State Ionics. 105 (1998) 167–173.

86. A. Rivera, A. Brodin, A. Pugachev and E.A. Rossler, Orientational and translational dynamics in room temperature ionic liquids, J. Chem. Phys.126 (2007)114503-114510.

87. A.C. Rodrigues, M. T. Viciosa, F. Danede, F. Affouard, N. T. Correia, Molecular mobility of amorphous S−Flurbiprofen: a dielectric relaxation spectroscopy approach*.,* Mol. Pharmaceutics.11 (2014)112−130.

88. J. C. Dyre, Colloquium: The glass transition and elastic models of glassformingliquids. Rev. Modern Phys. 78 (2006)953–972.

89. Z. Wojnarowska *et al.,*Molecular dynamics studies on the water mixtures of pharmaceutically important ionic liquid lidocaine HCl, Mol. Pharm. 9 (2012)1250–1261.

90. J. Sangoro *et al.,* Electrical conductivity and translational diffusion in the 1-butyl-3-methylimidazolium tetrafluoroborate ionic liquid, J. Chem. Phys. 128 (2008)214509-214 514.

91. A. Lasia, *Electrochemical Impedance Spectroscopy and its Applications, Modern Aspects of Electrochemistry* (Plenum Publishers, New York, 1999).

92. J.C. Dyre and N.B. Olsen. Landscape equivalent of the shoving model, Phys.Review B. 69 (2004)042501-042510.

93. S.Capaccioli,M.Shahin Thayyil and K.L Ngai, Critical issues of current research on the dynamics leading to glass transition,J.Phy.Chem.B.112 (2008)16035-16049.

94. J. C. Dyre, Master equation approach to glass transition,Phys. Rev. B. 51 (1995) 276-288.

95. Z. Wojnarowska *et al.,* Molecular dynamics, physical stability and solubility advantage from amorphous indapamide drug. Mol. Pharm.10(2013)3612–3627.

96. G. P. Johari, Intrinsic mobility of molecular glasses. J.Chem.Physic. 58 (1973) 1766-1776.

97. S.S.N Murthy, M.Shahin Thayyil, A note on sub–Tg relaxation process in poly(cyclohexylmethacrylate), Eur. Poly. Journ.42 (2006)715-720.

98. M. Shahin, S.S.N Murthy and L.P Singh, Glass transition phenomena in two – Component crystals: study of hexasubstituted benzenes, J. Phy. Chem.B. 110 (2006)18573-18582.

99. K. L. Ngai, M. ShahinThayyil and Li-Min Wang, Quasielastic neutron scattering evidence of coupling of caged molecule dynamics to JG β-relaxation, J. Mol. Liq.247(2017)300-303.

100. H. Niedermeyer *et al.*, Mixtures of ionic liquids, Chem. Soc.Rev.41(2012)7780-7802.

101. E.Thoms *et al.,* Dielectric study on mixtures of ionic liquids, scientific reports.7(2017) 7463-7471.

102. G. Chatel *et al.*, Mixing ionic liquids-“ simple mixtures” or “double salts”?,Green. Chem.16 (2014)2051-2083.

103. J. R. Sangoro, C. Iacob, L. Agapov, Y. Wang, S. Berdzinski, H. Rexhausen, V. Strehmel, C. Friedrich, P. Sokolov, F. Kremer, Decoupling of ionic conductivity from structural dynamics in polymerized ionic liquids, Soft Matter. 10 (2014) 3536–40.

104. T. Fahmy, M.T. Ahmed, Broadband Dielectric Spectroscopy and Electric Modulus Analysis of Poly (3-hydroxybutyrate-co-3- hydroxyvalerate) and Related Copolymers Films, Int. J. Phys. Appl. 8 (2016) 1–14.

105. F. Kremer, A. Schonhals,*Broadband Dielectric Spectroscopy* (Springer-Verlag Berlin Heidelberg, New York, 2003).

106. K. S. Cole and R. H. Cole, Dispersion and absorption in dielectrics I, Alternating current characteristics, J. Chem. Phys. 9 (1941)341-352.

107. R. Macdonald, *Impedance Spectroscopy*(John Wiley & Sons, New York, 1987).

108. S.P.S. Badwal,*Solid State Ionic Devices* (World Scientific, Singapore, 1988).

109. J.E. Bauerle, Solid electrolytes and their applications, J. Phys. Chem. Solid.30 (1969)2657-2670.

110. B.Y. Liaw, *Electrochemical Aspects of Ionic Solids* (Wiley, New York, 1997).

111. M. Köhler, P. Lunkenheimer, A. Loidl, Dielectric and conductivity relaxation in mixtures of glycerol with LiCl, Eur. Phys. J. ESoft Matter Biol. Phys. 27 (2008) 115–122.

112. A.K. Jonscher, The interpretation of non-ideal dielectric admittance and impedance diagram, Phys. Stat. Solid.32(1975)665-676.

113. A.K. Jonscher and J. M Reau, Analysis of the complex impedance data for beta-PbF_2,J. Mater. Sci. 13 (1978) 563-570.

114. A.K. Joncher, The universal dielectric response: A review of data and their new interpretation, Phys. Thin Films. 11 (1980) 205-317.

115. J.C. Wang, J.B. Bates, Dielectric response of ionic conductors, J. Solid State lonics.115(1988)28-30.

116. P.B**.** Macedo, C. T. Moynihan and R. Bose, The role of ionic diffusion in polarization in ionic vitreous conductors, Phys.Chem. Glasses.13(1972)171-179.

117. A.K. Joncher, The 'universal' dielectric response, Nature. 267 (1977) 673-679.

118. A.K. Joncher,New interpretation of dielectric loss peaks,Nature. 256 (1975) 566-568.

119. S. Schrodle, G. Annat, D. R. MacFarlane, M. Forsyth, R. Buchnerd and G. Hefter, Broadband dielectric response of the ionic liquid N-methyl-N-ethylpyrrolidiniumdicyanamide, Chem. Commun. **(**2006)1748–1750.

120. D. V Matyushov, On the theory of dielectric spectroscopy of protein solutions, J. Phys: Condens. Matter.24(2012)325105-325120.

121. C.T. Moynihan, Analysis of electrical relaxation in glasses and melts with large concentrations of mobile ions,J. Non-Cryst. Sol. 172 (1994) 1395-1407.

122. R. Brand, P. Lunkenheimer and A. Loidl, Relaxation dynamics in plastic crystals, J. Chem. Phys. 116 (2002) 10386-10401.

123. J. Sangoro, T. Cosby and F. Kremer, Chapter 2, *Rotational and translational diffusion in ionic liquids* (Springer,Switzerland, 2016).doi: 10.1007/978-3-319-32489-02.

124. J. R. Sangoro, C. Iacob, A. Serghei, C. Friedrich and F. Kremer, Universal scaling of charge transport in glass-forming ionic liquids, Phys. Chem. Chem. Phys. 11 (2009)913–916.

125. C.A. Angell, K.L. Ngai, G.B. McKenna, P.F. McMillan, S.W. Martin, Relaxation in glassforming liquids and amorphous solids, J. Appl. Phys. 88 (2000)3113–3157.

126. H. Tanaka, Two-order-parameter description of liquids. I. A general model of glass transition covering its strong to fragile limit, J. Chem. Phys. 7 (1999) 3163–3173.

127. R. Bohmer, K. L. Ngai, C.A. Angell, D. J. Plazek, Nonexponential relaxations in strong and fragile glass formers. J. Chem. Phys.99(1993)4201-4209.

128. K. Adrjanowicz *et al.,* Molecular mobility in liquid and glassy states of Telmisartan (TEL) studied by broadband dielectric spectroscopy, Eur. J. Pharm. Sci.38(2009)395–404.

129. W. Xu, E. I. Cooper, C. A. Angell, Ionic liquids: Ion mobilities, glass temperatures, and fragilities, J. Phys. Chem. B. 107 (2003)6170-6178.

130. E. Frackowiak, G. Lota, and J.Pernak, Roomtemperature phosphonium ionic liquids for super capacitor applications, Appl. Phys. Lett.86 (2005)164104-164107.

131. A. Al Kahtani, Photocatalytic degradation of rhodamine B dye in wastewater using Gelatin/CuS/PVA nanocomposites under solar light irradiation, J. Biomat.Nanobiotech. 8 (2017) 66-82.

132. Z. Talbi, B. Haddou, H. Ghouas,M. Kameche, Z. Derriche, and C. Gourdon, Cationic dye removal from aqueous solutions using ionic liquid and non−ionic surfactant−ionic liquid systems: a comparative study based upon experimental design, Chem. Eng. Comm. 201 (2014)41–52.

133. M.Sudha, A.Saranya, G. Selvakumar and N. Sivakumar,Microbial degradation of Azo Dyes: A review, Int.J.Curr.Microbiol.App.Sci.3(2014) 670-690.

134. M. Messali, M. R. Aouad, W. S. El-Sayed, A. Al-Sheikh Ali, T. B. Hadda and B. Hammouti, New eco-friendly 1-Alkyl-3-(4-phenoxybutyl) imidazolium−based ionic liquids derivatives: a green ultrasound-assisted synthesis, characterization, anti−bacterial activity and POM analyses,J. Molecules.19(2014)11741-11759.

135. N. Rezki, S. A. Al-Sodies, M.Messali, S. K. Bardaweel, P. K. Sahu, F. F. Al-blewi, P. K. Sahu, M. R. Aouad, Identification of new pyridinium ionic liquids tagged with Schiff bases:Design, synthesis, in silico ADMET predictions and biological evaluations,J. Mol. Liq. 264(2018)367–374.

136. T. B. Hadda, Z. K. Genc, V. H. Masand, N. Nebbache, I Warad, S. Jodeh, M. Genc, Y. N.Mabkhot, A. Barakat, H. S. Zamora, Computational POM and DFT evaluation of experimental *in–vitro* cancer inhibition of staurosporine-Ruthenium(II) complexes: The power force of organometallics in drug design. Acta. Chem. Slov. 62 (2015) 679-688.

137. Z. Hakkou, A. Maciuk, V. Leblais, N. E. Bouanani, H. Mekhfi, M. Bnouham, M. Aziz, A. Ziyyat, A. Rauf, T. B. Hadda, U. Shaheen, S. Patel, R. Fischmeiste, A. Legssyer,Antihypertensive and vasodilator effects of methanolic extract of Inulaviscosa: Biological evaluation and POM analysis of cynarin, chlorogenic acid as potential hypertensive. Biomed. Pharm.93 (2017) 62-69.

138. R.Raghavan, S. Cheriyamundath and J.Madassery, 14-Deoxy-11,12didehydroandrographolide inhibits proliferation and induces GSH-dependent cell death of human promonocytic leukemic cells, J. Nat Med. 68 (2014)387–394.

139. P. Thasnim and D. Bahulayan, Click-on fluorescent triazolylcoumarinpeptidomimetics as inhibitors of human breast cancer cell line MCF-7,New J. Chem.41 (2017)13483-13489.

140. P. Rajeenaand D. Bahulayan, MCR-click synthesis, molecular docking and cytotoxicity evaluation of a new series of indole–triazole–coumarin hybrid peptidomimetics, New J. Chem. 42 (2018) 6810-6816.

141. P. Jithin Raj, D. Bahulayan, MCR-Click synthesis of coumarin-tagged macrocycles with large Stokes shift values and cytotoxicity against human breast cancer cell line MCF-7, Tetrahedron Lett. 58(2017)2122–2126.

142. A. Bahuguna, I. Khan, V. K. Bajpai and S. C. Kang,MTT assay to evaluate the cytotoxic potential of a drug, Bangl. J. Pharmacol. 12 (2017)115-118.

143. B. H. Ho, M. Y. Cho, J. H. Hong, H. Poo, M. H. Sung and Y. T. Lim, Bio-Derived Poly(γ-Glutamic Acid) Nanogels as Controlled Anti–cancer Drug Delivery Carriers, J. Microbiol. Biotechnol.22(2012)1782–1789.

144. V. Kumar, S. Malhotra, Study on the potential anti-cancer activity of phosphonium and ammonium-based ionic liquids,Bioorg. Medic. Chem. Lett. 19(2009)4643–4646.

145. J. Iqbal, B. A. Abbasi, T. Mahmood, S. Kanwal, B. Ali, S. A. Shah, A. T. Khalil, Plant-derived anti–cancer agents: A green anticancer approach,Asian Pac. J. Trop Biomed, 7(2017)1129–1150.

146. S. M. Sundarraj, R. Thangama, M. V. Sujitha,K.Vimalaand S.Kannan, Ligand-conjugated mesoporous silica nanorattles based on enzyme targeted prodrug delivery system for effective lung cancer therapy, Toxic. Appl. Pharm.275 (2014)232–243.

147. M. Krishnamoorthy, S. Hakobyan, M. Ramstedt and J. E. Gautrot, Surface–initiated polymer brushes in the biomedical field: Applications in membrane science, biosensing, cell Culture, regenerative medicine and anti−bacterial coatings. Chem Rev. 114(2014) 10976-11026.

148. O. F. Doria, R. Castro, M. Gutierrez, D. G. Valenzuela, L. Santos, D. Ramirez and L. Guzman, Novel Alkylimidazolium ionic liquids as an anti−bacterial alternative to pathogens of the skin and soft tissueinfections,Molecules. 23 (2018) 2354-2369.

149. R. Ferraz, V.Teixeira, D. Rodrigues, R.Fernandes, C. Prudencio, J. P. Noronha, Z. Petrovski and L. C. Branco, Anti–bacterial activity of ionic liquids based on ampicillin against resistant bacteria,RSC Adv. 4 (2014)4301–4307.

150. P. Mozhiyarasi and R. Anuradha, A study on phytochemical analysis and anti–microbial activity of Hyptissuaveolens (L.) poit,J. Chem. Pharm. Res.8 (2016)438–442.

151. W. Brand-Williams, M. E.Cuvelier and C. Berset, Use of free radical method to evaluate anti–oxidant activity, Lebensm. Wiss. Technol. 28 (1995)25–30.

152. N. A. Ahmad, K.Jumbri, A. Ramli, N. A.Ghani, H. Ahmad and M. A.Kassimd, Synthesis, characterisation and antioxidant properties of ferulate-based protic ionic liquids: Experimental and modelling approaches, J. Mol. Liq. 278 (2019)309–319.

.N. K. Kaushik, P.Attri, N.Kaushik and E. H. Choi,Synthesis and antiproliferative activity of ammonium and imidazolium ionic liquids against T98G brain cancer cells, Molecules.17(2012)13727-13739.

153. N. Murugan, L. Kavitha, E. Shinyjoy, D. Rajeswari, K. Vimala, S. Kannane and D. Gopi, Smart rose flower like bioceramic/metal oxide dual layer coating with enhanced anti-bacterial, anticancer, anti-corrosive and biocompatible properties for improved orthopedic applications,RSC Adv. 5 (2015)85831–85844.

154. E. Taylor, T. Webster, reducing infections through nanotechnology and nanoparticles. Int. J.Nanomedicine. 6 (2011)1463–1473.

155. P. Veeru, M. P. Kishor and M.Meenakshi, Screening of medicinal plant extracts for anti–oxidant activity, J. Med. Plant. Res. 3 (2009)608-612.

156. S. Chanda, R. Dave and M. Kaneria, *in vitro* anti–oxidant property of some Indian medicinal plants,J. Med. Plant. Res. 5 (2011)169-179.

157. K. Agarwal, R.Varma, Anti–oxidant activity and phytochemical analysis of hyptissuaveolens (L.) Poit, J. Adv. Pharm. Edu& Res. 3 (2013) 541-549.

158. M. Zahin, F. Aqil and I. Ahmad, The *in vitro* anti–oxidant activity and total phenolic content of four indian medicinal plants, Int. J. Pharm.Pharmaceut sci.1 (2009) 88-95.

159. M. Cai, Y. Liang, M. Yao, Y. Xia,F. Zhou, and W. Liu, Imidazolium Ionic Liquids As Anti–wear and Anti–oxidant Additive in -Poly(ethylene glycol) for Steel/Steel Contacts, AppLl. Mat. Int. 3 (2010)870-876.

160. G. P. Johari and M. Goldstein. Viscous liquids and glass transition. II.Secondary relaxations in glasses of rigid molecules. J. Chem. Phys. 53 (1970)2372-2388.

161. C. Iacob, J. R. Sangoro, W. K. Kipnusu, R. Valiullin, J. Karger and F. Kremer, Enhanced charge transport in nano-confined ionic liquids, J. Soft Matter. 8 (2012)289–293.

162. B. T. Schrøder and J. C. Dyre, Ac Hopping Conduction at Extreme Disorder Takes Place on the Percolating Cluster, Phys. Rev. Lett. 101 (2008)025901-025906.

163. G. P. Johari and M. Goldstein. Viscous liquids and glass transition III secondary relaxations in aliphatic alcohols and other nonrigid molecules, J. Chem. Phys. 55 (1971)4245-4252.

164. P. Shabeeba, K.K. Thasneema.,M. Shahin Thayyil, M. P Pillai and C. V. Niveditha, A high voltage supercapacitor based on ionic liquid with an activated carbon electrode. Mater. Res. Express. 4 (2017)075503-075511.

165. P. Shabeeba, K.K. Thasneema.,M. Shahin Thayyil, M. P Pillai and C. V. Niveditha, A graphene-based flexible supercapacitor using trihexyl (tetradecyl) phosphonium bis (trifluoromethylsulfonyl) imide ionic liquid electrolyte. Mater. Res. Express.4(2017)085501-085509.

166. P. Shabeeba, K.K. Thasneema.,M. Shahin Thayyil, M. P Pillai and A. P. Jemshihas, Inorganic salt grafted ionic liquid gel electrolytes for efficient solid state supercapacitors : Electrochemical and dielectric studies. J. Mol. Liq.264(2018)72–79.